The University of Sheffield

School of Mathematical and Physical Sciences

The Boulby Underground Laboratory, STFC

Environmental background in a dual-phase xenon dark matter experiment

Author: Jemima Tranter

Supervisors: Prof. Vitaly Kudryavtsev, Dr. Paul Scovell

Submitted to The University of Sheffield in fulfilment
of the requirements for the award of the degree of
Doctor of Philosophy



The University Of Sheffield.



Science and Technology Facilities Council

Boulby Underground Laboratory

May 2025

Abstract

There is an abundance of cosmological and astrophysical evidence for dark matter. The best-motivated candidate for particle dark matter is the Weakly Interacting Massive Particle (WIMP). The search for WIMPs and the hypothesised neutrinoless double beta ($0\nu\beta\beta$) decay requires detectors with exceptionally low background levels. Next-generation rare-event searches must be shielded from various backgrounds, including gamma-rays from rock. This thesis describes simulations of gamma-ray transport through water shielding and assesses the thickness needed to suppress rock-induced background to a negligible level. The study focuses on a next-generation xenon observatory targeting both WIMP and $0\nu\beta\beta$ searches in ^{136}Xe. For rock radioactivity of 1 Bq kg^{-1}, results show that 3.5 m of water plus 0.5 m of liquid scintillator reduces background in the $0-20$ keV WIMP range to negligible levels. For $0\nu\beta\beta$, fewer than 1 background event in 10 years can be achieved with a fiducial mass of 39.3 tonnes. Reducing the water shielding by 1 m lowers the $0\nu\beta\beta$ fiducial mass to 19.1 tonnes, while still ensuring negligible WIMP background.

This thesis also presents the measurements of radioactivity in rock in the Boulby Mine, a potential site for a future dual-phase xenon experiment. The measurements normalise simulation results and assess Boulby's suitability as host. Polyhalite, the Boulby rock type likely to surround a future detector, shows very low ^{232}Th and ^{238}U concentrations. At these levels, reducing the water shielding by 1 m remains viable for WIMP search, yet decreases the $0\nu\beta\beta$ decay fiducial mass due to ^{238}U. Additionally, an overview of the new radon emanation facility at Boulby is provided, along with preliminary results from polyhalite.

Finally, this thesis includes a study of the muon flux at SURF using LZ data and simulations, identifying a 20 % discrepancy due to rock density assumptions. This contributes to improved modelling of cosmogenic backgrounds for LZ and future experiments hosted at SURF.

Dedication

This thesis is dedicated to my dad. I can only imagine what adventures we would have had this summer to celebrate the end of my studies. You continue to inspire me to be a better person; I can only hope that I make you proud.

Acknowledgements

"So long, and thanks for all the fish." - Douglas Adams

My first thanks must go to Vitaly, I could not have wished for a better supervisor to guide me through this PhD. Thank you for your knowledge, humour and endless wisdom. Your supervisory efforts continuously helped improve the quality of my presentations and my written work (I can *almost* reference properly now). Many thanks also to Paul, you always made time for me and my countless questions. Working with you at Boulby really fired up my interest in low-background, experimental physics, and I appreciate the effort you put into keeping up with me as a remote student for most of the PhD. Thank you both for helping me complete this research; it has been immensely enjoyable.

I would also like to thank those who assisted me at Boulby, particularly Chris and Emma. You made every day there an absolute joy. Sue, Lou and Maria, thank you for putting up with me and getting me to the lift "on time" every day. Thanks to Sean as well for being very supportive of my research and making me feel welcome at Boulby. To Beth, Jonny and George, keep being wonderful, thank you for the amazing company.

To my adopted science family, QSHS, thank you for accepting me into the fold. I have enjoyed your company so much over the last few years. Claude, I love our random office conversations, thank you for keeping me company in E18a. Ed and Susan, you are both fountains of wisdom and wonderful (usually hilarious) stories. Thank you for your excellent company and sage advice every Friday lunchtime. Thanks especially to Ed for your support, encouragement and for not letting me quit 6 months into my PhD. Michael, words cannot describe how much your friendship means to me; I have had so much fun spending time with you; being around such a like-minded soul has helped me get through this PhD.

Many thanks go to the members of the LZ Collaboration. Harvey, I am indebted to you for your help and leadership over the last three years - thank you for putting up with me for so long. I really enjoyed collaborating with you and nattering about climbing. Thanks also to Ewan for all your help and patience. I have met so many lovely people in LZ that I cannot mention all of them here, but to Albert, Amy, Tom, Ellie, Hark, and the SoUP Group, thank you for making conferences and workshops so brilliant.

Finally, I wish to thank my family (including my Yorkshire family) and friends for always supporting me, and even occasionally trying to understand my research. I appreciate you all more than you could ever know. Mum and Alice, thank you for always being there for me, for listening to me, and for entertaining me. You mean the world to me.

Mitch, with all my heart, thank you for the IT support over the last few years, you've been really helpful. Also I love you etc. etc.

Declaration

The contents of this thesis are entirely my own original work unless explicitly stated. Where the work of others has been used, the author has been properly referenced. This includes work done by others in the LZ collaboration. This thesis has not been submitted for consideration for any other qualifications in this, or any other, university.

Personal Contributions

The research presented in Chapters 5 and 6 has been summarised in a paper by J. K. Tranter, V. A. Kudryavtsev and P. R. Scovell entitled "Gamma-ray background from rock: studies for a next-generation dark matter experiment based on liquid xenon", published in Astroparticle Physics, 171 (2025) 103119, DOI: 10.1016/j.astropartphys.2025.103119. The work was carried out by myself, with assistance from the staff at Boulby Underground Laboratory, and with materials provided by ICL Mining Company and two of their geologists, P. Edey and D. Webb. For this project, I designed a stand-alone, full Monte Carlo simulation in GEANT4 to model gamma-ray transport through water shielding and applied analysis cuts to mimic gamma-ray background suppression in the time projection chamber. Building and running the simulation included geometry construction, particle generation, particle transportation, and utilisation of tracking tools. Whilst on-site at Boulby, I screened various rock types from the mine using high-purity germanium detectors and analysed the results using InterSpec and ISOCS software. By normalising simulation results to experimental gamma-ray measurements, I evaluated the impact of Boulby's gamma-ray background on the future detector.

I have been involved in the installation and development of the radon facility at Boulby since 2022, testing and adapting the calibration and sample measurement procedures (originally developed at UCL); and helping to set-up the concentration line and new digitiser. This was alongside general work with electronics, Raspberry Pis, mass flow controllers and Swagelock equipment. I carried out multiple detector calibrations and sample measurements. Additionally, I independently developed new analysis code for the facility to use for processing the data from the detector. This code incorporates decay chain modelling (Bateman equations) to determine the efficiency of the detectors from calibration runs and calculate the radon concentration in samples.

Lastly, the analysis in Sections 8.2 and 8.3 was performed by myself and Harvey Birch in equal measures. We have used simulation tools developed by many people in the LUX-ZEPLIN (LZ) Collaboration and the data from the LZ experiment, hence, the entire LZ Collaboration is credited here for its contributions. I analysed data from 366 days of detector operation, comparing measured muon rates with simulations of cosmic-ray muons travelling through the detector. Using LZ software frameworks, including the simulation framework BACCARAT (based on the GEANT4 toolkit), I evaluated discrepancies between these measured and simulated muon rates, which enabled us to reconstruct the muon flux and estimate the rock density above the cavern that surrounds the LZ detector. The paper that describes the results of this project is under internal review and I am one of the two prime authors.

Contents

1 Introduction **1**

2 Dark matter and rare event searches **3**

2.1 Evidence for dark matter 3

2.1.1 Velocity dispersion of the Coma cluster 3

2.1.2 Rotation curves 4

2.1.3 Gravitational lensing 4

2.1.4 The cosmic microwave background and Big Bang nucleosynthesis 6

2.2 WIMPs 8

2.3 Direct detection experiments 10

2.3.1 Scintillating cryogenic bolometers 10

2.3.2 Cryogenic bolometers with charge readout 11

2.3.3 Dual-phase noble element detectors 12

2.4 $0\nu\beta\beta$ decay 15

3 Backgrounds to rare event searches **17**

3.1 Radionuclides 17

3.2 Radon 20

3.3 Cosmic-ray muons 22

4 Principles of gamma spectroscopy and germanium detectors **26**

4.1 Gamma spectroscopy 26

4.2 Features of gamma-ray spectra 27

4.2.1 Compton scattering and Compton continua 27

4.2.2 Pair production, annihilation and escape peaks 28

4.2.3 Coincidence summing 29

4.3 Germanium detectors 30

5 Gamma-ray background from rock: studies for a next-generation dark matter experiment based on liquid xenon 33

5.1 Gamma-ray background of rare event searches . . . 33

5.2 GEANT4 simulation of gamma-rays from rock . . . 35

5.2.1 Physics processes . . . 35

5.2.2 Simulation geometry . . . 36

5.2.3 Gamma-ray production . . . 38

5.3 Gamma-ray propagation through the shielding and energy deposition in the TPC . . . 41

5.4 Analysis and results for shielding thickness . . . 44

5.5 Discussion of shielding thickness and reduction effects . . . 51

5.6 Conclusions on shielding requirements for the future detector . . . 54

6 Measurements of gamma-rays from rock samples in the Boulby Underground Laboratory 56

6.1 The Boulby Underground Laboratory . . . 56

6.1.1 Overview . . . 56

6.1.2 The Boulby UnderGround Screening facility . . . 58

6.1.2.1 Boulby's high-purity germanium detectors . . . 58

6.1.2.2 Nitrogen purge system . . . 61

6.2 Rock sample measurements . . . 62

6.2.1 Methodology . . . 62

6.2.1.1 Systematic uncertainties . . . 64

6.2.1.2 Accounting for TCS . . . 64

6.2.1.3 Calibration . . . 66

6.2.1.4 Calculating specific activity . . . 68

6.2.2 Results of sample measurements . . . 70

6.2.3 Discussion of sample measurements . . . 73

6.2.4 Conclusions . . . 75

7 The radon facility in the Boulby Underground Laboratory 77

7.1 Facility overview . . . 77

7.1.1 Radon detector . . . 78

7.1.2 Detector electronics . . . 78

7.1.3 Radon reduction system and emanation chambers 80
7.1.4 Concentration line 81
7.2 Radon detection methods 83
7.2.1 Method to calculate activities of nuclides in the ^{222}Rn decay chain 83
7.2.1.1 ^{222}Rn activity 84
7.2.1.2 ^{218}Po activity 85
7.2.1.3 ^{214}Pb, ^{214}Bi and ^{214}Po 85
7.2.2 Measuring radon emanation via the spike method 86
7.3 Detector calibration, background and sample measurements 88
7.3.1 Calibration procedure 88
7.3.2 Detector and chamber background measurements 91
7.3.3 Minimum detectable activity 92
7.3.4 Sample measurement procedure 95
7.4 Radon emanation measurements 96
7.5 Scope for future work 98
7.5.1 Titanium disc radon emanation study 98
7.5.2 Facility progression 99

8 Muon flux measurements with LZ 100
8.1 The LUX-ZEPLIN experiment 100
8.1.1 Detector overview 101
8.1.2 Signal detection 101
8.1.3 Veto detectors 104
8.1.4 LZ software 105
8.2 Muon flux measurements 106
8.2.1 The muon model 106
8.2.2 Data selection 111
8.2.2.1 Live time 112
8.2.2.2 Outer Detector and Skin selection 112
8.2.2.3 Inter-detector timing selection 112
8.2.2.4 TPC energy selection 114
8.2.3 Energy deposition spectra in data and simulations 116

8.3 Evaluation of the muon flux 118
8.3.1 Muon rate measurements 118
8.3.2 Reconstruction of the muon flux 121
8.3.3 Evaluation of average rock density 123
8.3.4 Conclusions 124

9 Conclusions **125**

Glossary of Terms **127**

Bibliography **129**

Appendices **141**

A Principles of semiconductor detectors 142
B Muon traversing the LZ detector 144
C Macro files for generating gamma lines from ^{232}Th and ^{238}U decay chains 145
D Systematic uncertainties of Boulby rock measurements 147
E Gamma-rays from NORM isotopes identified in Boulby Mine rock samples 148
F Calibrating a germanium detector 149
G Detecting radon with the CAEN digitiser 149
H Systematic uncertainties in radon detector calibration and radon emanation measurements 150
I Minimum detectable signal derivation 151

Glossary of acronyms

Acronym	Definition
$0\nu\beta\beta$ decay	Neutrinoless double beta decay
ADC	Analog-to-Digital Converter
BACCARAT	Basically A Component-Centric Analog Response to AnyThing
BBN	Big Bang Nucleosynthesis
BEGe	Broad-Energy Germanium
BUGS facility	Boulby UnderGround Screening facility
CJPL	China JinPing underground Laboratory
CL	Confidence Level
CMB	Cosmic Microwave Background
CoMPASS	CAEN Multi-PArameter Spectroscopy Software
CRESST	Cryogenic Rare Event Search with Superconducting Thermometers
CPH	Clear Pink Halite
CREF	Cold Radon Emanation Facility
CV	Chamber Volume
DAQ	Data acquisition system
DER	Detector Electronics Response
DRIFT experiment	Directional Recoil Identification From Tracks experiment
DV	Detector Volume
ER	Electron Recoil
FWHL	Footwall Halite
FWHM	Full Width Half-Maximum
FV	Fiducial Volume
HPGe	High Purity Germanium
GdLS	Gadolinium-loaded Liquid Scintillator
GPS	G4GeneralParticleSource (GEANT4 tool)
GXe	Gaseous Xenon
HG	High-Gain
HV	High-Voltage
ICP-MS	Inductively Coupled Plasma Mass Spectrometry
LabSOCS	Laboratory Sourceless Calibration Software
LAr	Liquid Argon
ΛCDM	Lambda Cold Dark Matter
LEC	Large Experimental Cavern
LHC	Large Hadron Collider
LG	Low-Grade (potash); Low-Gain (PMTs)
LNGS	Laboratori Nazionali del Gran Sasso
LPM	Litres Per Minute
LSP	Lightest Supersymmetric Particle
LUX experiment	Large Underground Xenon experiment
LV	Low-Voltage
LXe	Liquid Xenon
LZ experiment	LUX-ZEPLIN experiment (see LUX and ZEPLIN)
LZap	LZ analysis package
LZLAMA	LZ Light Analysis Monte Carlo Application

Term	Definition
MDA	Minimum Detectable Activity
MFC	Mass Flow Controller
MPE	Multiple Photoelectron
MUSIC	MUon SImulation Code
MUSUN	MUon Simulations UNderground
NAA	Neutron Activation Analysis
NaCl	halite, salt rock (geology)
NAIAD	NaI Advanced Detector
NEST	Noble Element Simulation Technique
NNDC	National Nuclear Data Center
NORM	Naturally Occurring Radioactive Materials
NR	Nuclear Recoil
NTD	Neutron-Transmutation-Doped
OCV	Outer Cryostat Vessel
OD	Outer Detector
PandaX	Particle and Astrophysical Xenon Detector
PMT	Photomultiplier Tube
POD	Pulse-Only Digitisation
PSD	Pulse Shape Discrimination
$Q_{\beta\beta}$	Q-value of $0\nu\beta\beta$ decay of ^{136}Xe
RCS	Random Coincidence Summing
RFR	Reverse Field Region
ROI	Region Of Interest
RQ	Reduced Quantity
S1 signal	Prompt scintillation signal
S2 signal	Secondary scintillation signal
SD	Spin-Dependent
SE	Single Electron
SI	Spin-Independent
SM	Standard Model
SPE	Single Photoelectron
S-ULB	Specialty Ultra-Low Background
SURF	Sanford Underground Research Facility
SUSY	Supersymmetry
TCS	True Coincidence Summing
TES	Transition Edge Sensor
TPC	Time Projection Chamber
UCL	University College London
UoT	University of Tokyo
VUV	Vacuum Ultraviolet
WIMP	Weakly Interacting Massive Particle
WMAP	Wilkinson Microwave Anisotropy Probe
WS2022(2024)	WIMP Search 2022(2024)
WT	Water Tank
ZEPLIN experiment	ZonEd Proportional scintillation in LIquid Noble gases experiment

Chapter 1

Introduction

There is ample evidence for the presence of dark matter that has been observed since the early 20th century, the majority of which is briefly discussed in Chapter 2. However, despite decades of theoretical and experimental efforts, the fundamental nature of dark matter remains unknown. Numerous direct detection experiments have been conducted to probe for dark matter candidates, particularly Weakly Interacting Massive Particles (WIMPs), which remain among the most promising candidates. These experiments employ a variety of target materials and detection strategies, some of which are also described in Chapter 2. Although none have yielded a definitive signal, they have significantly constrained the parameter space for dark matter models. Among these experiments, dual-phase liquid xenon time projection chambers have achieved the most stringent limits. To fully explore the remaining WIMP parameter space before reaching the irreducible background from coherent neutrino scattering (often referred to as the neutrino fog), the next-generation xenon detector must be significantly larger while reducing the background even further. Such a detector will also offer sensitivity to other rare processes, including neutrinoless double beta ($0\nu\beta\beta$) decay, given the presence of ^{136}Xe and the requirement for ultra-low background conditions. The detection of $0\nu\beta\beta$ decay would have considerable implications for particle physics beyond the Standard Model. Achieving the necessary sensitivity for both dark matter and $0\nu\beta\beta$ decay searches demands an exceptionally low background environment, which is the motivation of the work presented in this thesis.

The backgrounds for rare-event searches originate from both internal and external sources. Gamma-rays and neutrons produced by the decay chains of ^{238}U, ^{235}U, and ^{232}Th, as well as from ^{40}K and activation products like ^{60}Co and ^{137}Cs, pose significant challenges. While ^{137}Cs and ^{60}Co are mainly concerns if found in detector materials, the decay chains and potassium contribute to backgrounds both from the detector and the surrounding

rock. Gamma-rays can mimic WIMP-like nuclear recoils if they deposit energy within the region of interest (ROI), typically $0 - 20$ keV, and are not rejected as multiple scattering events. Similarly, high-energy gamma-rays near 2.458 MeV, the Q-value of $0\nu\beta\beta$ decay of ^{136}Xe ($Q_{\beta\beta}$), constitute backgrounds for that search. Discrimination between nuclear recoils (NRs) expected from WIMP interactions and electron recoils (ERs) from gamma-ray background will suppress the gamma-induced background in WIMP search.

To design the shielding of the next-generation xenon-based experiment, detailed simulations and experimental characterisations of background sources are required. In particular, gamma-rays originating from the cavern walls represent a potentially significant background if not properly mitigated. Chapter 5 presents a simulation built to evaluate the required shielding thickness for the suppression of these gamma-ray backgrounds. As the Boulby Underground Laboratory is one of the candidate sites for this future experiment, rock samples from Boulby Mine have been screened using high-purity germanium detectors to determine the specific activities of the radionuclides ^{40}K, ^{232}Th, ^{238}U and ^{235}U. The simulation results are subsequently normalised to these measured activities in Chapter 6, providing a quantitative assessment of Boulby's suitability to host the experiment regarding gamma-ray backgrounds from rock. If Boulby were not to be selected as the site for XLZD, the gamma-ray measurements of the many rock types in the mine can be used by any prospective experiment to contribute towards their background models.

Alpha and beta particles from radionuclide decays in detector materials can be problematic if they occur within or near the active volume. Of particular concern is ^{214}Pb, a decay product of ^{222}Rn, whose beta spectrum extends into the WIMP ROI. Moreover, if the transition to ^{214}Bi is to the ground state, no accompanying gamma-rays are emitted. Therefore, radon emanation from materials and its subsequent mixing into the detector's target material can contribute significantly to the low-energy background. Chapter 7 gives an overview of a new radon facility installed in the Boulby Underground Laboratory. Details of a new set of analysis codes, written to calibrate the detectors and to calculate the amount of radon emanated from samples, are included. This code will continue to be used by the facility to screen materials for the XLZD experiment and other future screening campaigns.

Cosmogenic muons that penetrate the Earth's surface can produce backgrounds via electromagnetic cascades and neutron generation. At great depths, the cosmic-ray muon flux is attenuated by several orders of magnitude and further reduced by employing active veto systems, which reject events in time coincidence with muons. Chapter 8 details an investigation into the muon flux through the Davis Cavern in the Sanford Underground Research Facility (SURF). The flux measurement is used to renormalise the muon model used in simulations and evaluate the density of the rock overburden, which will be to the benefit of future experiments at SURF.

Chapter 2

Dark matter and rare event searches

The universe has been studied extensively; first with electromagnetic radiation, then more recently with neutrinos and gravitational waves in a new era of multi-messenger astronomy, which gives a greater meaning to the phrase "observable universe". However, most of what we can observe is baryonic matter which makes up less than 5 % [1] of the universe. What makes up the majority is yet to be determined and we call this remainder dark matter and dark energy. A review of the evidence for the existence of dark matter is given in Section 2.1 and one of the most promising dark matter candidates, the WIMP, is discussed in Section 2.2. Different experimental techniques for the direct detection of WIMPs are described in Section 2.3, and lastly, Section 2.4 gives a brief overview of $0\nu\beta\beta$ decay, as many dark matter experiments also possess the ability to probe this rare process.

2.1 Evidence for dark matter

2.1.1 Velocity dispersion of the Coma cluster

Discussions about the presence of non-luminous matter in the universe date back to the early 20th century, prompted by studies of stellar dynamics aimed at estimating the total mass of the Milky Way. However, the first concrete observational evidence for dark matter was presented in 1933, when Zwicky analysed the velocities of nebulae in the Coma cluster [2]. Zwicky estimated the velocity dispersion to be approximately 1000 $\mathrm{km\,s^{-1}}$, which is orders of magnitude larger than what would be expected based on the mass inferred from visible matter alone. According to the virial theorem, the predicted velocity dispersion from luminous matter in the Coma cluster is only about 80 $\mathrm{km\,s^{-1}}$. If the observed

velocities are accurate, the gravitational potential must be significantly stronger to maintain the cluster's gravitationally bound state. Zwicky concluded that this discrepancy implied the existence of a substantial amount of non-luminous matter, which he referred to as "dunkle Materie" (dark matter), possessing a density far greater than that of luminous matter. This mass discrepancy was revisited over subsequent decades by numerous astrophysicists, many of whom remained sceptical of the dark matter interpretation [3].

2.1.2 Rotation curves

In 1970, following the development of an image tube spectrograph, Rubin and Ford provided the next piece of key evidence for dark matter by measuring the rotation curve of the M31 galaxy (Andromeda galaxy) [4, 5]. In a spiral galaxy like the M31, the luminous mass distribution outside the galactocentric bulge falls exponentially outwards from the centre. Following Kepler's laws of gravitational motion, the orbital velocity, v, of the stars would be expected to fall as:

$$v \propto \frac{1}{\sqrt{r}}, \tag{2.1}$$

where r is the galactocentric radius. However, Rubin and Ford's observations of the hydrogen 21 cm line showed that at large radii, the orbital velocity remained constant and the rotation curves of M31 were flat. The M31 galaxy is not unique in having this unexpected velocity distribution: later studies found that many other spiral galaxies display similar rotation curves [6]. These findings suggest the presence of an extended dark matter "halo" around spiral galaxies, causing the total enclosed mass to continue increasing with galactic radius. As shown in Figure 2.1, the observed rotation curve cannot be accounted for by the contributions from the luminous disc and gas alone. Without the additional gravitational influence of a dark matter halo, the outer regions of these galaxies would be rotating too rapidly to remain gravitationally bound.

2.1.3 Gravitational lensing

The limit to observing rotation curves is constrained by the amount of light or neutral hydrogen, which tapers off as the galactocentric radius increases. To trace the dark matter halos far beyond this point, physicists employ gravitational lensing - a phenomenon predicted by Einstein's theory of general relativity [7], where massive objects curve spacetime and thus, bend the path of light. As a result, one can measure the amount of mass between a highly luminous object and the observer. The image of the background object becomes stretched around the foreground mass (the lens), forming a quasi-circular shape that is called an "Einstein Ring", as pictured in Figure 2.2.

Gravitational lensing has been used to analyse mass distribution in galaxy clusters in conjunction with X-ray maps of those clusters. By comparing lensing-based mass profiles with X-ray maps, studies have shown that a substantial fraction of the mass in galaxy clusters must be attributed to a component of non-luminous matter. A famous case study is that of the Bullet Cluster, where two galaxy clusters are merging [9]. The collision, seen in Figures 2.3a and 2.3b, separates the intracluster plasma from the clusters.

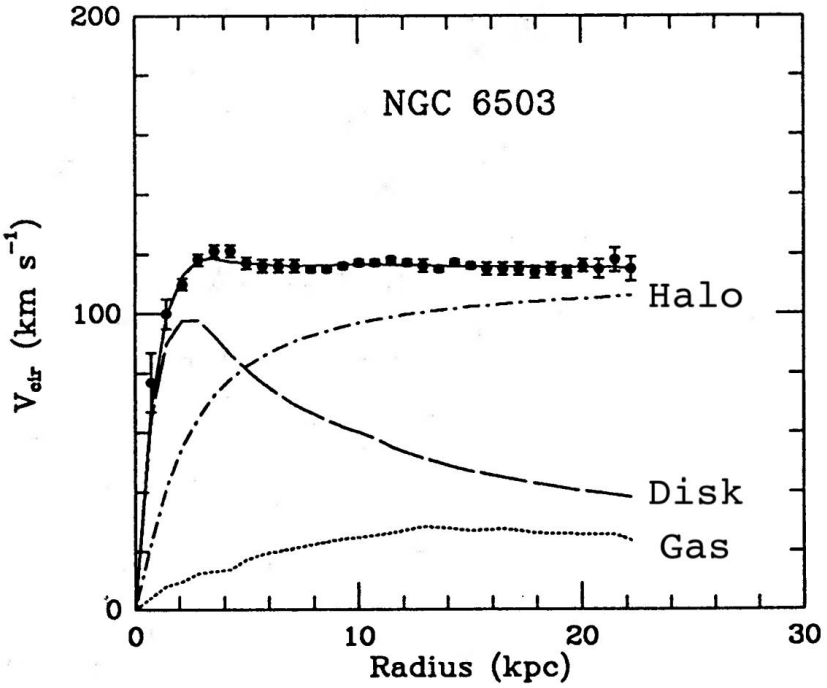


Figure 2.1: The observational data of the NGC 6503 galaxy's rotation curve fitted with a solid line that is the combination of the dark matter halo (dot-dashed line), luminous disk (dashed line) and gas (dotted line) components. From Ref. [6].

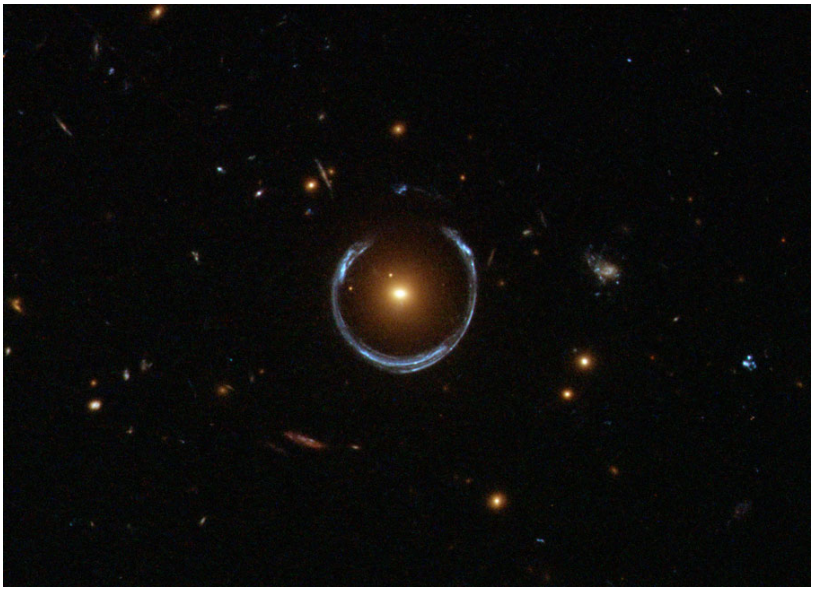
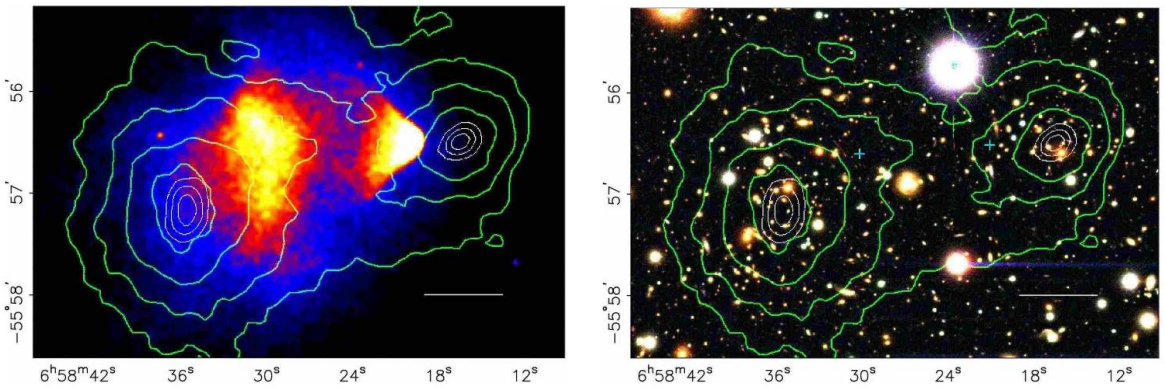


Figure 2.2: An image of an Einstein ring taken by the Hubble Space Telescope. A galaxy in the centre of this image lies between the telescope and a blue galaxy. The light from the blue galaxy is distorted by how spacetime bends around the galaxy in the foreground. Image credit: ESA/Hubble and NASA [8].

Without dark matter, the gravitational potential would have traced the plasma, as it is the dominant baryonic mass component. As depicted by the contours in Figures 2.3a and 2.3b however, the gravitational potential instead traces the distribution of visible galaxies in clusters. As dark matter is the main source of the gravitational potential, this distribution indicates that it is collisionless as well as non-luminous.



(a) (b)

Figure 2.3: (a) A Chandra image and (b) a Magellan image of the Bullet cluster. In both images, the green contour lines represent the mass distribution deduced from gravitational lensing effects. In (a), the red region in the centre of the image corresponds to hot gas, and the white bar corresponds to a length of 200 kpc. From Ref. [9].

2.1.4 The cosmic microwave background and Big Bang nucleosynthesis

The cosmic microwave background (CMB), discovered in 1965 [10], is the relic radiation from the early universe, dating back to the epoch of decoupling and recombination approximately 380,000 years after the Big Bang. As the temperature of the universe decreased, photons decoupled from baryons and electrons were captured by nuclei, resulting in a "frozen" picture of the last of the density fluctuations and baryon acoustic oscillations in the plasma. High-precision measurements of the CMB anisotropies, such as those from the Wilkinson Microwave Anisotropy Probe (WMAP) [11] and Planck [12] missions, provide strong evidence for the existence of dark matter.

The CMB power spectrum describes the strength of temperature anisotropies as a function of angular scale on the sky; it is characterised by a series of acoustic peaks, displayed in Figure 2.4. These peaks arise from oscillations in the tightly coupled photon–baryon fluid before recombination. These can be modelled as a system of driven harmonic oscillators, where gravitational potential perturbations act as the driving force and radiation pressure provides the restoring force. These peaks contain information about density fluctuations, and the geometry and composition of the early universe. The power spectrum is derived by decomposing the temperature anisotropies into spherical harmonics, which is a natural way of defining patterns on a sphere. This process separates the fluctuations by scale, with each multipole, ℓ, corresponding to features of size roughly $180°/\ell$. This expansion of spherical harmonics produces a set of coefficients that quantify how much each angular pattern contributes to the observed sky. The variances of the coefficients define the power spectrum, providing a statistical description of the temperature anisotropies across different angular scales.

The Lambda Cold Dark Matter (ΛCDM) model posits that the universe is composed primarily of dark energy (in the form of a cosmological constant, Λ), cold dark matter (non-relativistic at the time of structure formation), and baryonic matter. By fitting this model to the power spectrum of the CMB temperature anisotropies, it is possible

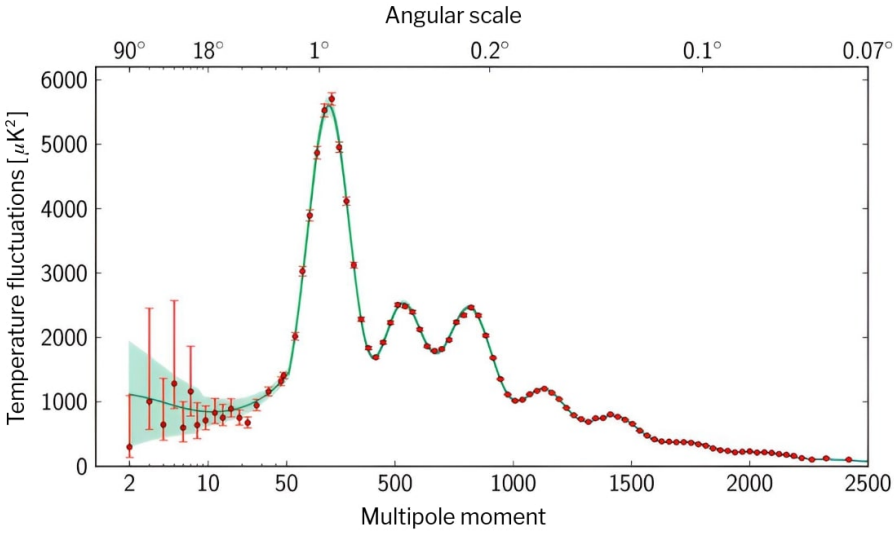


Figure 2.4: Temperature anisotropies in the CMB as measured by Planck (2013). Adapted from Ref. [13].

to extract precise estimates for the cosmological density parameters [1]. Each density parameter, Ω_x, represents the ratio of the present-day energy density of component x to the critical density, ρ_c. The critical density is the value required for a spatially flat universe, corresponding to one where the expansion rate asymptotically approaches zero in the absence of dark energy. Observational data indicate that the total density parameter of the universe is very close to 1, consistent with spatial flatness [1]. The individual density parameters are summarised in Table 2.1.

Table 2.1: The ΛCDM best-fit parameters from Planck 2018 results [1]. Ω_Λ is the dark energy density parameter, Ω_m is the total matter density parameter, Ω_b is the baryonic matter density parameter and Ω_c is the dark matter density parameter. H_0 is the Hubble constant and h is the Hubble parameter, defined from H_0 as $H_0 = 100\,h$ km s^{-1} Mpc^{-1}.

Parameter	**Planck results**
Ω_Λ	0.726 ± 0.015
$\Omega_m h^2$	0.143 ± 0.001
$\Omega_b h^2$	0.0224 ± 0.0001
$\Omega_c h^2$	0.120 ± 0.001
H_0	67.8 ± 0.9 [km s^{-1} Mpc^{-1}]

Supporting these results is the baryon density independently inferred from the primordial abundances of the light elements deuterium, helium (^{3}He & ^{4}He) and lithium. These nuclei were synthesised during Big Bang Nucleosynthesis (BBN), approximately three minutes after the Big Bang [14]. The relative abundances of these nuclei are sensitive to both the baryon-to-photon ratio and the expansion rate of the universe during BBN, which are in turn governed by the baryon density parameter $\Omega_b h^2$. Among these light

elements, deuterium is particularly sensitive to the baryon density. Based on spectroscopic measurements of the primordial deuterium abundance, Ref. [15] reports a baryon density of $\Omega_b h^2 = 0.0226 \pm 0.0034$. This value is in good agreement with the 2018 Planck observations of the CMB, further implying that only a small percentage of the universe is made up of baryonic matter.

2.2 WIMPs

Approximately 26.4 % of the critical density in the universe is accounted for by dark matter [16]. Despite extensive research, the exact nature of this component remains unknown, as all evidence to date is indirect. Consequently, a wide range of dark matter candidates have been proposed and are actively being investigated, including WIMPs and axions.

Dark matter can be categorised as hot, warm, or cold, depending on how relativistic the dark matter particles were when they decoupled from the thermal plasma in the early universe. In the case of cold dark matter (CDM), which refers to non-relativistic particles at the time of decoupling, WIMPs are among the most well-motivated candidates. Although WIMPs do not rely on any single theoretical framework, they arise naturally from supersymmetry (SUSY), a theoretical extension of the Standard Model (SM) that introduces a supersymmetric partner for each known particle, which differs in spin by a half; fermions are partnered with bosons and vice versa. The supersymmetric partners are also much more massive than their SM counterparts [17].

To be a viable candidate for CDM, a particle must meet several key criteria: it must be electrically neutral, non-relativistic, non-baryonic, massive, stable (or at least extremely long-lived), and interact only weakly with ordinary matter. One of the most promising WIMP candidates is the neutralino, which is a mixture of the superpartners of the gauge and Higgs bosons. In this framework, a discrete quantum number called R-parity, R_p, is introduced, defined as:

$$R_p = (-1)^{3(B-L)+2s}, \tag{2.2}$$

where B is baryon number, L is lepton number and s is spin. As it relies partially on the spin of a particle, it can distinguish between SM particles and their supersymmetric partners. All SM particles have $R_p = +1$, while their supersymmetric partners have $R_p = -1$. If R-parity is conserved, supersymmetric particles must be produced in pairs, and the lightest supersymmetric particle (LSP) cannot decay into SM states. While the exact identity of the LSP depends on the SUSY-breaking scenario, in most phenomenologically viable models the lightest neutralino is the LSP, making it stable and thus, the most favoured dark matter candidate in this framework [18]

WIMPs remain the leading candidates for dark matter, and there are three methods of detection:

1. **Indirect detection:** searching for the secondary SM particles (which include neutrinos, positrons, anti-protons and gamma-rays) produced by the annihilation of dark matter particles in astrophysical environments. High-energy gamma-ray telescopes, such as H.E.S.S. and Fermi-LAT, search for excess emission from regions of high dark matter density (eg. the galactic centre) [19, 20]. Neutrino observatories,

such as IceCube, probe dark matter captured in the Sun, where annihilations could produce an observable flux of high-energy neutrinos [21]. Space-based experiments, such as AMS-02, measure e^+ and $\bar{p}$ spectra for potential dark matter signatures [22].

2. **Collider searches:** experiments such as the LHC search for missing transverse momentum that would result from the production of dark matter in high-energy collisions [23].
3. **Direct detection:** searching for the rare interactions between WIMPs and atomic nuclei, further discussed in Section 2.3.

These methods complement each other by providing different constraints on WIMP interactions.

WIMPs are hypothesised to have been thermally produced in the early universe, with expected masses in the range of approximately 10 GeV to a few TeV. This mass window corresponds to the "WIMP miracle", where particles with weak-scale couplings naturally yield the observed dark matter relic abundance [24, 25]. They are predicted to interact very weakly with baryonic matter. Due to their large mass compared to electrons, WIMPs are expected to primarily undergo elastic scattering with atomic nuclei, producing observable NRs. The expected total rate of WIMP-nucleus scattering events in a target with nucleus mass m_N is given by [26]:

$$\frac{dR}{dE_{\mathrm{nr}}} = \frac{\rho_0\, M}{m_N\, m_\chi} \int_{v_{\mathrm{min}}}^{v_{\mathrm{esc}}} v\, f(v) \frac{d\sigma}{dE_{\mathrm{nr}}}\, dv, \tag{2.3}$$

where ρ_0 is the local dark matter density, M is the total mass of the detector target, m_χ is the WIMP mass, and $f(v)$ is the local WIMP velocity distribution in the Earth's frame. The velocity integral runs from v_{min}, the minimum velocity required for a WIMP to transfer energy to a nucleus, up to the galactic escape velocity v_{esc}. $\frac{d\sigma}{dE_{\mathrm{nr}}}$ is the differential scattering cross-section, which expresses how the likelihood of a WIMP scattering off a target nucleus varies per unit recoil energy.

The minimum velocity is [26]:

$$v_{\mathrm{min}} = \sqrt{\frac{E_{\mathrm{nr}}\, m_N}{2} \cdot \frac{(m_N + m_\chi)^2}{(m_N\, m_\chi)^2}} = \sqrt{\frac{E_{\mathrm{nr}}\, m_N}{2\mu^2}}, \tag{2.4}$$

where μ is the reduced mass of the WIMP-nucleus system:

$$\mu = \frac{m_N m_\chi}{m_N + m_\chi}. \tag{2.5}$$

The velocity distribution $f(v)$ is typically taken to be Maxwellian with a cut-off at the galactic escape velocity $v_{\mathrm{esc}} = 544^{+64}_{-46}$ km s^{-1} [27], beyond which WIMPs are no longer gravitationally bound to the Milky Way.

The WIMP-nucleus differential scattering cross-section appearing in Equation (2.3) is [26]:

$$\frac{d\sigma}{dE_{\mathrm{nr}}} = \frac{m_N}{2\,\mu^2\, v^2} \left(\sigma_{\mathrm{SI}}\, F^2_{\mathrm{SI}}(E_{\mathrm{nr}}) + \sigma_{\mathrm{SD}}\, F^2_{\mathrm{SD}}(E_{\mathrm{nr}})\right), \tag{2.6}$$

where σ_{SI} and σ_{SD} are the spin-independent (SI) and spin-dependent (SD) WIMP-nucleus cross-sections, respectively, and $F_{\mathrm{SI}}(E_{\mathrm{nr}})$ and $F_{\mathrm{SD}}(E_{\mathrm{nr}})$ are the associated nuclear form factors, which encode the loss of coherence at higher momentum transfers. These form factors satisfy $F(E_{\mathrm{nr}}) < 1$ and depend on the nuclear structure and recoil energy.

For spin-independent interactions, the cross-section scales with the square of the atomic mass number, A, leading to an enhancement for heavier nuclei like xenon. The SI cross-section can be related to the WIMP-nucleon cross-section σ_n as [26]:

$$\sigma_{\mathrm{SI}} = \sigma_n \frac{\mu^2}{\mu_n^2} A^2, \tag{2.7}$$

where m_n is the nucleon mass and μ_n is the reduced mass of the WIMP-nucleon system:

$$\mu_n = \frac{m_n m_\chi}{m_n + m_\chi}. \tag{2.8}$$

The recoil energy spectrum resulting from WIMP interactions typically exhibits an exponential fall-off, approximately described by [26]:

$$\frac{dR}{dE_{\mathrm{nr}}} \propto \exp\left(-\frac{E_{\mathrm{nr}}}{E_0} \cdot \frac{(m_\chi + m_N)^2}{4\, m_\chi\, m_N}\right), \tag{2.9}$$

where E_0 is the most probable kinetic energy of the incident WIMPs. However, the actual signal observed in a detector is a function of its energy response and efficiency. The differential event rate in observed energy, E_{obs}, is given by:

$$\frac{dR}{dE_{\mathrm{obs}}} = \frac{dR}{dE_{\mathrm{nr}}} \times S(E_{\mathrm{nr}}), \tag{2.10}$$

where $S(E_{\mathrm{nr}})$ is the detector response function, incorporating energy resolution, threshold effects, and detection efficiency. As the rate $\frac{dR}{dE_{\mathrm{obs}}}$ is normalised per unit target mass and time, increasing either the detector mass or the exposure time enhances the total number of observable WIMP-nucleon scattering events.

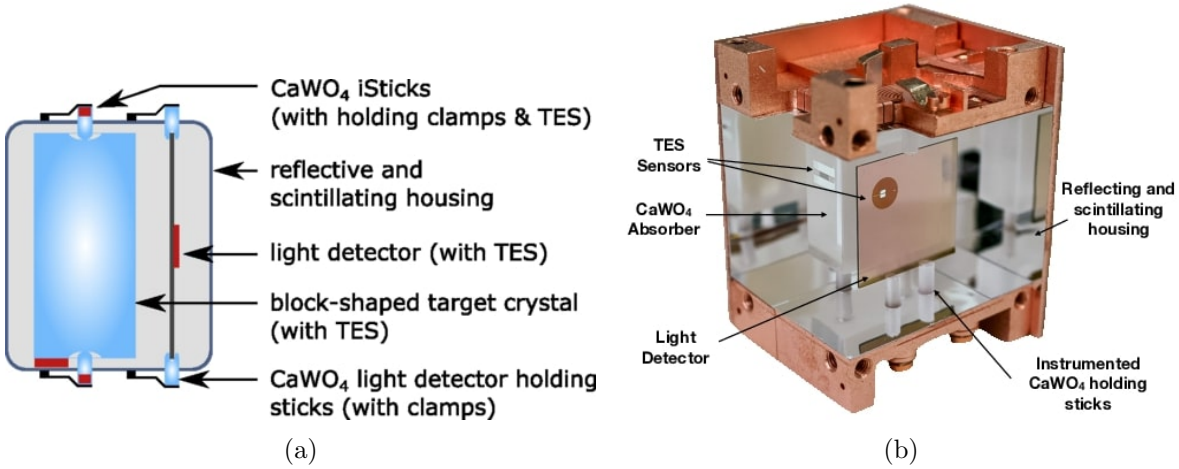
2.3 Direct detection experiments

There are three detection channels used to detect nuclear recoils: phonon detection, ionisation and scintillation. Most current experiments use a combination of any two of these channels. This allows discrimination between NRs that are produced by neutrons and WIMPs, and ERs that are produced by charged particles and gamma-rays interacting with the atomic electrons. The majority of background events come from ERs.

2.3.1 Scintillating cryogenic bolometers

The Cryogenic Rare Event Search with Superconducting Thermometers III (CRESST-III) experiment [28] is located 1400 m underground at the Laboratori Nazionali del Gran Sasso (LNGS) in Italy [29]. The detector is designed to detect low-energy NRs from dark

matter particles with masses down to the sub-GeV range. CRESST-III uses scintillating cryogenic bolometers: each detector module consists of a calcium tungstate ($CaWO_4$) crystal that serves as both target and phonon detector, coupled to a separate light detector. Transition edge sensors (TESs) are used for phonon readout. A typical module can be seen in Figures 2.5a and 2.5b. The simultaneous measurement of phonon and scintilla-



(a) (b)

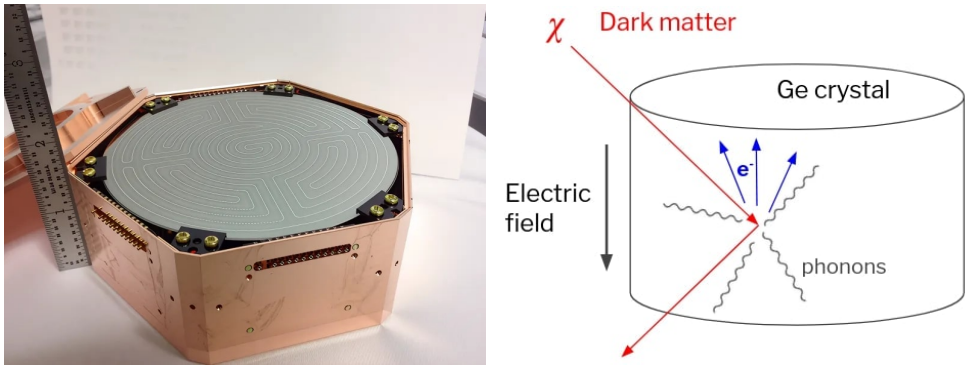
Figure 2.5: (a) A diagram and (b) a photo of a CRESST-III detector module. The transition edge sensors are the phonon sensor components of the module. From [28, 30].

tion signals allows for discrimination between ERs and NRs, as NRs produce significantly less light due to quenching.

2.3.2 Cryogenic bolometers with charge readout

Two major dark matter experiments, EDELWEISS [31] and SuperCDMS [32], combine phonon and ionisation readout to distinguish between NRs and ERs. Both experiments operate cryogenic germanium detectors in deep underground laboratories: EDELWEISS at the Laboratoire Souterrain de Modane (France) [33], and SuperCDMS at SNOLAB (Canada) [34]. Although both use germanium as a target material, due to its excellent semiconductor properties that make it extremely sensitive to radiation, they differ in their sensor technologies and readout approaches. EDELWEISS employs thermistors based on neutron-transmutation-doped (NTD) germanium to measure heat signals, and uses interleaved electrodes for ionisation collection, allowing for effective rejection of surface background events. SuperCDMS also uses interleaved electrodes for charge readout, but uses TESs rather than NTDs for phonon readout. A detector module of SuperCDMS can be seen in Figure 2.6a, alongside a diagram of a theoretical WIMP interaction inside the module that demonstrates the concept of the dual-readout system.

While upgrades to individual cryogenic bolometer experiments may continue, there are currently no efforts directed toward a collaborative project. A previous initiative aimed at combining the expertise of the CRESST, EDELWEISS, and SuperCDMS collaborations was once under consideration. This proposal, envisioned as the EURECA experiment [36], has since been discontinued.



(a) (b)

Figure 2.6: (a) A photo of a SuperCDMS detector module. (b) A simplified diagram of a dark matter particle interacting with a nucleus in the module's germanium crystal, leading to energy deposition that produces both ionisation and phonon signals. Photo taken from Ref. [35].

2.3.3 Dual-phase noble element detectors

Dual-phase liquid noble element detectors measure primary scintillation light and secondary ionisation. The current and upcoming experiments employing this technique are listed in Table 2.2. These are the Particle and Astrophysical Xenon Detector (PandaX-4T) [37] and its future upgrade PandaX-xT [38] at the China JinPing underground Laboratory (CJPL) [39] in Sichuan; DarkSide-20k [40] and XENONnT [41] at LNGS; and the LUX-ZEPLIN (LZ) experiment [42] at SURF [43] in Lead, South Dakota. XLZD [44] will be another new experiment, with the location yet to be decided.

Table 2.2: Information about current and potential future dual-phase liquid noble element detectors.

Experiment	**Target material**	**Fiducial mass [tonne]**	**Location**	**Status**
PandaX-4T	LXe	3.7	CJPL	Operating
XENONnT	LXe	5.9	LNGS	Operating
LUX-ZEPLIN	LXe	7.0	SURF	Operating
PandaX-xT	LXe	43	CJPL	R & D*
DarkSide-20k	LAr	51	LNGS	In construction
XLZD	LXe	60-80	n/a	R & D*

*Research and development.

In each of these experiments, the liquid noble element is encased in a chamber that has a layer of gas at the top and two layers of photomultiplier tubes (PMTs) at both the top and bottom, as seen in Figure 2.7. An incoming particle interacts with either liquid argon (LAr) or liquid xenon (LXe), depending on the experiment. This particle scatters off either a Xe/Ar nucleus or an electron, producing both scintillation photons and ionisation electrons. The prompt scintillation from this event is measured as the primary "S1" signal. An electric field is applied between a cathode grid at the base and a gate grid just below the liquid surface. This field enables the electrons produced in the

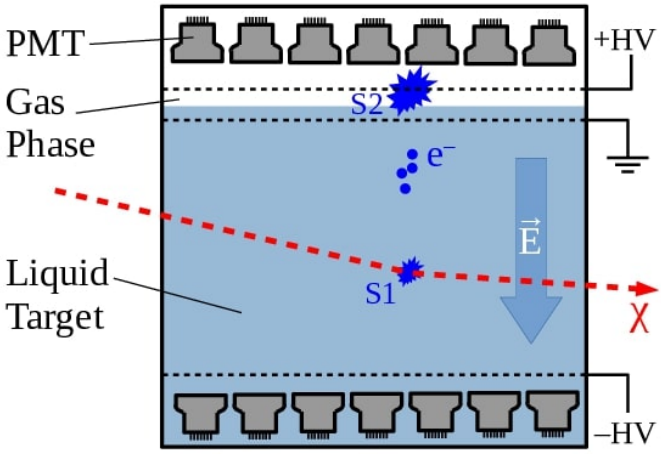


Figure 2.7: An illustration of a dual-phase noble element detector. The dark matter particle, χ, will scatter on a nucleus and deposit energy. The dual-phase detector measures the primary and secondary scintillation signals. From Ref. [26].

interaction to drift upwards towards the gas-liquid interface. A stronger electric field is applied across the liquid-gas boundary, allowing for the extraction of electrons into the gas phase[1], where they are accelerated through it and produce secondary scintillation - the "S2" signal. The time delay between the S1 and S2 signals is proportional to the depth (z-position) of the interaction. Because the detector can convert this time difference into a spatial coordinate, it is referred to as a time projection chamber (TPC). The distribution of S2 light in the top PMT array allows reconstruction of the position in the plane perpendicular to the drift field ($x - y$ position).

Uniformity of the drift field is maintained using field-shaping rings arranged along the TPC walls and a high-voltage cathode, ensuring linear and distortion-free transport of electrons. Electron lifetime, the time electrons can survive before being captured by impurities, is an important parameter to maximise. Typically, electron lifetime is influenced by electronegative contaminants such as O_2 or H_2O, therefore, the liquid is continuously circulated and purified to remove them.

The S2 signal is particularly crucial in dual-phase xenon detectors due to its high amplification gain in the gas phase, which enables single-electron sensitivity. This allows the detectors to achieve very low energy thresholds, enhancing sensitivity to low-mass WIMP interactions. Additionally, the densities and high atomic masses of LXe and (to a lesser extent) LAr enable these materials to provide excellent self-shielding against external gamma-ray and neutron backgrounds.

The initial scintillation mechanism is the same for both NRs and ERs. Particles such as neutrons and WIMPs interact via elastic scattering off nuclei, producing NRs, while gamma-rays interact with electrons through photoelectric absorption, Compton scattering, and pair production, resulting in ERs. These recoils then excite or ionise surrounding atoms, depending on the interaction type. Excited and ground-state atoms

[1]LXe (LAr) has a higher dielectric constant than GXe (GAr), meaning that without this strong electric field, it is energetically favourable for electrons to remain in the liquid phase. Electrons will immediately recombine with atoms, adding to the scintillation signal, so only an S1 signal will be seen.

form excimers (excited dimers[2]), which decay by emitting vacuum ultraviolet (VUV) photons [45]:

$$
\begin{aligned}
e^- + \mathrm{Xe} &\rightarrow \mathrm{Xe}^* + e^- && \text{impact excitation} \\
\mathrm{Xe}^* + \mathrm{Xe} &\rightarrow \mathrm{Xe}_2^{*,\nu} && \text{excimer formation} \\
\mathrm{Xe}_2^{*,\nu} + \mathrm{Xe} &\rightarrow \mathrm{Xe}_2^* + \mathrm{Xe} && \text{vibrational relaxation} \\
\mathrm{Xe}_2^* &\rightarrow 2\mathrm{Xe} + h\nu && \text{VUV emission,}
\end{aligned}
$$

where the superscript ν represents excited states with additional vibrational energy, the relaxation of which can sometimes emit infrared radiation. Ionisation leads to the formation of ionised dimers, which can recombine with free electrons and follow a similar relaxation process, ultimately producing the same VUV emission [45]:

$$
\begin{aligned}
e^- + \mathrm{Xe} &\rightarrow \mathrm{Xe}^+ + 2e^- && \text{ionisation} \\
\mathrm{Xe}^+ + 2\mathrm{Xe} &\rightarrow \mathrm{Xe}_2^+ + \mathrm{Xe} && \text{dimer formation} \\
e^- + \mathrm{Xe}_2^+ &\rightarrow \mathrm{Xe}^{**} + \mathrm{Xe} && \text{recombination} \\
\mathrm{Xe}^{**} + \mathrm{Xe} &\rightarrow \mathrm{Xe}^* + \mathrm{Xe} + \text{heat} && \text{relaxation} \\
\mathrm{Xe}^* + 2\mathrm{Xe} &\rightarrow \mathrm{Xe}_2^* + \mathrm{Xe} + \text{heat} && \text{excimer formation} \\
\mathrm{Xe}_2^* &\rightarrow 2\mathrm{Xe} + h\nu && \text{VUV emission.}
\end{aligned}
$$

In the absence of an electric field, nearly all electrons produced during ionisation recombine with ions, contributing to the S1 signal. When a strong electric field is applied, this recombination is suppressed, allowing a fraction of the electrons to escape. The exact recombination fraction depends on the target material, the kinematic properties of the ionising particle and the strength of the applied field. The electrons that avoid recombination are drifted upward by the electric field toward the liquid-gas interface. Upon entering the gas phase, they are accelerated by a stronger extraction field and excite xenon atoms, leading to the production of an S2 signal via electroluminescence:

$$
\begin{aligned}
e^- + \mathrm{Xe\ (gas)} &\rightarrow \mathrm{Xe}^* && \text{impact excitation} \\
\mathrm{Xe}^* + \mathrm{Xe} &\rightarrow \mathrm{Xe}_2^* && \text{excimer formation} \\
\mathrm{Xe}_2^* &\rightarrow 2\mathrm{Xe} + h\nu && \text{VUV emission.}
\end{aligned}
$$

Both LXe and LAr are excellent target materials for WIMP detection due to their strong scintillation response and ability to become ionised. However, each has its advantages and limitations. The VUV scintillation photons emitted have characteristic wavelengths of approximately 178 nm for xenon and 128 nm for argon. The shape of the S1 pulse depends on the type of interacting particle because the ratios of singlet (short-lived) and triplet (long-lived) excimer states differ for NRs and ERs. This distinction allows for pulse shape discrimination (PSD) between NRs and ERs. PSD is particularly effective in LAr due to the large difference in de-excitation lifetimes compared to LXe. These lifetimes are, respectively, 7 ns and 1.6 µs for singlet and triplet states in LAr, and similarly, 4 ns and 22 ns for singlet and triplet states in LXe, respectively.

Additionally, LAr is significantly cheaper than LXe. However, naturally occurring argon contains the long-lived beta-emitting isotope ^{39}Ar ($T_{1/2}$ = 269 y) [46], necessitat-

[2]Two identical molecules linked together.

ing much higher background rejection capabilities. In contrast, xenon has no long-lived radioactive isotopes aside from ^{136}Xe and ^{124}Xe , both of which decay only via extremely rare second-order weak processes. Using argon that is depleted in ^{39}Ar slightly reduces the requirement for background rejection, but increases cost considerably. Concerning performance, LXe offers greater sensitivity than LAr due to its higher density and atomic mass, A. These properties allow for comparable exposure with a smaller detector volume or shorter run-time. In particular, for SI WIMP-nucleon interactions, the cross-section scales approximately with A^2 (see Equation (2.7)), making xenon particularly advantageous for such searches, as it enhances the expected interaction rate even at lower target mass.

In summary, while both noble liquids are effective for dark matter detection, the choice between LXe and LAr involves a trade-off between cost, intrinsic background levels and discrimination performance.

2.4 $0\nu\beta\beta$ decay

$0\nu\beta\beta$ decay is a hypothesised second-order weak nuclear process in which a nucleus undergoes beta decay, emitting two electrons, but no neutrinos:

$$(Z, A) \rightarrow (Z + 2, A) + 2\, e^{-}.$$

This process violates lepton number conservation by two units and, if observed, would unambiguously demonstrate physics beyond the Standard Model. Two-neutrino double beta ($2\nu\beta\beta$) decay, which is allowed by the Standard Model, has been experimentally observed in several isotopes [47] and proceeds via:

$$(Z, A) \rightarrow (Z + 2, A) + 2\, e^{-} + 2\, \bar{\nu}_e.$$

The $0\nu\beta\beta$ decay process requires that the neutrino is a Majorana particle rather than a Dirac particle, meaning that the neutrino is its own antiparticle. The Feynman diagrams for $2\nu\beta\beta$ and $0\nu\beta\beta$ are displayed in Figures 2.8a and 2.8b, respectively. An overview of the $0\nu\beta\beta$ decay physics and the status of experimental searches for it is given in Ref. [48].

One of the main reasons for searching for $0\nu\beta\beta$ decay is that it could help explain why the universe is made mostly of matter, rather than equal parts matter and antimatter. This imbalance, known as the "baryon asymmetry", might be explained by a process called leptogenesis, described in Ref. [49]. This process requires lepton number violation, which the observation of $0\nu\beta\beta$ decay would directly confirm. Another key motivation is that $0\nu\beta\beta$ decay is sensitive to the absolute mass of neutrinos, which is not accessible through neutrino oscillation experiments. By measuring or placing limits on the $0\nu\beta\beta$ decay rate, information about the neutrino mass scale could be gained.

The experimental signature of $0\nu\beta\beta$ decay is a monoenergetic peak in the summed electron energy spectrum at the Q-value of the decay. This contrasts with the broad continuum spectrum of $2\nu\beta\beta$ decay, as a result of the neutrinos carrying away some of the available energy. Both signals are shown in Figure 2.9. Experiments searching for $0\nu\beta\beta$ decay aim to achieve a large exposure, excellent energy resolution to distinguish the

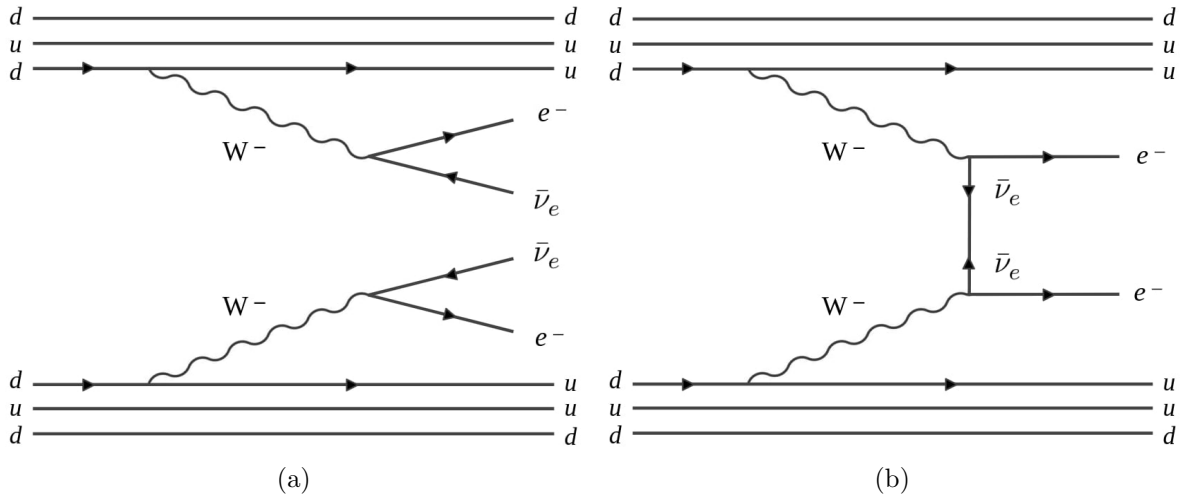


Figure 2.8: Feynman diagrams for (a) two-neutrino double beta decay and (b) neutrinoless double beta decay.

0νββ decay peak from the 2νββ decay background, and ultra-low background levels in the ROI. Several isotopes are candidates for 0νββ decay searches, with those most commonly used including ^{76}Ge, ^{136}Xe, ^{130}Te, and ^{100}Mo. No experimental evidence for 0νββ decay has yet been found, but stringent limits have been placed [48].

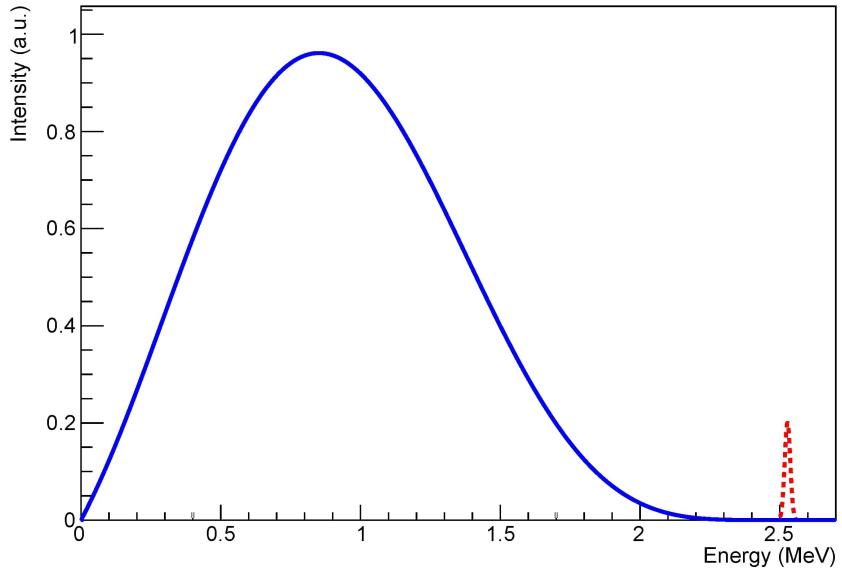


Figure 2.9: The energy spectrum from two-neutrino double beta decay (solid line) and the energy peak expected from neutrinoless double beta decay (dashed line). From Ref. [50].

Several dark matter detectors, particularly those employing large volumes of ultra-pure materials like xenon, are also capable of probing 0νββ decay. These detectors benefit from extremely low background environments, high energy resolution, and massive target masses, making them well-suited to search for the rare signature of 0νββ decay alongside dark matter interactions. A study of the gamma-ray background to both WIMPs and 0νββ decay in a next-generation dark matter detector is presented in Chapter 5.

Chapter 3

Backgrounds to rare event searches

All WIMP-search experiments discussed in Chapter 2 are located in underground laboratories. While the overburden significantly reduces the background from cosmic-ray muons, the surrounding rock contains trace amounts of radioactive elements, which emit gamma-rays and neutrons. As a result, the experiments require shielding from these particles originating from the cavern walls. To further minimise backgrounds, the experiments are constructed in cleanrooms to prevent contamination of detector materials. Trace levels of radioactive impurities or dust, whether in the materials themselves or deposited on surfaces, can introduce beta and alpha particle backgrounds, especially as these contaminants are often located very close to or in direct contact with the sensitive detector regions. Therefore, careful selection of ultra-pure materials and stringent control of contaminants are critical to background reduction. In this chapter, I describe the origins and characteristics of gamma-ray and neutron backgrounds, radon-related backgrounds and muon-induced backgrounds in sensitive dark matter detectors.

3.1 Radionuclides

During the late 19th and early 20th centuries, it was observed that radioactive substances emit three distinct types of radiation: α, β and γ decay. They are classified according to their differing ionisation signatures. Radionuclides are isotopes with mean decay lifetimes on the order of 10^9 years or longer, which have survived since the formation of the solar system from stellar material. These long-lived isotopes remain present in the Earth's crust, atmosphere and, consequently, in the raw materials used to construct sensitive low-background experiments, such as those searching for dark matter and $0\nu\beta\beta$ decay.

Achieving the exceptionally low background levels required for these experiments necessitates extensive shielding, in addition to the careful cleaning and selection of detector materials to minimise contamination by radionuclides. Variations in ore chemistry and geological history can lead to significant differences in radionuclide concentrations between sources of the same element. Therefore, materials intended for use in low-background experiments must undergo rigorous assay and selection procedures.

Radioactivity is present in materials for several reasons: intrinsic presence of long-lived isotopes, contamination of raw ore underground, or contamination during industrial processing. Additionally, materials can become activated through exposure to cosmic-rays at the Earth's surface. Copper, which is widely used in low-background experiments due to its excellent purity, thermal, and mechanical properties, can become activated in this manner, producing long-lived radioisotopes such as ^{60}Co via spallation reactions[1]. To mitigate cosmogenic activation, high-purity copper is often stored and, in some cases, electroformed underground to shield it from cosmic radiation. Similarly, lead is an important material for radiation shielding due to its high density and high atomic number. Natural lead, extracted from ore, is composed primarily of four stable isotopes: ^{204}Pb, ^{206}Pb, ^{207}Pb, and ^{208}Pb, with the latter three being the stable end-products of the ^{238}U, ^{235}U, and ^{232}Th decay chains, respectively. However, recently refined modern lead contains traces of radioactive ^{210}Pb (half-life 22.3 years), which originates from the decay of atmospheric ^{222}Rn and contributes to the background through β decay. In contrast, ancient lead, such as Roman lead recovered from archaeological contexts like shipwrecks, has been shielded from cosmic-rays and environmental radon exposure for centuries. As a result, the short-lived radioactive isotopes have largely decayed away, rendering Roman lead exceedingly low in intrinsic radioactivity [51]. For this reason, ancient lead is highly sought after for use as shielding material in rare event searches [32, 52].

Among radionuclides, the uranium (^{238}U and ^{235}U) and thorium (^{232}Th) series are particularly critical, as they are the primary sources of low-energy neutrons and high-energy gamma-rays underground. Their presence, both in the surrounding rock and in detector components, presents significant challenges for rare event experiments, including searches for dark matter and $0\nu\beta\beta$ decay. The decay chains of ^{238}U and ^{232}Th, depicted in Figures 3.1 and 3.2, respectively, involve a sequence of alpha and beta decays ultimately terminating at stable lead isotopes (^{206}Pb, ^{208}Pb).

Throughout these decay cascades, high-energy gamma-rays are emitted, contributing significantly to experimental backgrounds. Particularly notable are emissions from isotopes such as ^{208}Tl (thorium chain) and ^{214}Bi (uranium chain). ^{208}Tl emits a 2.614 MeV gamma-ray with an intensity of 99.97 % of the time following the alpha decay of ^{212}Bi, which occurs with a branching ratio of 35.94 % [53]. ^{214}Bi emits a 2.204 MeV gamma-ray with a 4.99% intensity and a 2.447 MeV gamma-ray with a 1.55% intensity following the beta decay of ^{214}Pb [54]. Separately, ^{40}K, which is also commonly found in rock, emits a 1461 keV gamma-ray during its decay to ^{40}Ar, with a branching ratio of 10.72 % [55]. These high-energy gamma-rays pose a severe background for detectors, as they can penetrate significant shielding and mimic signals of interest, particularly in dark matter experiments where ER rejection must be extremely efficient, or in $0\nu\beta\beta$ decay searches where the region of interest around the Q-value lies near similar energies.

[1]Spallation here refers to the fragmentation of nuclei when bombarded by cosmic-ray neutrons and protons. See Section 3.3 for a description of muon-induced spallation.

In underground laboratories, passive shielding is employed to suppress the external background from the decay of uranium and thorium in the rock. The shielding design must account for the total flux contributed by the high-energy gamma-rays of the decay chains. Water tanks, polyethylene, lead layers, or active veto systems are commonly used to attenuate these photons before they reach the sensitive detector volume.

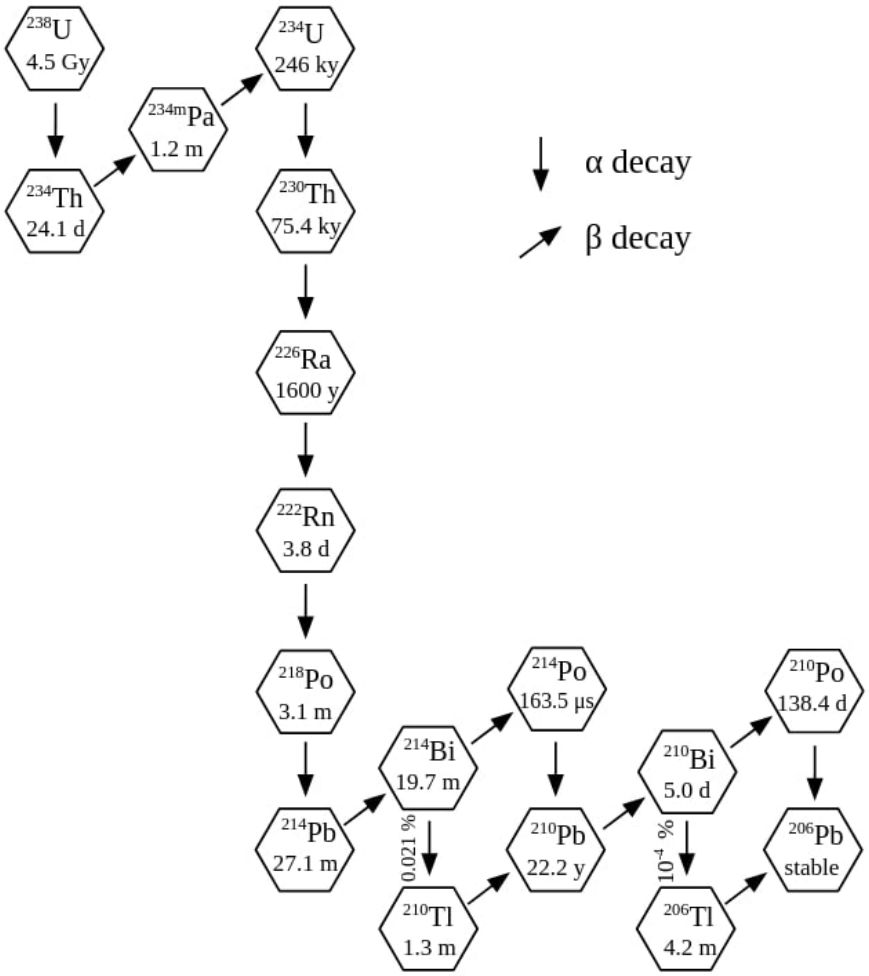


Figure 3.1: The ^{238}U decay chain, also known as the uranium series or radium series. α decays are indicated by downwards arrows and β decays are shown as upward, rightward arrows. Isotopes of an element are aligned horizontally. For isotopes with multiple decay modes, the branching fractions are marked on the α transitions.

In addition to external backgrounds, intrinsic contamination from construction materials can contribute to the internal gamma-ray background. Detector materials, such as photomultiplier tubes, wiring, support structures, and reflective coatings, must be rigorously screened for radionuclides. Techniques such as gamma spectroscopy, inductively coupled plasma mass spectrometry (ICP-MS), and neutron activation analysis (NAA) are employed to assay material purity.

Despite extensive screening, residual background events from material radioactivity are unavoidable. Consequently, modern detectors implement powerful event selection techniques to reject background events, such as identifying multiple-scatters, employing fiducial volume (FV) cuts, pulse shape discrimination, and active veto tagging to distinguish WIMP or $0\nu\beta\beta$ decay signals from background-induced events.

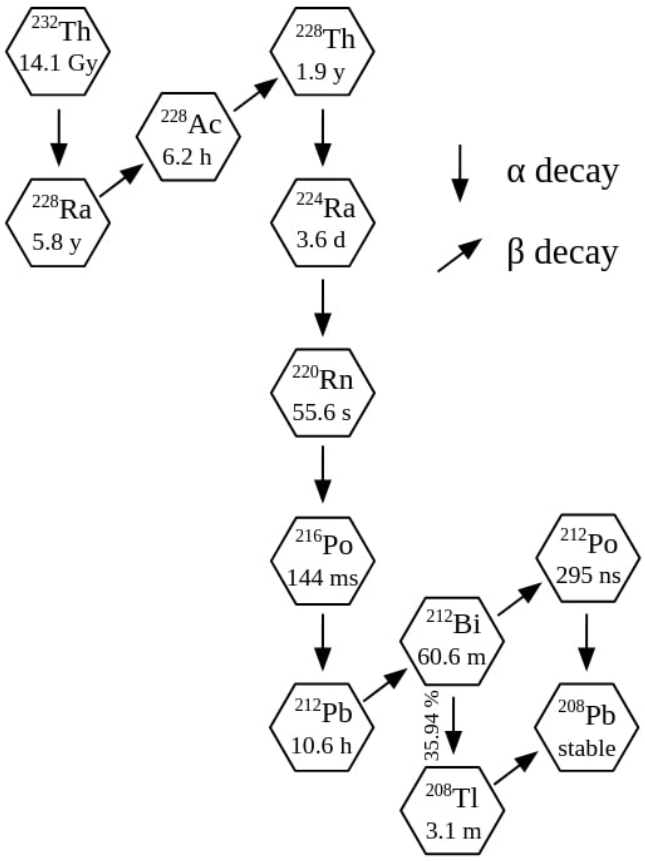


Figure 3.2: The ^{232}Th decay chain, also referred to as the thorium series. The notation used is the same as in Figure 3.1.

3.2 Radon

Radon is a noble gas characterised by the unique property that all its isotopes are radioactive. It exists in nature in monatomic form and is chemically inert. In the early 20th century, spectroscopic studies of radioactive gases from radium salts and thorium oxide were conducted, from which similarities with the noble gases argon, krypton, and xenon were observed. In 1920, the gases were formally named radon (from radium), thoron (from thorium), and actinon (from actinium), corresponding to isotopes ^{222}Rn, ^{220}Rn, and ^{219}Rn, respectively.

Radon is the heaviest of the noble gases, with a density of approximately 9.73 kg m^{-3} at standard temperature and pressure. Its melting and boiling points, -71°C and -61.7°C respectively, are high relative to other noble gases. Although colourless and odourless under ambient conditions, radon exhibits radioluminescence when solidified. It exhibits low solubility in water, but is more soluble in organic solvents, such as liquid scintillator [56]. Due to its inertness, radon is chemically non-reactive and cannot be efficiently removed from systems using standard chemical methods.

Four radon isotopes occur in nature as part of the decay chains of long-lived parent isotopes [57, 58, 54]:

- **^{222}Rn**: Produced in the ^{238}U decay chain; half-life: 3.8235 d.

- **^{220}Rn (thoron)**: Produced in the ^{232}Th decay chain; half-life: 55.8 s.
- **^{219}Rn (actinon)**: Produced in the ^{235}U decay chain; half-life: 3.96 s.

Of these, ^{222}Rn is the most relevant for rare-event physics due to its longer half-life, which permits diffusion and accumulation in detector volumes, enabling radon progeny to be present in the active volume.

In rare-event searches such as dark matter or $0\nu\beta\beta$ decay experiments, radon and its progeny pose a significant background threat. The decay chains of ^{238}U and ^{232}Th (see Figures 3.1 and 3.2) include multiple alpha-, beta-, and gamma-emitting isotopes, as well as neutron production via spontaneous fission and (α, n) reactions. These processes can mimic the signatures of WIMP interactions or other rare decays. The uranium and thorium decay chains are sometimes assumed to be in secular equilibrium, owing to the long half-lives of their parent isotopes. Under this assumption, the activity of one progeny can be used to infer that of others, as demonstrated in Chapter 7. However, secular equilibrium is often broken due to radon transport or chemical processes, and therefore, cannot be assumed without experimental verification.

Radon atoms emanate from materials and may enter a detector through two principal mechanisms: diffusion and recoil. The latter refers to the kinetic recoil of a radon atom following the alpha decay of its parent nucleus. Because radon is chemically inert, it has long diffusion lengths in solids, complicating efforts to reduce radon backgrounds in dark matter experiments. The diffusion length, L_i, of radon in a material i is given by:

$$L_i = \sqrt{\frac{D_i}{\lambda}}, \tag{3.1}$$

where D_i is the diffusion coefficient (depending on material properties such as porosity, grain structure, and surface roughness), and λ is the decay constant of radon.

Radon exposure and contact with environmental dust during detector construction can lead to surface contamination through the plate-out of long-lived progeny, most notably ^{210}Pb (half-life: 22.3 years). This isotope decays to ^{210}Po, which emits a 5.3 MeV alpha particle. When emitted near low-Z materials such as PTFE, these alpha particles can induce neutrons via (α,n) reactions. Single-scatter neutrons may produce NRs that are indistinguishable from WIMP signals. Additionally, the recoil of ^{206}Pb, the stable daughter of ^{210}Po, can deposit energy within the WIMP signal region.

A significant contributor to the ER background in liquid noble element detectors is the decay of ^{214}Pb, a progeny of ^{222}Rn. In approximately 11.0 % of decays, ^{214}Pb undergoes a "naked" beta decay directly to the ground state of ^{214}Bi, emitting only an electron and no accompanying gamma [54]. Given the broad energy spectrum of these electrons, some will have energies within the WIMP search ROI. Other decays in the ^{222}Rn chain are less problematic as they are accompanied by gamma-rays from de-excitation, or they are alpha decays, which fall outside of the WIMP ROI. In the LZ experiment, they account for a substantial fraction of the total ER background [59]. Since ^{214}Pb decays are difficult to tag directly, their rate is constrained via measurements of nearby alpha-emitters (e.g. ^{218}Po and ^{214}Po) and energy spectrum fitting.

To mitigate these backgrounds, LZ employs radon removal systems, such as activated charcoal traps, that lower the concentration of ^{222}Rn in xenon. Delayed coincidence

techniques are also used to try and identify ^{214}Pb background events by searching for the correlated[2] beta and alpha signals from ^{214}Bi decay and ^{214}Po decay (known as "BiPo tagging"), although this is not effective for the naked beta decay. Furthermore, the LZ experiment implements a conservative FV cut, excluding a 4 cm radial band near the TPC wall. The next-generation xenon-based dark matter experiment will similarly define its FV based on radon backgrounds. In parallel, strict cleanliness protocols are followed during transport and assembly to further suppress radon-related contamination.

3.3 Cosmic-ray muons

Primary cosmic-rays consist predominantly of protons (90 %) and helium nuclei (9 %), with heavier nuclei contributing the remainder [60]. Low-energy cosmic-rays (with energies $\sim$MeV) are largely deflected by the Earth's geomagnetic field, whereas higher-energy cosmic-rays penetrate the atmosphere. These higher-energy particles are believed to originate primarily within our galaxy, with sources including supernova remnants, where particles are accelerated by expanding shock fronts [61, 62]. The arrival directions of cosmic-rays are effectively isotropic due to deflections by galactic magnetic fields during propagation through the interstellar medium, which is composed mainly of hydrogen and helium, with a small fraction of heavier elements. The typical energy of primary cosmic-rays in space peaks around 0.1 – 1.0 GeV, although ultra-high-energy cosmic-rays ($\sim 10^{18}$ eV) have been observed and are thought to originate from extragalactic sources, such as jets emitted by active galactic nuclei [63].

The empirical fit to the observed cosmic-ray nucleon flux at Earth, in the energy range from a few GeV up to about 100 TeV, is given by [64, 60]:

$$I_N(E) \approx 1.8 \times 10^4 \left(\frac{E}{1\ \text{GeV}}\right)^{-\alpha}\ \text{nucleons m}^{-2}\ \text{s}^{-1}\ \text{sr}^{-1}\ \text{GeV}^{-1}, \tag{3.2}$$

where $I_N(E)$ is the differential flux of nucleons per unit energy, E is the energy per nucleon (including rest mass energy) and $\alpha = \gamma + 1$ is the differential spectral index of the cosmic-ray flux (γ is the integral spectral index).

Secondary cosmic-rays are generated when primary cosmic-rays interact with nuclei in Earth's atmosphere. In the atmosphere, these interactions produce extensive hadronic cascades, yielding large numbers of mesons, primarily pions and kaons. Charged pions decay predominantly (with branching ratio $>$ 99.98) via:

$$\pi^{\pm} \rightarrow \mu^{\pm} + \nu_{\mu}\ (\overline{\nu}_{\mu}), \tag{3.3}$$

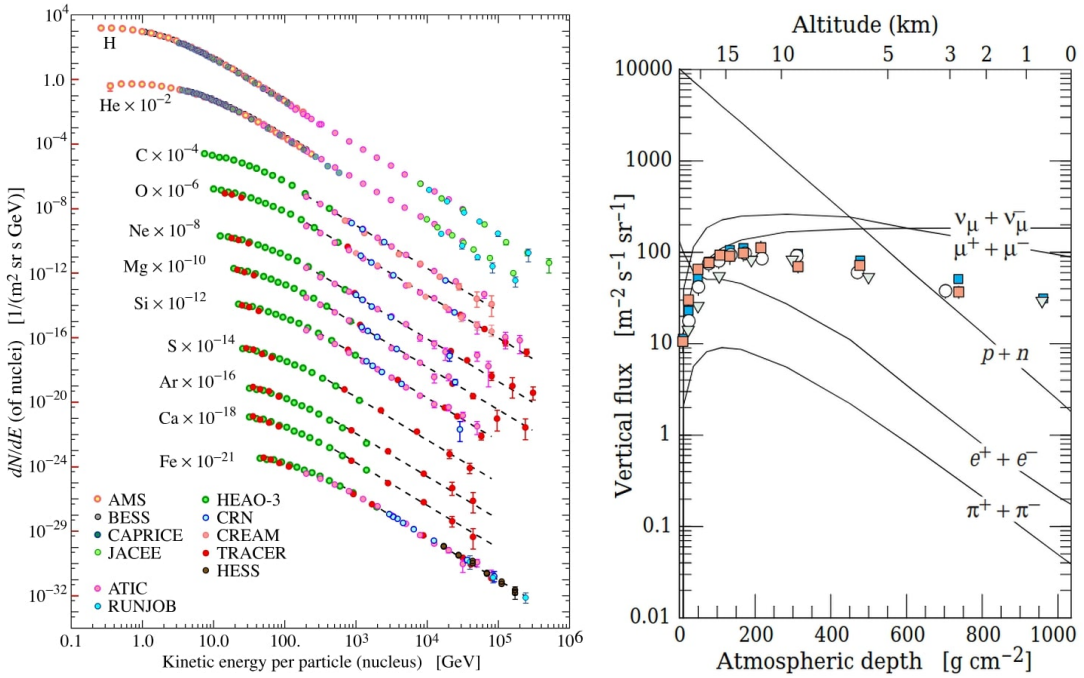
while charged kaons decay 63.56% of the time via:

$$K^{\pm} \rightarrow \mu^{\pm} + \nu_{\mu}\ (\overline{\nu}_{\mu}). \tag{3.4}$$

Consequently, muons constitute a major component of the secondary cosmic-ray flux. Due to their relatively long lifetime and ability to penetrate dense matter, muons dominate the cosmic-ray spectrum at sea level and underground, accompanied by neutrinos, which

[2]Correlated due to the short half-life of ^{214}Po - 163.5 µs.

also survive in significant numbers. Figure 3.3a shows the energy spectra of various nuclei at the top of the atmosphere, and the altitude dependence of the secondary cosmic-ray flux components, particularly for muons and neutrinos, is displayed in Figure 3.3b.



(a) (b)

Figure 3.3: (a) The flux of primary cosmic-ray nuclei as a function of energy per nucleus; this plot shows that protons dominate at all energies. (b) The altitude dependence of the composition of the vertical flux of secondary cosmic-rays. The points are measurements of the μ^- flux with $E > 1$ GeV and the curves are estimations. Neutrinos and muons dominate down to sea level. From [64].

Muons are a primary source of background to underground experiments as they directly ionise material in the sensitive regions of the detectors, but if the experiment is sufficiently deep, there will be only a few muon events per day. These are not as serious as other backgrounds since they are quite easily identified and/or vetoed as they traverse the detectors. However, muons also provide a secondary source of background by producing neutrons via interactions in the surrounding rock and detector materials. These neutrons can elastically scatter off nuclei, mimicking low-energy dark matter signals. Therefore, it is important to have precise estimates of muon-induced backgrounds.

The production of neutrons from cosmic-ray muons can occur via several processes: muon-induced spallation, photo-nuclear interactions and muon capture (neutrons are emitted by the resultant excited isotopes). Muon-induced spallation is where a muon interacts via a virtual photon, causing a nuclear disintegration. The Feynman diagram of this process is illustrated in Figure 3.4. Spallation products include myriad types of particles (neutrons, photons, radioisotopes, etc.). Hence, in addition to contributing to an NR background via neutron interactions, spallation can increase the ER background. Unwanted events from this process and primary muon events can be rejected from the experiment's data, either from multiple scattering cuts or muon veto cuts. The disadvantage of this is the increased dead time of the experiment. Secondary neutrons produced

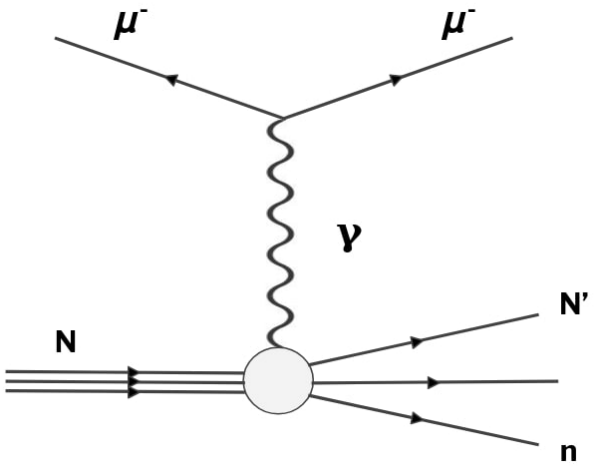


Figure 3.4: Feynman diagram of the virtual photon exchange that occurs during spallation.

in the adjacent rock may not be related to any muon events tagged in a muon veto or seen via a large energy deposit in the detector.

When travelling vertically, muons typically traverse approximately 15 km of atmosphere before reaching the Earth's surface. During this passage, they lose about 2 GeV of energy primarily through ionisation [65]. The muon flux at sea level exhibits a zenith angle (θ) dependence, corresponding to the varying thickness of atmosphere that muons must pass through along different trajectories.

Muons have a mean lifetime of 2.2×10^{-6} s in their rest frame, which would correspond to a distance travelled of roughly 660 m at nearly the speed of light. However, due to special relativistic time dilation, their effective range is significantly extended. Provided they have sufficient energy, muons can reach the ground before decaying. Energy losses during propagation, particularly through ionisation, gradually reduce the muons' energy, thereby decreasing the degree of time dilation and slightly shortening their effective range.

The differential muon flux at sea level is given by the following approximation [64]:

$$\frac{dN_\mu}{dE_\mu d\Omega} \approx \frac{0.14\, E_\mu^{-2.7}}{\text{cm}^2 \text{ s sr GeV}} \times \left(\frac{1}{1 + \frac{1.1 E_\mu \cos\theta}{115 \text{ GeV}}} + \frac{0.054}{1 + \frac{1.1 E_\mu \cos\theta}{850 \text{ GeV}}} \right), \tag{3.5}$$

where the two terms in brackets correspond to contributions from charged pion and kaon decays, respectively. This expression is valid for zenith angles $< 70°$ where the curvature of the Earth can be neglected, and it does not account for muon decay. For larger angles, corrections can be applied (see Section 8.2.1).

Muons and neutrinos are the only charged particles capable of penetrating large depths of rock and are the only cosmic-rays that provide a background to detectors deep underground. A muon loses energy through four main channels: bremsstrahlung, pair production, ionisation and inelastic scattering. The energy loss per distance X, as a muon travels through the earth, can be expressed in terms of continuous ionisation losses, a, and discrete radiative losses, b [60]:

$$-\frac{dE}{dX} = a + E\, b, \tag{3.6}$$

where $b = b_{brem} + b_{pair} + b_{had}$ The critical energy, ϵ, is the energy at which continuous energy loss (ionisation) and discrete energy losses (bremsstrahlung, pair production, hadronic production) become equally important ($\epsilon \equiv ab$). This is a few hundred GeV in rock. Below the critical energy, ionisation dominates and energy loss is slow and steady. Above the critical energy, radiative processes dominate and energy loss happens suddenly through electromagnetic cascades. Figure 3.5 shows how the muon intensity decreases as the thickness of the rock traversed increases.

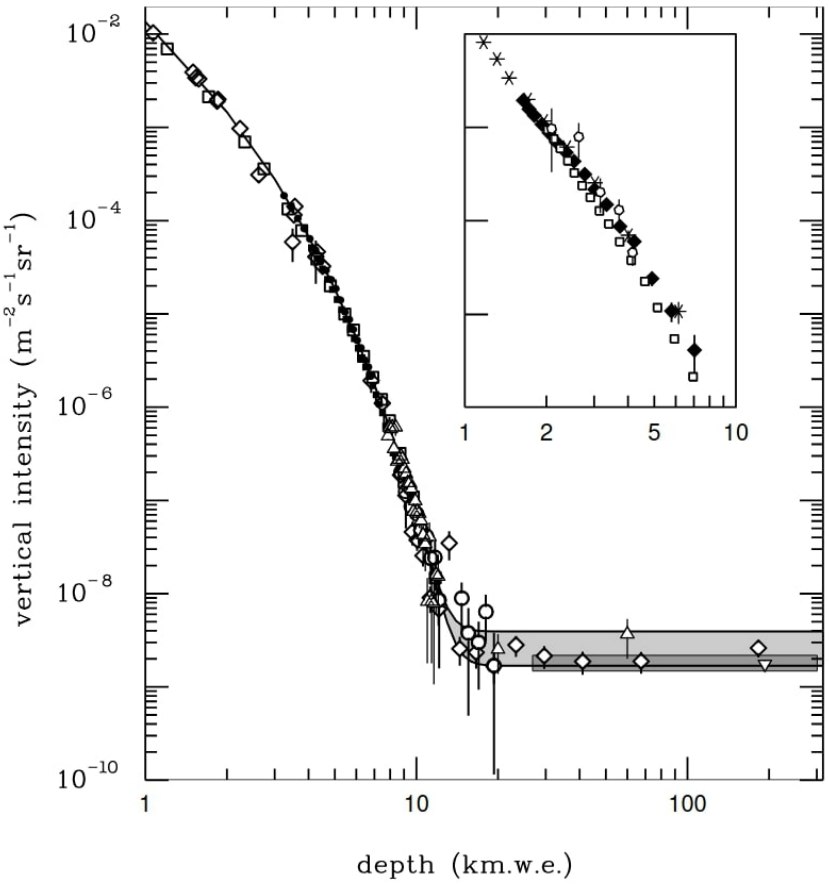


Figure 3.5: Vertical muon intensity as a function of underground depth (in km water equivalent (km w. e.), taken from Ref. [64], where data from SNO [66], LVD [67], MACRO [68], Frejus [69], and compilations by Crouch [70] and Baksan [71] are shown. The shaded regions indicate neutrino-induced muons with $E_\mu > 2$ GeV, and the inset displays corresponding measurements in water and ice [72, 73, 74].

Chapter 4

Principles of gamma spectroscopy and germanium detectors

Low-background detectors such as those searching for dark matter and other rare events, are sensitive to the background from radioactive decay chains (detailed in Section 3.1). The background radiation levels from materials, such as cavern rock and detector components, may affect an experiment's sensitivity and therefore, must be measured to devise appropriate levels of shielding and estimate the overall expected background. High-purity germanium (HPGe) detectors are sensitive to very low levels of radiation due to the small band gap energy of germanium, and are used widely to radioassay materials for low-background experiments. This chapter aims to describe the processes underpinning how germanium detectors operate. Sections 4.1 and 4.2 give an overview of gamma spectroscopy and the spectral features expected in a gamma spectrum from a gamma-ray detector. Section 4.3 discusses the use of germanium in gamma-ray detectors, materials used in the cryostat and shielding, and different configurations of detectors.

4.1 Gamma spectroscopy

Gamma spectroscopy relies on gamma-rays interacting with an absorbing material, transferring all or part of their energy to electrons in the material via photoelectric absorption, pair production and Compton scattering. The electrons lose the energy they have gained from gamma-rays to the material through ionisation, bremsstrahlung emission and excitation of atoms, all contributing to the signal seen by a gamma-ray detector. Some of these gamma-ray and charged particle interactions are illustrated in Figure 4.1.

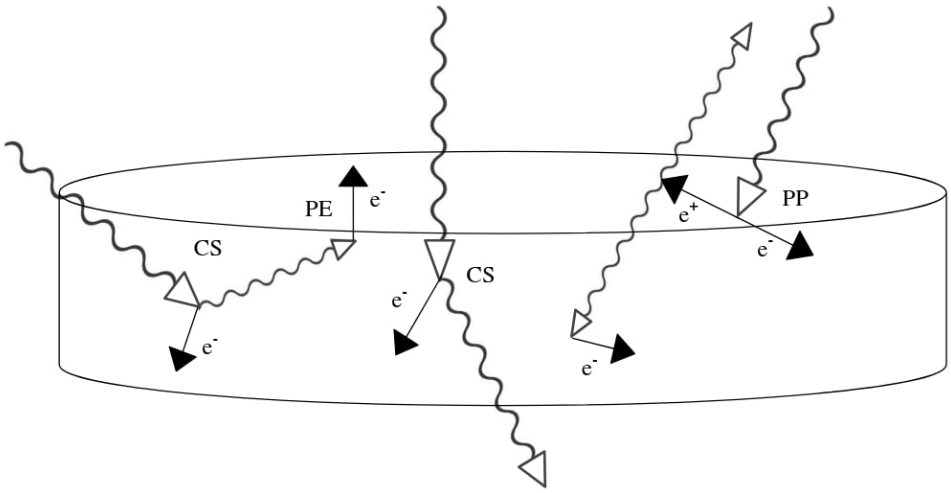


Figure 4.1: Examples of gamma-ray interactions occurring within an absorbing material in a medium-sized gamma-ray detector, of a few centimetres thickness. PP = pair production, PE = photoelectric absorption, CS = Compton scattering.

In an ideal gamma-ray detector, only photons directly from a source placed on or near the detector would interact, depositing their full energy within the detector, with no coincident events. In practice, measured signals include contributions from detector background, secondary radiation, and incomplete energy absorption. The latter arises when scattered gamma-rays or high-energy electrons escape the detector volume, often following interactions in surrounding materials. A gamma-ray may undergo multiple Compton scatterings before being fully absorbed via the photoelectric effect. The resulting recoil electrons deposit energy over timescales much shorter than the detector's response time, leading to a single observed pulse. If total energy deposition occurs, this appears as a full-energy peak; otherwise, features such as Compton continua and escape peaks emerge. Using sufficiently thick, non-gaseous absorber materials mitigates energy losses by reducing electron escape probability, improving spectral resolution.

4.2 Features of gamma-ray spectra

4.2.1 Compton scattering and Compton continua

If a gamma-ray interacts with an electron in the detector material via Compton scattering, the energy of the scattered gamma-ray will have a range of energies determined by the scattering angle, from zero up to a maximum. Less energy is transferred when this angle is small. The Klein-Nishina formula predicts the shape of the resulting Compton continuum [75]. Figure 4.2 depicts the energy spectra of a polyhalite sample and a halite sample[1] measured by a germanium detector. Both spectra have a clear Compton continuum starting at 0 keV and ending at the Compton edge (dashed rectangle) just before the characteristic 1461 keV peak from ^{40}K decay via electron capture. The Compton edge marks the maximum energy that can be deposited by a gamma-ray in a single Compton scattering event, corresponding to a photon backscattered in the germanium

[1]Specifically Halite 3, described in text in Section 6.2.2.

crystal at 180°. This is just one example of this type of feature that focuses on the most prominent line in each spectrum. The polyhalite sample is high in potassium and consequently has a large Compton continuum, obscuring many peaks below 1461 keV. This effect worsens at lower energies because other peaks within the ^{40}K decay continuum have Compton continua of their own, adding to the overall Compton background at lower energies. In contrast, the halite sample has a much lower ^{40}K content and the peaks from 0 - 1461 keV are much more visible. The continuum between 0 and the Compton edge arises from gamma-rays scattering at various angles and depositing a range of energies. The sloped region above the Compton edge that leads up to the full-energy peak results from gamma-rays undergoing multiple Compton scatterings within the detector. If the scattered photon escapes the detector before being fully absorbed, only a fraction of the initial energy is recorded, contributing to this continuum rather than the photopeak.

Another feature arising from the Compton effect is the backscatter peak, where gamma-rays from the source travel towards the shielding material and undergo Compton scattering with a large scattering angle such that the gamma-rays rebound off electrons into the detector material. This produces a low-energy "backscatter peak" as higher scattering angles produce similarly low photon energies, whereas below a $\sim 100°$ angle there is a broader spectrum of higher photon energies.

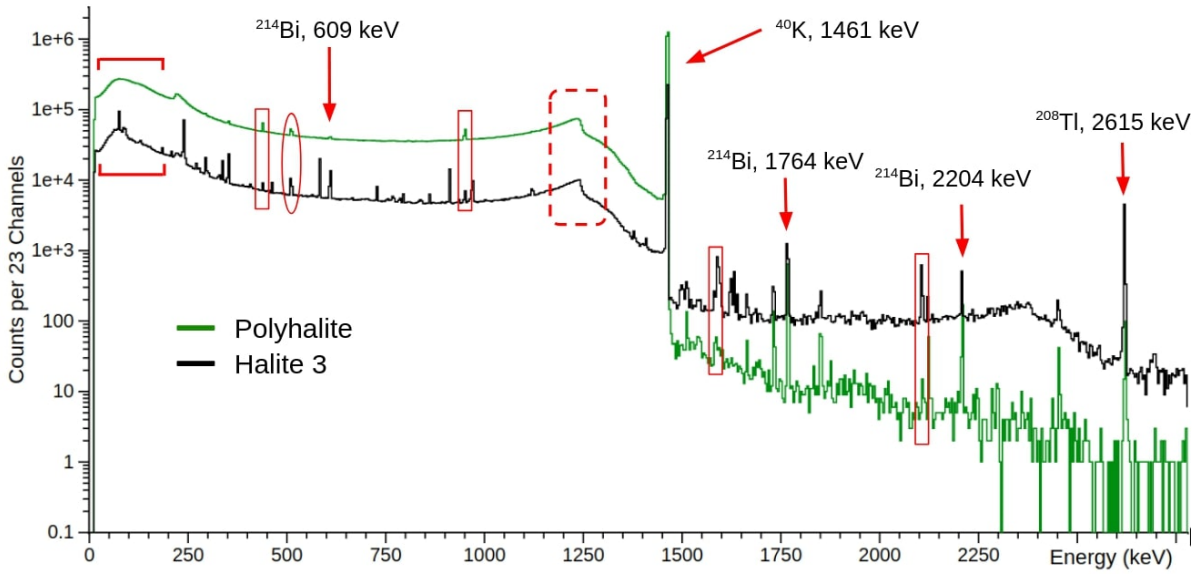


Figure 4.2: Energy spectra of a polyhalite sample and a Halite 3 sample with a few of the main decay peaks highlighted. The polyhalite spectrum is green and has more counts than the Halite 3 spectrum (black) before the 1461 keV peak and fewer counts after. The horizontal square brackets at the lower end of each spectrum enclose the broad backscatter peaks. The rectangles surround single and double escape peaks (see Section 4.2.2) which are 511 keV and 1022 keV lower, respectively, than both the 1461 keV and 2615 keV peaks. The dashed rectangle outlines the Compton edges and the oval encompasses the 511 keV annihilation peaks.

4.2.2 Pair production, annihilation and escape peaks

Other features visible in Figure 4.2 are escape peaks. Following pair production in the absorbing material (only possible for photons with energies > 1022 keV), the positron

will lose its energy and stop, then most likely it will annihilate at rest, resulting in a fixed gamma energy. If annihilation photons both escape the detector, there will be a "double escape peak" ∼1022 keV below the full-energy peak of the incident gamma-ray. If only one of the annihilation photons escapes and the other is completely absorbed, there will be a "single escape peak" ∼511 keV below the full-energy peak. For example, in Figure 4.2, below the 1461 keV peak there is a single escape peak at 950 keV and a double escape peak at 439 keV. Another feature to point out is the "annihilation peak" at 511 keV which is from annihilations occurring in the shield cavity, where the resulting photons (each with energy 511 keV) escape the shielding material and interact in the detector.

4.2.3 Coincidence summing

Coincidence summing is where two gamma-rays are detected nearly simultaneously, outside of the detector's ability to resolve signals. This results in a "summation peak", the sum of the energies the coincident gamma-rays deposited. These could be partial or full energy depositions. The more coincidental gamma-rays are detected as single pulses, the more peaks there will be in the spectrum, some of which may be misidentified. Additionally, the loss of counts in the full-energy peak can lead to underestimating the sample activity. The two types of coincidence summing are random coincidence summing (RCS) and true coincidence summing (TCS). RCS occurs when two photons are emitted from the decay of separate atoms. For a signal pulse rate per second, a, measured by a detector with resolving time, Δt, the probability of a second pulse arriving within Δt after an initial pulse is proportional to $a\Delta t$, therefore, the rate of coincidences by chance per second, R, can be found with the following equation [75]:

$$R = a^2 \Delta t. \tag{4.1}$$

As R is proportional to the pulse frequency squared, RCS can be mitigated by increasing the distance from the source to the detector, thereby reducing the overall count rate and the probability of RCS. This will also reduce the detection rate and hence, the sensitivity of the measurement.

TCS occurs when a nuclide decays to an excited state of its daughter nuclide. Eventually, the daughter nuclide will de-excite via gamma-ray emission until it has transitioned to its ground state. There are often multiple intermediate energy levels between the initial excited state and the ground state. In this case, if the initial excited state is short-lived, multiple cascade gamma-rays can occur, which are coincidental from the detector's point of view. Figure 4.3 displays a simplified decay scheme of ^{208}Tl, which undergoes β^- decay to various excited states of ^{208}Pb and not directly to the ground state. TCS is reduced the further away the source is from the detector. Unlike RCS, TCS scales linearly with the count rate and is affected more by the probability of gamma-rays arriving at the detector after travelling from the source. As the distance between the detector and source increases, the probability of coincident events decreases dramatically.

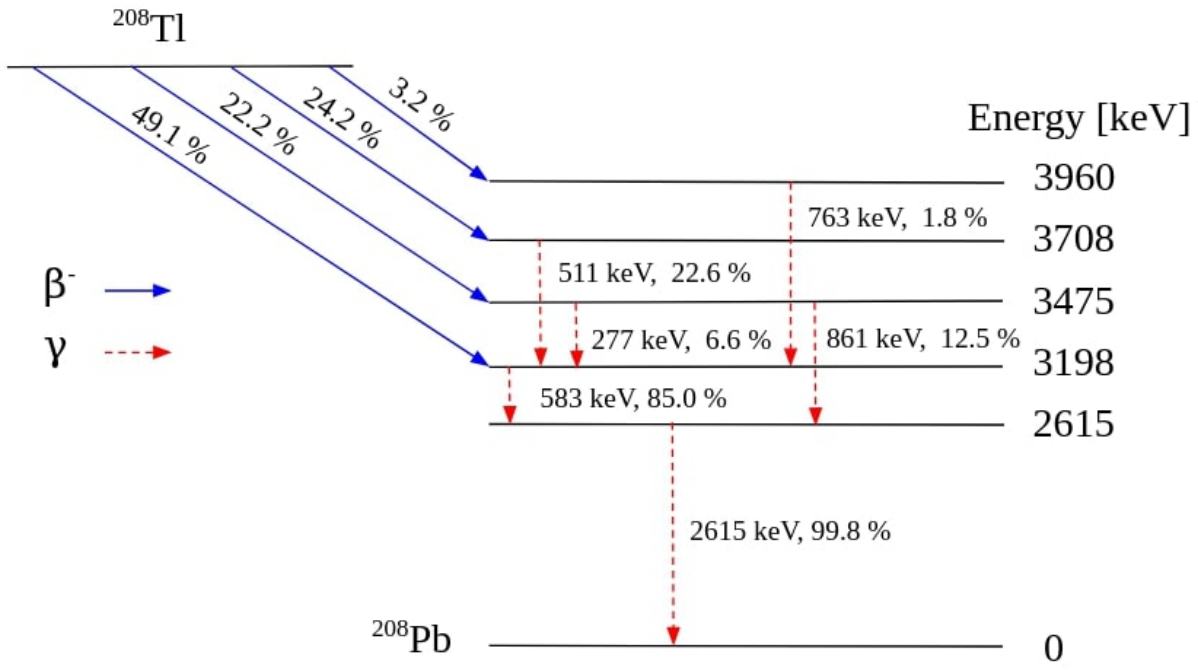


Figure 4.3: A simplified decay scheme of ^{208}Tl. The most probable β^- lines (blue, solid) are shown alongside their respective intensities. Also included are the highest intensity gamma lines (red, dashed) emitted as the ^{208}Pb nuclide transitions to lower energy states, with the gamma-rays' energies and intensities stated. All values are taken from Ref. [53].

4.3 Germanium detectors

The ideal detector for gamma-ray spectroscopy will have a good energy resolution, a high absorption coefficient and a simple signal collection method. The main types of detectors used for gamma spectroscopy are semiconductors and scintillators. Scintillator detectors are much cheaper and more efficient, but their energy resolution is poor compared to semiconductor detectors.

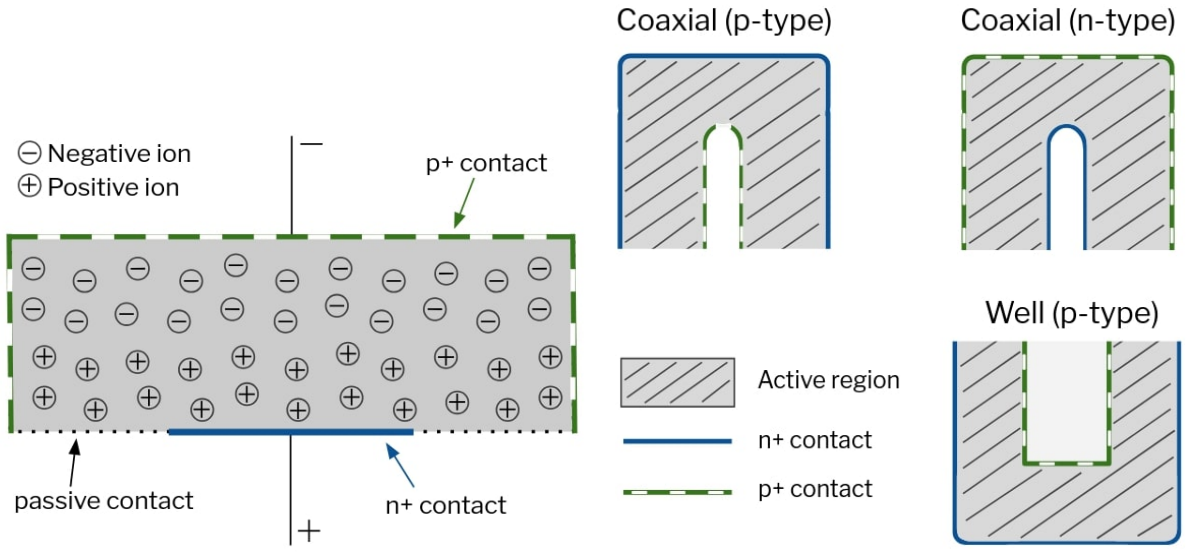
Germanium crystals are commonly used for gamma spectroscopy. There are many practical reasons for using germanium over other materials such as silicon. For example, due to the small band gap of 0.67 keV at 77 K [76] (operating temperature), the energy resolution of germanium is higher than that of silicon, which has a band gap of 1.11 keV (operating at room temperature). Additionally, the density of silicon is lower than that of germanium, meaning that a germanium detector can detect higher-energy gamma-rays. As a result of the ever-growing demand for more efficient detectors, improvements in standard techniques such as the Czochralski method, described in Ref. [77], have been continuously made since the early 20th century and the crystals can now be grown with very few impurities.

A germanium detector is constructed similarly to how p-n junctions are configured (described in Appendix A), but there are limitations to the width of the depletion region that can be reached with typical levels of doping [76]. Instead of physically joining different semiconductor materials, a detector is typically made by starting with a singular block of p-type germanium crystal. One face of the crystal is transformed into an n+ layer (a highly doped n-type region) through processes such as evaporation and diffusion, where

atoms of an n-type dopant are diffused into the p-type germanium; or ion implantation, where ions are accelerated into the crystal with high energy to form the n+ layer. The depletion region forms at the junction where the p-type and n-type meet. Since the product of the impurity concentration and depletion width is the same for both sides of the junction (the number of charge carriers removed due to recombination must balance on both sides), the high concentration of impurities in the n+ layer creates an extended depletion layer. If the germanium is of sufficiently high purity, applying a reverse bias can enable the depletion region to span the whole crystal (see Figure 4.4a). This means the entire volume of the germanium becomes sensitive to incoming radiation, which generates electron-hole pairs in the depletion region. The other faces of the germanium crystal have a p+ contact formed by ion implantation of p-type dopants. Leaving a passive contact between n+ and p+ contacts ensures reduced leakage current and therefore, improved resolution.

Apart from the size of the germanium crystal, the detector's response is primarily influenced by the thickness of the "dead layer" and the distance between the crystal and the cryostat window. A p-type contact is usually formed via boron implantation, while an n-type contact is created through lithium diffusion. These contacts form inactive (not depleted) regions close to the outer surface of the detector that are referred to as "dead layers". Gamma-rays must cross through this region to reach the sensitive part of the detector, hence, any gamma-ray absorption in a dead layer leads to a decrease in efficiency. The manufacturing of the n+ contact usually creates a thicker dead layer than that of the p+ contact.

There are three main types of detector design: coaxial, well and planar. A diagram of a planar configuration is shown in Figure 4.4a, with details of the depletion region included. The other types of detectors are more generally illustrated in Figure 4.4b. The various configurations of HPGe detectors are each optimised for different energy



(a) (b)

Figure 4.4: (a) A diagram of the configuration of a planar detector. The depletion region covers the whole crystal due to the concentration gradient of the impurities across the junction between the p+ contact, the p-type germanium and the n+ contact. (b) Configurations of coaxial and well detectors. The active region refers to the depletion region, as illustrated in (a).

ranges and applications. Well configurations offer nearly 4π solid angle coverage for small samples that can be placed in the central compartment. Planar detectors have a very thin dead layer on the front face due to the p+ contact, making them particularly sensitive to low-energy gamma-rays. In contrast, p-type coaxial and well detectors have the n+ contact on the outer surface, resulting in a slightly thicker dead layer. However, their larger crystal volumes make them more suitable for detecting higher-energy gamma-rays. N-type coaxial detectors, which have the thinner p+ contact on the outer surface, combine the advantages of a thin entrance window with a large crystal volume. This makes them highly sensitive to both low- and high-energy gamma-rays. The main drawbacks of n-type coaxial detectors are their higher production cost and, due to their larger crystal size, a slightly lower energy resolution compared to planar detectors.

Bulletisation refers to the rounding of corners in the crystal geometry, particularly in well or coaxial HPGe detectors. Sharp corners can lead to distortions or concentrations in the electric field, which may cause incomplete charge collection or increased noise. Bulletisation helps maintain a more uniform electric field throughout the detector volume and ensures that charge carriers are collected more efficiently, leading to better energy resolution.

The materials used in germanium detectors are chosen for their ability to attenuate gammas and high radiopurity, amongst other practical features such as durability and cost-effectiveness. Diagrams of the inside of a cryostat and the detector chamber are displayed in Figures 4.5a and 4.5b, respectively. The detector holder is either made of

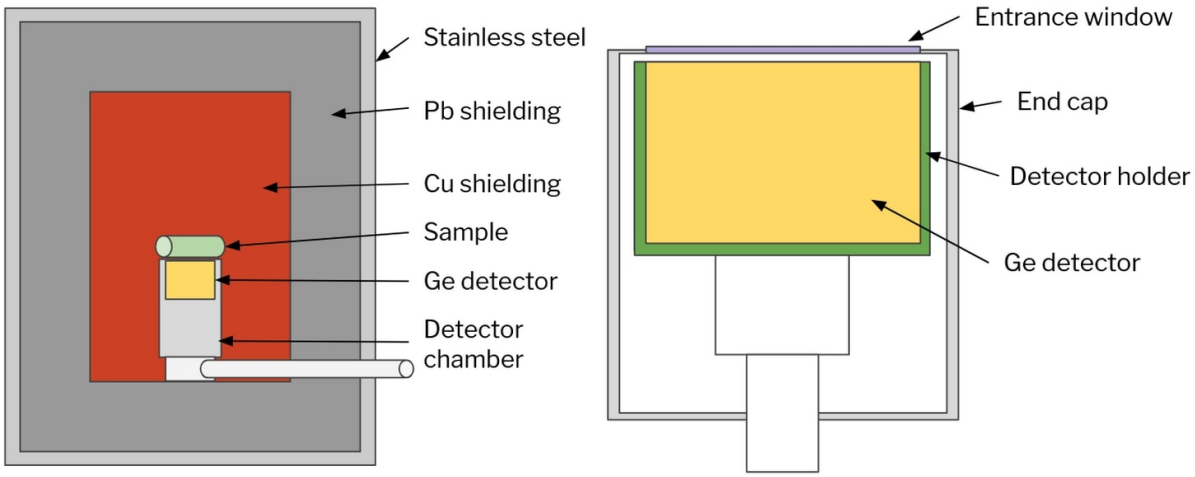


Figure 4.5: Simplified diagrams of (a) a typical cryostat design for a HPGe detector and (b) the detector chamber.

high-purity copper or high-purity aluminium. The endcap is designed for high geometric efficiency and is most commonly made of ultra-pure aluminium. The thin entrance window on coaxial detectors is also made of ultra-pure aluminium, but for planar types such as a broad-energy germanium (BEGe) detector, higher detection efficiency at lower gamma-ray energies is required. Beryllium transmits a higher percentage of low-energy gamma-rays, but is not of a high enough purity for ultra-low background screening. An alternative is a carbon-fibre window: very durable, non-toxic, non-corroding, extremely low in radioactive contaminants and absorbs few low-energy gamma-rays (80 % of 10 keV photons) [78].

Chapter 5

Gamma-ray background from rock: studies for a next-generation dark matter experiment based on liquid xenon

This chapter focuses on a next-generation xenon observatory with a wide range of measurements including the search for WIMPs and $0\nu\beta\beta$ decay of ^{136}Xe. Below, I describe the simulation of gamma-ray transport through the water shielding of a future detector, and the assessment of the thickness needed to suppress the background from rock down to a negligible level. Although relevant to the XLZD experiment [44], the design of the detector and shielding is simplified to make conclusions more generic.

5.1 Gamma-ray background of rare event searches

Recent results from current LXe detectors searching for WIMPs with masses ranging from a few GeV/c^2 to tens of TeV/c^2 have established the most stringent limits on spin-independent cross-sections [79, 80, 37, 41]. The sensitivity of the future detector is projected to be more than a magnitude better than current limits, down to a spin-independent cross-section of 3×10^{-49} cm^2 at 40 GeV/c^2 [44]. The detector will also be able to conduct a range of other low-background searches. Since LXe contains the isotope ^{136}Xe, it will be possible to search for evidence of $0\nu\beta\beta$ decay, complementing other experiments dedicated to finding the Majorana nature of neutrinos with LXe [81, 82] and germanium [83].

One of the critical challenges for the success of the next-generation experiment is minimising the background. Gamma-rays, from radioactive nuclides in the underground

rock, will produce electrons with low energies that can mimic WIMPs if they are in the WIMP signal range, 0 - 20 keV, and either scatter outside the detector's ability to resolve interactions spatially or only interact once. Gamma-induced signals in the 0 - 100 keV range are also assessed here as it covers an extended WIMP signal range. Higher energy gamma-rays serve as a background to $0\nu\beta\beta$ decay signals near the decay's Q-value of 2.458 MeV. Discrimination between NRs expected from WIMP interactions and ERs from gamma-ray background will suppress the gamma-induced background in WIMP search.

As discussed in Section 3.1, rock gamma-rays are produced by naturally occurring radioactive materials (NORM) which are ubiquitous in the rock in trace amounts. The most prevalent sources of rock gamma-rays are the radionuclides ^{232}Th, ^{238}U and ^{235}U, their progeny, and ^{40}K. A range of monoenergetic gamma-rays are emitted during the radioactive decays of the nuclides in the decay chains. As they travel through shielding and detector materials, most gamma-rays will lose some or all of their energy via various processes, such as Compton scattering, photoelectric absorption and pair production. By the time they reach the detector, there is a large spectrum of gamma-rays with energies from 0 - 2.615 MeV. The upper limit here is set by the highest energy gamma-ray with high intensity: ^{208}Tl decaying to ^{208}Pb with an intensity of 99.754 %, late in the ^{232}Th decay chain [53]. Further discussion of gamma-ray background from decay chains is in Section 3.1.

Water was selected as the shielding material for the Large Underground Xenon (LUX) experiment [84], one of the two precursors to LZ. The advantages over other common shielding materials, such as lead and steel, are: lower cost, lower background from the material itself, and better neutron shielding. The hydrogen atoms in water have a similar mass to a neutron and thus, are more efficient at moderating then absorbing neutrons. This water shielding has been relatively easy to scale up to the current LZ detector, and the same is expected for the next generation detector.

The shielding of the detector must be thick enough to deter the majority of these gamma-rays such that after stringent analysis cuts, there is < 1 event per year in the WIMP energy ROI, and < 1 event per 10 years around the $0\nu\beta\beta$ decay Q-value. For WIMPs, a powerful discrimination of > 99.5 % between NRs from WIMPs and ERs from electrons and gamma-rays will suppress the background from rock gamma-rays further by at least two orders of magnitude [79]. For $0\nu\beta\beta$ decay, there is no further suppression as signal events will look almost exactly like gamma-induced electrons. It should be noted that neutrons from spontaneous fission and (α, n) reactions in the rock are attenuated quicker in water than gamma-rays. Therefore, it is assumed that shielding thickness sufficient to reduce the gamma-ray background will be adequate for rock neutrons as well. Section 5.2 describes the establishment of a simulation developed to investigate the shielding thickness and the production of gamma-rays in rock. Section 5.3 outlines the propagation of gamma-rays from rock, transported through this simulation's geometry. Section 5.4 summarises the analysis of the results of gamma-induced background in the detector. Lastly, further considerations regarding the effects of a reduction in water shielding on the background to WIMP and $0\nu\beta\beta$ decay searches are discussed in Section 5.5.

XLZD [44] will be the next-generation dark matter detector. This project started before a more advanced design of the XLZD detector became available. The experiment

has now progressed much further in regards to the research and development carried out for its design. However, the detector will be a dual-phase LXe detector and the mass of the xenon is very similar. Hence, this work, although with a simplified design, provides a general guidance on the required thickness of shielding.

5.2 GEANT4 simulation of gamma-rays from rock

To determine sufficient shielding thickness, a simulation has been developed in GEANT4 [85]. Gamma-rays have been sampled in a layer of rock surrounding a large, cylindrical cavern and are propagated towards the detector. The detector is surrounded by a water tank and built on top of a steel plate. As there is no current designated location for a future detector, results from the simulation have been normalised here to 1 Bq kg^{-1} of radiation for ^{238}U, ^{232}Th and ^{40}K. Therefore, for a specific cavern and detector location, the background event rate can be scaled with the measured activity of these radionuclides. Similar work by the LZ collaboration has been done to look at the contribution of gamma-rays from surrounding rock to the ER background [86]. Simulations such as these inform experimentalists of the required thickness of shielding so the cavern can be designed to accommodate all systems including shielding.

5.2.1 Physics processes

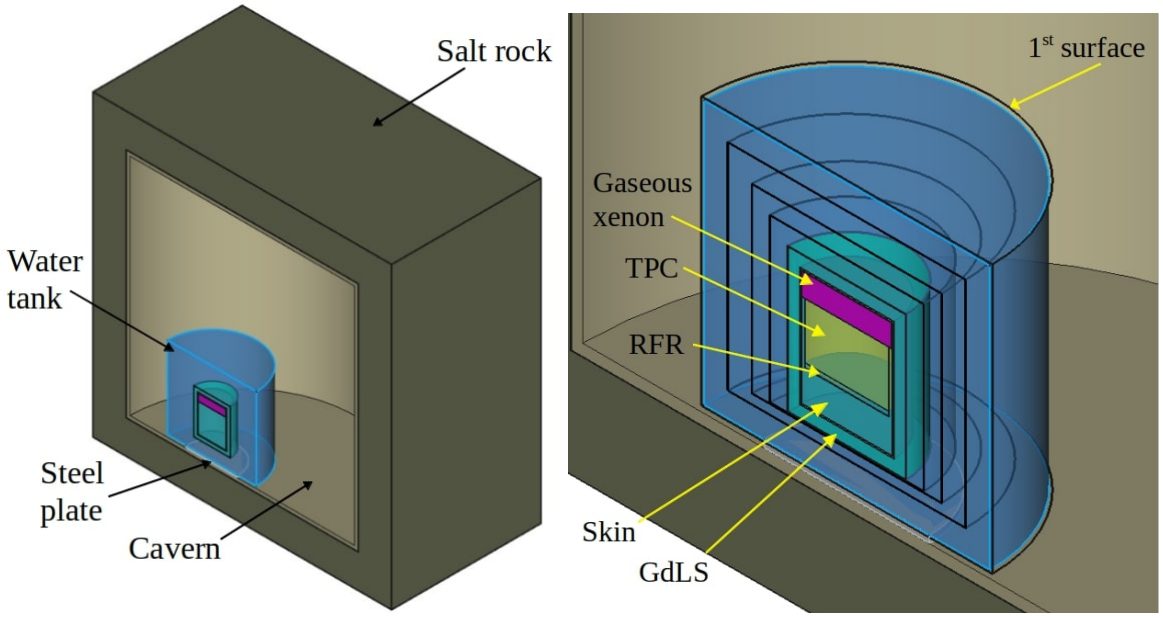
The simulation in this thesis was created with GEANT4 version 10.7.2 and the relevant, standard GEANT4 physics list, named "Shielding", was used [87]. This physics list encompasses the electromagnetic and hadronic processes necessary for testing the shielding of an experiment. There are several constructors that account for the different categories of physics, namely: boson, lepton, hadron, meson, nucleon, hyperon, anti-baryon and ion physics. The range of physics processes covered in these constructors is too vast to introduce in full here, but the main processes that are vital to include for the simulation are listed below:

- Pair production
- Compton scattering
- Photoelectric absorption
- Bremsstrahlung
- e^-e^+ annihilation
- Ionisation
- Multiple scattering of leptons
- Inelastic scattering of photons on nuclei
- Radioactive decay

The Shielding list is based on the physics list "FTFP_BERT", which handles the above processes with the Fritiof Precompound model (FTFP) [88] and the Bertini cascade model (BERT) [89]. The main differences between Shielding and FTFP_BERT are the inclusion of the radioactive decay process and improved neutron cross-sections using the Neutron HP (high precision) model. The "G4ParallelWorldPhysics" process was added to Shielding to handle the construction and use of "parallel worlds". These useful tracking tools are explained in the next section.

5.2.2 Simulation geometry

The simulation's geometry, similar to that described in Ref. [90], has been developed based on the scaled-up design of the LZ detector [42], described earlier in Section 8.1. The model is pictured in Figure 5.1 and includes a cylindrical cavern of 30 m height and 30 m diameter surrounded by salt rock (NaCl). The detector sits at the bottom of the



(a) (b)

Figure 5.1: (a) A 3D cross-sectional schematic diagram of the simulated rock, cavern, water tank and detector. (b) A closer look at the internal structure of the LXe detector, surrounded by the water tank and the 50 cm thick rock layer from which the gamma-rays were generated. The thick black lines represent the surfaces that the gamma-rays were stopped at and re-propagated from.

cavern, offset from the centre, and consists of a titanium, double-walled vacuum cryostat, surrounded by 0.5 m of gadolinium-loaded liquid scintillator (GdLS) and a water tank. The walls of the cryostat are 2 cm thick with 5 cm of vacuum separating them. No material separates the GdLS from the water or the water from the cavern air in this simulation. The cryostat houses a dual-phase time projection chamber (TPC) filled with LXe, providing an active mass of 71 tonnes with density 2.953 g cm^{-3}. There is a layer of LXe between the TPC field-cage and the inner cryostat wall, called the "skin" which acts as a gamma-ray veto. Above the TPC is a dome of gaseous xenon (GXe) with 30 cm of PTFE and steel[1] representing where the top array of PMTs will be in the detector when constructed. Below the TPC is the reverse field region (RFR) filled with 5.7 tonnes of LXe and another 30 cm layer of PTFE and steel[1] representing the bottom array of PMTs. In the actual construction of the detector, the gate and anode grids will be at the base and top of the GXe dome, respectively, while the cathode grid will be above the RFR at the base of the TPC. However, no structures or materials for any of the grids are included in the simulation.

[1] 5 % of original steel density

The GdLS is used as a veto primarily for neutron interactions in the TPC due to a high thermal neutron capture cross-section on ^{157}Gd. Both the skin and GdLS allow the rejection of neutron- and gamma-induced events that may mimic a WIMP signal in the TPC. There is 3.5 m of water shielding on the sides and top of the GdLS layer, and 1.5 m of water below the GdLS layer. The overall height of the water tank is 10.94 m with a diameter of 11.90 m. There is a 30 cm thick stainless steel plate underneath the water tank which allows us to reduce the required thickness of water and hence, the height and weight of the support structure for the TPC and GdLS tanks, but can be replaced by a similar thickness of water as needed on the top and sides. Each volume within the simulation geometry and its dimensions can be found in Table 5.1.

Table 5.1: The geometrical parameters of the volumes within the GEANT4 simulation. The salt rock cavern is the only volume constructed using G4Box, the other volumes are constructed with G4Tub (cylinder). G4Box and G4Tub refer to classes within GEANT4 that allow users to build different volumetric shapes.

Volume	Material	Height [m]	Diameter [m]
Rock environment	NaCl	40.00	40.00
Rock layer*	NaCl	31.00	31.00
Cavern	Air	30.00	30.00
Steel plate	Steel	0.30	6.90
Water tank	Water	10.94	11.90
Gd-loaded liquid scintillator	Gd, LAB	5.94	4.90
Outer cryostat vessel	Titanium	4.94	3.90
Cryostat vacuum	Vacuum	4.90	3.86
Inner cryostat vessel	Titanium	4.80	3.76
Gaseous xenon	GXe	0.93	3.72
Liquid xenon skin	LXe	4.23	3.66
PMT array (top & bottom)	Steel†	0.40	3.50
Reverse field region	LXe	0.20	3.50
PTFE (top and bottom)	PTFE	0.03	3.56
PTFE (side cylinder)	PTFE	2.70	3.56
TPC	LXe	2.50	3.50

*The volume from which gamma-rays are generated.
†5 % of original steel density.

Extra volumes were added around the detector and cavern: a 50 cm thick rock layer, within which gamma-rays were generated, was placed around the cavern volume, and "parallel world" volumes were placed around and coaxially throughout the water tank. Parallel world volumes can overlap with "real" volumes without intervening in particle transport, unlike normal geometry volumes. However, information about particles can still be extracted as they cross a parallel world volume boundary because GEANT4's transportation method recognises both the real and parallel world volumes the particles are in. Particle transport is divided into steps, the lengths of which are defined by physics processes and volume boundaries. These steps allow particles to be tracked. For example, if a photon undergoes Compton scattering, the current step is interrupted and a new step begins with the updated energy, position and direction information of the scattered photon and recoil electron. Similarly, at any boundary (including those in and

of the parallel world volume) the current step is stopped, the new volume is recognised, and information such as the medium through which a particle travels is updated. The updated density and atomic properties allow the smooth continuation of correct particle interaction simulation.

In this particular simulation, when a particle begins a new step within a parallel volume it is stopped and the physical information is extracted at that point. This feature allows a multi-stage tracking process, further outlined in Section 5.2.3, which is required because over several trillion gamma-rays need to be generated to obtain statistically acceptable data in the detector after they are attenuated through shielding, and this is computationally unattainable. The parallel volumes are treated like surfaces and hence, are hereafter named 1st surface, 2nd surface and so on as they are placed coaxially deeper within the water shielding, from 10 cm outside of the water tank to 1 cm outside of the outer cryostat vessel. The surfaces are separated as listed in Table 5.2. Figure 5.1 displays the geometric sections in more detail, including these added surfaces.

Table 5.2: The geometrical parameters of the tracking surfaces within the GEANT4 simulation. The water tank (WT), GdLS, and outer cryostat vessel (OCV) volumes are included for reference. The last two columns give distances subtracted inwards from the edges of the water tank.

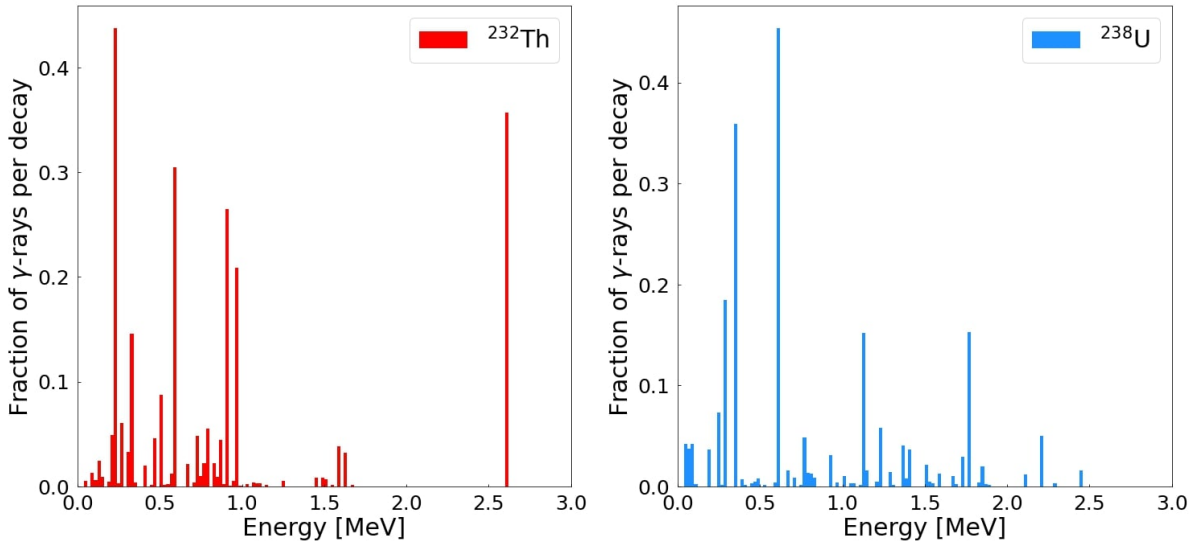
Volume	**Height [m]**	**Diameter [m]**	**Distance from WT [m]**	
			Top & sides	**Base**
1st surface	11.14	12.10	-0.10	-0.10
WT	10.94	11.90	0	0
2nd surface	8.94	9.90	1.00	1.00
3rd surface	7.54	7.90	2.00	1.40
4th surface	6.74	6.40	2.75	1.45
5th surface	5.96	4.92	3.49	1.49
GdLS	5.94	4.90	3.50	1.50
6th surface	4.96	3.92	3.99	1.99
OCV	4.94	3.90	4.00	2.00

5.2.3 Gamma-ray production

Gamma-rays were simulated as individual photons with energies and intensities. Coincident gamma-rays were not considered as they can be neglected when the source is far away from the target. To replicate ^{232}Th and ^{238}U activity, gamma lines with high intensities from their respective decay chains were generated in the rock volume around the cavern using the GEANT4 tool G4GeneralParticleSource (GPS) [85]. GPS allows more control over the characteristics of primary particles inputted into a GEANT4 simulation than the more widely used G4ParticleGun. For this study, GPS enabled isotropic emission of gamma-rays from a thin rock layer around the cavern and allowed multiple particles of differing energies to be emitted during a single simulation run. Each generated particle marked the start of an event, with the total number of events comprising a

single simulation run. Macro files were created to define gamma lines and their respective intensities, which were used as inputs for the energy spectrum, expressed as a histogram. Only gamma lines with intensities $\geq 0.1\%$ from the ^{232}Th and ^{238}U decay chains were included. The resulting energy spectra effectively represented the decay chains, with gamma emissions per parent nuclide decay. The macro files used for ^{232}Th and ^{238}U are provided in Section C. This approach was adopted as the alternative would be to simulate many particles from one parent decay per event. Tracking multiple gamma-rays from decays in the whole chain in a single event would be onerous and the probability of more than one rock gamma-ray hitting the detector within any anti-coincidence time windows (< 1 µs, see Section 5.4) is negligible, so simulating individual gamma-rays as events is justified.

Accounting for only these gamma lines, the average number of gamma-rays emitted per parent decay, N_γ, is 2.4567 for ^{232}Th and 2.0955 for ^{238}U. The intensity of each of these gamma lines is expressed as a fraction of N_γ for the decay chain they belong to. 10^6 gamma-rays have been generated with GEANT4 and their intensities have been plotted in Figure 5.2. The fraction of gamma-rays in each line agrees very well with gamma-ray intensities from NNDC [53], proving that there is no bias in the simulation at the particle generation stage. It was initially assumed that the activity of the parent radionuclides was 1 Bq kg^{-1}. To normalise the gamma-ray emission to 1 Bq kg^{-1}, the number of gamma-rays initially generated from each of the ^{232}Th and ^{238}U decay chains are multiplied by their corresponding values of N_γ.



(a) (b)

Figure 5.2: Initial energy spectra of the 10^6 gamma-rays for (a) the ^{232}Th decay chain and (b) the ^{238}U decay chain, normalised to each parent decay.

The isotope ^{40}K decays to ^{40}Ar with a branching ratio of 10.72 % via electron capture, with the emission of a neutrino and a 1461 keV gamma-ray, hence, this decay was generated as a monoenergetic gamma-ray. In one of the simulations, the monoenergetic gamma line of 2.615 MeV from ^{208}Tl decay (99.7 % intensity) was also generated. ^{208}Tl is the result of ^{212}Bi alpha decay with a 35.94 % branching ratio. The purpose of this particular simulation was to compare the transport of gamma-rays with the highest energy

(2.615 MeV) with the whole ^{232}Th decay chain spectrum. This comparison is discussed further in Section 5.3.

The rock layer's thickness was chosen to be 50 cm as it was estimated that gamma-rays more than 50 cm into the rock would be heavily attenuated, thereby providing insignificant statistics compared to gamma-rays closer to the cavern. To validate this assumption, different thicknesses were tested to see the change in the percentage of gamma-rays reaching the first surface. These results are presented in Table 5.3.

Table 5.3: Fraction of gamma-rays that reached the first surface from the 50 cm thick rock layer. Just over half of the gamma-rays that reached the first surface came from the first 10 cm of the rock layer, with only 1.7 % arriving from the deepest 10 cm into the rock layer (40 - 50 cm).

Thickness [cm]	10	20	30	40	50
γ-ray fraction [%]	54.5	81.3	93.5	98.3	100

When generated within a 50 cm thick rock layer, 98.3 % of the gamma-rays that reached the surface originated from the first 40 cm into the rock. Hence, a 50 cm layer was considered further on as producing almost all gamma-rays reaching the surface of the cavern. Additionally, the gamma-rays were stopped at the first surface and plotted their coordinates to check that they are being fired isotropically. Positions of gamma-rays are displayed in Figure 5.3.

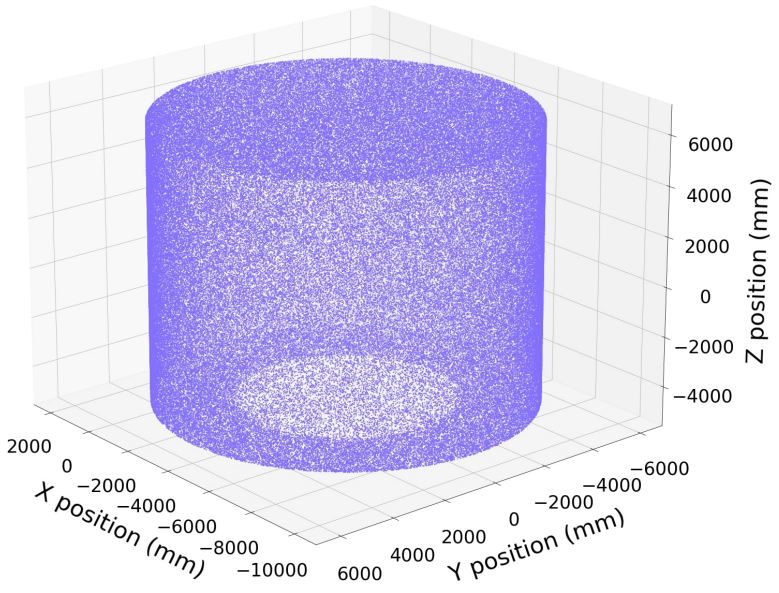


Figure 5.3: The (x,y,z) positions of 0.3 million gamma-rays from ^{208}Tl decay stopped at the 1st surface. The lack of events at the base is due to the steel plate that absorbs most gamma-rays coming from beneath the water tank.

5.3 Gamma-ray propagation through the shielding and energy deposition in the TPC

Once generated, the gamma-rays are transported through the cavern and shielding towards the TPC. They are stopped at each of the coaxial surfaces before being propagated again towards the next surface in increased numbers. This is an event biasing method and the initial number of gamma-rays is increased by a factor F:

$$F = \prod_{i=1}^{n} m_i, \tag{5.1}$$

where m_i represents the multiplication factor by which each gamma-ray is re-propagated and n is the number of surfaces. This allows the user to boost statistics by enlarging the total number of gamma-rays generated. F is a statistical factor for all events; no additional statistical weights have been applied. The energy, position and momentum direction at each surface are stored. The values of F for ^{232}Th, ^{238}U, and ^{40}K are, respectively: 1.8×10^9, 5.1×10^9 and 2.5×10^9.

The decay rate of the parent radionuclide was normalised to 1 Bq kg^{-1}, and the energy spectrum of gamma-rays at each surface was expressed in counts cm^{-2} s^{-1} (Bq/kg)$^{-1}$ keV^{-1}. Figure 5.4 shows the energy spectra of gamma-rays at each surface from decays of the nuclides ^{232}Th (the whole decay chain) and ^{208}Tl. It shows that by the time the gamma-rays reach the TPC, only those originating from ^{208}Tl remain, meaning that the ^{208}Tl and ^{232}Th spectra are very similar. This occurs due to the higher attenuation coefficient, A, for lower-energy gamma-rays. For completeness, the full ^{232}Th spectrum was used for the final analysis in Section 5.4.

According to a separate, simple GEANT4 simulation, the attenuation coefficient of a 2.615 MeV gamma-ray through water is 0.0426 cm^2 g^{-1} and that of a 1.764 MeV gamma-ray from ^{212}Bi decay, for comparative purposes, is 0.0528 cm^2 g^{-1}. The flux ratio of the two isotopes can be found with the following equation:

$$\frac{I_{\mathrm{Tl}}}{I_{\mathrm{Bi}}} = e^{(A_{\mathrm{Bi}} - A_{\mathrm{Tl}})x}, \tag{5.2}$$

where x is distance in cm, I is flux in cm^{-2} s^{-1}, and A_{Bi} and A_{Tl} are the attenuation coefficients for a 1.764 MeV gamma-ray from ^{212}Bi and a 2.615 MeV gamma-ray from ^{208}Tl, respectively. After 3.5 m of water shielding, the flux of the 2.615 MeV gamma-ray is 35 times higher. The 2.448 MeV line from ^{214}Bi (^{238}U decay chain) also has a higher attenuation coefficient than the 2.615 MeV line, but this peak overlaps with the Q-value of $0\nu\beta\beta$ decay of ^{136}Xe, $Q_{\beta\beta}$, so the ^{238}U background is still important for this search. The branching ratio of the line is low, at about 1.5 %, but a high concentration of ^{238}U in rock can make this background dominant.

Table 5.4 presents the flux of 2.615 MeV gamma-rays at each surface throughout the water shielding and the GdLS; the fluxes have been normalised to the first surface. Gamma-rays that lose energy during propagation are not included in the flux. The bases

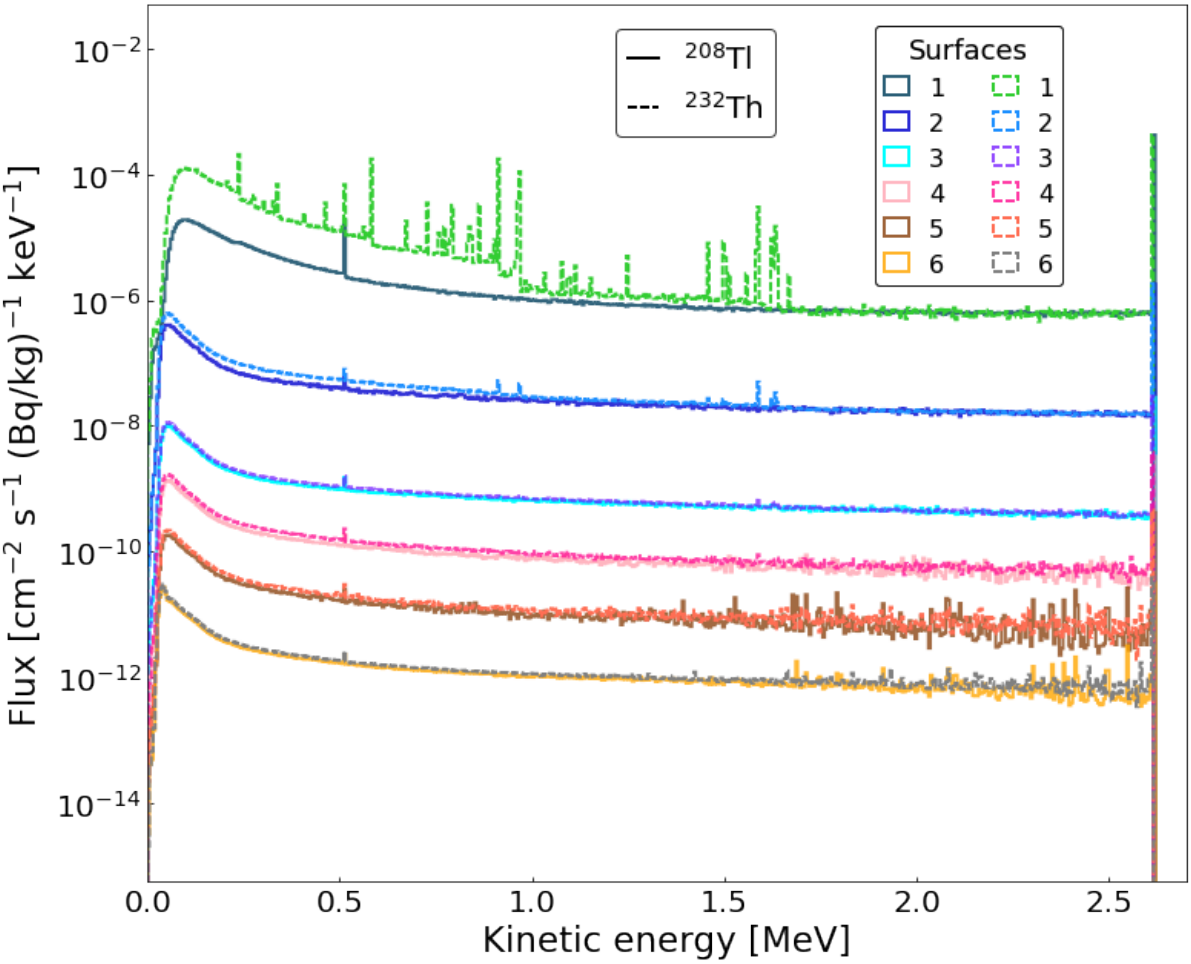


Figure 5.4: Gamma-ray energy spectra from ^{208}Tl (solid line) and the whole chain of ^{232}Th (dashed line) decays at each surface from the outside of the water tank (surface 1) and in stages throughout until reaching the outside of the TPC (surface 6). The surfaces through the shielding are illustrated in Figure 5.1b and the distances between each of these surfaces and certain detector volumes are listed in Table 5.2. The peak at 0.511 MeV is due to electron-positron annihilation, where positrons are produced via the pair production process by high-energy gamma-rays in the water.

of each surface are closer together than each of their tops and sides, and there is a steel plate on the bottom of the water tank. Accounting for the impacts of these differences would be difficult and not worthwhile, thus, to calculate the attenuation coefficient, only the flux on the top and sides of each surface have been used. The attenuation coefficient decreases as distance increases because the gamma-rays with momentum in the direction of the TPC are the most likely to reach it as they will cross the least amount of water. At the first surface, the range of the gamma-rays' momentum vector is broad, but after several stages of re-propagation, the majority of gamma-rays are heading straight towards the detector.

The systematic uncertainty from GEANT4's propagation of gamma-rays has been assessed by finding the difference between attenuation coefficients calculated in GEANT4 (with a separate, simple simulation) and those published by NIST [91]. Comparing results from gamma-rays with energies 2 MeV and 3 MeV, and taking the largest difference between GEANT4 and NIST attenuation coefficients, the systematic uncertainty was

calculated to be ~ 0.7 %. After 4 m of shielding, the flux ratio (I/I_0) will have a similarly negligible systematic uncertainty, therefore, it is not quoted for these flux values.

Table 5.4: Attenuation of 2.615 MeV gamma-rays. The surfaces in the first column are shown in Figure 5.1b. The flux at each surface has been normalised to the flux at the first surface. The distance is measured from one surface to the next, corresponding to the fourth column in Table 5.2. Only the top and sides of the surfaces have been used here because the gamma-rays are not uniformly spread across the base of the water tank and detector, owing to the effect of the steel plate underneath. The flux ratio in the fourth column is the ratio between the flux at the current surface and the flux at the previous surface. The distances and the attenuation coefficients are cumulative, except for surfaces 5 to 6 where attenuation through the 0.5 m of GdLS is calculated separately, attributable to differences in material composition.

Surface	**Normalised flux**	**Distance [cm]**	**Flux ratio**	**Attenuation coefficient [cm^2 g^{-1}]**
1	1.00	0	n/a	n/a
2	4.03×10^{-3}	100	4.03×10^{-3}	5.51×10^{-2}
3	3.82×10^{-5}	200	9.48×10^{-3}	5.09×10^{-2}
4	1.34×10^{-6}	275	3.5×10^{-2}	4.92×10^{-2}
5	5.18×10^{-8}	349	3.87×10^{-2}	4.82×10^{-2}
6	8.36×10^{-9}	50	0.161	4.24×10^{-2}

The final stage of the simulation involves propagating the gamma-rays once more from the final, 6th surface. Information is collected from every particle that deposits more than 0.1 keV in the TPC, skin and GdLS volumes. These particles are primarily electrons resulting from the physical processes of Compton scattering and the photoelectric effect, with occasional positrons created from pair production. The information recorded includes energy deposits and their positions and time, as well as the parameters of the particles that release this energy in the detector volumes.

The energy spectra of ^{208}Tl, ^{232}Th, ^{238}U, and ^{40}K are displayed in Figure 5.5 where the energy deposits are summed per event. As expected, the spectra of ^{208}Tl and ^{232}Th are very similar, with event rates of 1185 and 1155 year^{-1} (Bq/kg)$^{-1}$, respectively. The ^{238}U spectrum has a lower event rate of 47 year^{-1} (Bq/kg)$^{-1}$, primarily due to the low intensity of its highest-energy gamma line, ^{214}Bi at 2448 keV. The event rate of the ^{40}K spectrum is 0.50 year^{-1} (Bq/kg)$^{-1}$. The two orders of magnitude difference between ^{40}K and ^{238}U rates reflects the higher attenuation of the 1461 keV gamma line relative to the 2448 keV ^{214}Bi line.

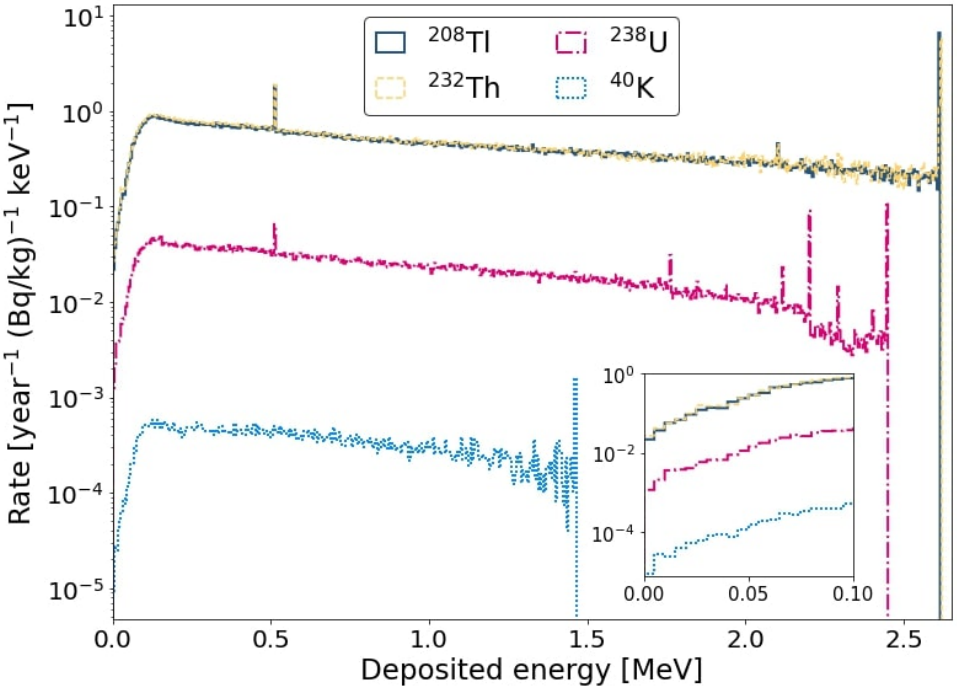


Figure 5.5: The energy deposited by gamma-induced events (mainly electrons) from ^{208}Tl and ^{40}K decays, and whole chain ^{232}Th and ^{238}U decays. The inset plot shows the spectra from 0 - 100 keV which is an extended WIMP region of interest investigated in Section 5.4.

5.4 Analysis and results for shielding thickness

A signal from either a WIMP interaction or a 0νββ decay will be a single energy deposition from one event. The number of events that would contribute to the background by depositing energy, E_{dep}, once in either the WIMP energy range or around the 0νββ decay signal, is extracted in the following analysis. The WIMP ROI in this analysis was 0 - 20 keV, similar to an extended ROI used to search for a wide range of WIMP masses [79]. The background in the larger WIMP range of energies of interest for WIMP-nucleon effective field theory couplings, 0 - 100 keV, is also assessed [92]. For 0νββ decay, the energy resolution (σ/E) of the detector at 2.458 MeV was assumed to be 1 % around $Q_{\beta\beta}$ from the LZ simulation model [93]. The ROI considered in this analysis is conservatively taken as $\pm$ 2 σ, 2.408 $< E_{dep} <$ 2.508 MeV. It should be noted, however, that the energy resolution can be improved, as LZ has already demonstrated [94], and the energy ROI reduced to optimise the sensitivity.

Analysis cuts similar to those developed by LUX and LZ to suppress the gamma-ray background have been implemented. Before cuts, the total numbers of gamma-rays simulated for ^{232}Th, ^{238}U, and ^{40}K were, respectively: 9.63×10^{17}, 2.81×10^{18} and 1.03×10^{18}. The baseline threshold for the GdLS was chosen to be 200 keV to avoid false vetoes from the decays of ^{14}C, ^{152}Gd, and ^{147}Sm [86]. A similar threshold for events in the skin was taken as 100 keV, which is sufficient to detect most Compton electrons from MeV gamma-rays [95, 96].

To reduce the amount of data stored on disk, information about energy depositions in the GdLS was only saved at the last stage of the simulation where the gamma-rays are transported from the 6th surface to the TPC. Any depositions from previous stages have

not been stored and thus, the results presented here are conservative. In the analysis of real data, gamma-rays may leave a signal in the GdLS before reaching the TPC. These cuts were implemented by adding up all energy depositions of an event in the TPC within 1 µs (anti-coincidence time window), then similarly and separately adding up all energy depositions of the same event in the skin and scintillator, also within 1 µs. If an event in the TPC had a companion event in either the skin or liquid scintillator, within 1 µs and above their respective thresholds, this event is rejected. The effects of these cuts applied to raw data are illustrated in Figures 5.6 and 5.7.

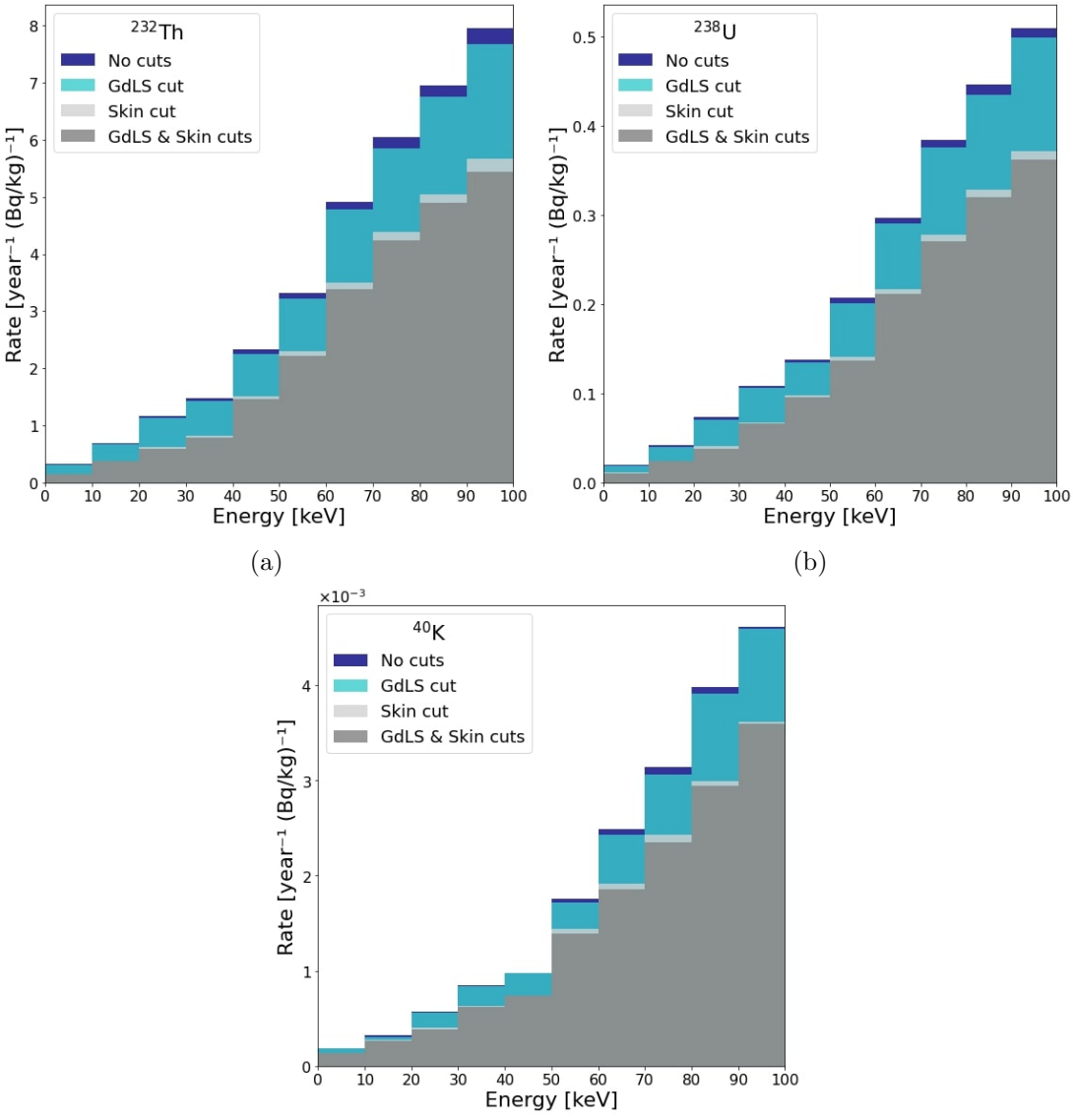
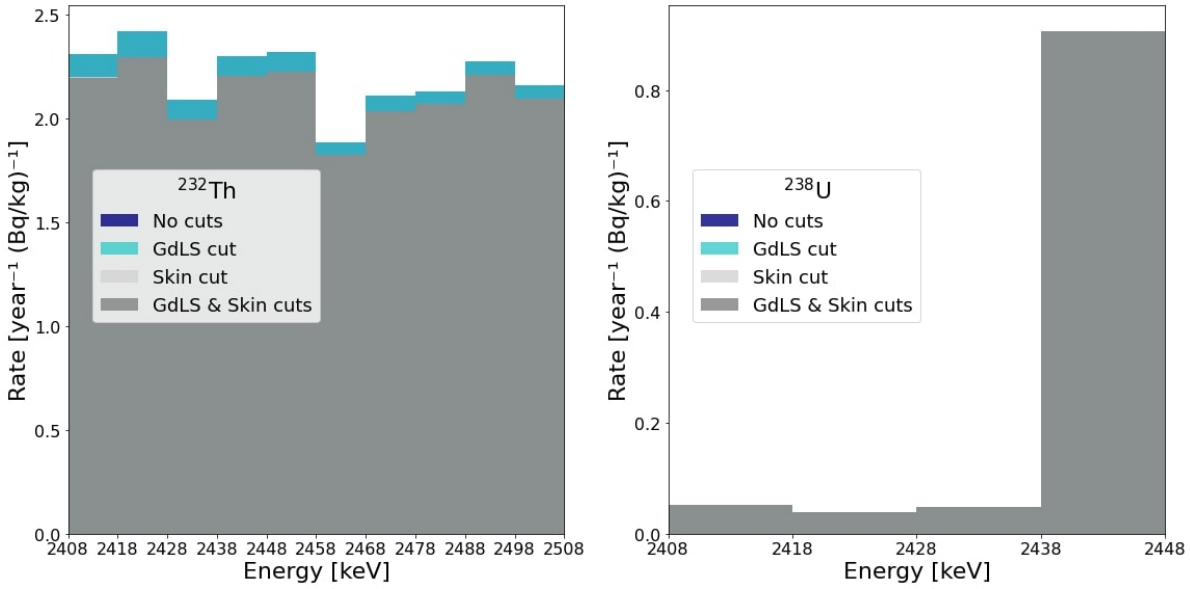


Figure 5.6: Rate of energy deposits from (a) the ^{232}Th decay chain, (b) the ^{238}U decay chain and (c) the ^{40}K decay with the following cuts applied: the 200 keV GdLS threshold, the 100 keV skin threshold and both thresholds. The total number of events with no cuts applied in the range $0 - 20$ keV is (a) 2490 ± 50, (b) 576 ± 24 and (c) 26 ± 5. For the total number of simulated events, see Section 5.4 text.



(a) (b)

Figure 5.7: Rate of energy deposits from (a) the ^{232}Th decay chain and (b) the ^{238}U decay chain with the same cuts applied as in Figure 5.6. The total number of events with no cuts applied at ± 50 keV around $Q_{\beta\beta}$ (2.458 MeV) in each bin is approximately 5400 in (a) and 2200 in (b). There is significant overlapping of histograms due to inefficiency of the Skin and GdLS cuts in this energy range.

The impact of the cuts on event rates is consistent across the decay chains of ^{232}Th, ^{238}U and ^{40}K within the energy range of $0 - 100$ keV. The skin cut demonstrates a higher rejection efficiency than the GdLS cut across all nuclides. In the 0νββ ROI, only the skin cut significantly reduces the event rate for ^{232}Th. The total number of events at ± 50 keV around $Q_{\beta\beta}$ is reduced from 56765 to 54415 after the skin cut - a 4% decrease. For ^{238}U, no cuts notably affect the event rate in the 0νββ ROI. This behaviour can be attributed to the low probability of 2448 keV gamma-rays from the decay of ^{214}Bi depositing sufficient energy in both the skin and GdLS to surpass their respective thresholds, while still retaining enough energy to interact in the TPC within the ROI. Instead, the observed counts in the final bin in Figure 5.7 ($2438 - 2448$ keV) are likely dominated by complete photoelectric absorption of the gamma-rays within the TPC. Although there are gamma lines in the ^{238}U chain with energies higher than the 2448 keV gamma-ray from ^{214}Bi, their intensities are sufficiently low that background rates from them would be negligible. Hence, there are no bins at energies higher than 2448 keV for ^{238}U.

The deposited energy and (x, y, z) positions of each interaction are stored. The z-axis spans the entire height of the TPC, while the orthogonal x- and y- axes, in a plane perpendicular to the electric field and electron drift direction[2], are combined to parameterise the resolution along the radius, r, of the TPC. To reject multiple scattering gamma-rays, the energy-weighted standard deviations (σ_z and σ_r) of separate clusters of energy de-

[2]A description of how the TPC operates is in Section 8.1. This simulation analysis is based on the same operation and similar geometry dimensions as the LZ experiment, but scaled up to accommodate a larger TPC.

posits per event are required to be less than the spatial resolution of the detector. σ_z and σ_r are calculated using Equations (5.3) and (5.4), respectively:

$$\sigma_z = \sqrt{\frac{\sum_{i=1}^{N} w_i (z_i - \bar{z})^2}{\sum_{i=1}^{N} w_i}}, \tag{5.3}$$

$$\sigma_r = \sqrt{\frac{\sum_{i=1}^{N} w_i ((x_i - \bar{x})^2 + (y_i - \bar{y})^2)}{\sum_{i=1}^{N} w_i}}, \tag{5.4}$$

where for an interaction, i, in an event with N interactions, w_i is the fraction of the event's total energy released by i, and x_i, y_i and z_i are the positions of i in the TPC. All positions in an event have been averaged and weighted with w to obtain $\bar{x}$, $\bar{y}$ and $\bar{z}$, the weighted mean positions of energy deposits. Similar work has been done by LZ [86] and LUX [84, 97]. Based on position reconstruction carried out by LUX and accounting for the up-scaled size of the detector, the spatial resolutions of the future detector were conservatively assumed to be 0.5 cm in the vertical direction and 5 cm in the horizontal direction. Thus, it was assumed that events with $\sigma_z > 0.5$ cm and $\sigma_r > 5.0$ cm will be reconstructed as multiple scatter events and will be rejected. These thresholds are larger than those used for the LUX and LZ experiments because the increased size of the detector causes a decrease in resolution. The number of multiple scattered events for ^{232}Th, ^{238}U and ^{40}K are shown in Figures 5.8 and 5.9 and it is clear that at higher energies there are many more of these events, as expected.

The impact of the multiple scatter cut on the rate in the TPC is therefore greater at higher energies, as is demonstrated in Figure 5.11. The lack of effect that the standard deviation cuts have on the events in the WIMP ROI, as is demonstrated particularly well in Figures 5.8e and 5.8f.

Lastly, an FV cut vetoes events caused by X-rays, alpha particles and beta particles from surfaces in contact with the xenon in the TPC. Thus, to remove these background events for the WIMP ROI a cylindrical "WIMP FV" has been set with boundaries: -123 cm $< z <$ 113 cm and radius $<$ 170 cm, which translates to 2 cm from the cathode grid at the base of the TPC, 12 cm from the gate grid at the top of the TPC and 5 cm from the TPC wall. These boundaries, containing approximately 63.3 tonnes of LXe, are outlined in Figure 5.10, where the multiple scatters cut has already been applied. Almost all events for each nuclide in the energy range 0 - 100 keV are single scatters and, as the attenuation lengths of low-energy ($\sim 10^2$ keV) gamma-rays in LXe are around a few centimetres [91], are mainly located near the TPC walls outside of the WIMP FV.

To remove background events from the $0\nu\beta\beta$ decay ROI, the FV was selected to ensure that the rate of events from ^{232}Th and ^{238}U after all cuts were each < 0.1 year^{-1} (Bq/kg)$^{-1}$. The FV limits were minimised separately for each nuclide and these reduced "$0\nu\beta\beta$ FVs" are illustrated in Figure 5.11 and correspond to fiducial masses of 39.3 tonnes and 59.6 tonnes for ^{232}Th and ^{238}U, respectively. The boundaries of these $0\nu\beta\beta$ FVs are: 9 cm and 2 cm from the cathode grid; 25 cm and 12 cm from the gate grid; and 35 cm and 10 cm from the TPC wall (the first value corresponds to the background from ^{232}Th

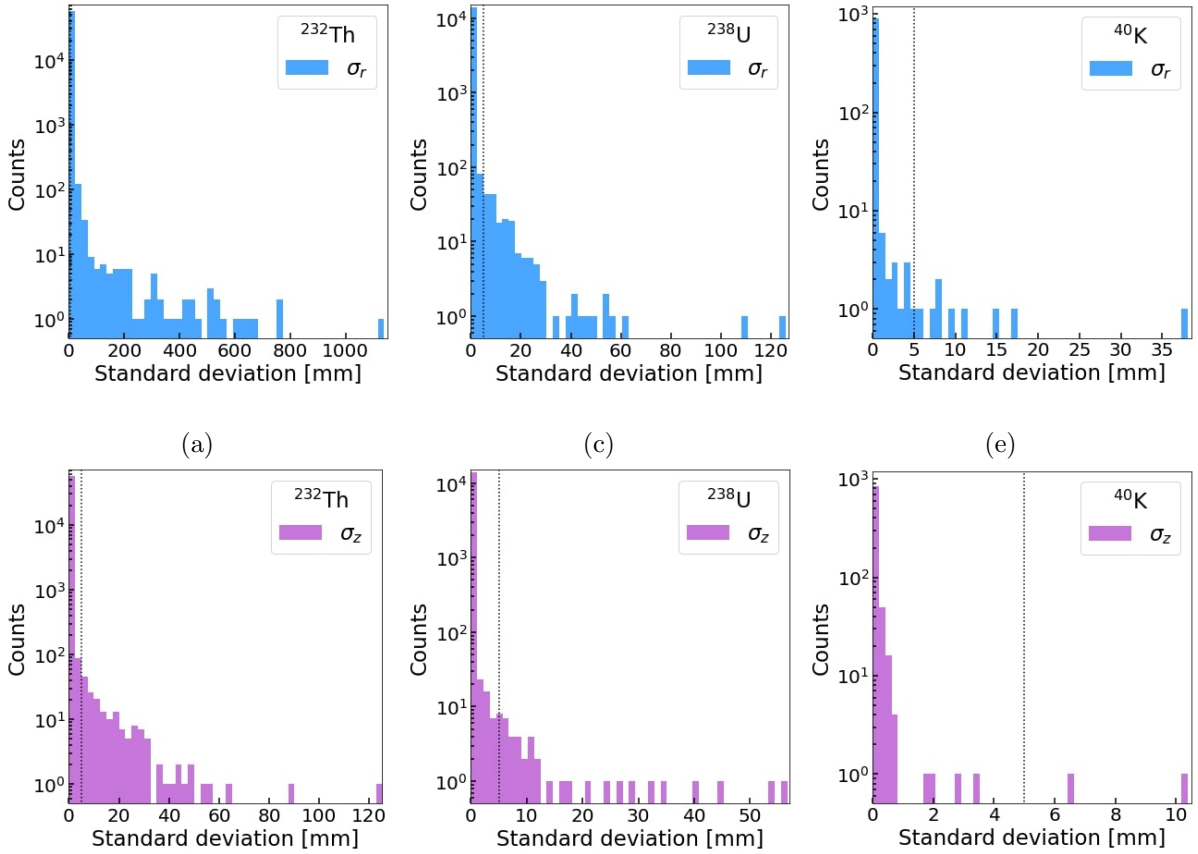


Figure 5.8: Radial (top) and z-coordinate (bottom) standard deviations of ^{232}Th (a and b), ^{238}U (c and d), and ^{40}K (e and f) events in the TPC in the energy range 0 - 100 keV.

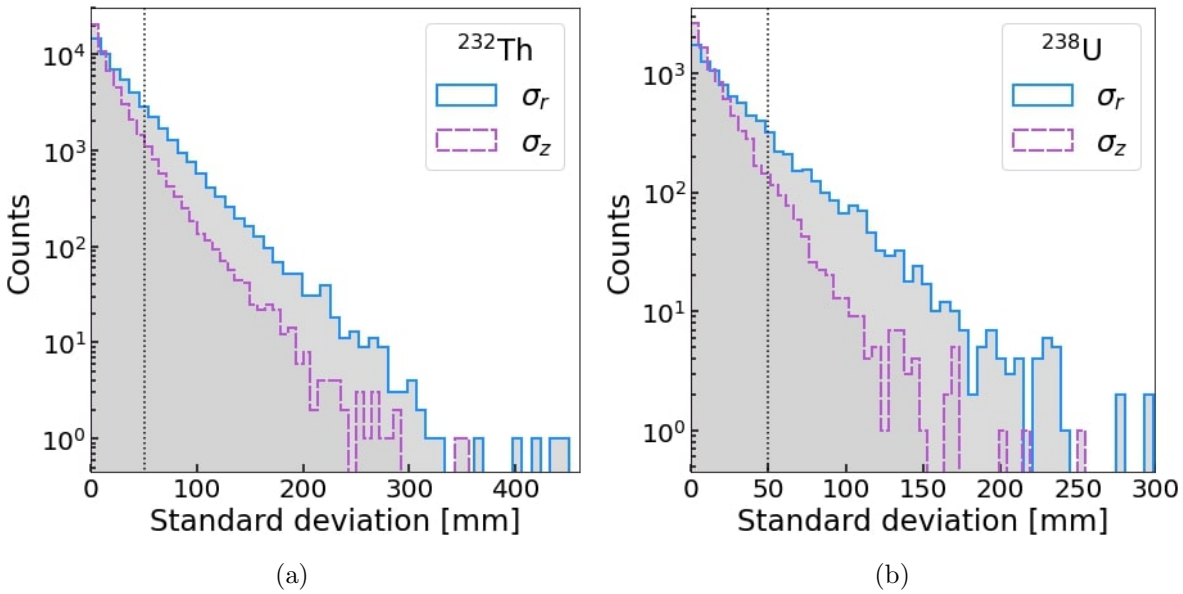


Figure 5.9: Radial and z-coordinate standard deviations of (a) ^{232}Th and (b) ^{238}U events in the TPC in the energy range 2408 - 2508 keV, ± 50 keV around $Q_{\beta\beta}$.

and the second value from ^{238}U). The most stringent FV of the two will be chosen for the experiment, and this will be determined by the concentration of ^{232}Th or ^{238}U in the cavern rock around the experiment. Note that the FV is expected to be smaller than anticipated here due to additional, and higher, contributions from the radioactivity in detector components not considered here. Further discussion on reducing the FV for $0\nu\beta\beta$ decay search is in Section 5.5. The effects of all analysis cuts on the total number of events from each nuclide are summarised in Table 5.5.

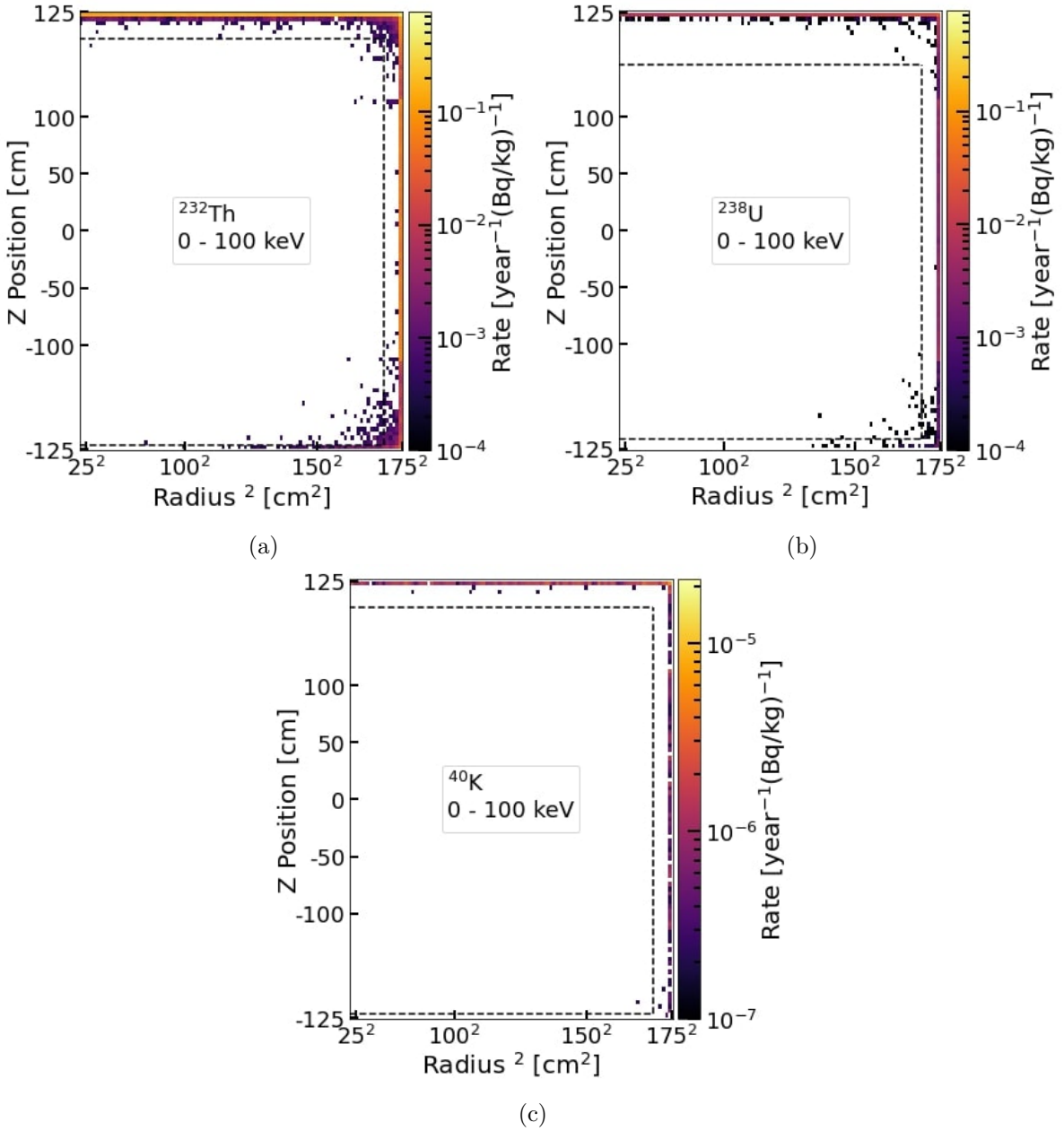


Figure 5.10: Scatter plots of the mean position of events from the (a) ^{232}Th, (b) ^{238}U decay chains and (c) ^{40}K decay in the TPC. They show the event positions within the energy range 0 - 100 keV after multiple scatter cuts have been applied. The dotted black line outlines the FV boundaries for WIMP search. To improve visibility of events, the z-positions are displayed using a piecewise linear rescaling, applied symmetrically around $z = 0$. was compressed to occupy 60 % of the y-axis (instead of 92 % in linear scaling), while the outer regions were expanded to 40 % in total (instead of 8 %), making features near the detector edges more apparent.

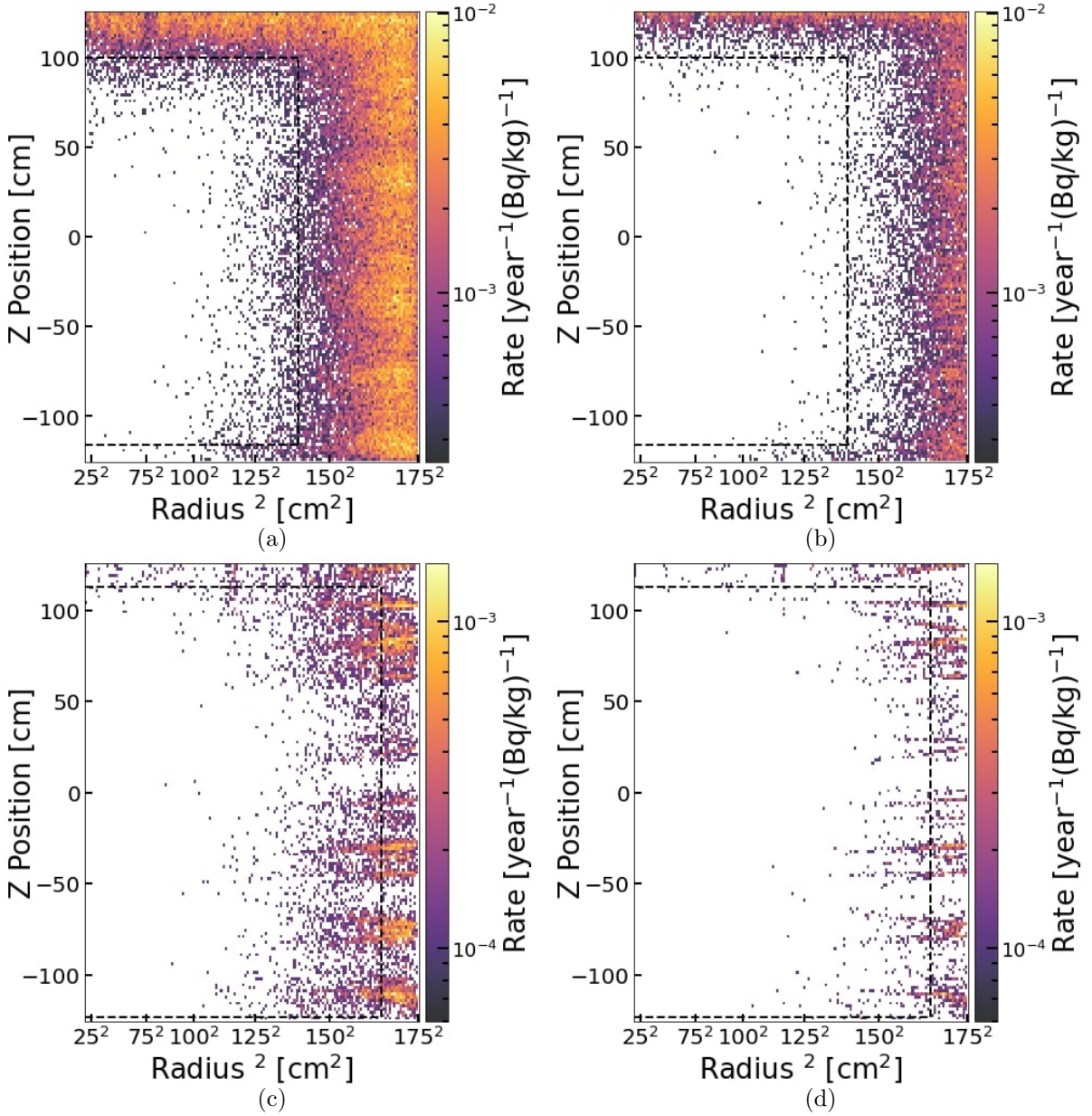


Figure 5.11: Scatter plots of the mean position of events from the ^{232}Th and ^{238}U decay chains in the TPC. (a) and (b) depict the mean position of events from ^{232}Th in the energy range 2.408 - 2.508 MeV (50 keV around $Q_{\beta\beta}$) before and after multiple scatter cuts have been applied, respectively. The dotted black line outlines the reduced FV that will need to be in place for $0\nu\beta\beta$ decay background sensitivity. (c) and (d) are the equivalent to (a) and (b), but for ^{238}U chain events with the ^{238}U fiducial outlined. The clusters of events apparent in all plots, but particularly obviously in (c) and (d) result from boosting, exacerbated by the fact that a high-energy (2.448 MeV) gamma-ray from the uranium chain must deposit almost all of its energy in a single interaction to be included in the $0\nu\beta\beta$ decay ROI.

The event rate for each radioactive nuclide depositing energy in the TPC per year, normalised to 1 Bq kg^{-1} is presented in Table 5.6. Asymmetric uncertainties are quoted at 68.27 % confidence level (CL) limits for the Poisson signal mean and 90 % CL limits for 0 values. The percentage systematic uncertainty on the rates is quoted in the table caption and is derived from varying the multiple scatter cut thresholds, σ_z and σ_r, by

Table 5.5: A summary of the analysis cuts outlined in Section 5.4 and their effects on the number of events depositing energy in the TPC. After each cut, the remaining events are expressed as a fraction of the total number of events. GdLS and Skin thresholds are applied in the first row, then the σ_r and σ_z thresholds that constitute the multiple scatter cuts are applied in rows 2 and 3, respectively. The last row includes the FV cuts, displaying the fraction of events that survive all of the analysis cuts.

	^{232}**Th**		^{238}**U**		^{40}**K**
Cuts	**0 - 100 keV**	**2408 - 2508 keV**	**0 - 100 keV**	**2408 - 2508 keV**	**0 - 100 keV**
GdLS & Skin	0.68	0.93	0.67	1.00	0.76
MS (x, y)	0.66	0.75	0.67	0.80	0.74
MS (z)	0.66	0.27	0.66	0.29	0.74
FV	4.7×10^{-4}	4.4×10^{-3}	7.4×10^{-4}	2.9×10^{-2}	0

$\pm$ 20 %. The rates in the energy ranges 0 - 20 keV and 0 - 100 keV include the WIMP FV cut, and the rates in the 2408 - 2508 keV energy range include the $0\nu\beta\beta$ FV cut corresponding to either ^{232}Th or ^{238}U. In addition to these analysis cuts, discrimination between NRs and ERs will contribute to the suppression of background events for WIMP search [79].

5.5 Discussion of shielding thickness and reduction effects

For dark matter searches, a background of < 1 event per year is required to ensure a potential signal can be found. Further NR/ER discrimination can reduce the background that mimics NR events by more than two orders of magnitude. At such a low rate, the experiment could run for 10 years, with the background after discrimination remaining negligible (< 0.1 events over 10 years), assuming the 99.5 % discrimination already achieved [79]. The sensitivity requirement for $0\nu\beta\beta$ decay is even stricter, as signal events may be indistinguishable from background events (both being produced by electrons). Therefore, the background must be limited to < 1 event over 10 years of data collection. Our findings (Table 5.6, columns 2 - 5) show that 4 m of water and scintillator on the top and sides, combined with 2 m on the bottom and a 30 cm thick steel plate, is more than sufficient to reduce the gamma-ray background from rock for WIMPs to a negligible level, for an initial radioactivity in rock of about 1 Bq kg^{-1}. For $0\nu\beta\beta$ decay search, the rate of background events for 1 Bq kg^{-1} of ^{232}Th and ^{238}U concentrations (Table 5.6, columns 6 - 7) suggests that the FV needs to be reduced compared to that typically used for WIMP searches. Depending on the concentration of radionuclides in the rock at the future site, the FV in the TPC needs to be adjusted to meet the background requirements for the $0\nu\beta\beta$ decay search.

Due to other sources of background, such as those from the detector materials themselves, the FV for $0\nu\beta\beta$ decay will be much smaller than the one defined above in Section 5.4. Given the much smaller FV for $0\nu\beta\beta$ decay due to the background from detector components and the sufficiently low background in the WIMP ROI, the water tank could be reduced in size which would consequently reduce the cost of construction. The simulated water shielding thickness is 3.5 m on the top and sides of the detector and 1.5 m

Table 5.6: Background events in the TPC with the analysis cuts applied. The second column provides the total number of generated gamma-rays, including the boosting factor F (see Equation (5.1)), for each nuclide. The WIMP FV cut is applied for 0 – 20 keV and 0 – 100 keV energy ranges. For 2408 - 2508 keV, the ^{232}Th $0\nu\beta\beta$ FV cut is applied to ^{232}Th rates, while the ^{238}U $0\nu\beta\beta$ FV cut is applied to ^{238}U rates. See Section 5.4 text for the evaluation of the WIMP and $0\nu\beta\beta$ FVs. Using a Feldman-Cousins approach [98], the statistical uncertainties are shown at 1 σ for non-zero event rates and an upper limit of 90 % CL is quoted for zero events. Systematic uncertainties from varying the multiple-scatter cut thresholds by $\pm$20 % are isotope- and energy-dependent: for ^{232}Th they are 2.7 % (0 – 100 keV) and 14.8 % (2408 – 2508 keV); for ^{238}U it is 16 % (2408 – 2508 keV); and for ^{40}K, no changes were observed. In the 0 – 20 keV range, no changes were observed for any isotope.

		0 - 20 keV		**0 - 100 keV**		**2408 - 2508 keV**	
Isotope	**No. of gamma-rays simulated**	**Events**	**Rate [year^{-1} (Bq/kg)$^{-1}$]**	**Events**	**Rate [year^{-1} (Bq/kg)$^{-1}$]**	**Events**	**Rate [year^{-1} (Bq/kg)$^{-1}$]**
^{232}Th	9.63×10^{17}	$4^{+2.78}_{-1.66}$	$\left(1.5^{+1.1}_{-0.6}\right) \times 10^{-3}$	37 ± 6.1	$(1.42 \pm 0.23) \times 10^{-2}$	253 ± 15.9	$(9.69 \pm 0.61) \times 10^{-2}$
^{238}U	2.81×10^{18}	$2^{+2.25}_{-1.26}$	$\left(2.2^{+2.5}_{-1.4}\right) \times 10^{-4}$	$14^{+4.32}_{-3.70}$	$\left(1.6^{+0.5}_{-0.4}\right) \times 10^{-3}$	820 ± 28.6	$(9.19 \pm 0.32) \times 10^{-2}$
^{40}K	1.03×10^{18}	$0^{+2.44}_{-0}$	$\left(0^{+3.8}_{-0}\right) \times 10^{-5}$	$0^{+2.44}_{-0}$	$\left(0^{+3.8}_{-0}\right) \times 10^{-5}$	n/a	n/a

underneath. The detector is also shielded by 0.5 m of GdLS on all sides and a 30 m thick steel plate beneath the water tank. Surfaces 1 - 5, which are detailed in Table 5.2, are coaxially layered throughout the water shielding from just outside of the water tank to just outside the GdLS layer, as illustrated in Figure 5.1b.

To estimate the resultant factor of increase in the rate at different shielding thicknesses, the innermost attenuation coefficient was used (the attenuation from surface 4 to surface 5). For ^{232}Th, the attenuation coefficient of the 2.615 MeV gamma-ray is used because after 3 m of shielding the spectrum is fully determined by the initial ^{208}Tl line. For ^{238}U, the attenuation coefficient of the 2.448 MeV gamma-ray is used because it is the highest energy gamma-ray in the decay chain and the largest contributor to the spectrum in the TPC after 3 m of shielding. Additionally, it is the only gamma-ray whose energy will affect the background in the $0\nu\beta\beta$ decay ROI. The flux ratio is calculated using the following equation:

$$\frac{I}{I_0} = \exp^{(-Ax)}, \tag{5.5}$$

where I is the flux at surface 5 and I_0 is the flux at surface 4 with $x = 1$ m separating them. A is found to be 0.0439 $\mathrm{cm^2\,g^{-1}}$ for the flux ratio of 2.615 MeV gamma-rays and 0.0472 $\mathrm{cm^2\,g^{-1}}$ for the flux ratio of 2.448 MeV gamma-rays. Using these attenuation coefficients, Equation (5.5) can be applied to calculate the increase in background rate when reducing water thickness. The reduction of water thickness is listed in the first column of Table 5.7. The relative increases in background rates are given in columns 2 and 3 for ^{232}Th and ^{238}U decay chains, respectively. Multiplying the original background event rates in the WIMP ROI (Table 5.6, column 4) by these rate increase factors, new rates are gained, given in columns 4 and 5 of Table 5.7. These rates indicate that even with one metre less water shielding from all sides, the background provided by cavern gamma-rays still falls below sensitivity requirements for WIMP search. The thickness of water shielding and GdLS around the detector would be 3 m on the top and sides of the detector and 1 m beneath the detector, with the 30 cm thick steel plate at the base of the water tank. The volume of the water tank would decrease by 43.4 %, from 1216.7 $\mathrm{m^3}$ to 688.2 $\mathrm{m^3}$.

Using these rate increases, the size of the FV necessary for sensitivity to $0\nu\beta\beta$ decay can be estimated for the corresponding decreases in shielding. The results of this analysis are presented in Table 5.8 and illustrated in Figure 5.12. The systematic uncertainty on the attenuation coefficients is 0.7% (see Section 5.3), and this was propagated with Equation (5.5) to obtain the associated uncertainty on the rate increases. These were found to be negligible and therefore, the systematic uncertainties quoted in Tables 5.7 and 5.8 are only calculated from varying the thresholds that constitute the multiple scattering cut, as described in Section 5.3.

Table 5.7: Estimated event rates from 1 Bq kg^{-1} of ^{232}Th and ^{238}U in the TPC, depositing energy in the WIMP region of interest (0 - 20 keV), are shown for different water shielding thicknesses. Column 1 specifies how much the shielding is reduced from the top, base, and sides of the simulated water tank. The rate increases show how much the event rates (see Table 5.6) rise as shielding thickness decreases from the original simulated thickness, with the updated rates presented in columns 4 and 5. Statistical and systematic uncertainties are quoted as described in the Table 5.6 caption.

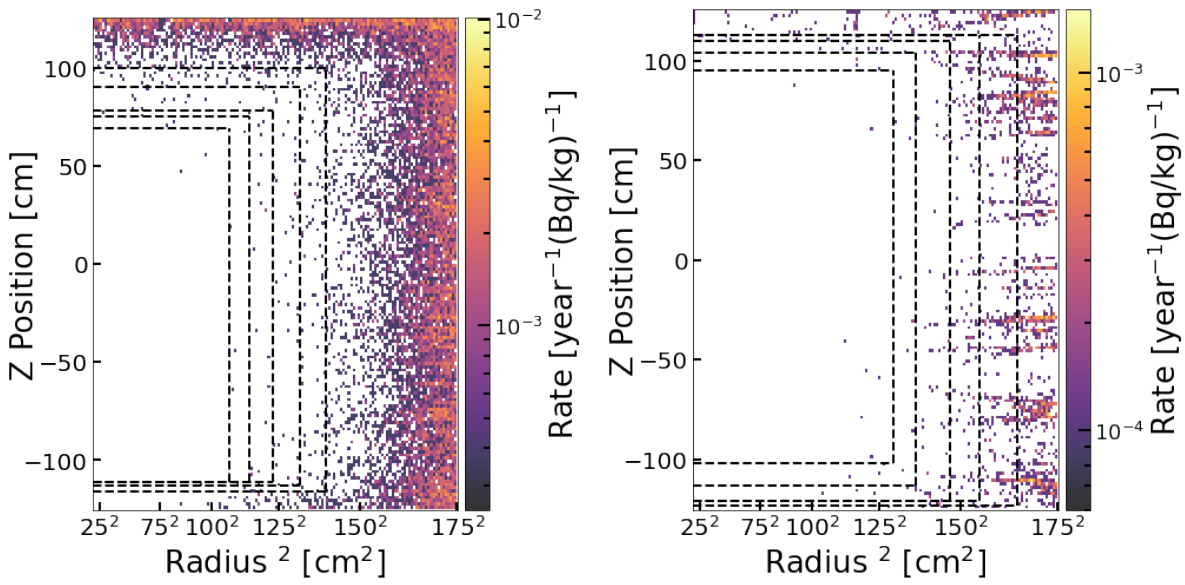
Thickness reduction [cm]	**Rate increase ^{232}Th**	**Rate increase ^{238}U**	**^{232}Th Rate [year^{-1}(Bq/kg)$^{-1}$]**	**^{238}U Rate [year^{-1}(Bq/kg)$^{-1}$]**
0	1.0	1.0	$\left(1.5^{+1.1}_{-0.6}\right) \times 10^{-3}$	$\left(2.2^{+2.5}_{-1.4}\right) \times 10^{-4}$
25	3.0	3.3	$\left(4.6^{+3.2}_{-1.9}\right) \times 10^{-3}$	$\left(7.3^{+8.2}_{-4.6}\right) \times 10^{-4}$
50	9.0	10.6	$\left(1.4^{+1.0}_{-0.6}\right) \times 10^{-2}$	$\left(2.4^{+2.7}_{-1.5}\right) \times 10^{-3}$
75	27.0	34.4	$\left(4.1^{+2.9}_{-1.7}\right) \times 10^{-2}$	$\left(7.7^{+8.7}_{-4.9}\right) \times 10^{-3}$
100	80.9	111.9	$0.12^{+0.09}_{-0.05}$	$\left(2.5^{+2.8}_{-1.6}\right) \times 10^{-2}$

Table 5.8: Rates of events in the TPC that deposit energy in the 0νββ decay region of interest ($\pm$ 50 keV around $Q_{\beta\beta}$) from 1 Bq kg^{-1} of ^{232}Th and ^{238}U, multiplied by their respective rate increase factors listed in Table 5.7. The FV was gradually decreased until the rate fell to less than 1 event per 10 years for each reduction in shielding thickness, from each of the top, sides, and base of the water tank. Statistical and systematic uncertainties are quoted as described in the Table 5.6 caption. As the FV decreases, the number of events decreases; hence, the uncertainty on the rate increases.

Thickness reduction [cm]	**^{232}Th rate [year^{-1} (Bq/kg)$^{-1}$]**	**^{232}Th FV [tonne]**	**^{238}U rate [year^{-1} (Bq/kg)$^{-1}$]**	**^{238}U FV [tonne]**
0	$(9.69 \pm 0.61) \times 10^{-2}$	39.3	$(9.19 \pm 0.32) \times 10^{-2}$	59.6
25	$(9.88 \pm 1.07) \times 10^{-2}$	32.9	$(9.90 \pm 0.60) \times 10^{-2}$	51.2
50	$(9.99 \pm 1.86) \times 10^{-2}$	26.5	$(9.24 \pm 1.05) \times 10^{-2}$	45.1
75	$\left(9.30^{+3.92}_{-2.80}\right) \times 10^{-2}$	22.9	$(9.64 \pm 1.93) \times 10^{-2}$	37.8
100	$\left(9.30^{+7.13}_{-5.89}\right) \times 10^{-2}$	19.1	$\left(8.78^{+4.14}_{-3.45}\right) \times 10^{-2}$	30.9

5.6 Conclusions on shielding requirements for the future detector

To shield the next-generation dark matter detector from the surrounding rock's gamma-ray and neutron background, 4 metres of water and GdLS shielding on the top and sides, and 2 metres on the bottom with a steel plate base, has been shown to be sufficient for WIMP search and 0νββ decay detection, based on a full GEANT4 Monte Carlo simulation. In the WIMP search ROI, 0 - 20 keV, ^{40}K, ^{238}U and ^{232}Th each contribute $<<$ 1 event per year to the background assuming their activity of 1 Bq kg^{-1}. Similarly, there was $<$ 1 event per 10 years in the 0νββ decay ROI, 2.408 - 2.508 MeV, from ^{238}U and ^{232}Th, each having an activity of 1 Bq kg^{-1}.



(a) (b)

Figure 5.12: Colour maps of positions of background events from (a) ^{232}Th and (b) ^{238}U (using the same data plotted as that in Figures 5.11b and 5.11d, respectively). The FV was decreased gradually to maintain a rate of less than 1 event per 10 years in the TPC as the water shielding was reduced from the top, sides and base by values in Table 5.8. This is a 51.3 % decrease in LXe mass for ^{232}Th and a 48.2 % decrease in LXe mass for ^{238}U.

Using attenuation factors of the highest energy gamma-rays in the ^{232}Th and ^{238}U decay chains, it has been estimated that with 1 m less water shielding on all sides of the detector, the TPC event rates in the WIMP ROI increase from $\left(1.5^{+1.1}_{-0.6}\right) \times 10^{-3}$ to $0.12^{+0.09}_{-0.05}$ year^{-1} (Bq/kg)$^{-1}$ and $\left(2.2^{+2.5}_{-1.4}\right) \times 10^{-4}$ to $\left(2.5^{+2.8}_{-1.6}\right) \times 10^{-2}$ year^{-1} (Bq/kg)$^{-1}$, for ^{232}Th and ^{238}U, respectively. This decrease in shielding necessitates stricter FVs for the $0\nu\beta\beta$ decay ROI to remain below 1 event per 10 years. Specifically, fiducial xenon masses for ^{232}Th and ^{238}U background rates would decrease from 39.3 to 19.1 tonnes and 59.6 to 30.9 tonnes, respectively. Other sources of background such as those originating from the detector materials will reduce the FV further.

Chapter 6

Measurements of gamma-rays from rock samples in the Boulby Underground Laboratory

There is a potential for a future dark matter detector, such as XLZD, to be housed in Boulby Mine, North Yorkshire, UK [99, 100]. The site where the future cavern would be built is approximately 1300 m below sea level [101], 200 m deeper[1] than where the current Boulby Underground Laboratory is situated [102]. Descriptions of the laboratory and its radioassay facilities are given in Section 6.1. Rock samples from both 1100 m and 1300 m depths in the mine have been retrieved by ICL mining company via boreholes. They were given to the Boulby Underground Laboratory to be screened by sensitive HPGe detectors in the Boulby UnderGround Screening (BUGS) facility [100]. The methodology used to screen the rock samples for gamma-rays with Boulby's HPGe detectors and the results of this screening are presented in Section 6.2, intended for use by any prospective experiments that Boulby Mine may host. The normalisation of the simulation results from Section 5.4 to the screening results is discussed in Section 6.2.3.

6.1 The Boulby Underground Laboratory

6.1.1 Overview

The Boulby Underground Laboratory, pictured in Figure 6.1, is located at a depth of 1100 m in Boulby Mine. A description of the laboratory and its facilities is given in

[1] Due to the nature of the strata, a large excavation, such as the one needed for the future detector, is likely easier in polyhalite compared to salt and polyhalite sits 200 m below the salt horizon. The extra muon flux reduction is also welcome, particularly for $0\nu\beta\beta$ decay.

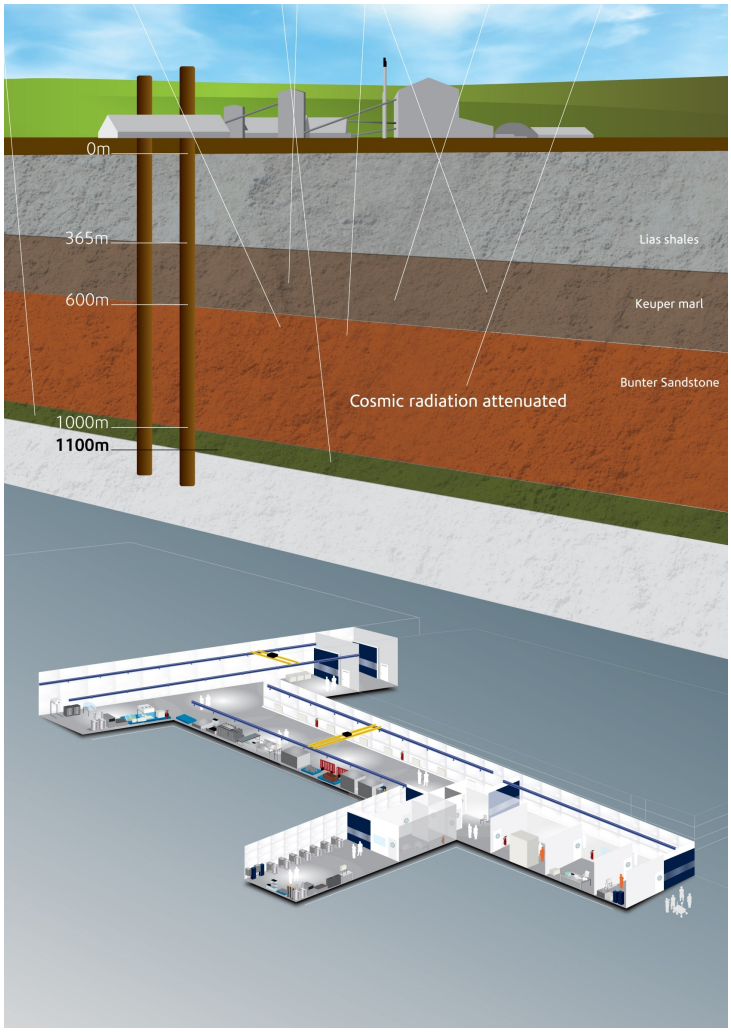


Figure 6.1: CAD image of the Boulby Underground Laboratory. The stratigraphic sequence above the laboratory is: Lias shales, Keuper marl and Bunter sandstone. Beneath the sandstone and surrounding the laboratory, are Zechstein evaporites, namely halite, potash and polyhalite. Image credit: Boulby Underground Laboratory.

Ref. [100]. Since becoming operational in the 1990s, the Boulby laboratory has served as a key site for deep underground scientific research. Its initial focus centred on the direct detection of dark matter, specifically WIMPs. Over the past two decades, Boulby has hosted the development and operation of several pioneering dark matter experiments, including NAIAD (NaI Advanced Detector) [103], DRIFT (Directional Recoil Identification From Tracks) [104] and the ZEPLIN I-III (ZonEd Proportional scintillation in LIquid Noble gases) series of dual-phase liquid xenon detectors [105, 106, 107]. Notably, ZEPLIN contributed technological advancements that underpin current-generation dark matter observatories such as XENONnT and LZ (see Section 2.3.3).

In recent years, the scientific programme at Boulby has become highly multidisciplinary due to the unique characteristics of the deep underground environment. In addition to ultra-low background dark matter searches, research now encompasses geology and geophysics, environmental and climate studies, and the development of instrumentation for planetary exploration. Investigations of microbial life in extreme environments have

also been conducted as part of astrobiology studies towards the search for life beyond Earth.

The Boulby laboratory comprises a 4000 m^3 facility situated within a salt rock band, offering an ISO Class 7 (10^4 particles/ft^3) cleanroom environment throughout its primary areas. BUGS, the dedicated low-background counting suite, covers an area of 15.5 m × 7 m and is maintained at ISO Class 6 (10^3 particles/ft^3) standards. The main experimental hall, measuring 4 m in height and 7 m in width, is a steel-based construction that ensures both the maintenance of cleanroom conditions and provides partial shielding from cavern rock radiation. An adjoining section, named the Large Experimental Cavern (LEC), reaches a height of 6.5 m. The main hall and the LEC are equipped with $x - y$ overhead crane systems, facilitating material transfer and the installation of medium to large-scale experiments. The laboratory is also supported by high-capacity air handling and filtration systems, as well as reliable internet infrastructure.

Adjacent to the clean facility, Boulby operates an additional 3000 m^3 "outside experimental area" situated within a separate salt cavern. This space supports research requiring direct access to the geological environment or extended underground presence beyond the main clean facility.

The surrounding halite is particularly well-suited for low-background experiments. Measured specific activities in the salt rock are 11 Bq kg^{-1} for ^{40}K, 0.6 Bq kg^{-1} for ^{232}Th and 0.4 Bq kg^{-1} for ^{238}U [108]. While gamma-rays from these nuclides can be attenuated via appropriate shielding, the naturally low uranium content results in minimal airborne ^{222}Rn levels (recently measured as 2.23 Bq m^{-3} on average in the main lab [109]), making the laboratory a suitable location for rare event searches and other ultra-low background measurements.

6.1.2 The Boulby UnderGround Screening facility

Radioassay screening campaigns, such as those used by LZ, are imperative to the experiment's success. The BUGS facility, pictured in Figure 6.2, has been in operation since 2015 and has contributed to multiple assay campaigns for sensitive experiments [110, 111]. Before the construction of LZ, the high-purity germanium detectors in the BUGS facility assayed various detector materials such as titanium and steel samples; cryostat and field rings; and PMT materials. Since the LZ screening campaign, Boulby has developed the capability to provide additional methods of measuring radioactivity by establishing a new surface-level laboratory equipped to perform ICP-MS analysis, installing two XIA surface alpha counters in BUGS and constructing a radon emanation system. Descriptions of the radioassay detectors and equipment in Boulby are given in Ref. [102, 109, 100], and an overview of the radon facility is given in Chapter 7. Whether or not Boulby Mine is chosen as the host for the next-generation dark matter detector, the facilities there will contribute substantially to the material screening campaign already underway.

6.1.2.1 Boulby's high-purity germanium detectors

The HPGe detectors at Boulby differ in their energy resolution and their efficiency in detecting gamma-rays across a wide energy range. Each detector is housed in an ultra-low-background cryostat, which is constructed from carefully selected materials, such as



Figure 6.2: The Boulby UnderGround Screening facility. Credit: T. Palin.

^{60}Co reduced stainless steel, to minimise intrinsic gamma-ray backgrounds. Section 4.3 gives more information about the materials and designs of HPGe detectors, whereas the following information in this section is specific to the HPGe detectors in BUGS: Chaloner, Lunehead, Belmont, Merrybent, Roseberry and Lumpsey. The latter four are classed as S-ULB (Specialty Ultra-Low Background) detectors. S-ULB detectors are a class of HPGe detectors specifically engineered for extremely low-background gamma-ray spectroscopy. These detectors are optimised for uses requiring the highest radiopurity, such as material screening for rare-event searches including dark matter and $0\nu\beta\beta$ decay experiments. All materials located within the lead shield and in close proximity to the germanium crystal are selected based on their intrinsic radioactivity. This includes structural components such as aluminium and copper, as well as all electronics. Each component undergoes detailed screening and approval to ensure that no significant background contributions are introduced. The entire manufacturing process is tightly controlled to ensure a consistent and reproducible background signature across all S-ULB detectors. To mitigate cosmogenic activation of sensitive materials, susceptible components are stored underground at depths of approximately 800 m w.e until final assembly. This suppresses the presence of long-lived activation products in the final detector [109].

Each detector has a 9 cm thick outer shield made from lead that had remained underground for two years prior. The inner shield is 9 cm of oxygen-free high thermal conductivity copper, which is present to absorb fluorescent X-rays and Bremsstrahlung radiation that result from gamma-ray interactions in the lead[2]. Both shielding materials are ultra-pure, ensuring a low background environment surrounding the germanium crystal inside.

[2]Copper has the atomic number $Z = 29$, which is high enough to absorb low-energy gamma-rays and X-rays from lead, but low enough that no significant radiation is produced as result of the absorption within the copper layer itself.

Chaloner, pictured in Figure 6.3, is a Mirion (BE5030), p-type BEGe detector (planar configuration), which can measure gamma-rays in the range 3 keV - 3 MeV with a relative efficiency of 48 % [100]. The relative efficiency of a germanium detector refers to how



Figure 6.3: A photo of the high-purity germanium detector "Chaloner" in BUGS. The detector is in the lead and copper casings and the dewar contains cooling nitrogen. Credit: Boulby Underground Laboratory.

well it detects gamma-rays compared to a standard sodium iodide (NaI(Tl))[3] detector. Specifically, a 3-inch diameter, 3-inch long NaI(Tl) crystal measuring the 1.332 MeV gamma-ray peak from a ^{60}Co source, placed 25 cm away from the detector. This is a standard procedure as outlined in Ref. [112]. The detector resolution measures the FWHM of the ^{60}Co 1332 keV peak; Chaloner's resolution is 1.56 keV. The dimensions of the internal cavity of Chaloner's shielding castle are 200 × 220 × 510 mm^3. The germanium crystal weighs ∼0.8 kg and its front face has a surface area of 50 cm^2 and is 30 mm thick. A thin outer contact is used on the detector to have a very thin (∼ µm) residual dead-layer, and there is a carbon fibre window to reduce absorption of low-energy gamma-rays. Roseberry is another Mirion BEGe (BE6530) detector, similar to Chaloner with a resolution of 1.58 keV, but different in that it is S-ULB. Roseberry features a 65 cm^2 front face, a thickness of 30 mm and has a thin outer contact, resulting in a thin dead layer. Instead of a carbon fibre window, Roseberry has a full aluminium endcap, which sacrifices some low-energy efficiency to avoid potential increased background from the carbon fibre.

Belmont is a 600 cm^3 Mirion, p-type coaxial detector with a relative efficiency of 160 % and a resolution of 1.92 keV. Several of the materials used in the cryostat were pre-screened using earlier BUGS detectors to ensure minimal intrinsic background. The germanium crystal was "freshly pulled", meaning that it was brought underground very soon after it was grown to limit cosmogenic activation. With its large volume and mass, Belmont offers excellent sensitivity across a wide energy range, and is the highest-efficiency germanium detector in BUGS. Merrybent is a 375 cm^3 Mirion, p-type coaxial detector with a relative efficiency of 100 % and a resolution of 1.87 keV. Its germanium crystal was

[3]Thallium-activated sodium iodide.

also freshly pulled. Lunehead is an Ortec (GEM-XX240-S) standard p-type coaxial detector with a relative efficiency of 100 % and a resolution of 1.86 keV. It previously served in the material screening programmes for the ZEPLIN and DRIFT experiments. To improve its performance, the detector was refurbished, and its original magnesium end-cap was replaced with one made from carbon fibre. This upgrade significantly reduced the intrinsic background and improved low-energy gamma-ray sensitivity.

Lumpsey is a Mirion (GSW275L) small anode germanium (SAGe) well detector that exhibits a relative efficiency of 69 % and a detector resolution of 1.66 keV. The detector well has a diameter of 28 mm and a depth of 40 mm, with an active volume of 275 cm^3. Its geometry provides nearly 4π coverage for small samples placed inside the well, allowing for highly efficient low-background screening. The detector can also be used in a coaxial mode for screening larger samples.

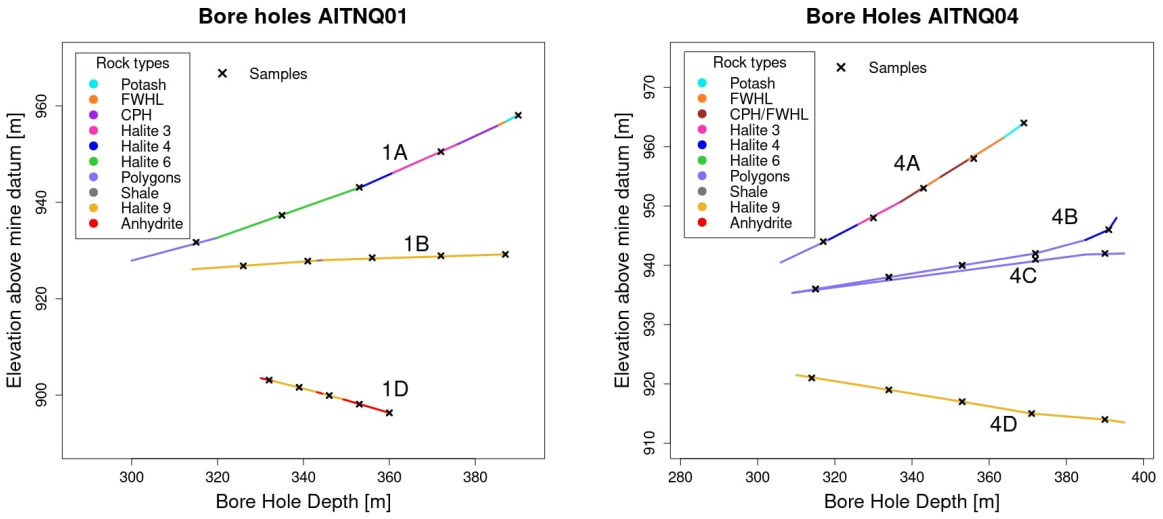
6.1.2.2 Nitrogen purge system

A critical requirement for achieving ultra-low background levels in HPGe detectors is the reduction of radioactive contamination from the atmosphere. In particular, the ingress of ^{222}Rn must be prevented due to its radiogenic progeny, notably ^{214}Pb and ^{214}Bi, which emit gamma-rays that would increase background counts and thus, reduce detector sensitivity. Throughout the laboratory, the ambient radon concentration is lessened by the mine's ventilation system, which introduces fresh air through one access shaft and exhausts it through a separate access shaft. 12 months of monitoring data taken during 2022 confirm that the mean radon concentrations at the surface, in the main laboratory and in BUGS are comparable, with values of 2.10 $\pm$ 0.03 $Bq\,m^{-3}$, 2.23 $\pm$ 0.03 $Bq\,m^{-3}$ and 2.09 $\pm$ 0.03 $Bq\,m^{-3}$, respectively [109]. However, temporary shutdowns of the ventilation system, such as during scheduled maintenance, can result in radon concentrations rising, thereby increasing detector background rates. Therefore, radon mitigation techniques that are independent of the mine's ventilation are required to maintain consistent low-background environments within the shield cavities.

To achieve this, the detector shielding cavities are purged with high-purity nitrogen gas, maintaining a positive pressure that displaces radon-infused air. In the BUGS facility, nitrogen is extracted from underground air using a Parker-Hannifin NITROSource Pressure Swing Adsorption nitrogen gas generator. The generated nitrogen is first dried and then passed through an activated charcoal trap maintained at -80°C, which adsorbs the vast majority of the radon from impurities in the nitrogen. Nitrogen gas delivery is regulated using Bronkhorst El-Flow Select mass-flow controllers, which provide precise flow rates in the range of 0.2 – 10.0 litres per minute with a precision of $\pm\,0.6$ %. Continuous monitoring of gas flow and radon levels allows periods of suboptimal purging or elevated background to be identified. Since data are recorded in hourly files and stored separately, any periods with significant changes in conditions can be excluded without discarding the entire measurement run. The nitrogen system is critical to the sensitivity of the germanium detectors in BUGS and, therefore, to the material screening needs of rare-event experiments.

6.2 Rock sample measurements

The majority of rock samples were collected by the ICL-Boulby exploratory geology team via boreholes which span the various strata of rock types that are vertically spread over roughly 60 m from ∼1040 to 1100 m below the surface [113]. Graphical interpretations of these boreholes are given in Figure 6.4. The mine's rock is predominantly halite-based



(a) (b)

Figure 6.4: Plots of the boreholes (a) AITNQ 01 (A, B and D) and (b) AITNQ 04 (A, B, C, D). The × marks represent the locations of samples that were measured as a function of the elevation above the mine datum and the distance along the borehole. The mine datum is a depth that is 2000 m below sea level, set by the mine to account for varying surface topology.

as the area used to be part of the Zechstein Sea ∼250 million years ago [114]. Around a depth of 1040 m, the rock tends to be mainly potash, clear pink halite (CPH) and footwall halite (FWHL). Venturing deeper, there are bands of different types of halite and salt polygons, before reaching anhydrite. It should be noted that the stratum of each rock type undulates across hundreds of metres horizontally around the 1100 m level [113]. Samples of polyhalite were collected from different boreholes to those mentioned previously, at depths of around 1100 m and 1300 m. The locations of the boreholes, for polyhalite and the other samples, can be seen in Figure 6.5, relative to where the current laboratory is situated and where a future laboratory would be built.

6.2.1 Methodology

The collected rock samples were placed individually in a sample holder within a grip-seal plastic bag. The sample holder tube is made from acrylic while the base disc material is perspex. The samples were then positioned inside Chaloner (see Section 6.1.2) and measured for 117 - 740 hours. A planar detector was chosen as opposed to a coaxial or well detector, as this configuration has a high resolution at low energies. LabSOCS (Laboratory Sourceless Calibration Software) [115] can simulate each of the germanium detectors and any sample placed on it within a sample holder. Depending on the density,

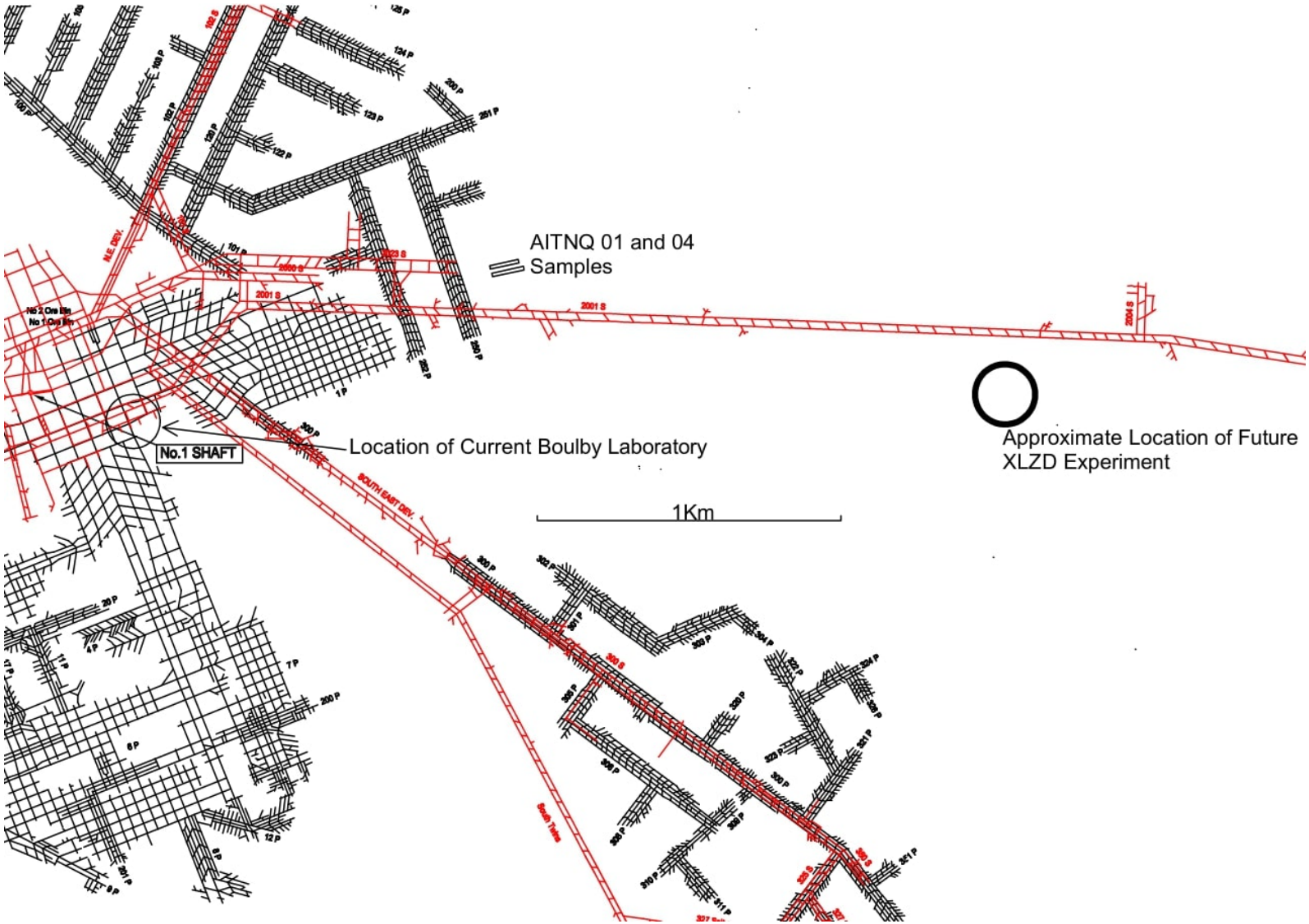


Figure 6.5: A schematic of the tunnels in Boulby Mine around the main lift shafts, the current laboratory, and the location of a potential future lab. AITNQ 01 and AITNQ 04 are the two boreholes from which all samples except polyhalite were taken from. The circle indicating a potential location of a future experiment is the area near which the polyhalite samples were taken from, at a depth of about 1300 m. Image credit: P. Edey.

size, geometry and alignment of the sample, LabSOCS will configure an efficiency curve spanning the required energy range [116], meaning that at each energy peak, the user can extract an efficiency for that exact energy. By inputting these physical parameters of a sample and the sample holder, LabSOCS will calculate the fraction of gamma-rays that might interact with the detector assuming isotropic emission, and account for all of the gamma-ray interactions described in Sections 4.2.1 and 4.2.2 that may lead to incomplete absorption (fewer counts in the main peak).

6.2.1.1 Systematic uncertainties

Systematic uncertainty associated with sample geometry arises from the measurement of sample sizes. The rocks were not perfectly uniform in shape and the majority of rock types came in disc form, with a height of 1.5 - 2.5 cm (see later Figures 6.9b, 6.9d to 6.9f, 6.9h and 6.9i in Section 6.2.2). Anhydrite and polyhalite samples were usually single, cylindrical blocks and much less prone to breaking up into fragments than the other rock types. The diameter and total length of the samples (in the case of multiple discs, they were stacked and the length is that of the total stack) were measured with a standard ruler. The estimated uncertainty in the diameter and length is 1 mm and 5 mm, respectively, and the uncertainty in mass is 0.1 g. This results in an uncertainty of approximately 10% in the rock density.

The systematic uncertainty associated with the sample's length, diameter, and density was evaluated by varying each parameter within its uncertainty range and generating new efficiency curves in LabSOCS. For example, if a sample has a diameter of 50 mm, additional efficiency curves were created for diameters of 49 mm and 51 mm, while keeping the length and density unchanged. A similar approach was applied to length and density variations. The effects these changes have on the efficiency curves can be seen in Figures 6.6a to 6.6c. At each peak energy, the fractional difference was recorded to quantify the impact of varying each parameter. There is a strong energy dependence on density, affecting low-energy gamma-rays in particular, as they are less likely to escape the sample as the density increases, whereas high-energy gamma-rays are much more independent of density. Efficiencies decrease for gamma-rays with higher energies as they are less likely to be absorbed by the detector. Additional systematic uncertainties arise from LabSOCS at different energies, which are also taken into account [117]. All of the systematic uncertainties described above are summarised in Appendix D.

Other sources of potential uncertainties that require awareness of, but contribute negligible uncertainties, were nitrogen flow levels and radon background. The nitrogen flows through a freezer at a temperature around -80°C, in which there are charcoal filters that absorb radon from out of the nitrogen. Further information on the use of charcoal as a radon filter is in Section 7.1.

6.2.1.2 Accounting for TCS

A GEANT4 simulation [100, 118] was utilised[4] to investigate the effects of TCS, a feature of gamma spectroscopy described earlier in Section 4.2.3, in the peaks resulting from

[4]The GEANT4 version 10.7.2 was employed for this task.

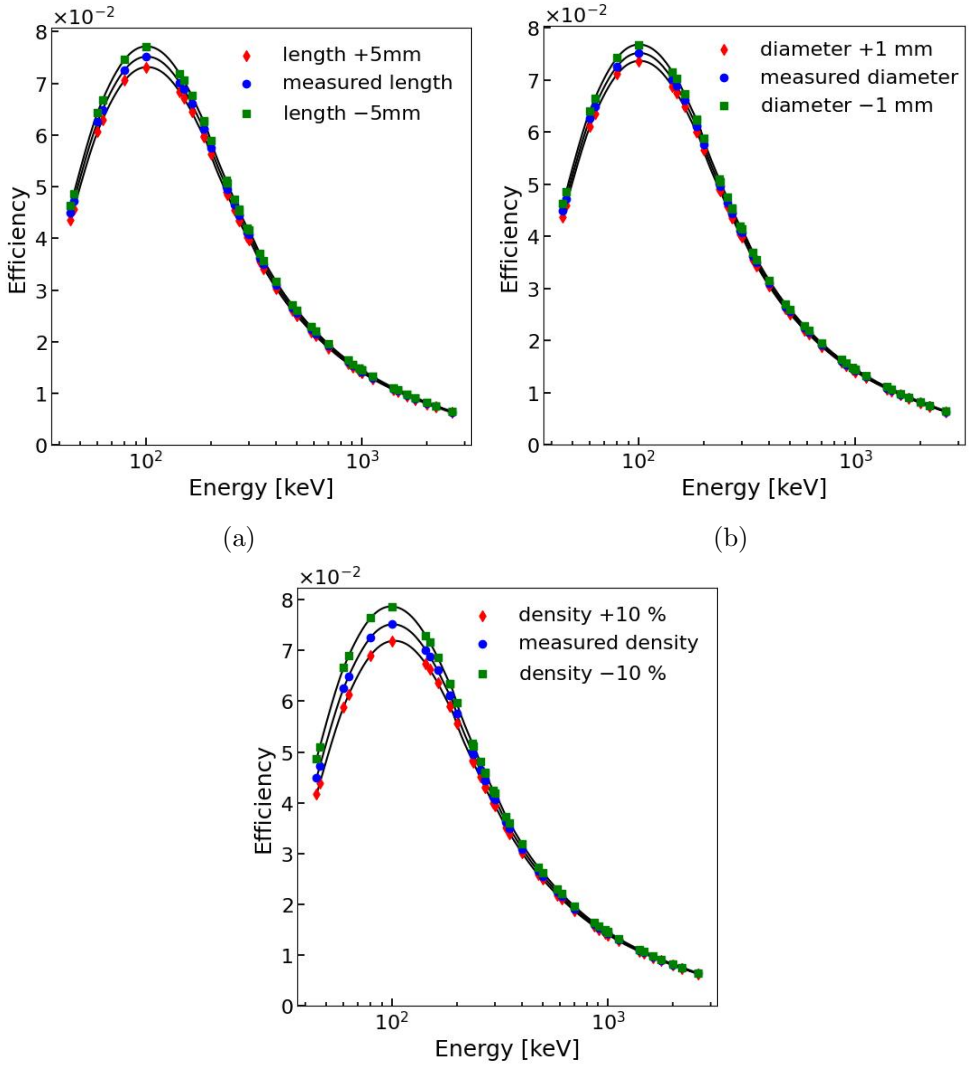


Figure 6.6: Plots demonstrating the effect of the uncertainty on the detector efficiency from measuring sample dimensions. Each marker on the plots represents the energy of a gamma-ray from NORM isotopes, listed in Appendix E.

^{214}Bi and ^{208}Tl decay, as these are known to have non-negligible reductions in counts due to TCS. The simulation geometry was that of Chaloner and its germanium crystal; the lead and copper shielding surrounding the internal cavity; and a cylinder on its side (the sample). The simulation was repeated for two different sample densities: the average density of the halitic rock samples (1.9 $\mathrm{g\,cm^{-3}}$) and the average density of the polyhalite samples (3.0 $\mathrm{g\,cm^{-3}}$). The simulation uses a custom physics list combining several standard GEANT4 physics lists. Most relevantly, electromagnetic physics, decay physics and radioactive decay physics are included. The physics list enables the simulation of decay chains and branching ratios for radioactive processes.

To account for TCS, the ^{214}Bi and ^{208}Tl decays were first generated as ions and then as individual gamma lines. Both mechanisms are provided by GEANT4's GPS. The creation of gamma lines with a range of energies and intensity (obtained from NNDC [53, 54]) is described in Section 5.2.3. Similarly, in this simulation, the number of gamma-rays emitted from the source was the sum of the intensities (average number of gamma-rays

emitted per parent decay, N_γ) multiplied by 10^6, as this is the number of ions generated in the source in the simulation of parent isotope ions. For ^{214}Bi decay, $N_\gamma = 0.7695$ and for ^{208}Tl decay, $N_\gamma = 1.9725$[5]. Neither is representative of the full decay schemes, as only the main peaks that are affected by TCS are included, meaning the N_γ values are reduced. The GPS ion option allows the user to create a population of the desired ion by defining its Z and A numbers, and can prevent simulation of further radioactive decay of the daughter products, effectively ensuring the simulation focuses solely on the decay of ^{214}Bi. The results of the simulation, displayed in Table 6.1, were analysed with InterSpec to find a TCS correction factor for each peak, which was then applied to the corresponding peak measurements in each sample. The results imply that a difference in density of $\sim 1\,\mathrm{g\,cm^{-3}}$ affects the number of counts, as expected from effects detailed in Section 4.2, but does not significantly affect the correction factor for each peak ($1 - 5\,\%$ difference). Figures 6.7a and 6.7b display the differences between the spectra from ion simulations and individual gamma-ray peak simulations, for ^{214}Bi and ^{208}Tl decay, respectively.

The efficacy of the simulation can be realised by comparing the radioactivities of the parent nuclide derived from peaks that are affected by TCS and peaks that are not. Table 6.2 compares the radioactivity of ^{232}Th and ^{239}U each calculated from two of their daughter nuclides, before and after the TCS correction factors were applied. The correction factor accounts for TCS accurately as the corrected radioactivities are closely matched with those from the unaffected peaks. This indicates further that the efficiency curves are calculated with reasonable accuracy as incomplete absorption of gamma-rays is not corrected by the simulation.

6.2.1.3 Calibration

An example of a spectrum produced by Chaloner measuring a sample of anhydrite can be seen in Figures 6.8a and 6.8b. The software InterSpec [119, 120] takes data recorded by the germanium detector. Before analysing any unknown samples, the energy calibration of Chaloner's HPGe detector needed to be determined using a reference material with well-defined gamma-ray lines. During its operation, the British Nuclear Fuels reprocessing plant at Sellafield in Cumbria released a variety of radionuclides into the Irish Sea [121]. Therefore, a sample of Irish sea sediment was measured because it contains many radionuclides spanning the energy range 3 keV - 3 MeV. The calibration procedure is outlined below:

1. The Irish sea sediment sample was measured with Chaloner to acquire a reference spectrum. Well-known peaks were identified, such as the characteristic ^{40}K peak.
2. Using InterSpec, the whole energy spectrum can be manually shifted up or down the energy scale in keV, allowing the reference peaks to line up with their known energies (from NNDC).
3. InterSpec automatically calculated the linear calibration coefficient from the conversion of the data acquisition system (DAQ) units to energy, which was henceforth applied to all future spectra.

The sediment sample's reference spectrum after calibration is displayed in Appendix F.

[5] On average there are 0.7695 gamma-rays emitted per decay of ^{214}Bi and 1.9725 gamma-rays emitted per decay of ^{208}Tl.

Table 6.1: Results of a GEANT4 simulation of (a) ^{214}Bi and (b) ^{208}Tl decays from a sample inside Chaloner. The TCS correction factors (columns 4 and 7) are the number of counts in the main peaks[a] from individual decay gamma-rays ("Energy" column) divided by the number of counts in the same main peaks from the radioactive decay of ^{214}Bi and ^{208}Tl ions ("Ion" column). Halite and polyhalite samples require different correction factors due to the difference in their densities.

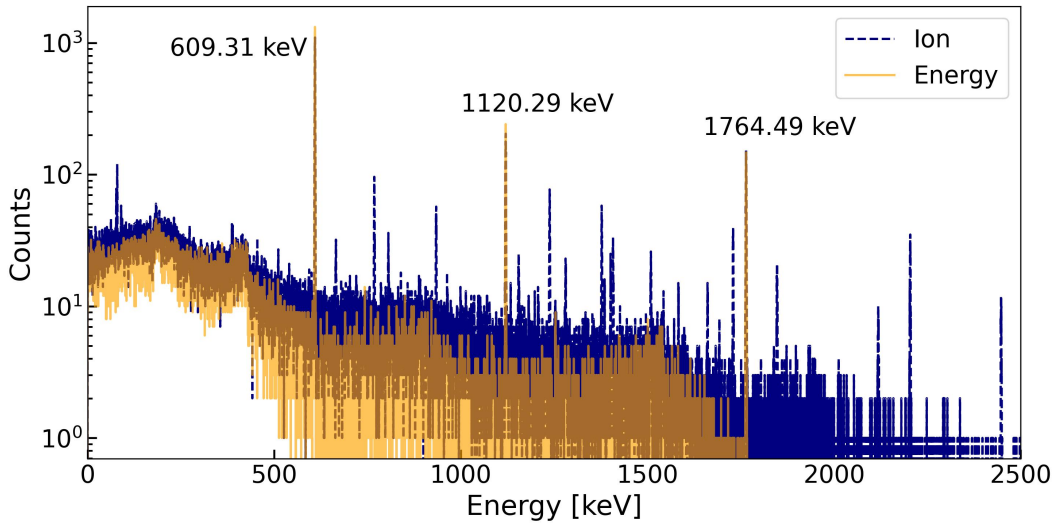
(a) ^{214}**Bi**

Peak energy	**Halite 1.9 g cm^{-3}**			**Polyhalite 3.0 g cm^{-3}**		
[keV]	**Energy**	**Ion**	**CF**	**Energy**	**Ion**	**CF**
609.31	10193 ± 102	8488 ± 92	1.201 ± 0.018	8721 ± 94	7335 ± 87	1.189 ± 0.019
1120.29	2054 ± 46	1775 ± 44	1.157 ± 0.038	1734 ± 42	1516 ± 41	1.144 ± 0.042
1764.49	1483 ± 39	1444 ± 39	1.027 ± 0.039	1265 ± 36	1249 ± 36	1.013 ± 0.041

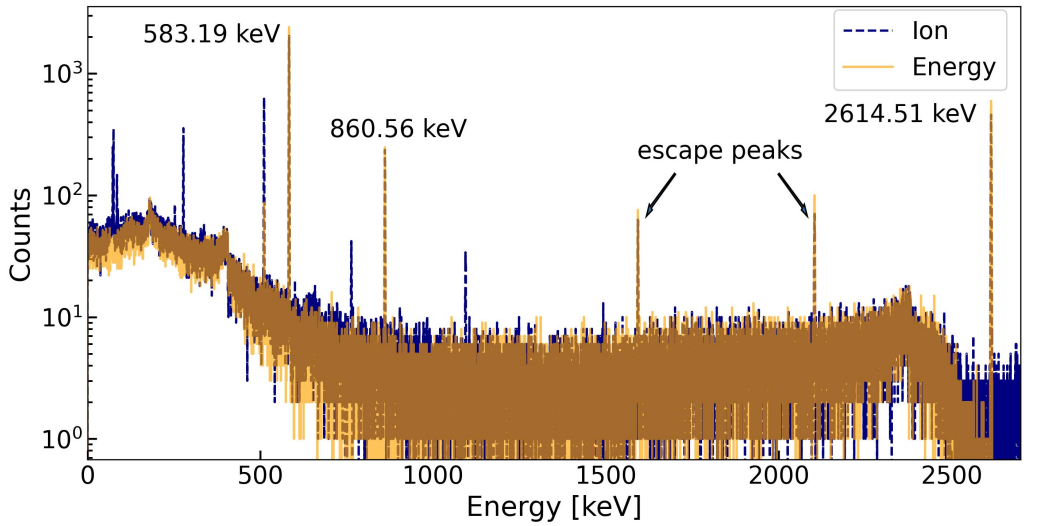
(b) ^{208}**Tl**

Peak energy	**Halite 1.9 g cm^{-3}**			**Polyhalite 3.0 g cm^{-3}**		
[keV]	**Energy**	**Ion**	**CF**	**Energy**	**Ion**	**CF**
583.19	19570 ± 141	16380 ± 129	1.195 ± 0.013	16380 ± 129	13242 ± 117	1.237 ± 0.015
860.56	2127 ± 47	1934 ± 46	1.100 ± 0.036	1828 ± 44	1688 ± 42	1.083 ± 0.038
2614.51	6599 ± 81	5207 ± 73	1.28 ± 0.024	5942 ± 77	4702 ± 69	1.264 ± 0.025

[a]The 510.77 keV gamma line from ^{208}Tl decay with an intensity of 22.60 % is not included as it is not used in the gamma-ray measurements described in Sections 6.2 and 6.2.2. This is due to the overlap of the 511 keV peak that arises from pair production.



(a)



(b)

Figure 6.7: Spectral plots comparing the outputs of (a) ^{214}Bi decay and (b) ^{208}Tl decay from the GEANT4 simulation detailed in Section 6.2.1.2 text. The ion spectra are from the fully simulated decay of each nuclide, whereas the energy spectra are from individual gamma lines of the main peaks that are labelled by their energies on the plots. Clear escape peaks can be seen in (b), resulting from the ^{208}Tl decay peak at 2614.51 keV. Also in (b), the 511 keV line is very prominent from the ion simulation which is a result of pair-produced gamma-rays summed with the 510.77 keV gamma line with intensity 22.60 %.

6.2.1.4 Calculating specific activity

Once a rock sample's data is uploaded and the calibration coefficient is applied, InterSpec automatically fits each user-selected peak with a Gaussian. The gamma-rays from typical NORM isotopes expected in rock are listed in Section E, along with their energies and intensities, as reported in Ref. [76][6]. The number of counts, N, and the statistical un-

[6]While more recent values are available from NNDC, the differences are minimal and do not significantly impact the conclusions of this study.

Table 6.2: The activities of ^{232}Th and ^{238}U derived from peak calculations (see Equation (6.1)). For the TCS-affected peaks, ^{208}Tl at 2615.51 keV and ^{212}Pb at 238.63 keV, these activities are shown before and after being multiplied by the correction factor (CF) from Table 6.1. From the ^{232}Th decay chain, the ^{212}Pb peak at 238.63 keV can be compared with the ^{208}Tl peak. From the ^{238}U decay chain, the ^{214}Pb peak at 351.93 keV can be compared with the ^{214}Bi.

Before CF	**After CF**	
^{208}**Tl** [**Bq kg**$^{-1}$]	^{208}**Tl** [**Bq kg**$^{-1}$]	^{212}**Pb** [**Bq kg**$^{-1}$]
2.176 ± 0.091	2.764 ± 0.123	2.747 ± 0.053
^{214}**Bi** [**Bq kg**$^{-1}$]	^{214}**Bi** [**Bq kg**$^{-1}$]	^{214}**Pb** [**Bq kg**$^{-1}$]
1.947 ± 0.064	2.314 ± 0.081	2.343 ± 0.061



(a) (b)

Figure 6.8: (a) A photo of an anhydrite sample inside the sample holder and plastic bag being weighed. (b) A photo of the anhydrite sample placed in the BEGe detector, "Chaloner", in the Boulby Underground Screening facility.

certainties, σ_N, from each fitted Gaussian is recorded and normalised with respect to the sample's mass, m, the energy-specific detector efficiency, η, the time the sample was measured for, t, the branching ratio of the radioactive isotope that produced the gamma-rays of the peak, b, and the effects of TCS, C_{TCS}, (if applicable)[7]. The subtracted background is that of the empty sample holder in a plastic bag.

The specific activity, A, of a decay chain's parent nuclide (^{232}Th, ^{238}U, ^{235}U) from a single peak is calculated as follows:

$$A_i = \frac{N \cdot C_{TCS}}{t \cdot \eta \cdot b \cdot m}, \tag{6.1}$$

$$\sigma_{A_i} = \frac{\sigma_N \cdot C_{TCS}}{t \cdot \eta \cdot b \cdot m}. \tag{6.2}$$

[7]A relevant TCS correction factor from Table 6.1 is included.

Multiple (n) peaks from the same decay chain in a sample are combined using weighted averages:

$$A_{tot} = \frac{\sum_{i=1}^{n} w_i A_i}{\sum_{i=1}^{n} w_i}, \tag{6.3}$$

$$w_i = \frac{1}{\sigma_i^2}, \tag{6.4}$$

$$\sigma_{A_{tot}} = \frac{1}{\sqrt{\sum_{i=1}^{n} \frac{1}{\sigma_i^2}}}. \tag{6.5}$$

Total specific activities and uncertainties of isotopes from multiple samples are averaged using the same method as above. If a peak had too few counts for the statistical uncertainty to be sufficiently low ($< 10\%$), the upper limit, L_U, was found using the following equations, taken from [76]:

$$N = C - B, \tag{6.6}$$

$$B' = \frac{B\Delta t_B}{\Delta t_C}, \tag{6.7}$$

$$L_U = N + 1.645\sqrt{(N + 2B')}, \tag{6.8}$$

where C is the total number of counts (including the background count rate B). The corrected background count rate, B', accounts for the difference in measurement durations between the sample and background data. 1.645 is the confidence interval for a 95 % CL (1-tailed)[8]. The highest intensity ^{235}U gamma-ray peak found in most spectra (185.72 keV with a branching ratio of 0.572) was the primary peak used to calculate upper limits. The statistical uncertainty was found using standard methods of error propagation for Equation (6.8). If a rock type had a mixture of upper limits and normal counts (CPH and Halite 9 are such examples), the weighted mean of all of the samples' ^{235}U activities was calculated. If the statistical uncertainty exceeded 10% of the activity, the result was reported as a 95 % CL upper limit.

6.2.2 Results of sample measurements

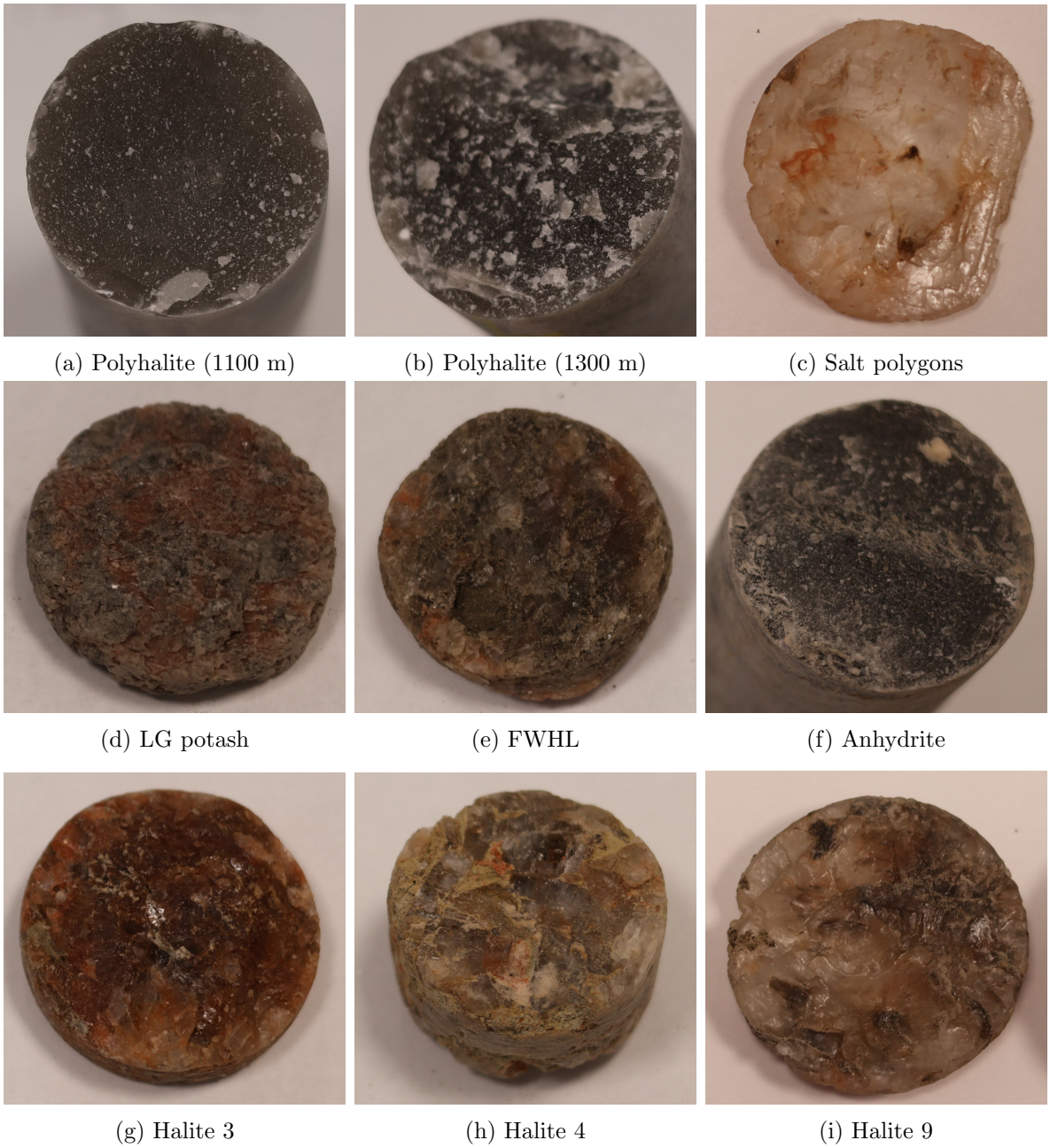
Table 6.3 lists the activities of ^{40}K, ^{232}Th, ^{238}U and ^{235}U in 10 types of rock. Three samples of halite are included to emphasise the variety in the abundance of radioactive contaminations in the salt band at the 1100 m level. Although all samples from the 1100 m level are mainly salt rock in composition (halites), some have more contaminants than others and consequently have differing abundances of radioactive nuclides. To aid the sample descriptions, Figure 6.9 displays images of the measured rock types.

Table 6.3 includes the measurements of ^{40}K, ^{232}Th, ^{238}U and ^{235}U in 10 types of rock from mainly the 1100 m level, but also some polyhalite from the 1300 m level. Measurements of multiple samples of each rock type were averaged. Some of the ^{235}U measurements have upper limits quoted at 95 % CL because, in the gamma-ray energy

[8]Found by computing the inverse cumulative distribution function of a standard normal distribution.

Table 6.3: Averaged measurements of radioactive isotopes in rock samples from Boulby mine. The background is the measured radioactivity of the sample holder in a plastic bag. Statistical uncertainties as a standard deviation are quoted first and systematic uncertainties second. Where measurements of ^{235}U were statistically insignificant, an upper limit at 95% CL is reported.

Rock type	**^{40}K activity [Bq kg^{-1}]**	**^{232}Th activity [Bq kg^{-1}]**	**^{238}U activity [Bq kg^{-1}]**	**^{235}U activity [Bq kg^{-1}]**
Background	$0.850 \pm 0.089 \pm 0.051$	$(3.82 \pm 0.45 \pm 0.19) \times 10^{-2}$	$(7.63 \pm 0.70 \pm 0.38) \times 10^{-2}$	$< 7.7 \times 10^{-3}$
Polyhalite	$2500 \pm 1 \pm 126$	$(1.143 \pm 0.372 \pm 0.057) \times 10^{-2}$	$0.354 \pm 0.008 \pm 0.042$	$< 3.4 \times 10^{-2}$
Salt polygons	$47.09 \pm 0.27 \pm 2.66$	$0.161 \pm 0.005 \pm 0.004$	$0.145 \pm 0.006 \pm 0.004$	$< 1.3 \times 10^{-2}$
LG potash	$3578 \pm 3 \pm 88$	$3.364 \pm 0.028 \pm 0.096$	$2.514 \pm 0.029 \pm 0.294$	$0.139 \pm 0.009 \pm 0.008$
Potash	$1508 \pm 3 \pm 43$	$2.756 \pm 0.041 \pm 0.322$	$2.279 \pm 0.041 \pm 0.128$	$0.117 \pm 0.011 \pm 0.004$
FWHL	$281.9 \pm 1.2 \pm 32.9$	$1.144 \pm 0.019 \pm 0.064$	$1.140 \pm 0.021 \pm 0.042$	$(6.02 \pm 0.48 \pm 0.28) \times 10^{-2}$
CPH	$1709 \pm 3 \pm 96$	$0.358 \pm 0.023 \pm 0.013$	$0.492 \pm 0.025 \pm 0.023$	$< 4.2 \times 10^{-2}$
Anhydrite	$13.93 \pm 0.17 \pm 0.51$	$0.610 \pm 0.008 \pm 0.028$	$2.919 \pm 0.017 \pm 0.162$	$0.139 \pm 0.003 \pm 0.009$
Halite 3	$584.4 \pm 1.7 \pm 27.3$	$0.888 \pm 0.022 \pm 0.049$	$0.826 \pm 0.022 \pm 0.032$	$< 5.1 \times 10^{-2}$
Halite 4	$479.9 \pm 0.9 \pm 26.7$	$4.262 \pm 0.020 \pm 0.164$	$2.323 \pm 0.018 \pm 0.107$	$0.129 \pm 0.004 \pm 0.011$
Halite 9	$39.06 \pm 0.14 \pm 1.51$	$0.529 \pm 0.005 \pm 0.024$	$0.495 \pm 0.005 \pm 0.029$	$(4.37 \pm 0.12 \pm 0.25) \times 10^{-2}$



(a) Polyhalite (1100 m) (b) Polyhalite (1300 m) (c) Salt polygons

(d) LG potash (e) FWHL (f) Anhydrite

(g) Halite 3 (h) Halite 4 (i) Halite 9

Figure 6.9: Photographs of examples of the different types of rock samples measured, as listed in Table 6.3. Details of their compositions are given in Section 6.2.2 text.

spectra for these samples, the uncertainties of the peak counts were very high. This occurred when the potassium content tended to be very large and the ^{235}U content relatively low. The resulting, extensive Compton continuum obscured multiple smaller peaks below the ^{40}K peak at 1461 keV. The problem is compounded by a lower detector efficiency at higher energies. An example of this type of spectrum from a polyhalite sample is shown in Figure 4.2. The samples vary widely in characteristics such as composition, crystal size and density.

The primary components of potash (sylvinite), in roughly equal amounts, are sylvite (KCl), which is the mineral form of potassium chloride, and halite (NaCl). There tend to be many impurities disseminated throughout potash, rendering it relatively unclean,

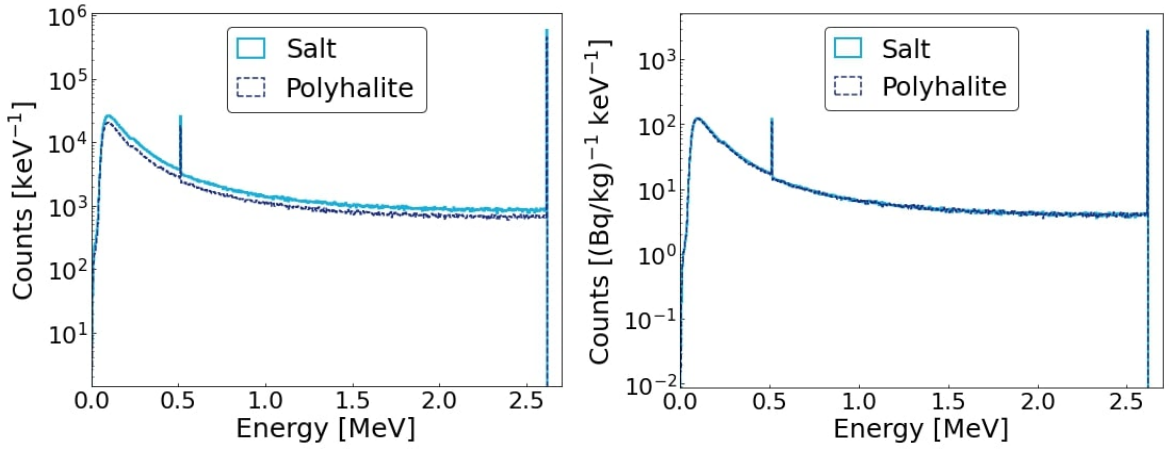
particularly with low-grade (LG) potash which is categorised separately here. Also high in potassium is CPH as it is mainly clean halite with varying amounts of sylvite and some silt impurities. FWHL is similar in composition to CPH, but the halite is less clean and has more silt deposits. Halites 3 and 4 are similar in composition, the bulk being halite with small fractions of potash and carnallite ($MgCl_2{\cdot}6(H_2O)$), differing in granularity and crystal size. Salt polygons are made from relatively clean halite, with little sylvite, silt or anhydrite ($CaSO_4$) and are structurally comprised of large crystals. Consequently, the polygons have low levels of ^{40}K and other NORM isotopes relative to the bands above. Halite 9 is a mixture of halitic anhydrite, anhydritic halite and silt, it is much lower in potassium than other samples with a higher halite content. Shale may also be present in some bands. The anhydrite band lacks halite and is low in potassium relative to other rock types, being further from the sylvite deposits. The traces of ^{238}U and ^{235}U are relatively high in anhydrite.

The polyhalite samples are from boreholes separate from those spanning all of the other bands of rock: one at a depth of $\sim$1100 m and two at a depth of $\sim$1300 m, the latter being closer in depth and location to where a future laboratory may be built. Polyhalite ($K_2Ca_2Mg(SO_4)_4{\cdot}2H_2O$) is a uniform material with a small grain size and high purity. The ^{40}K content is very high, similar to that of potash, but other contaminants are scarce, resulting in very low levels of ^{232}Th and relatively low levels of ^{238}U.

6.2.3 Discussion of sample measurements

Previous measurements of the background radioactivity at the 1100 m level in Boulby were carried out in 2006 [108]. Halite and mudstone samples were taken from the walls just outside the laboratory and measured with an HPGe detector. In situ measurements, next to the same walls where samples were collected from, were also performed with an HPGe detector. Although the location of the laboratory is about 1 km away from the borehole sources of our samples, and it was either not known or not disclosed exactly which type of halite they measured, the magnitude of the radioactivity can be compared. From halite samples (with some sylvite impurities), the average decay rate of ^{232}Th was measured as 0.6 Bq kg^{-1} and the average decay rate of ^{238}U was measured as 0.4 Bq kg^{-1}. From the in situ measurements (of a mixture of halite and mudstone in the walls) the average decay rate of ^{232}Th was measured as 1.88 Bq kg^{-1} and the average decay rate of ^{238}U was measured as 1.63 Bq kg^{-1}. Similarly low activity concentrations characterise our halite samples, but still with a large spread, of ^{232}Th: 0.161 $-$ 4.262 Bq kg^{-1}, and ^{238}U: 0.145 $-$ 2.323 Bq kg^{-1}. Note that these ranges do not include measurements from potash, anhydrite, or polyhalite as the majority of their compositions are not halite.

The rock composition in the simulation described in Chapter 5 mirrors that of Boulby mine at the 1100 m level, which is predominantly halite. To ensure the simulation yields consistent results with different initial rock compositions, the simulation was rerun with polyhalite instead of pure NaCl as they have vastly different elemental compositions. The results of this test, displayed in Figures 6.10a and 6.10b, show negligible differences between the shape of the two spectra. There is a spectrum-wide fractional difference of $\sim$23 % in raw counts. However, when the results are normalised to 1 Bq kg^{-1} it is clear that the difference in rock density is the determining factor in the raw counts difference



(a) (b)

Figure 6.10: Energy spectra of gamma-rays at the 1st tracking surface, 10 cm outside of the water tank. 3.6×10^8 gamma-rays, each with an energy of 2.615 MeV, were generated from salt and polyhalite rock separately to check for differences between the resultant spectra. The number of gamma-rays that reached the 1st surface from salt and polyhalite is 10702179 and 8170331, respectively. (a) displays the difference in the raw counts showing a clear distinction between the datasets, and (b) demonstrates the effect of normalising the counts to 1 Bq kg^{-1}, indicating that the difference between spectra in (a) is determined by the rock density.

(NaCl: 2.17 g cm^{-3}, polyhalite: 2.78 g cm^{-3})[9]. Therefore, the simulation results can be used with any rock type regardless of composition. Since the rock strata undulate, there is a chance that the future laboratory may be partially built in rock that is not polyhalite. A future detector can also be built at another site. Therefore, the measurements of the many types of rock serve as a future reference for what thickness of shielding will be needed for a location-specific, rock gamma-ray background.

We can now take the simulated results from Table 5.6 and normalise them to measurements of Boulby polyhalite since a potential future laboratory will be built in this rock-type band. The results are shown in Table 6.4. Additionally, the gamma-ray background rate at Boulby can be estimated if the water shielding thickness were to be reduced by 1 m on all sides of the detector. Using the rate results from Table 5.7, the ^{232}Th and ^{238}U rates in the WIMP ROI from Boulby polyhalite are calculated to be $(1.4^{+1.0}_{-0.6}) \times 10^{-3}$ year^{-1} (Bq/kg)$^{-1}$ and $(8.9^{+9.9}_{-5.7}) \times 10^{-3}$ year^{-1} (Bq/kg)$^{-1}$, respectively. Using the rate increase factors from Table 5.7 (but not decreasing the FV), the ^{232}Th and ^{238}U rates in the $0\nu\beta\beta$ decay ROI from Boulby polyhalite are estimated to be $(8.96 \pm 5.64) \times 10^{-2}$ year^{-1} (Bq/kg)$^{-1}$ and 3.64 ± 0.13 year^{-1} (Bq/kg)$^{-1}$, respectively.

SURF and LNGS are also under consideration as potential hosts for the next-generation dark matter detector. Both laboratories have screened the rock and shotcrete/concrete surrounding the caverns and the specific activities of ^{40}K, ^{232}Th, and ^{238}U from these materials are listed in Table 6.5. The SURF and LNGS results were obtained by measuring samples with HPGe detectors [122, 123].The gamma-ray background from shotcrete in the Davis Cavern is presented in row 1, and the gamma-ray backgrounds from dolomitic limestone and concrete in LNGS are in rows 2 and 3. For comparison, row 4 repeats

[9]These values are different to those given in Table 6.1 as they are the densities of chemically pure halite and polyhalite, whereas the values in Table 6.1 are the average densities of Boulby samples measured.

Table 6.4: Rates of events in the TPC with analysis cuts applied from Table 5.6, normalised to measurements of polyhalite from Boulby mine at 1100 m and 1300 m depths (see Table 6.3). The thickness of shielding is 3.5 m of water and 0.5 m of GdLS on the top and sides of the detector, with 1.5 m of water, 0.5 m of GdLS and and 30 cm steel plate underneath the detector. Using a Feldman-Cousins approach [98], the statistical uncertainties are shown at 1 σ for non-zero event rates and an upper limit of 90 % CL is quoted for zero events.

Isotope	**0 - 20 keV Rate [year^{-1}]**	**0 - 100 keV Rate [year^{-1}]**	**2408 - 2508 keV Rate [year^{-1}]**
^{232}Th	$\left(1.7^{+1.3}_{-0.7}\right) \times 10^{-5}$	$(1.62 \pm 0.26) \times 10^{-4}$	$(1.11 \pm 0.07) \times 10^{-3}$
^{238}U	$\left(7.8^{+8.9}_{-5.0}\right) \times 10^{-5}$	$\left(5.7^{+1.8}_{-1.4}\right) \times 10^{-4}$	$(3.25 \pm 0.11) \times 10^{-2}$
^{40}K	$\left(0^{+9.5}_{-0}\right) \times 10^{-2}$	$\left(0^{+9.5}_{-0}\right) \times 10^{-2}$	n/a

the Boulby polyhalite measurements reported in this chapter (see Table 6.3). The uncertainties quoted in Table 6.5 are the statistical and systematic uncertainties summed in quadrature.

Relative to SURF and LNGS, Boulby polyhalite exhibits substantially lower ^{232}Th and ^{238}U activities, indicating a more favourable environment with respect to gamma-ray background and the potential to reduce shielding thickness. However, there will be structural laboratory materials in addition to the rock that have not been measured as of yet. In contrast to the low ^{232}Th and ^{238}U activities, the ^{40}K content of polyhalite is considerably higher than in cavern rock and shotcrete/concrete at SURF and LNGS. However, as demonstrated in Table 6.4, this is not a major concern; the strongest ^{40}K gamma line (1461 keV) lies well below $Q_{\beta\beta}$, and the water shielding strongly attenuates these gamma-rays. When simulations are normalised to the measured polyhalite activities, the contribution to TPC rates from ^{40}K is limited to < 0.1 events per year in the WIMP ROI (0 – 20 keV), which is below the sensitivity goal of < 1 event per year.

Table 6.5: Specific radioactivities of the shotcrete that surrounds the Davis Cavern at SURF (from [122]); the dolomitic limestone rock and concrete in LNGS (from [123]); and polyhalite from Boulby.

Location	**^{40}K [Bq kg^{-1}]**	**^{232}Th [Bq kg^{-1}]**	**^{238}U [Bq kg^{-1}]**
SURF shotcrete	220 ± 30	11.4 ± 0.4	21 ± 1
LNGS limestone	26 ± 2	1.5 ± 0.1	1.8 ± 0.1
LNGS concrete	70 ± 2	3.7 ± 0.2	9.5 ± 0.3
Boulby polyhalite	2500 ± 126	$(1.143 \pm 0.376) \times 10^{-2}$	0.354 ± 0.043

6.2.4 Conclusions

The polyhalite samples from Boulby provide some insight into the radioactive background where a future laboratory may be constructed. Ideally, additional samples would be collected and measured to give a more accurate understanding of the surroundings. However,

polyhalite is known to be fairly uniform in composition, so the results in Table 6.4 can be used to give a general overview of the background.

When the simulation results are normalised to the screening results of the polyhalite samples, the background event rates of ^{232}Th and ^{238}U are much lower than necessary for the sensitivity requirements in either of the $0\nu\beta\beta$ decay or WIMP ROIs. Therefore, the water shielding thickness could be significantly reduced from 3.5 m to 2.5 m on the top and sides of the detector, and from 1.5 m to 0.5 m on the bottom of the detector. This can be done without reducing the FV for ^{232}Th, but not for ^{238}U, as the rate in the $0\nu\beta\beta$ decay ROI is not < 1 event per 10 years. Despite the rates from ^{40}K decay being much higher, the ^{40}K gamma-rays will not affect the $0\nu\beta\beta$ decay search, and the rate is still < 1 event per year in the WIMP ROI.

With the potential of housing the future detector in Boulby Mine, different rock types from various geology bands were measured to construct a guide to the radioactive backgrounds that could be encountered. The polyhalite, although high in ^{40}K, is low in ^{232}Th and ^{238}U with specific radioactivities of $(1.143 \pm 0.372\ (\text{stat.}) \pm 0.057\ (\text{syst.})) \times 10^{-2}$ Bq kg^{-1} and $0.354 \pm 0.008\ (\text{stat.}) \pm 0.042\ (\text{syst.})$ Bq kg^{-1}, respectively, which makes the location a suitable site for a high-sensitivity dark matter experiment.

Chapter 7

The radon facility in the Boulby Underground Laboratory

Mitigating radon background and measuring radon emanation from materials for low-background experiments, such as the next-generation dark matter experiment discussed in Chapter 5, is vital for optimising the detector's sensitivity. The longest-lived radon isotope, ^{222}Rn, can enter the detector during construction through exposure to air and dust particles, and during operation via emanation from detector materials. When ^{222}Rn decays, its progeny provides a constant background in the active region. The impact of radon contamination in low-background experiments is discussed further in Section 3.2.

In 2022, a radon emanation facility was installed in the Boulby Underground Laboratory as an addition to the BUGS facility (see Section 6.1.2). The Boulby radon system aims to be part of the radioassay campaign for the next-generation dark matter detector. The sensitivity requirement for WIMP and $0\nu\beta\beta$ decay searches is < 0.1 µBq/kg of ^{222}Rn activity in the liquid xenon target [44]. This chapter describes the setup of the new radon system in Section 7.1, the method used to estimate the amount of radon detected in Section 7.2, and the processes of detector calibration and sample measurement in Section 7.3. Section 7.4 presents the results of polyhalite measurements carried out in Boulby's radon facility. Lastly, Section 7.5 briefly discusses an ongoing project and outlines what is needed to improve the facility for future material screening.

7.1 Facility overview

The Boulby radon facility comprises two 80 L electrostatic, stainless steel detectors; four emanation chambers of different volumes - two 5 L and two 3 L; a low-temperature

radon reduction system, a bespoke radon concentration line, an analog-to-digital converter (ADC) board connected to a RaspberryPi, and a CAEN digitiser. Section 7.3 describes how this facility can be utilised, but to understand the purpose of the equipment listed in the subsequent sections, a general example of usage is given. To measure a sample's radon emanation rate, the sample is sealed in an emanation chamber for several days, during which radon nuclei emanate from the sample into the chamber. After this period, the chamber is purged with high-purity nitrogen gas to transfer the accumulated radon through a radon concentration line into the radon detector. Within the detector, alpha decays from ^{222}Rn and its progeny are recorded via the energy deposited on a photodiode by the emitted alpha particles. The resulting energy spectrum enables measurement of the radon emanation rate from the sample.

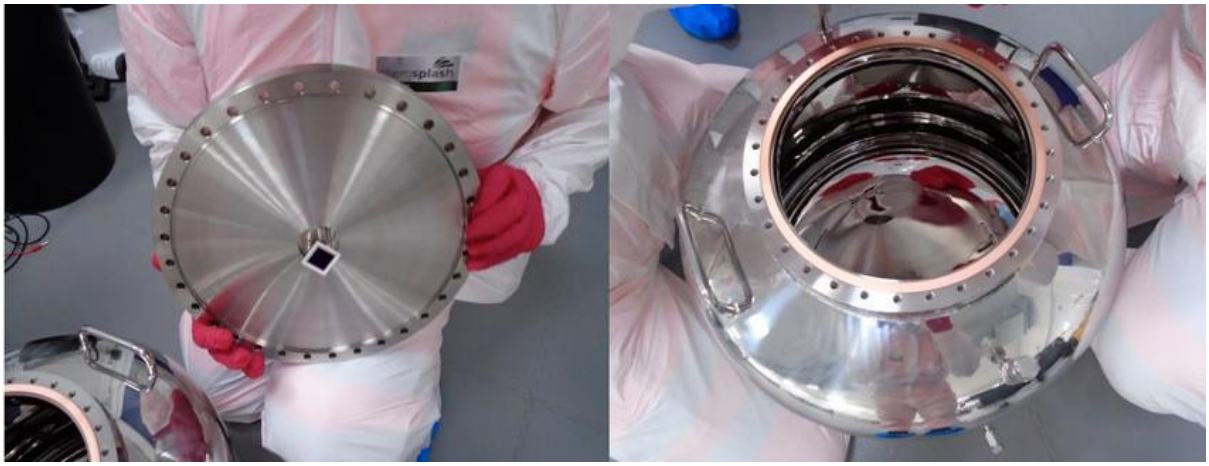
7.1.1 Radon detector

The electrostatic detector, described in Ref. [124] and pictured in Figure 7.1a, was developed at the University of Tokyo (UoT) as an improvement to an earlier 70 L model [125] that was designed to meet sensitivity requirements in Super-Kamiokande [126]. That earlier model achieved sensitivities of 1 - 2 mBq/m^3, an improvement of two orders of magnitude over the best commercial radon detectors available at the time. The more recent design reduced the detector background to one-third of the 70 L detector's background. Subsequent validation and development of the upgraded 80 L detector has been extensively carried out at the University College London (UCL) radon facility in parallel with that of the UoT. This includes detailed performance studies and contributions to the LZ screening campaign through dedicated radioassay measurements [127, 128, 129, 130] at UCL, while RaspberryPi electronics and new radon detector designs were being developed by the UoT at the Kamioka Observatory [131].

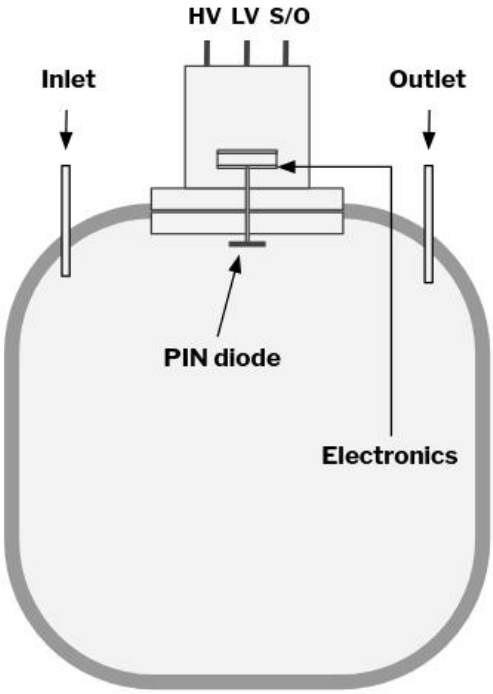
The detector, depicted in Figures 7.1a and 7.1b, consists of an 80 L electropolished stainless steel vessel, finished to a surface roughness of < 0.8 µm. A high-voltage electric field is applied to draw positively charged radon progeny, such as polonium isotopes, onto a HAMAMATSU S3204-09 PIN photodiode. Studies have shown that 87.3 ± 1.6 % of radon decays in air result in positively charged ions [132]. The photodiode measures the energy deposits from alpha decays, differentiating the polonium isotopes as these energy signatures are well-separated (see Table 7.1). By applying corrections for detector and transfer efficiencies, the radon emanation rate from a given source material can be reconstructed from these alpha decay signals.

7.1.2 Detector electronics

All detector electronics are housed within the detector lid, minimising the distance of signal cable to the pre-amplifier, which is pictured in Figure 7.2a. The lid also protects the electronics from external noise. The 18 mm $\times$ 18 mm photodiode is mounted face-down inside the chamber, positioned 5 cm below the electronics feed-through. The windowless design reduces energy loss from incident alpha particles, while the absence of an insulating layer around the bias electrodes on the p- and n-layers of the diode reduces background noise. The detector operates with a HV divider, pictured in Figure 7.2b, which is supplied with -1900 V from a CAEN DT5470N desktop power supply. The HV divider is used to



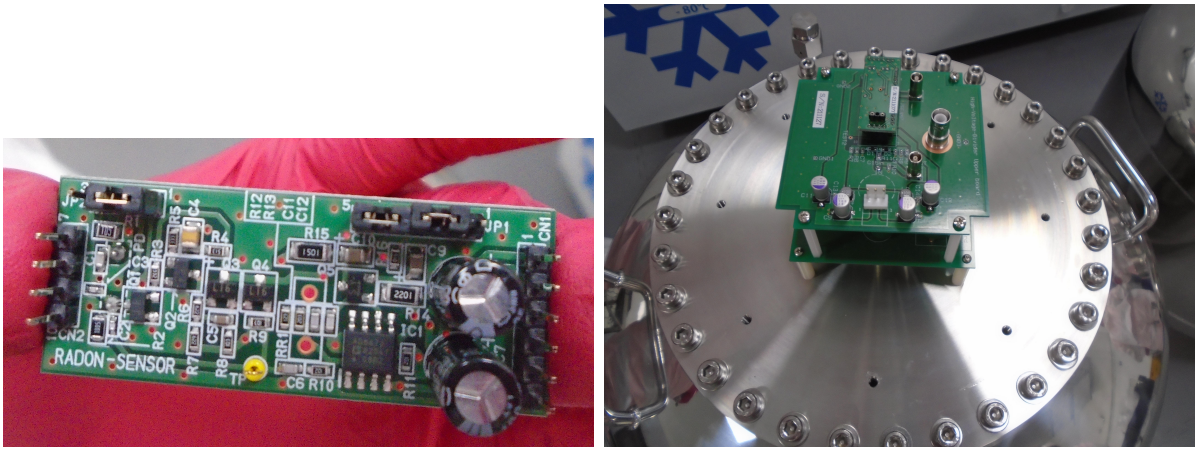
(a)



(b)

Figure 7.1: Photos (a) and a diagram (b) of the electrostatic radon detector developed at the UoT. The pictures in (a) show the detector with the top section disconnected during installation, where the PIN diode can be seen on the underside of the top section. The schematic in (b) illustrates the gas inlet and outlet pipes; the electronics inside the detector lid; and the PIN diode inside the vessel. The thick lines on the top of the detector lid indicate where the high-voltage (HV) and low-voltage (LV) supplies enter and where the signal output (S/O) cable exits the lid of the detector.

bias the PIN diode and generate the required electric field within the chamber while the vessel remains at ground potential. Alpha particle-induced charge deposits are converted into positive voltage pulses by a pre-amplifier powered by a 12 V DC supply. These signals are then passed to an ADC board developed by UoT for Raspberry Pi systems, which is detailed in Ref. [131]. Signal amplitudes are converted to channel numbers before being transmitted to a Raspberry Pi running the software that the UoT developed



(a) (b)

Figure 7.2: The electronics inside the radon detector lid: (a) is the pre-amplifier and (b) is the HV divider.

specifically for these radon detectors. This software integrates the counts detected by the PIN photodiode over a default period of 10 minutes, saving the data in text files with ADC bin values and timestamps. Analysis code has been written by the UoT to extract data from these text files, converting from channels to energy and using energy "windows" to discriminate between alpha signatures.

Trials with this ADC and DAQ system revealed its unsuitability for high-sensitivity, low-background assays [130], leading to an upgrade: the CAEN DT5730S desktop digitiser and the complementary DAQ software - CAEN Multi-PArameter Spectroscopy Software (CoMPASS). From early tests to understand the software, a CoMPASS graph was generated after flushing an arbitrary amount of radon into a detector, and this plot can be seen in Section G. Unfortunately, the new digitiser in the Boulby radon facility was not fully operational at the time of writing, hence, the analysis in Sections 7.3 and 7.4 was performed using the data processed by the RaspberryPi system.

7.1.3 Radon reduction system and emanation chambers

All components of the radon facility are connected to the nitrogen system described in Section 6.1.2. There are naturally low levels of radon in the Boulby laboratory [109], however, to have minimal radon contamination throughout the radon system, the pre-dried nitrogen gas is passed through several charcoal traps, where radon from the gas is adsorbed. These traps are maintained at -80℃, below the freezing point of ^{222}Rn (-71℃), as lower temperatures increase the amount of radon adsorption on activated charcoal [133]. The now radon-reduced nitrogen can be used to flush the emanation chambers, concentration line and detectors to reduce the backgrounds of measurements.

There are four stainless steel emanation chambers, shown in Figure 7.3, each sealed with a copper gasket. Their internal dimensions are:

- "3 L" chamber ($\times 2$): diameter = 14.6 cm, length = 17.3 cm, volume = 2.896 L
- "5 L" chamber ($\times 2$): diameter = 14.6 cm, length = 28.9 cm, volume = 4.838 L

The chambers are connected to the nitrogen supply (after the radon reduction system) and the concentration line via Swagelok pipes and fittings - all made from stainless steel. The nitrogen is regulated using Bronkhorst El-Flow Select mass flow controllers (MFCs). Samples are placed inside the chambers to emanate for several days, then the build-up of radon in the chamber from the sample is flushed into the detector following the procedures outlined in Sections 7.3.1 and 7.3.4.



Figure 7.3: Radon emanation chambers. The 5 L chambers are to the left of the image and the 3 L chambers are to the right.

7.1.4 Concentration line

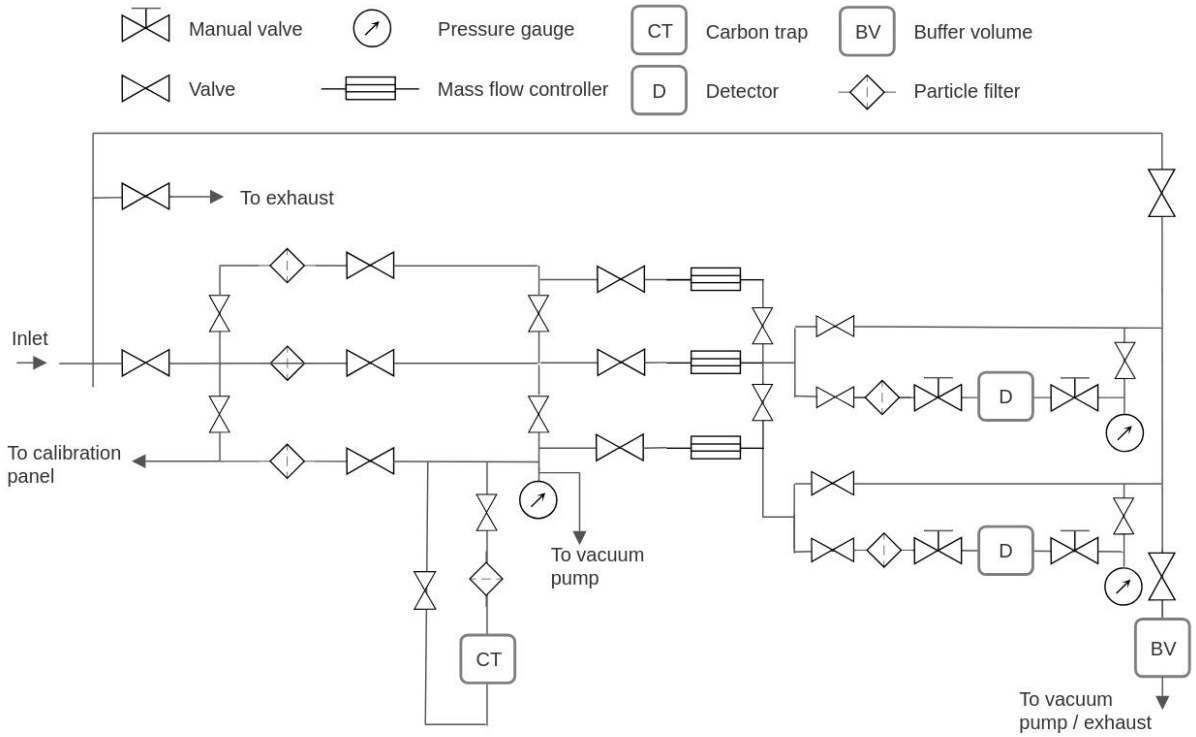
A radon concentration line is a piece of equipment that increases the sensitivity of radon measurements. First, radon atoms that have emanated from a sample are collected from a large volume of carrier gas onto a cooled charcoal trap. Second, the trap is heated and the atoms are released with a lower volume of carrier gas (thereby concentrating the radon) and flushed into a detector. This concentration process allows trace levels of radon, which would otherwise fall below the detection threshold, to be measured accurately.

The UCL radon emanation facility used the electrostatic radon detectors as part of the SuperNEMO experiment's [134] material screening campaign, which has a radon background requirement of 150 µBq/m^3 [135]. However, the detectors were not sensitive enough to make a measurement at this level. Therefore, a radon concentration line was developed for use in conjunction with the electrostatic detectors [127, 128]. This apparatus was based on previous work carried out for the Borexino experiment [136, 137]. A similar concentration line, pictured in Figure 7.4a, was built specifically for Boulby by Swagelok, with all pipework made from stainless steel. As can be seen from Figure 7.4b, there are parts designed to be connected to vacuum pumps. Evacuating the system of air between sample measurements provides reproducible starting conditions and enhances the sensitivity of the radon detector by removing all residual gases and water vapour. This ensures that the only radon is from the sample material and the intrinsic detector background. The Boulby concentration line is not currently operating under vacuum between measurements or calibrations.

The principle behind the radon concentration line is straightforward: emanated radon carried by nitrogen gas is directed through an activated, high-purity charcoal trap, where



(a)



(b)

Figure 7.4: A photo (a) and a process flow diagram (b) of the radon concentration line in Boulby laboratory with two electrostatic detectors connected. The section designated for the radon trap can be seen on the left-hand side of the image in (a).

the radon is adsorbed onto the carbon surface while the carrier gas continues downstream. During the trapping phase, the charcoal trap is actively cooled to enhance its adsorption efficiency. Once the collection is complete, the trap is heated to release the radon, which is then flushed (with nitrogen) into an electrostatic detector for measurement. In the schematic shown in Figure 7.4b, the carrier gas enters from the left and flows toward the right. A 0.5 µm, stainless steel particle filter is positioned at the inlet to remove particulates before the gas encounters a series of valves that determine its flow path.

Additional particle filters are placed upstream of sensitive components such as the MFCs, detectors, and vacuum pumps. During a standard measurement cycle, the gas flows through the charcoal trap and an MFC, continues into the detector, and is finally vented to exhaust via a buffer volume. The charcoal trap is not yet fully assembled in the Boulby radon system and is currently bypassed during measurements.

7.2 Radon detection methods

The electrostatic detectors, described in the previous section, measure radon emanation from materials by detecting alphas from the decay of the daughter polonium nuclides. Therefore, it is important to understand how the activity of these isotopes is related to that of radon. The relationships between the activities in ^{238}U decay chain are derived in this section. The relationship between ^{220}Rn and ^{212}Po from the ^{232}Th decay chain is found using the same method, but is not outlined in this section. In rock and detector materials, secular equilibrium is assumed because the half-life of ^{226}Ra ($\sim$ 1600 years) is much longer than any half-lives of its daughter nuclides listed above. This means that the concentration of daughter nuclides in the rock remains equal to that of ^{226}Ra, and they have the same activity, A.

7.2.1 Method to calculate activities of nuclides in the ^{222}Rn decay chain

Key information about the decay of each nuclide relevant to radon emanation techniques in the ^{238}U decay chain is compiled in Table 7.1. To aid the description of detector

Nuclide	**Decay type**	**Half-life**	**α energy [MeV]**	**Q-value [MeV]**
^{226}Ra	α	1603 y	4.784 (94%), 4.601 (6%)	4.871
^{222}Rn	α	3.822 d	5.489	5.590
^{218}Po	α	3.097 m	6.003	6.115
^{214}Pb	β	27.06 m	n/a	1.018
^{214}Bi	β	19.71 m	n/a	3.269
^{214}Po	α	163.6 µs	7.687	7.833

Table 7.1: Details of the nuclides in the ^{238}U decay chain. Each row states information about the parent, starting from ^{226}Ra in the first row, with the next row describing its daughter nuclide. Continuing this trend, each subsequent row describes the daughter nuclide of the parent in the previous row. The half-lives, alpha particle energies (and intensities for ^{226}Ra), and Q-values are taken from Refs. [138, 57, 54, 139].

calibration and sample measurement procedures, the following notation will be used for nuclides in this lower section of the ^{238}U decay chain:

$$\underset{N_{-1},\lambda_{-1}}{^{226}\text{Ra}} \rightarrow \underset{N_0,\lambda_0}{^{222}\text{Rn}} \rightarrow \underset{N_1,\lambda_1}{^{218}\text{Po}} \rightarrow \underset{N_2,\lambda_2}{^{214}\text{Pb}} \rightarrow \underset{N_3,\lambda_3}{^{214}\text{Bi}} \rightarrow \underset{N_4,\lambda_4}{^{214}\text{Po}}$$

where N_i is the number of atoms of a nuclide in the decay chain and λ_i is the corresponding decay constant. The activity of that nuclide is:

$$A_i = N_i \lambda_i. \tag{7.1}$$

The rate of change of N_i is governed by the number of nuclide atoms decaying to the next daughter, $\lambda_i N_i$, and the number of nuclide atoms produced by the parent nuclide's decay, $\lambda_{i-1} N_{i-1}$:

$$\frac{dN_i}{dt} = \lambda_{i-1} N_{i-1} - \lambda_i N_i. \tag{7.2}$$

Secular equilibrium within a sample is reached when $\frac{dN_i}{dt} = 0$.

The number of nuclides in the above section of the chain after time t can be found by iteratively solving Equation (7.2). ^{222}Rn is a noble gas and chemically inert, so its neutral atoms are not influenced by the electric field within the detector. As a result, alpha particles from its decay are typically not detected by the PIN diode, since the decay often occurs far from the sensitive volume. Therefore, measurement of radon emanation relies on alpha decay from positively charged progeny, which are electrostatically attracted to the diode surface. Since the radon detector works by measuring signals from ^{218}Po and ^{214}Po alpha particles, solutions to Equation (7.2) are used to calculate the amount of ^{222}Rn emanated from a sample.

7.2.1.1 ^{222}Rn activity

The intrinsic background activity of the detector, A_B, needs to be taken into account when computing the number of atoms that have emanated from a sample. This is a low-level production of radon and its progenies inside the detector from radium decay, which is assumed to be constant due to the long half-life of radium. Using Equation (7.2), the amount of radon inside the detector at any given point can be found by solving the following equation:

$$\frac{dN_0}{dt} = A_B - \lambda_0 N_0. \tag{7.3}$$

Multiplying by $e^{\lambda_0 t}$ and rearranging gives:

$$e^{\lambda_0 t} A_B = e^{\lambda_0 t} \left(\frac{dN_0}{dt} + \lambda_0 N_0 \right). \tag{7.4}$$

By noting that the right hand side of the equation is equal to the derivative of $e^{\lambda_0 t} N_0$, it follows that:

$$e^{\lambda_0 t} N_0 = \int e^{\lambda_0 t} A_B dt = \frac{A_B e^{\lambda_0 t}}{\lambda_0} + C. \tag{7.5}$$

After flushing the detector before a measurement, all radon is removed, although the background activity is naturally still present. A source of radon is flushed into the detector at time $t = 0$, at which point $N_0 = N_S = A_S/\lambda_0$, where N_S is the number of radon atoms in the source. Substituting N_S into Equation (7.5) gives the integration

constant as:

$$C = \frac{A_S}{\lambda_0} - \frac{A_B}{\lambda_0}. \tag{7.6}$$

Therefore, the number of radon atoms from a source in the detector at time t is found via the sum of the increasing background activity term and the decreasing radon activity term:

$$N_0 = \frac{A_B}{\lambda_0}(1 - e^{-\lambda_0 t}) + \frac{A_S}{\lambda_0}e^{-\lambda_0 t}. \tag{7.7}$$

7.2.1.2 ^{218}Po activity

The same method is applied to calculate the activity of ^{218}Po, namely Equation (7.2) needs to be solved for N_1:

$$\frac{dN_1}{dt} = \lambda_0 N_0 - \lambda_1 N_1 = A_B(1 - e^{-\lambda_0 t}) + A_S e^{-\lambda_0 t} - \lambda_1 N_1. \tag{7.8}$$

Using the processes carried out in Equations (7.4) to (7.6) it can be shown that

$$e^{\lambda_1 t} N_1 = \int \left(A_B e^{\lambda_1 t} + (A_S - A_B)e^{(\lambda_1 - \lambda_0)t}\right) dt \tag{7.9}$$

$$= \frac{A_B e^{\lambda_1 t}}{\lambda_1} + (A_S - A_B)\frac{e^{(\lambda_1 - \lambda_0)t}}{\lambda_1 - \lambda_0} + C \tag{7.10}$$

and

$$N_1 = \frac{A_B}{\lambda_1}(1 - e^{-\lambda_1 t}) + (A_S - A_B)\left(\frac{e^{-\lambda_0 t}}{\lambda_1 - \lambda_0} + \frac{e^{-\lambda_1 t}}{\lambda_0 - \lambda_1}\right). \tag{7.11}$$

7.2.1.3 ^{214}Pb, ^{214}Bi and ^{214}Po

Predictably, the formulae for N_2, N_3 and N_4 become more protracted with each daughter in the chain. Hence, the following notation, derived in Ref. [140], is implemented[1]:

$$k^j_{l,N} = \prod_{m=N-j}^{N} [1 + (1 - \delta_{lm})(\lambda_m - \lambda_l - 1)], \tag{7.12}$$

where j is the number of $(\lambda_m - \lambda_l)$ terms and δ_{lm} is the Kronecker delta, used to exclude the term where $m = l$ from the product. Some examples are shown below:

$$k^1_{1,2} = (\lambda_2 - \lambda_1),$$
$$k^2_{0,2} = (\lambda_2 - \lambda_0)(\lambda_1 - \lambda_0),$$
$$k^3_{1,3} = (\lambda_3 - \lambda_1)(\lambda_2 - \lambda_1)(\lambda_0 - \lambda_1),$$
$$k^4_{2,4} = (\lambda_4 - \lambda_2)(\lambda_3 - \lambda_2)(\lambda_1 - \lambda_2)(\lambda_0 - \lambda_2).$$

[1]This particular notation style, adapted from Ref. [140], is taken from Ref. [127].

Using k notation, Equation (7.11) can be written as:

$$N_1 = \frac{A_B}{\lambda_1}(1 - e^{-\lambda_1 t}) + (A_S - A_B)\left(\frac{e^{-\lambda_0 t}}{k^1_{0,1}} + \frac{e^{-\lambda_1 t}}{k^1_{1,1}}\right). \tag{7.13}$$

Beyond N_0 and N_1, the solution to Equation (7.2) can be formatted as the combination of product and sum terms. For $i > 1$:

$$N_i = \frac{A_B}{\lambda_i}\left\{1 - \sum_{n=0}^{i}\left[\left(\prod_{m=n+1}^{i}\lambda_m\right)\sum_{l=n}^{i}\frac{e^{\lambda_l t}}{k^{i-n}_{l,i}}\right]\right\} + A_S\left(\prod_{m=1}^{i-1}\lambda_m\right)\sum_{l=0}^{i}\frac{e^{-\lambda_l t}}{k^i_{l,i}}. \tag{7.14}$$

To illustrate these solutions, the activities of nuclides in the ^{222}Rn decay chain from a 1 Bq source have been plotted in Figure 7.5. The time between the different daughter nuclides reaching equilibrium with ^{222}Rn depends on their respective half-lives.

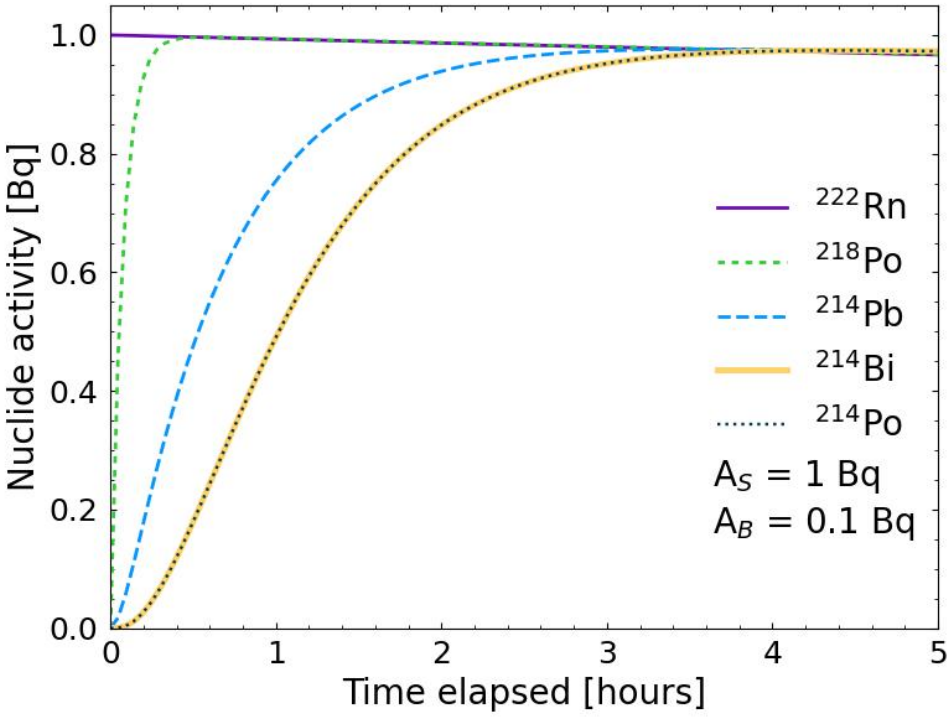


Figure 7.5: Activities of nuclides in the ^{222}Rn decay chain if a 1 Bq source of ^{222}Rn is flushed into the detector at time $t = 0$ and there is an intrinsic detector background of 0.1 Bq. The activities of the alpha-emitting isotopes are what a detector with 100% efficiency would expect to see.

7.2.2 Measuring radon emanation via the spike method

There are two main techniques to measure radon emanation, both outlined in Ref. [127]. The flow-through method involves continuously applying a steady stream of nitrogen gas over the radon source in its container/chamber and the detector, then measuring a constant signal rate. The spike method allows the radon source to emanate in a sealed chamber for a period of time, and then the air in the chamber is later flushed into the

detector, causing the measured counts in the data to peak and produce a spike, rather than reporting a constant value. This action is hereafter referred to as "spiking" a source into the detector. There are merits to using either method with respect to sources of uncertainty, but only the spike method has been used with the Boulby radon system at the time of writing. The signal rates of ^{218}Po and ^{214}Po as measured by the detector will be dictated by Equations (7.11) and (7.14). ^{210}Po decay rates are not used to estimate the ^{222}Rn activity because its half-life is 138.4 days. Therefore, this background will gradually increase as more radon is introduced to the detector during calibrations and sample measurements.

The spike method is reasonably uncomplicated, but requires precise timing. Initially, a sample to be measured is put in an emanation chamber and nitrogen is flushed through the chamber to remove all radon. To achieve 99.995% of radon removal, the chamber needs to be flushed with 10 times the volume of the chamber. This value comes from the exponential relation between the number of chamber volumes (CVs) flushed, N_V, and the percentage of radon removed from the chamber, P:

$$P = (1 - e^{-N_V}) \times 100. \tag{7.15}$$

After flushing with 10 CVs, the chamber is sealed to let the source emanate at room temperature and pressure for an emanation time, t_{em}, of 30 days. The radon emanating from a source of activity, A, within a chamber can be calculated using the increasing term from Equation (7.7):

$$N_0 = \frac{A_{-1}}{\lambda_0}(1 - e^{-\lambda_0 t_{em}}). \tag{7.16}$$

This relationship has been plotted in Figure 7.6, which demonstrates that after 30 days, the source has reached an equilibrium between the emanation and decay of ^{222}Rn. Therefore, leaving the source to emanate for 30 days or more simplifies the process that determines the amount of radon entering the detector and maximises the radon activity. To reduce the background of a measurement, the detector is flushed about a day before the source is spiked into the detector (this allows the residual daughters ^{218}Po and ^{214}Po to decay overnight). Using Equation (7.15), the flow rate and flush time are determined such that 10 CVs of nitrogen are flushed through the chamber into the detector. For example, if the CV is 5 L, it would be flushed for 10 minutes at a flow rate of 5 litres per minute (LPM). After 10 minutes, the detector is sealed and left for at least a day to allow A_1 and A_4 to reach equilibrium with A_0. However, leaving the detector to measure radon daughter activity for several days means that the detector can maximise its sensitivity (see Section 7.3.3) and allows more accurate fitting of Equations (7.11) and (7.14) to the ^{218}Po and ^{214}Po data, respectively.

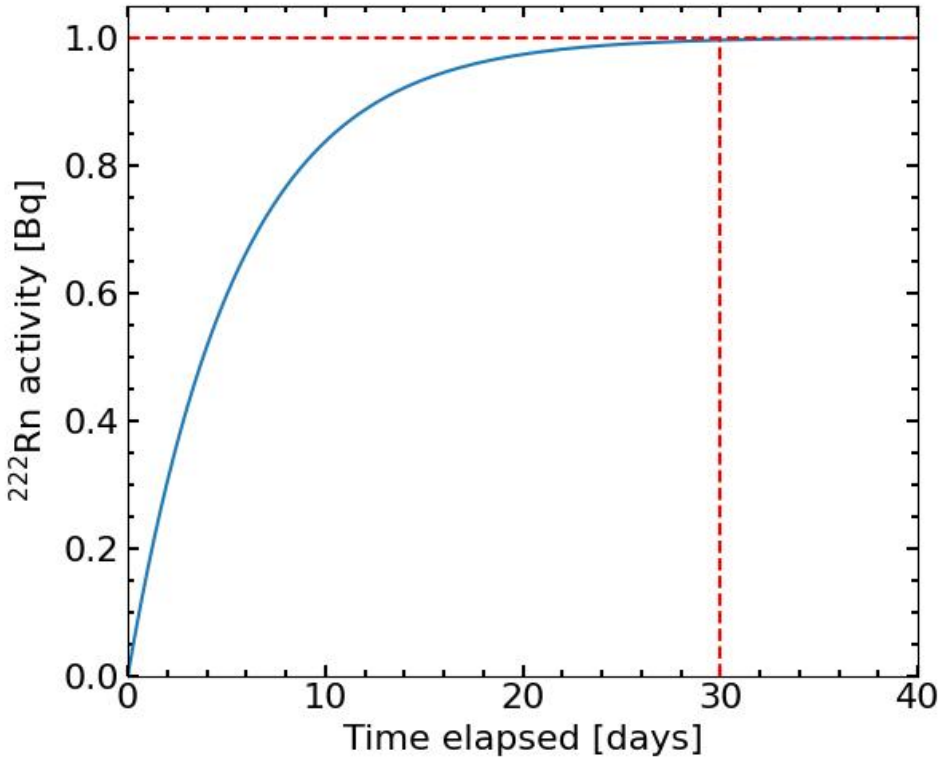


Figure 7.6: Activity from a 1 Bq radon source inside an emanation chamber. The same relationship describes the activity of the intrinsic detector background and also radon produced from a ^{226}Ra calibration source. The vertical dashed line illustrates the minimum time a sample should be left emanating to ensure that its radon activity has reached equilibrium, marked by the horizontal dashed line.

7.3 Detector calibration, background and sample measurements

7.3.1 Calibration procedure

The detection efficiency, ϵ, is influenced by various physical factors. Some can be controlled, such as humidity, temperature, and the choice of gas. These factors affect the fraction of polonium atoms that become neutralised by trace amounts of impurities in the nitrogen gas. Other factors are inherent to the detector design, namely its size, shape, and the limitation of the PIN diode, which can detect at most 50% of the alpha particles emitted from ^{218}Po and ^{214}Po decay[2]. Calibration accounts for the combined effects of these factors, providing a measure of the overall efficiency in radon emanation measurements. A ^{226}Ra source of known activity is required for this process. The model used for the calibration results presented in Table 7.2 is the RN-1025 from Pylon Electronics. The calibration procedure was originally developed by the UCL radon facility and adapted at Boulby; it is carried out over two days[3] and the steps are outlined below:

[2]Polonium nuclei on the surface of the diode emit alpha particles isotropically upon decay, hence, only 50 % of emissions interact with the diode.

[3]this procedure could conceivably be carried out in one day, but due to time constraints set by the Mine's lift ride schedule, doing so would be very difficult.

Day 1

1. **Flush the detector:**
   Purge the detector with a minimum of 10 detector volumes (DVs) of high-purity nitrogen gas to remove residual radon and humidity. After flushing, seal the detector overnight to allow short-lived radon progeny, such as ^{218}Po and ^{214}Po isotopes, to decay.
2. **Flush the ^{226}Ra source:**
   Connect the Pylon RN-1025 ^{226}Ra source to the nitrogen gas line and flush gas through it at a flow rate of 1.5 LPM for at least 4 hours to expel any residual radon. This flushing can either be done on the morning of Day 2 or continuously overnight, depending on logistical preference.

Day 2

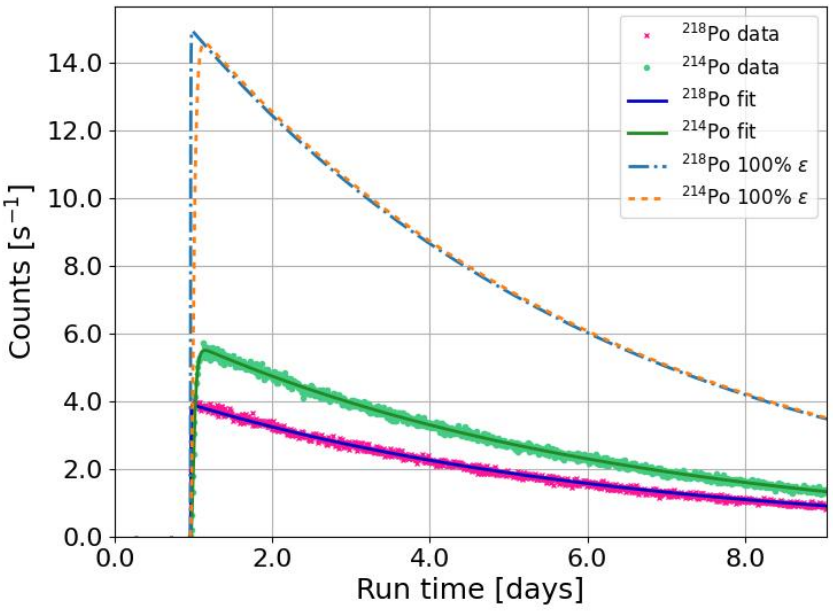
3. **Flush the source (if not done overnight)**:
   If the source was not flushed continuously overnight, carry out step 2.
4. **Allow source to emanate radon:**
   After flushing, seal the source and allow it to accumulate radon for approximately 70 minutes. This emanation period ensures that a known quantity of radon builds up in the source volume.
5. **Transfer radon to the detector ("spiking"):**
   Flush the emanated radon from the source into the detector by flowing nitrogen through the system at 4 LPM for 5 minutes. This process transfers the radon into the detector volume.
6. **Seal and measure:**
   After spiking, seal the detector and allow it to sit undisturbed for at least 7 days. This period ensures that the radon and its progeny reach secular equilibrium. Also, the detector is most sensitive after 7 days (see Section 7.3.3).

The Pylon source has an activity of $A_{-1} = 1595 \pm 64$ Bq. The theoretical number of ^{222}Rn atoms produced from this source over an emanation period $t_{em} = 70$ minutes is calculated using Equation (7.16), which amounts to $N_0 = (7.144 \pm 0.286 \text{ (stat. + syst.)}) \times 10^6$ atoms and $A_0 = 14.99 \pm 0.60$ (stat. + syst.) Bq.

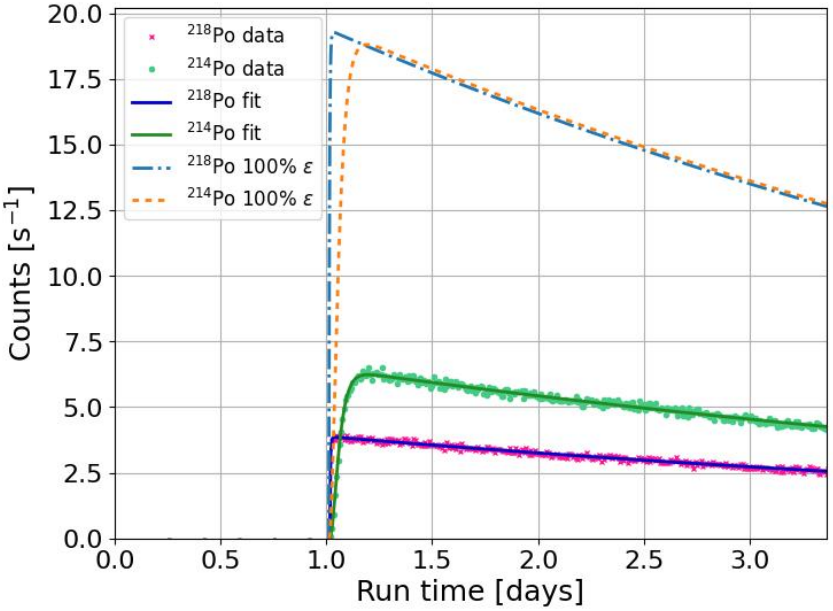
The background before the spike is measured and averaged so that a "flat" background can be subtracted from the polonium decay rates. The background-corrected decay rate data for ^{219}Po and ^{214}Po are fitted using Equations (7.11) and (7.14), respectively. The amplitudes of the fits give the measured ^{222}Rn activity since they peak when secular equilibrium with the ^{222}Rn decay curve is reached, as illustrated in Figure 7.5. The detector efficiency for each isotope is calculated by dividing these measured values with the theoretical values found using Equation (7.7).

It should be noted that the procedures outlined in this section, and in the remaining sections of this chapter, have only been performed on one of the detectors in the Boulby radon facility to date. This detector was first calibrated in 2022 and later in 2025. Figures 7.7a and 7.7b display the data from these calibration runs. The detector efficiencies, for ^{218}Po and ^{214}Po decay that are calculated from these fits, are summarised

in Table 7.2. The 2025 calibration yielded much lower efficiencies than expected[4]. The measurement was done after the installation of the concentration line and the relocation of the radon system from BUGS to the main hall in Boulby lab. Investigations are ongoing to determine the cause of this large decrease in efficiency.



(a)



(b)

Figure 7.7: The counts measured by the radon detectors during the 2022 (a) and 2025 (b) calibration runs. The 100% ϵ curves represent what the detector would theoretically measure with 100% efficiency. During the 2025 run, the emanation time was longer than during the 2022 run, hence the theoretical activity of ^{222}Rn is higher in (b). A standard statistical uncertainty has been assumed for all points and has not been plotted.

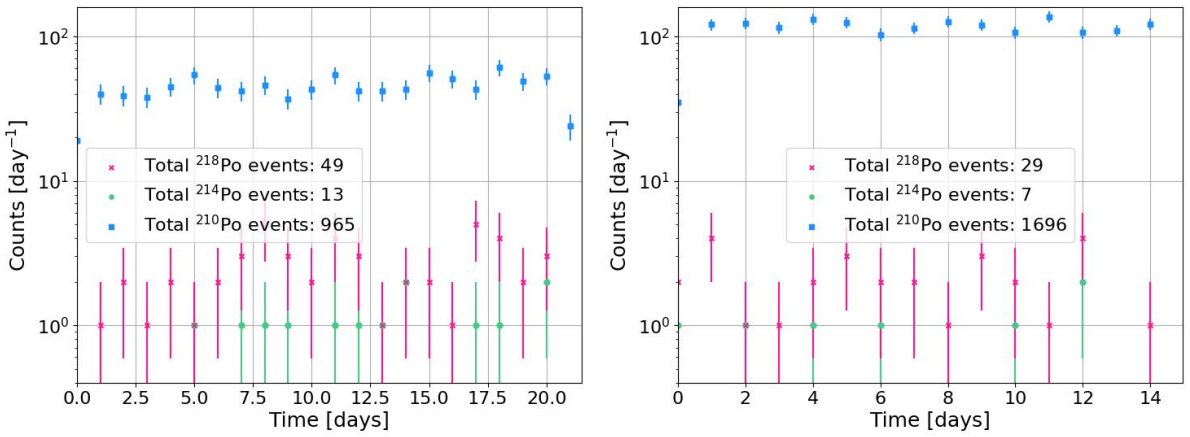
[4]The 2022 calibration results matched detector efficiencies found previously using the same type of detectors [130].

Table 7.2: Detector efficiencies for ^{218}Po and ^{214}Po. The uncertainties quoted here are a combination of the statistical and systematic uncertainties. The sources of uncertainty are summarised in Appendix H.

Isotope	**2022 ϵ [%]**	**2025 ϵ [%]**
^{218}Po	26.020 ± 1.042	20.005 ± 0.803
^{214}Po	37.741 ± 1.512	33.141 ± 1.327

7.3.2 Detector and chamber background measurements

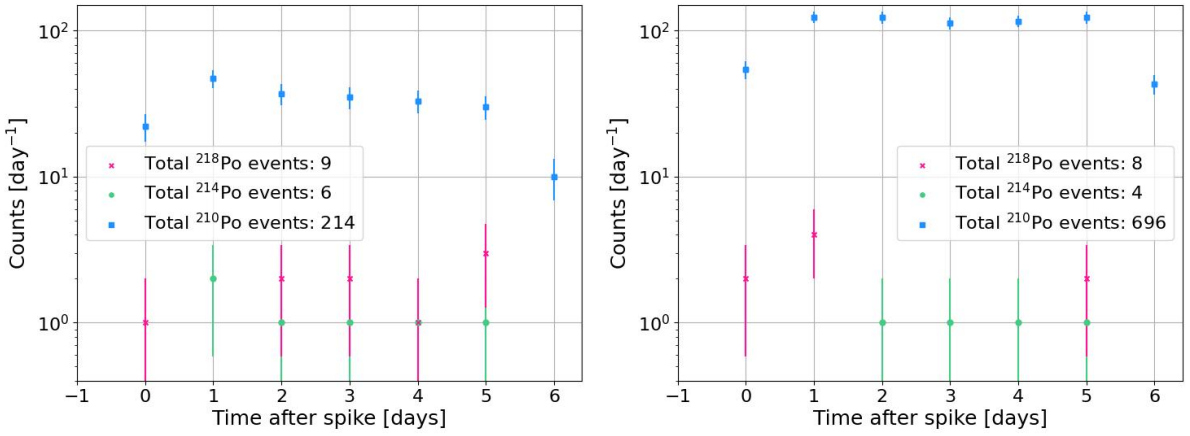
To ensure accurate radon emanation measurements and assess the detector's sensitivity, it is essential to characterise the intrinsic backgrounds of the emanation chambers and the detector. Therefore, the chambers and detectors should be periodically flushed and sealed (at standard pressure) for approximately 30 days. The detector background is determined by measuring the number of counts associated with each polonium decay during this period. The background contribution from the emanation chambers is assessed by flushing their contents into the detector after this period, following the procedure described in Section 7.3.4. The background activities from each emanation chamber are subtracted from subsequent sample measurements to correct for intrinsic background contributions. Figures 7.8a and 7.8b display the background counts of the detector taken in December 2022 and October 2023, respectively. The increase in ^{210}Po rates is evident during these 10 months: the average rate climbs from 46.0 counts per day in Figure 7.8a to 117.4 counts per day in Figure 7.8b.



(a) (b)

Figure 7.8: The intrinsic background counts from ^{218}Po, ^{214}Po and ^{210}Po decays of one of the radon detectors at Boulby. These measurements were taken 10 months apart in (a) December 2022 and (b) October 2023. The error bars represent Gaussian uncertainties. While this approximation becomes less accurate for low count rates, it remains sufficient for the conclusions drawn from these plots.

Figures 7.9a and 7.9b display the raw background counts of a 3 L chamber and a 5 L chamber, respectively. These chamber background activities and that of the detector are listed in Table 7.3.



(a) (b)

Figure 7.9: The intrinsic background counts from ^{218}Po, ^{214}Po and ^{210}Po decays of two of the emanation chambers at Boulby; their respective volumes are (a) 3 L and (b) 5 L. Error bars are the same as described in the Figure 7.8 caption.

Table 7.3: The intrinsic ^{222}Rn background activity for two different emanation chambers and one of the radon detectors in Boulby, calculated from ^{214}Po decay. Upper limits at 95% CL have been found for the emanation chamber backgrounds using Equation (6.8), while standard Poisson uncertainty is used for the detector background.

Component type	**Volume [L]**	**Time measured [days]**	**Activity [mBq]**
Emanation chamber	3	5.9	$< 3.8 \times 10^{-2}$
Emanation chamber	5	5.9	< 0.107
Detector	80	49.4	$(6.6 \pm 0.12) \times 10^{-2}$

Radon activity is primarily derived from the decay rate of ^{214}Po for two main reasons: first, the ^{218}Po decay spectrum exhibits some overlap with that of ^{210}Po, leading to an inflated count rate; second, the detection efficiency of ^{218}Po is reduced due to its higher susceptibility to neutralisation compared to ^{214}Po and other intermediate nuclides such as ^{214}Pb and ^{214}Bi. Additionally, these intermediate nuclides, including ^{214}Pb and ^{214}Bi produced from neutralised ^{218}Po that decayed away from the diode, may subsequently become ionised and drift toward the PIN diode, increasing the number of ^{214}Po decays detected there.

7.3.3 Minimum detectable activity

As mentioned at the beginning of this chapter, the ^{222}Rn background requirement for XLZD is strict at a specific activity of < 0.1 µBq/kg. To be able to determine whether the sensitivity of the measurements satisfies the requirement for XLZD activity with Boulby's radon facility, the minimum detectable activity (MDA) of the radon detectors needs to be calculated. The following derivation is based on the definition of MDA in Ref. [75]. If the number of events detected in time T is N, the net signal counts will be $S = N - B$, where B is the number of background counts in time T. To decide on whether or not S is truly a signal above background, a critical threshold, N_C, is defined

based on the background counts alone. The critical threshold is set at a measurement CL such that < 1 - CL is the probability that a signal seen above N_C is a false positive. Due to statistical fluctuations, the observed counts will follow a Poisson distribution centred around the expected number of counts. The probability of observing N events in time T with an expected average number of background counts, B, can be expressed as a Poisson distribution:

$$P(N|B) = \frac{B^N e^{-B}}{N!}. \tag{7.17}$$

If only background is present, N_C is found by summing the probabilities of observing every possible value of N until the sum is equal to or just above CL:

$$P(N \geq N_C|B) = 1 - \sum_{N=0}^{N_C} P(N|B) \leq 1 - \text{CL}. \tag{7.18}$$

Once this summation reaches the conditions of the inequality, N is set as N_C. For a real signal to be detectable above the background, with a CL of 95% for example, the minimum value of S is determined such that counts are seen above N_C at least 95% of the time:

$$P(N \leq N_C|B + S) \leq 1 - CL. \tag{7.19}$$

Since Poisson distributions describe discrete probabilities, this equation can be rewritten using the cumulative sum:

$$P(N \leq N_C|B + S) = \sum_{N=0}^{N_C - 1} P(N|B + S) \leq 1 - CL, \tag{7.20}$$

where S is increased until the probability reaches the required CL and the value of S when this occurs is set as the minimum signal, N_D. Equations (7.18) and (7.20) are plotted in Figure 7.10 to give a visual demonstration of these two distributions.

For $B > 30$, the distribution can be approximated as Gaussian, with expected value, $\mu = B$, and variance, $\sigma = \sqrt{B}$. The MDA is calculated from the minimum number of signal events that are detectable, N_D. Appendix I contains the derivation of N_D from the Gaussian approximations of Equations (7.18) and (7.20), which demonstrate that N_D can be expressed as:

$$N_D = 2E(E + \sqrt{2B}), \tag{7.21}$$

where

$$E = \text{erf}^{-1}(2\text{CL} - 1) \tag{7.22}$$

and erf is the Gauss error function.

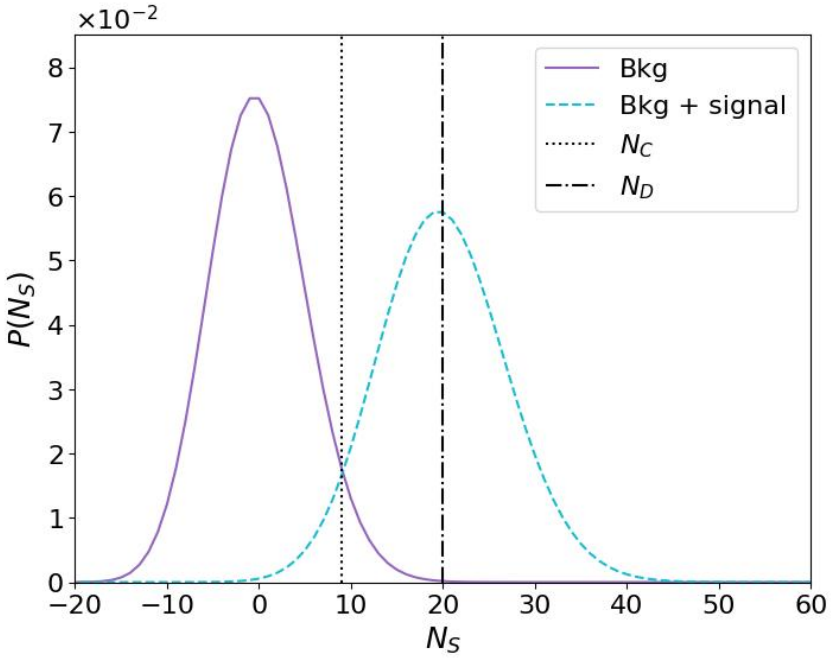


Figure 7.10: Two Poisson distributions of the net counts, N_S, expected for background only in purple (solid), and the net counts expected for background with activity present in turquoise (dashed). N_C marks the critical threshold at 95% CL and N_D is the minimum number of counts that a measurement needs to qualify as a signal above background at 95% CL The distributions were generated using the detector background in Table 7.3 (28 ^{214}Po decay events).

The MDA can therefore be calculated with the following equation:

$$\text{MDA} = \frac{N_D}{\epsilon\, t(1 - e^{-\lambda_0 t})}, \tag{7.23}$$

where t is total detection time and ϵ is the detector efficiency. Figure 7.11 displays the MDA curves generated at different CLs. The values for N_D and ϵ were taken from Tables 7.2 and 7.3 (2022 ϵ results). When t is short (run time $<$ 1 day), there is very little sensitivity since there has been little time for radon to decay. However, as t increases, the MDA falls rapidly before reaching a minimum at $\sim$7 days. After this point, the MDA begins to increase again as the rising number of background counts begins to take effect.

Table 7.4: Minimum MDA values for different confidence levels and the detection time taken for these minima to be reached, t_0.

CL [%]	**MDA [µBq]**	**t_0 [days]**
68	11.5	7.1
90	32.4	7.3
95	42.0	7.4

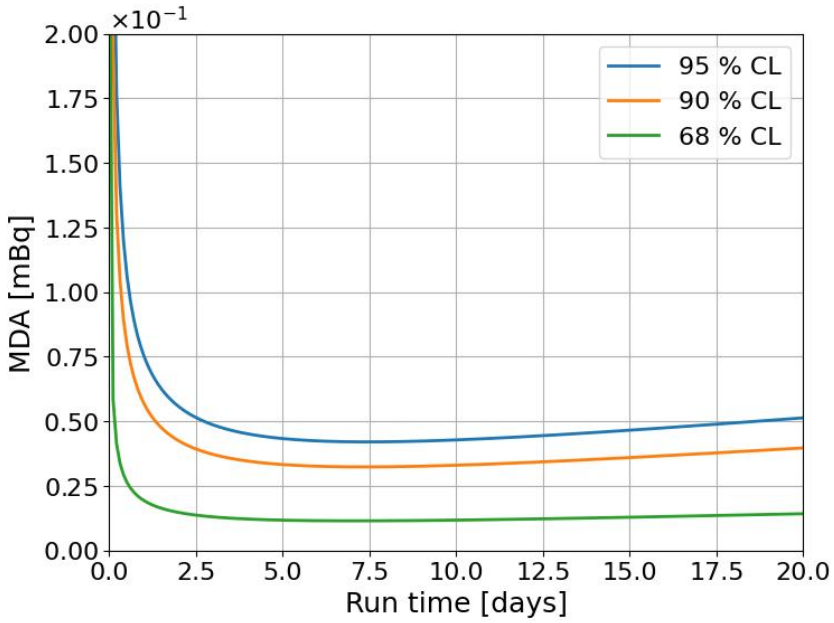


Figure 7.11: The minimum detectable activity of one of the radon detectors in Boulby for ^{214}Po decay, found at 95 %, 90 % and 68 % CLs. These curves were generated from 28 background counts detected over $\sim$ 50 days and a detector efficiency of 37.74 % (see Tables 7.2 and 7.3).

7.3.4 Sample measurement procedure

After a detector has been calibrated and the backgrounds of the chambers have been measured, the radon system is ready to measure samples. The procedure for measuring a sample's radon emanation activity is outlined below:

1. **Sample placement in emanation chamber:**
   Depending on the sample's size and shape, select an appropriate 5 L or 3 L emanation chamber. Place the sample inside and seal the chamber.
2. **Radon removal via nitrogen flushing:**
   Purge the chamber by flushing 10 CVs of high-purity nitrogen gas through the system. This removes any residual radon initially present in the chamber or introduced during sample placement.
3. **Emanation period:**
   Allow the sealed sample to emanate radon for, ideally, $>$ 30 days.
4. **Detector preparation:**
   Prepare the radon detector by flushing it with 10 DVs of nitrogen gas to eliminate any residual radon or moisture. After flushing, seal the detector and leave it overnight to allow ^{218}Po and ^{214}Po progeny to decay before introducing the sample.
5. **Spiking and measurement period:**
   Transfer the accumulated radon from the emanation chamber into the detector by flushing 10 CVs of nitrogen gas through the chamber and into the detector ("spiking"). Once the transfer is complete, seal the detector and leave it undisturbed for at least 7 days to allow radon and progeny to reach equilibrium and to enable sensitive alpha detection.

Overall, a reliable sample measurement takes ∼37 days. Hence, for the facility to continuously measure multiple samples within reasonable time frames, it is necessary to have multiple emanation chambers.

7.4 Radon emanation measurements

To complement the work done in Chapters 5 and 6, the radon emanation rate from polyhalite has been measured. The sample chosen was one of those that had previously been measured with Chaloner, one of the HPGe detectors in BUGS (see Section 6.1.2.1), and had contributed to the results of polyhalite radioactivity measurements presented in Section 6.2.2. The sample was enclosed in a grip-seal plastic bag to prevent dust from entering the emanation chambers and radon detector. As only a fraction of the emanated radon would permeate through the bag, another material needed to be measured beforehand, on its own and also inside a plastic bag. The fraction of radon diffusing through the plastic bag was determined by measuring a material known to have a sufficiently high radon activity, such that a slight reduction in activity would still produce a signal above the background activity of the detector and chamber. Mastic tape met this requirement and was measured on its own and inside the plastic bag. The data from these two measurements are displayed in Figure 7.12. The ratio of radon emanation from the mastic tape alone to radon emanation from mastic tape in the plastic bag was calculated to be 0.740 ± 0.042 (stat. + syst.).

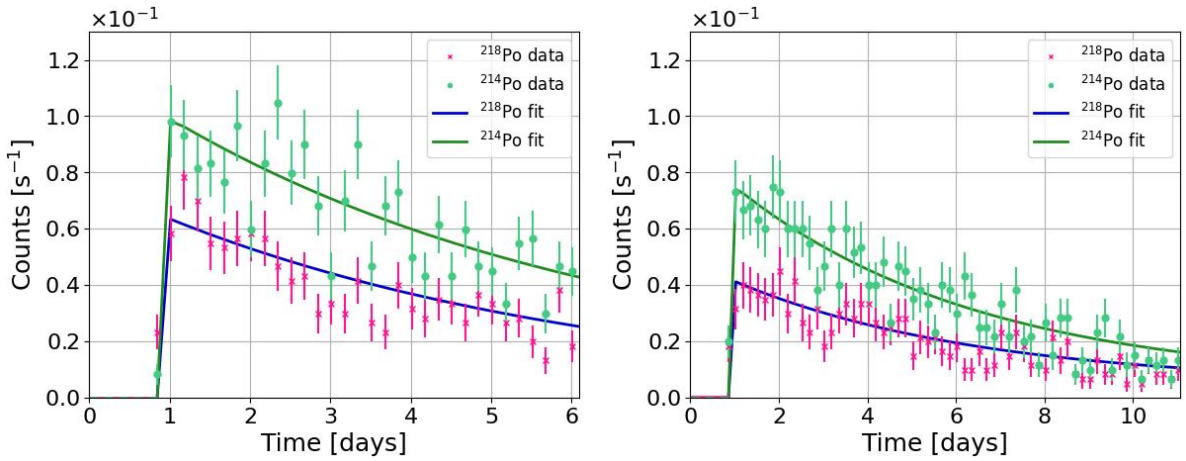


Figure 7.12: The detected event rate of the decaying isotopes, ^{218}Po and ^{214}Po, after radon from (a) mastic tape and (b) mastic tape inside a grip-seal plastic bag is flushed into the detector. Each data point is the mean rate of counts per second, sampled in 4-hour bins and the error bars are the same as described in the Figure 7.8 caption. The x-axis shows the total run time of the measurement, beginning from flushing the detector the day before the spike measurement takes place.

The detector background for each sample measurement was taken just before spiking the sample, to be subtracted later from the sample activity along with the emanation chamber background (see Figure 7.9). The plastic bag was emanated while empty as it provided an additional background to samples being measured inside it. The background

data from the plastic bag had a count rate that was not statistically significant, therefore an upper limit was found. After these preparatory measurements and background corrections, the polyhalite sample in a plastic bag was emanated and spiked onto the detector, the results of which are shown in Figure 7.13. Table 7.5 lists the activities of everything measured in order to calculate the radon activity from the polyhalite sample.

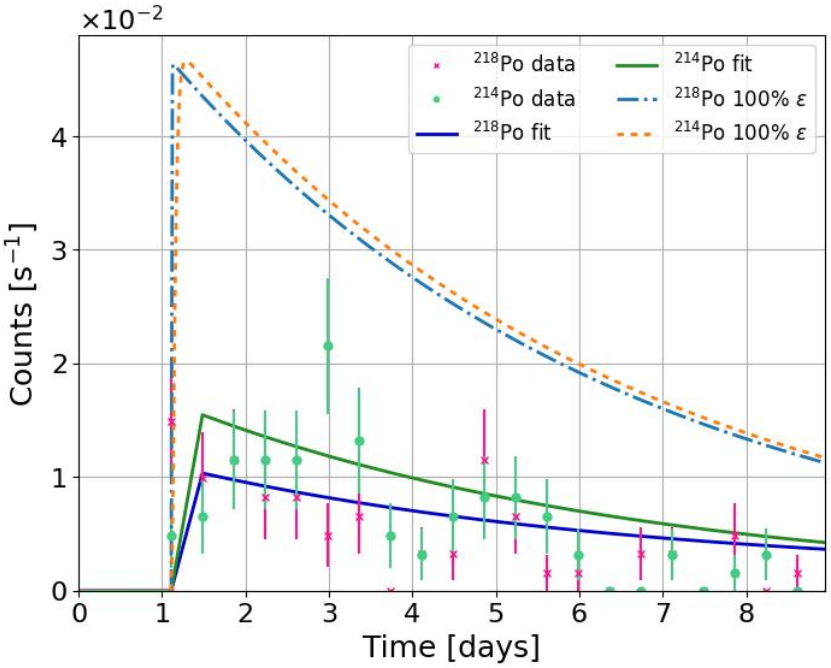


Figure 7.13: ^{218}Po and ^{214}Po decay rate from a sample of polyhalite shown with their 100% efficiency curves reconstructed from the fitted lines. The data points are the average counts per second within a period of 9 hours and the error bars are the same as described in the Figure 7.8 caption.

Table 7.5: Radon emanation measurements of materials that were required to determine the emanation rate from a polyhalite sample in a plastic bag. Activities are given for the whole sample. The corrected polyhalite activity, quoted in the final row, was obtained by measuring the activity of polyhalite enclosed in a plastic bag, subtracting the background activity from the plastic bag alone (this was also done with the Mastic tape in bag sample, row 2), and then dividing by the ratio of the activities measured in rows 2 and 3. This ratio accounts for the attenuation of radon through the bag. See Section 7.4 text for the specific activity of polyhalite. The uncertainties quoted are a combination of statistical uncertainties from the fit line and systematic uncertainties outlined in Appendix H.

Sample	**Activity [mBq]**
Empty plastic bag (PB)	< 0.081
Mastic tape in bag - PB	9.126 ± 0.369
Mastic tape	12.329 ± 0.494
Polyhalite in bag - PB	0.807 ± 0.042
Polyhalite (corrected)	1.090 ± 0.084

The polyhalite sample has a radius of 2.5 ± 0.1 cm and a length of 15.0 ± 0.5 cm, hence, a surface area of 278.03 ± 14.93 cm^2. Using the total measured activity of 1.090 ± 0.084 (stat. + syst.) mBq, the surface emanation activity of Boulby polyhalite was found to be 3.92 ± 0.37 (stat. + syst.) µBq cm^{-2}. This activity is not directly comparable with that measured using an HPGe detector (see Section 6.2.2) because the gamma-ray measurement reflects the total ^{226}Ra activity in the polyhalite sample, whereas the radon detector only measures the fraction of ^{222}Rn atoms that escape from the material. Emanation from the surface depends on the sample's physical characteristics, such as grain structure and porosity, thus, the two results represent different physical quantities.

7.5 Scope for future work

7.5.1 Titanium disc radon emanation study

There is an ongoing collaborative project between Boulby and the Cold Radon Emanation Facility (CREF), which resides at the Rutherford Appleton Laboratory on Harwell Campus. Achieving the required radon background for XLZD presents a significant challenge, with a target of 0.1 µBq/kg in the active region. The goal of this specific project is to determine the radon emanation from titanium discs before and after electroplating high-purity copper onto one of the flat surfaces of each disc. The titanium is a sample of the material that could be used to construct the xenon cryostat. Coating the inner surface with high-purity copper will significantly reduce the amount of radon recoiling into the liquid xenon target from ^{226}Ra decays in the titanium. 13 discs have been measured so far. Two were measured at Boulby, and the remaining eleven at CREF. They each have a surface area of 365.4 cm^2 and a mass of ∼715 g. All discs were cleaned in an ultrasonic ethanol bath. Initial results from the two sites exhibit a factor of ∼20 discrepancy. During the emanation measurement, a copper gasket was used to separate and support the titanium discs within a 3 L chamber, as can be seen in Figure 7.14. A separate

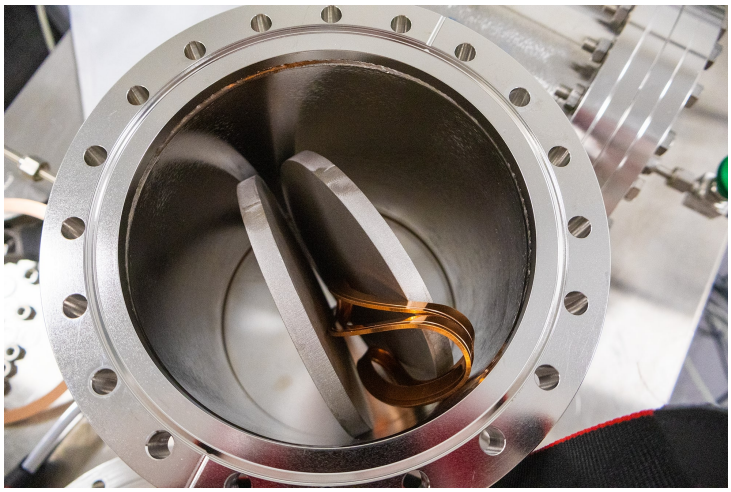


Figure 7.14: Titanium discs with a copper gasket support in a 3 L emanation chamber.

measurement of an identical copper gasket, assumed to be of high-purity and therefore low-background, revealed a higher-than-expected activity of 5.52 ± 0.22 mBq. This exceeds the disc-only activity (after subtracting the gasket contribution) of 3.19 ± 0.41 mBq.

The decay rates for these measurements are shown in Figures 7.15a and 7.15b. Since the exact gasket measured with the discs was not characterised independently, and the assumption of negligible activity no longer holds, the corrected disc activity is unreliable. To resolve this, the discs will be remeasured using plastic bags (with known negligible backgrounds as quoted in Table 7.5) as supports. The original copper gasket used in the first disc measurement will also be measured on its own, to retrospectively investigate the initial results.

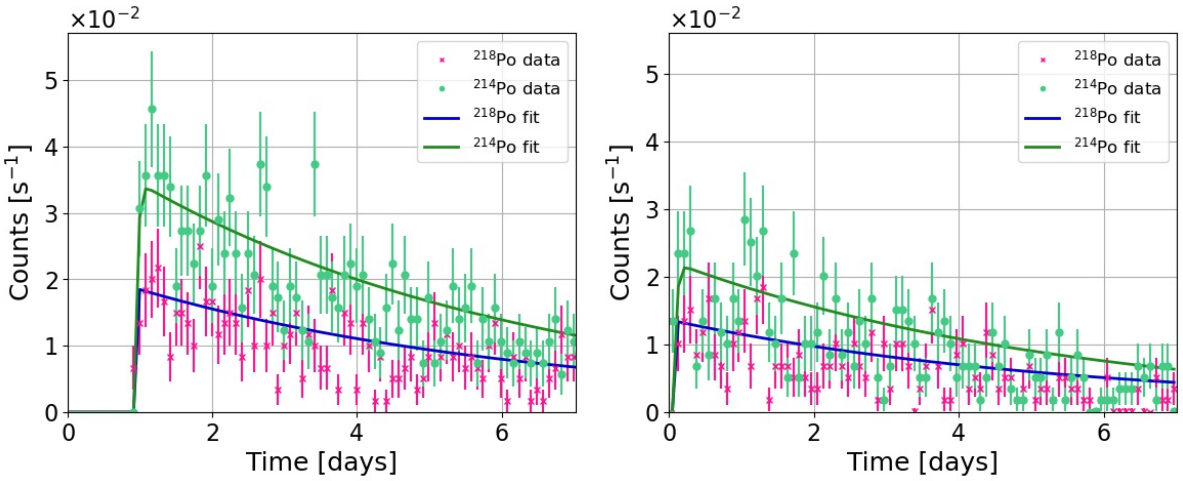


Figure 7.15: ^{218}Po and ^{214}Po decay rate from (a) two titanium discs and one copper gasket, and (b) a single copper gasket. The data points are the average counts per second within a period of 2 hours and the error bars are the same as described in the Figure 7.8 caption.

7.5.2 Facility progression

The Boulby radon measurement facility has demonstrated excellent sensitivity to low levels of radon, with an MDA of 42.0 µBq at 95 % CL after 7.4 days of measurement. To advance the system to full operational status, several steps are required. First, the second detector must be calibrated (along with the recalibration of the first detector), and its background activity measured to determine the corresponding MDA. Additionally, the background of the concentration line must be characterised. Second, the data acquisition parameters of the CAEN digitiser require optimisation, and the analysis code that is currently tailored to the Raspberry Pi data output must be adapted to interface with the digitiser's output format. Finally, the radon trap in the concentration line, currently bypassed, must be assembled. A heating element for releasing trapped radon into the detectors also needs to be constructed and installed to enable full utilisation of the concentration line. Building upon this, there is potential to enhance the efficiency of the radon emanation system by operating the concentration line and detectors under vacuum, investigating the electronic dead time during calibration, and installing additional PIN diodes at the top of the electronics section within each detector. These enhancements are expected to lower the MDA further and improve overall detection sensitivity.

Chapter 8

Muon flux measurements with LZ

A proportion of this chapter is under consideration for publication in *Astroparticle Physics*.

Rock above deep underground laboratories shields rare-event detectors, such as the LZ experiment [42], from atmospheric cosmic-ray muons. However, a fraction of high-energy muons penetrate the Earth sufficiently to reach these laboratories. Muon-related backgrounds can impact high-sensitivity experiments through various processes outlined in Section 3.3. A comprehensive simulation campaign for LZ demonstrated that neutron backgrounds from cosmic-ray muons are negligible, on account of the experiment's strong background rejection capabilities, including veto detectors [86]. However, this may not hold for larger detectors proposed or under construction at SURF, such as DUNE [141]. As a result, precise muon measurements are necessary for a broader range of experiments at SURF. This chapter describes the LZ experiment and how the data taken by LZ was used to measure the muon flux through the Davis Campus of SURF, where LZ is situated. Data collected during about 366 days of live time of detector operation was compared to the results of a simulation, which has a muon model embedded into it based on accurate muon transport through rock.

8.1 The LUX-ZEPLIN experiment

A complete description of the LZ experiment is given in Refs. [96, 42]. The detector design and experimental strategy are primarily derived from the LUX and ZEPLIN-III experiments [84, 107]. Justification for using noble element detectors such as these to detect WIMPs is discussed in Section 2.3.3. The primary science goal of LZ is the direct detection of WIMP dark matter in a wide range of WIMP masses, using dual-phase

liquid xenon technology. LZ is projected to be sensitive up to an SI WIMP-nucleon cross-section of 1.5×10^{-48} cm^{-2} for a WIMP mass of 40 GeV/c^2 (90 % C.L). To date, LZ has set world-leading constraints on SI cross-sections, achieving a limit of 2.1×10^{-48} cm^2 at the 90 % CL at a mass of 36 GeV/c^2 from 280 days of active WIMP search [80]. The time during which LZ was live and operating was split into two data-taking campaigns: WIMP search 2022 (WS2022) and WIMP search 2024 (WS2024). The first run, WS2022, was shorter to verify that the detector and all its components were operating as expected, and also to produce its first dark matter search result. After this commissioning phase, the experiment transitioned into a longer data-taking campaign, WS2024.

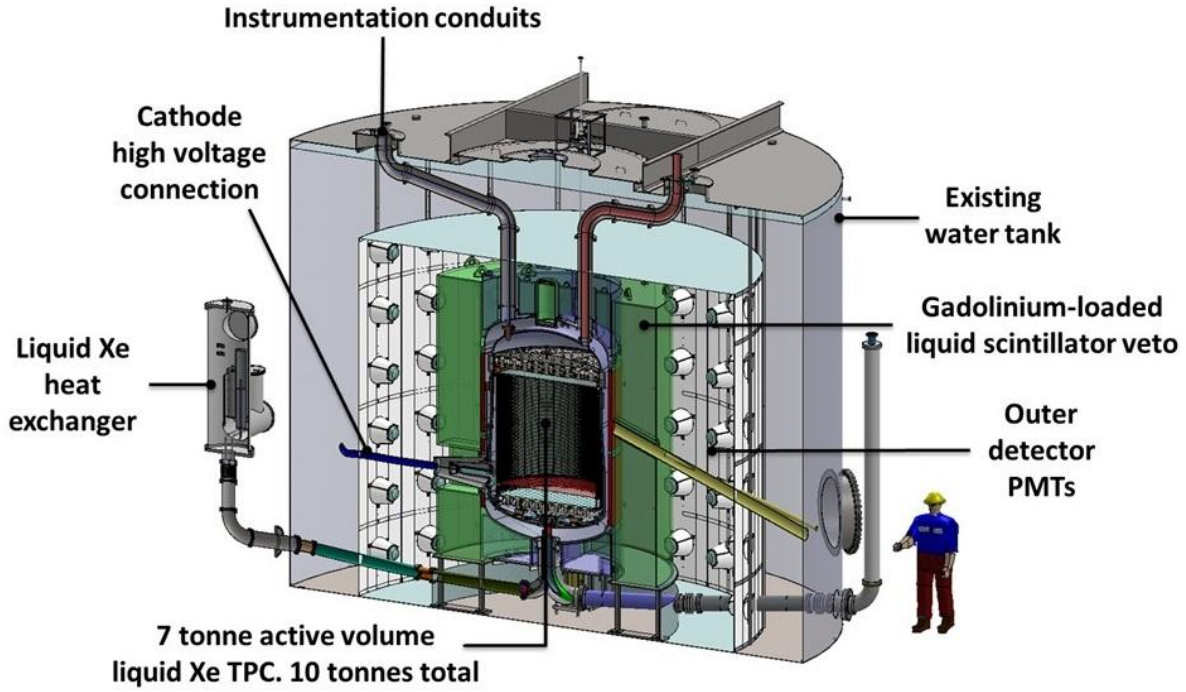
8.1.1 Detector overview

The detector features a double-walled, vacuum cryostat filled with 10 tonnes of LXe, with 7 tonnes being the active target mass that acts as a TPC. Of this active mass, the centre 5.5 tonnes make up the FV, meaning that events occurring in LXe near the surfaces of the TPC are ignored due to backgrounds from alpha and beta decays in the TPC walls and wires, including dust in minute quantities. The TPC is surrounded by a layer of LXe known as the "Xe Skin" detector. Both the TPC and Skin are housed within the cryostat vessel, with their LXe cooled by liquid nitrogen thermosyphons. Around the cryostat is a layer filled with 17 tonnes of gadolinium-loaded liquid scintillator called the outer detector (OD). The Skin and the OD are used primarily as gamma-ray and neutron vetoes, although the Skin also acts as a dielectric stand-off between the high-voltage field cage and the grounded cryostat wall. In all three volumes, signals are detected by Hamamatsu photomultiplier tubes (PMTs). There are two arrays of 3-inch PMTs in the TPC, totalling 494; 93 1-inch and 38 2-inch PMTs in the Skin; and 120 PMTs in the OD. A diagram of the full detector can be seen in Figure 8.1a, and a more detailed view of the TPC and Skin is displayed in Figure 8.1b.

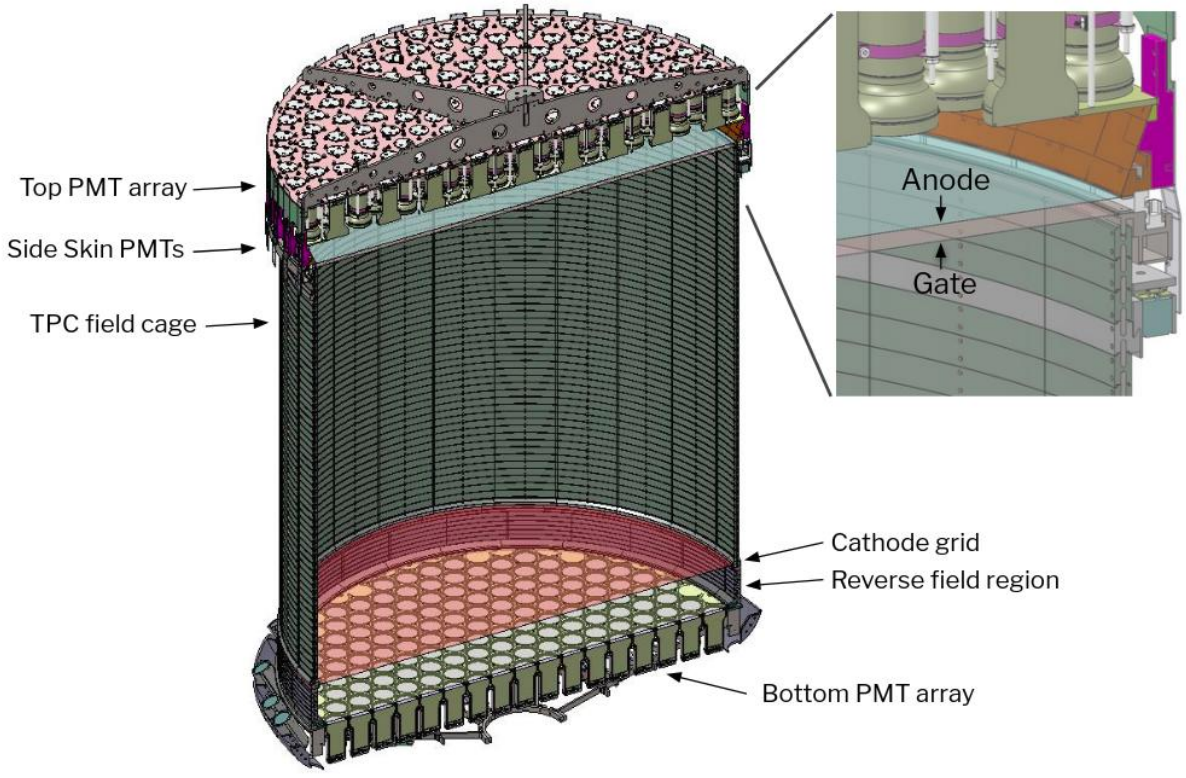
The active mass of LXe is constrained in the TPC field cage, which is clad in PTFE reflector panels. There is a drift field established in the active region from the cathode grid at the base to the gate grid at the top, just below the liquid surface. This amounts to a vertical drift region of 145.6 cm. The drift field for WS2022 was 193 V/cm, but this was decreased to 97 V/cm for WS2024 to lessen "dead time" caused by spurious electron and photon emissions. Below the cathode is the RFR where the potential voltage is graded from the cathode to the bottom PMT array over a distance of 13.75 cm. Above the gate grid is a layer called the electroluminescence region, which is 1.3 cm between the gate and anode grids, with the top 0.8 cm of that distance filled with GXe. A strong electric field of 3.4 kV/cm is applied in the gaseous region to extract electrons from the liquid phase.

8.1.2 Signal detection

As previously discussed in Section 2.3.3, ionisation of xenon from interactions in the TPC produces two signals: prompt scintillation from xenon excimer decay, producing VUV photons (S1 signal), and then secondary scintillation from electrons that have drifted to the top of the liquid xenon into the electroluminescence region by the applied electric field (S2 signal). The delay between S1 and S2 signals, or "drift time", gives the z-coordinate



(a)



(b)

Figure 8.1: (a) A schematic of the LZ detector's main components and subsystems, including the outer detector (Gd-loaded liquid scintillator) and the central TPC. (b) A cross-section of the TPC in more detail. The 7-tonne active mass of the detector lies between the cathode and gate electrodes, within the field cage. The gaseous xenon phase lies between the gate and anode electrodes. (a) is taken and (b) is adapted from Ref. [96].

of the interaction and the spatial distribution of the S2 signal provides the x- and y-coordinates of the interaction. From the energy partition between the S1 and S2 signals, it can be determined whether an interaction is an NR or an ER. S1 and S2 signals are corrected for position, creating the variables S1c and S2c. This adjustment is carried out because there is a significant variation of light collection throughout the detector. S1 light collection is higher near the lower region of the TPC as the bottom PMT array records more of the S1 signal than the top PMT array. S2 signals are less likely to reach the electroluminescence region if they are from an interaction in the lower region, owing to a longer drift time and therefore, a higher chance of the electrons interacting with any electronegative impurities in the LXe such as oxygen or water. S1c is the equivalent scintillation signal from an event in the centre of the FV, and S2c corresponds to an equivalent event at the GXe boundary in the centre of the $x-y$ plane and just above the gate grid [142]. Figure 8.2 shows the separation of ER and NR events into bands by looking at log10(S2c) versus S1c signals, allowing ERs and NRs to be distinguished.

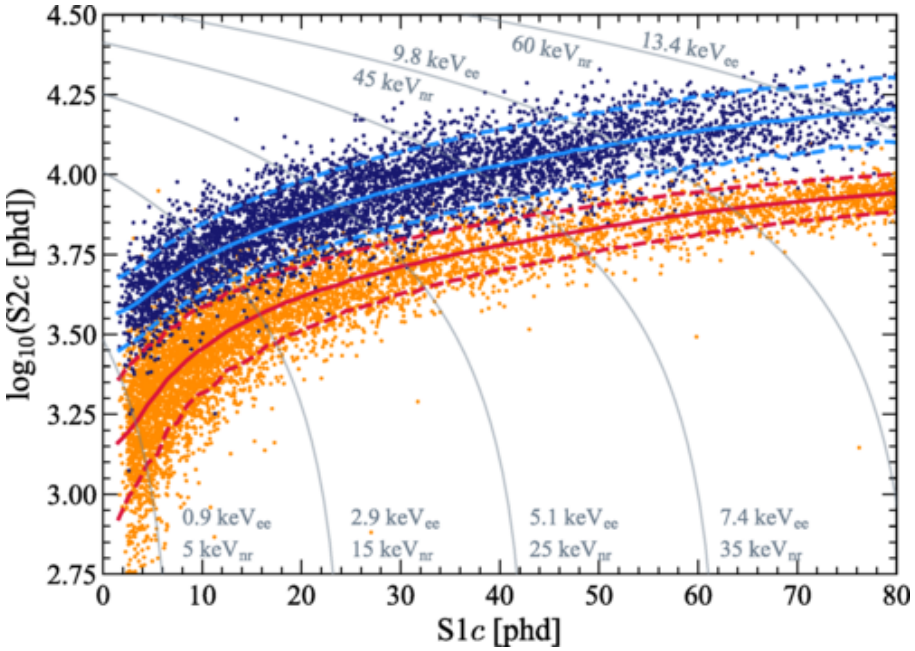


Figure 8.2: A scatter plot displaying the S2c and S1c signals from calibration events, in units of number of photons detected (phd). The dark blue points (higher band) are ERs from a tritium source (decay via β^-) and the orange points (lower band) are NRs from a deuterium-deuterium neutron source. Solid lines represent the median and dotted lines represent the 10th and 90th percentiles of the distributions. The grey lines are contours of constant energy. From Ref. [79].

LXe has high scintillation (light) and ionisation (charge) yields at low recoil energies ($\mathcal{O}$ keV) [143]. The light and charge yields represent, respectively, the number of photons, n_γ, or electrons, n_e, emitted after a particle interaction per keV of the energy transferred, E. The combined energy from ionisation and scintillation can be expressed as follows [94]:

$$E = W(n_\gamma + n_e). \tag{8.1}$$

Where W is the average energy required to produce either an excited xenon atom (which leads to scintillation) or an ionised xenon atom (which produces a free electron). The

yields are related to S1 and S2 signals by the following equations:

$$\mathrm{S1} = g_1 \times n_\gamma, \tag{8.2}$$

$$\mathrm{S2} = g_2 \times n_e, \tag{8.3}$$

where g_1 is the average number of photons detected per photon emitted; it is a combination of the quantum efficiency of the PMTs and the light collection efficiency. g_2 is the average number of ionisation electrons detected per electron emitted. Equation (8.1) can be rewritten as [142]:

$$E = \frac{W}{L} \cdot \left(\frac{\mathrm{S1}}{g1} + \frac{\mathrm{S2}}{g2} \right), \tag{8.4}$$

where L is a quenching factor. E is calculated differently for ERs and NRs because the fraction of energy transferred to atomic motion is significant for NRs and not for ERs. This difference is accounted for by L, which is assumed to be 1 for ERs, but defined by the Lindhard model for NRs [144, 145]. Therefore, the same amount of energy deposited by an ER and an NR will produce different light and ionisation signals in a detector. Energy deposited by ERs is often written in units of keV_{ee} ("electronic equivalent") as nearly all energy is visible. For NRs, however, the deposited energy may be given either in keV_{nr}, representing the true recoil energy, or in keV_{ee} after applying a quenching factor to account for the lower ionisation and scintillation yields compared to ERs.

8.1.3 Veto detectors

A WIMP interaction within the detector is expected to produce a single NR event. Consequently, a substantial fraction of background signals in the WIMP energy range ($\sim 5 - 50$ $\mathrm{keV}_{\mathrm{nr}}$) can be rejected if the interacting particle is observed to scatter multiple times. Since these interactions may occur outside the active volume, veto detectors are essential for identifying related signals originating from interactions within the TPC. Neutrons pose a particular challenge, as they interact with xenon nuclei, producing S1 and S2 signals that resemble WIMP-induced NRs. However, unlike WIMPs, neutrons can undergo multiple scatters, allowing them to be identified and rejected as background events. In some cases, a neutron may not undergo multiple interactions within the TPC itself but instead, escape and scatter in surrounding detector materials. By instrumenting the OD, it is possible to tag neutrons that interact in these regions within a defined time window, enabling their correlation with an NR in the TPC. High-energy ($\sim$ MeV) gamma-rays also contribute to the background for WIMP searches and $0\nu\beta\beta$ decay searches. Multiple interactions from these gamma-ray backgrounds can be similarly vetoed using the Skin and the OD.

The OD contains liquid scintillator (LS) that is loaded with gadolinium (GdLS) to increase the probability of tagging neutrons from the TPC. Neutrons are able to be captured on hydrogen nuclei in pure LS causing a photon with energy 2.2 MeV to be emitted and detected by the OD PMTs. However, ^{155}Gd and ^{157}Gd have such high thermal neutron cross-sections, that having a concentration of just 0.1 % by mass of natural gadolinium in the GdLS significantly decreases the average time taken for neutron capture to occur. When a neutron is captured on gadolinium, there is a cascade of

gamma-rays emitted as the nucleus de-excites, hence, a spectrum is observed, ending around 8 MeV. To optimise the neutron tagging efficiency while minimising the detector's dead time, a time window of 500 µs was applied. A detection threshold corresponding to approximately 200 keV was also applied [42, 86]. This threshold is defined by the number of detected photoelectrons and coincidences between PMTs. The dominant background driving this threshold arises from the alpha decay of ^{152}Gd, a naturally occurring isotope in gadolinium. The alpha particle has an energy of 2.2 MeV, but the quenching of scintillation signals results in the alpha mimicking an ER of only 150 - 170 keV.

The Skin contains ∼2 tonnes of LXe and lies just outside the TPC field cage, acting primarily as a gamma-ray veto. It is instrumented with PMTs and serves primarily as a veto for gamma-ray interactions originating from external backgrounds. Due to the high density and stopping power of LXe, gamma-rays are likely to interact within the Skin region. Although neutrons may also scatter in the Skin, the resulting NRs typically deposit too little visible energy to be detected, due to quenching and the Skin's relatively high energy threshold.

8.1.4 LZ software

The process of collecting data is as follows: signals from PMTs are passed to low-noise analogue electronics which amplify, shape and convert the readout charge into a voltage. These voltages are sampled every 10 ns producing a waveform with an area proportional to the number of photons detected. If the PMT signal averages above a certain "pulse-only digitisation" (POD) voltage threshold over 32 samples the DAQ is triggered, and the waveform is digitised and saved [146]. An LZ event comprises these waveforms, and an event window contains waveforms recorded during 2 ms pre-trigger and 2.5 ms post-trigger, with the triggered pulses being at $t = 0$. The electronics provide high-gain (HG) and low-gain (LG) outputs for all PMTs.

The LZ analysis package (LZap) [147], an event reconstruction tool built on the Gaudi framework [148], processes the PMT waveforms and classifies each pulse as one of the following: S1, S2, single electron (SE), single photoelectron (SPE), multiple photoelectron (MPE) and other. LZap produces many "reduced quantities" (RQs), which are analysis-ready characteristics of LZ events and the pulses within. RQs can be pulse level (amplitude, area etc.), interaction level (eg. position), or event level (pertains to the entire event), depending on which variables need to be analysed. Figure 8.3 depicts the pulses typically seen in different types of events.

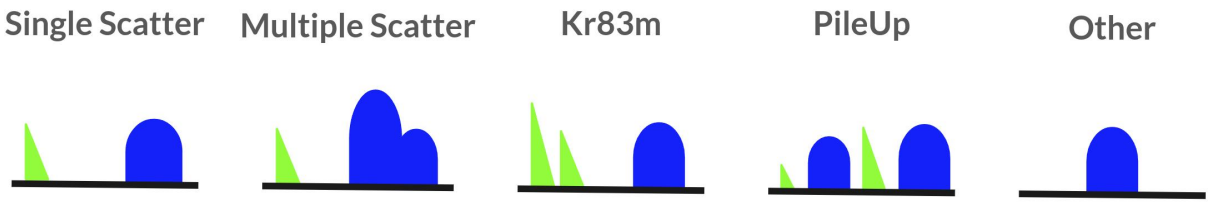


Figure 8.3: Categories of events in the TPC classified by LZap. The green, triangular pulses are "S1-like" and blue, rounded pulses are "S2-like". ^{83m}Kr is a short-lived isotope used to perform a spatially uniform calibration of the detector response [149]. From Ref. [147].

LZ's offline event viewer is a useful tool for visualising raw waveforms categorised by LZap; it displays the pulse amplitude (defined as number of photons detected per nanosecond, [phd/ns]) of each pulse in an event window, separated into the different detector volumes (TPC, Skin and OD), and has a PMT map indicating where pulses came from. Figure 8.4 shows a typical multiple-scattering event as seen with the offline event viewer. The analysis framework used by LZ is called ALPACA, which was written in C++ to analyse RQs produced by LZap. ALPACA allows the user to: skim data files - creating specific ROOT TTrees and speeding up analysis; write analysis modules that loop over events; and create and save ROOT histograms.

A simulation campaign was performed alongside radioactivity measurements to ensure the projected sensitivity of LZ. A full description of the simulation software is in Ref. [86]. The simulations allow LZ to model the background to WIMPs (and other physics such as $0\nu\beta\beta$ decay), model the detector's response to interactions, and estimate the background rejection efficiency. BACCARAT (Basically A Component-Centric Analog Response to AnyThing) is a GEANT4-based [85] simulation framework used by LZ, developed from LUXSim - a simulation framework for LUX [150]. BACCARAT is responsible for particle transport and detector response from particle interactions. There are two simulation chains: one that records only energy deposits (fast model chain) and one that also includes optical simulations of light and charge, and records PMT light collection (full model chain).

The output of the full model chain is passed to the DER (Detector Electronics Response), which simulates LZ's analog electronics and signal response. The DER takes PMT input from BACCARAT's recorded photon hits, enabling the PMT signals to be translated into waveforms that can be processed by LZap before further analysis. The fast model chain can be used to generate a large amount of statistics and, if required, the output can be passed to NEST (Noble Element Simulation Technique) [151] to generate S1 and S2 signals. NEST is a simulation package that converts energy depositions in LXe and GXe into observable signals from emitted light and charge. LZLAMA (LZ Light Analysis Monte Carlo Application) is a parametric detector response model that can process BACCARAT energy depositions (using NEST), producing observed quantities. A simplified flow diagram of both chains is shown in Figure 8.5.

8.2 Muon flux measurements

8.2.1 The muon model

Cosmic-rays and muon flux as a background to underground detectors are discussed in Section 3.3. Two Monte-Carlo codes are used to generate muons for the LZ muon simulations: MUSIC (MUon SImulation Code) and MUSUN (MUon Simulations UNderground) [152, 153]; the latter is adapted here for the LZ experiment. MUSIC, given initial parameters of energy, position and direction cosines, transports muons from the Earth's surface through various thicknesses of rock. In this particular application, MUSIC propagates muons with energies ranging from 10^2 GeV to 10^7 GeV and stores their energy spectra at distances of $100 - 15000$ m w. e. (metres of water equivalent). The rock composition used in this study is based on Ref. [154, 155]. Measurements of multiple

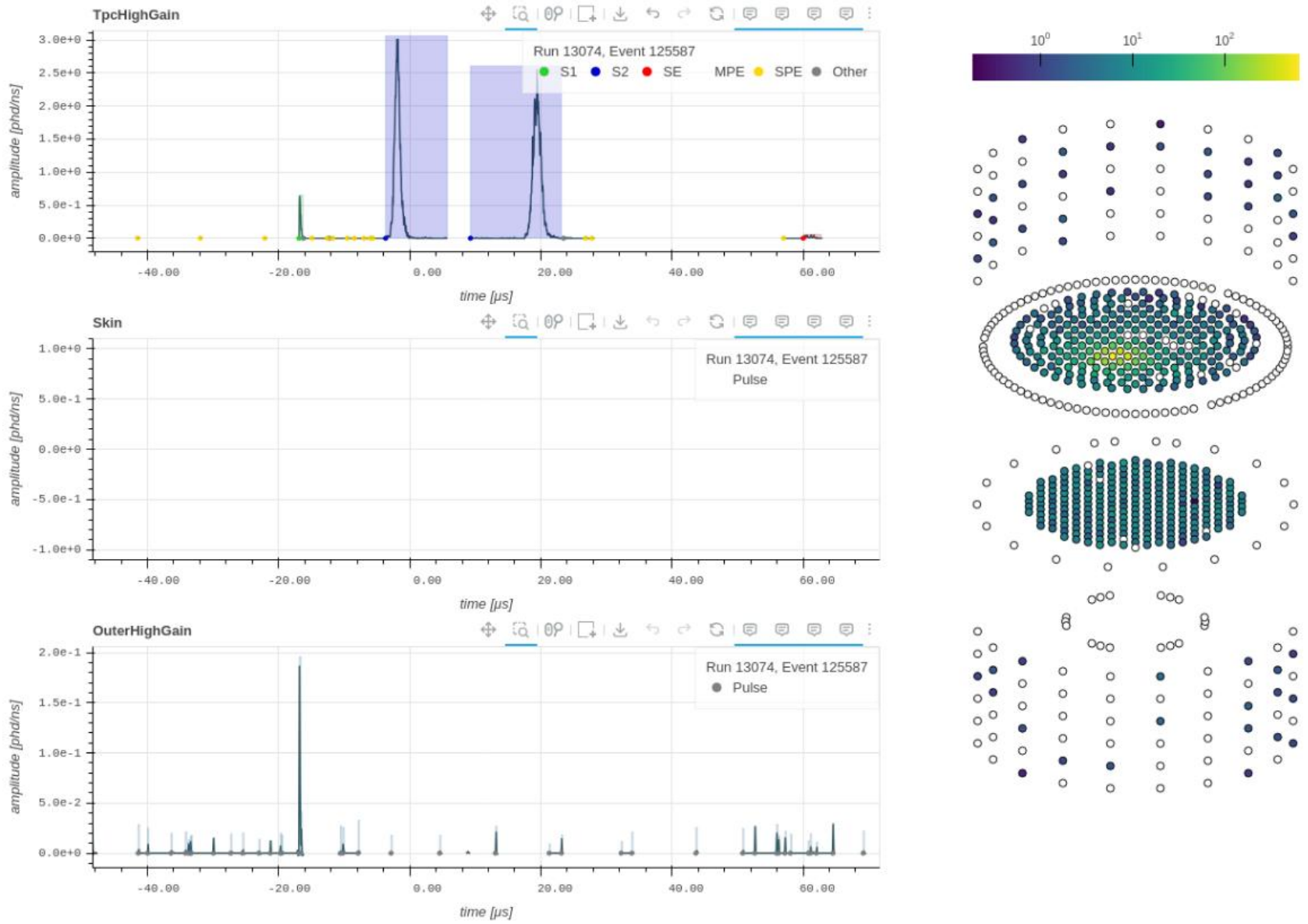


Figure 8.4: A screenshot of the offline event viewer displaying an event from a calibration run using a tritium source. The TPC high-gain plot at the top shows the amplitude as a function of time. An S1 and two S2 pulses are visible, making the event a multiple scatter event. Middle and bottom panels show the amplitudes of the signals in the Skin and the OD, respectively, as a function of time within the time window for the event. There is a PMT map on the right-hand side with an applied colour map according to the number density of signals within the event as registered by the PMTs. The outer cylinder split between the top and bottom of the map represents the OD PMTs. The 3 rings of PMTs represent the Skin PMTs. The circles filled with PMTs represent the top and bottom TPC arrays.

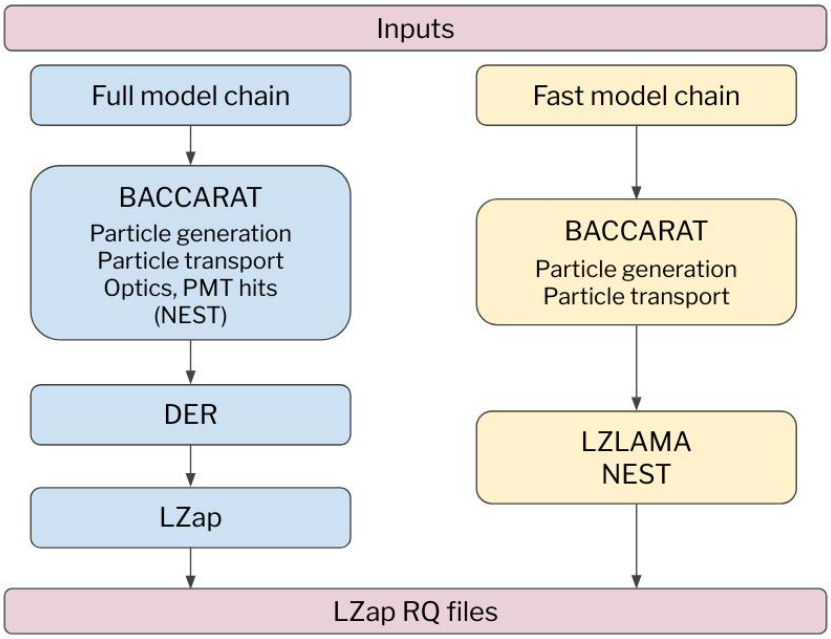


Figure 8.5: A simplified schematic of the two BACCARAT simulation chains. The main difference is the simulation of optical processes, PMT signal output and DER in the full chain.

rock samples have been reported [154, 155], from which the average elemental parameters were determined as $< Z > = 12.09$ and $< A > = 24.17$. In the MUSIC simulation, an average rock density of 2.70 g cm^{-3} was assumed [155]. However, alternative measurements [156], including muon flux data obtained from the Majorana Demonstrator veto system, indicate that the actual density may be larger, 2.8 - 2.9 g cm^{-3} [157].

The outputs from MUSIC are taken by MUSUN and convolved with the local surface profile above the cavern, muon energy spectra and angular distributions at the surface of the Earth to create a muon energy spectrum and angular distribution specific to SURF. The differential muon intensity underground is calculated using the following equation [158]:

$$\frac{dI_\mu}{dE_\mu d\Omega}(E_\mu, \theta, \phi) = \int_0^\infty P(E_\mu, X(\theta, \phi), E_{\mu 0}) \frac{dI_{\mu 0}}{dE_{\mu 0} d\Omega}(E_{\mu 0}, \theta^*) dE_{\mu 0}, \quad (8.5)$$

where E_μ is the energy of a muon at slant depth X and $E_{\mu 0}$ is the energy of a muon on the surface. Similarly, θ is the zenith angle at X and θ^* is the zenith angle at the surface. $\frac{dI_{\mu 0}}{dE_{\mu 0} d\Omega}(E_{\mu 0}, \theta^*)$ is the muon intensity at the surface and $P(E_\mu, X(\theta, \phi), E_{\mu 0})$ is the probability that a muon of energy $E_{\mu 0}$ has energy E_μ at X. ϕ is the azimuthal angle.

The distance from the underground laboratory and the Earth's surface for each azimuth and zenith angle has been obtained from the surface map and the position of the laboratory in the global coordinate system [159]. The differential muon energy spectrum at the surface is calculated using the modified Gaisser parameterisation. This amounts to Equation (3.5) modified for the curvature of the Earth to include large zenith angles [160], the fraction of muon decay and the fraction of prompt muons [158]:

$$\frac{dI_{\mu 0}}{dE_{\mu 0}d\Omega}(E_{\mu 0},\theta^*) = 0.14A(E_{\mu 0}+\Delta E_{\mu 0})^{-\gamma}p_d\times$$
$$\left(\frac{1}{1+\frac{1.1(E_{\mu 0}+\Delta E_{\mu 0})\cos\theta^{**}}{115\,\mathrm{GeV}}}+\frac{0.054}{1+\frac{1.1(E_{\mu 0}+\Delta E_{\mu 0})\cos\theta^{**}}{850\,\mathrm{GeV}}}+R_C\right), \quad (8.6)$$

where $\theta^{**}=\sqrt{1-0.99(1-\cos^2\theta^*)}$ is the zenith angle at the altitude where the muons are produced, accounting for Earth's curvature; $\Delta E_{\mu 0}$ is an energy loss correction, accounting for energy lost by muons travelling through the atmosphere; $R_C = 10^{-4}$ is the ratio of prompt muons (produced from heavy meson decays) to pions; p_d is the probability that a muon survives without decaying before reaching the surface; A is a normalisation constant; and γ is the spectral index. MUSUN uses the parameters $\gamma = 2.77$ and $A = 1.84$. These values of parameters fit the measured depth - vertical muon intensity relation measured by the LVD experiment at LNGS [160]. The model gives the total muon flux through a sphere as 6.16×10^{-9} cm^{-2} s^{-1} with a mean muon energy of 283 GeV, a mean zenith angle of 27° and a mean slant depth of 4500 m w. e.

MUSUN operates within BACCARAT and generates muons around a box surrounding the LZ detector. Figure 8.6 shows the positions of muons as generated by MUSUN around the detector. The simulation box volume extends from 7 m above the cavern boundary

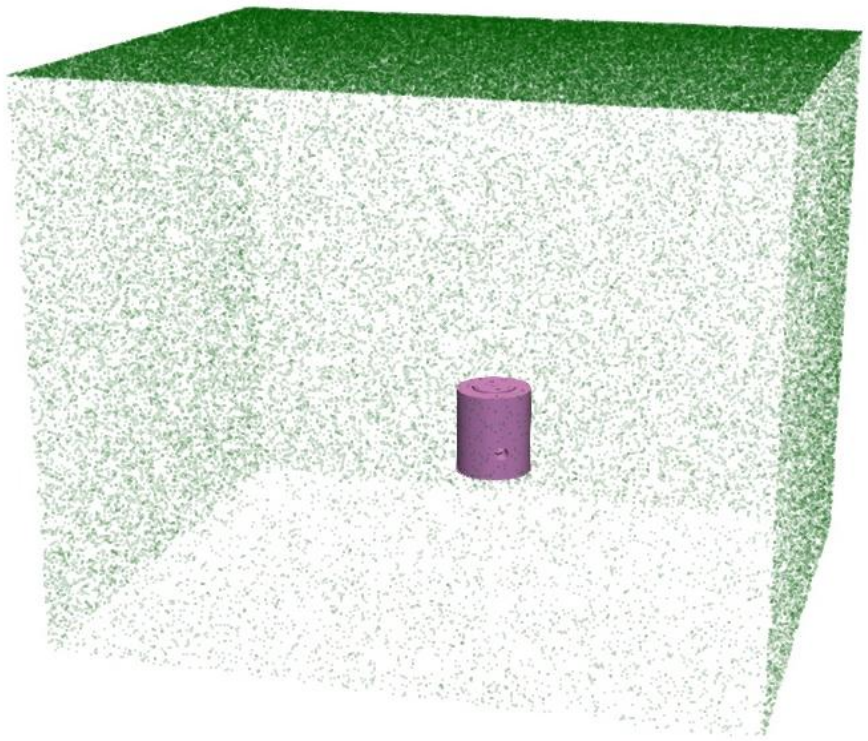
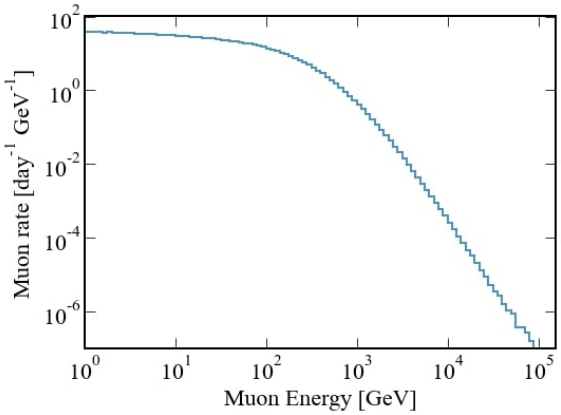
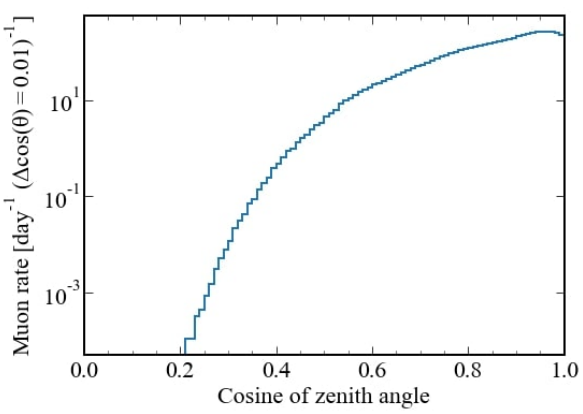


Figure 8.6: A visualisation of the primary positions of muons (green dots) generated by MUSUN, made with Paraview software [161]. The outermost volume of LZ detector (pink, central) in this image is the OD. The cavern walls are not included.

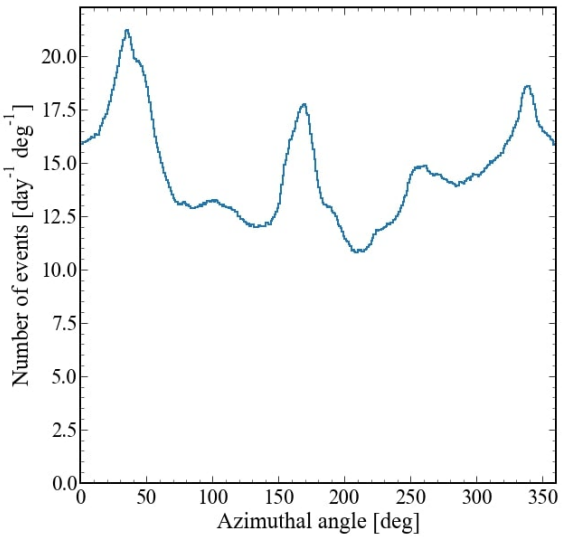
to 3 m below, with its walls positioned 5 m away from the boundary. Shifting the box surfaces further into the surrounding rock, away from the cavern, allows muon-induced cascades to develop within the rock before muons and their secondary particles enter the cavern. The primary energy spectrum and the angular distributions of muons generated by MUSUN are presented in Figure 8.7. After BACCARAT transports muons through



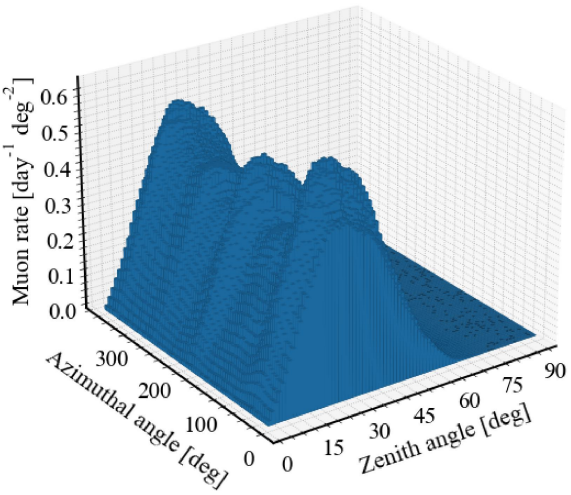
(a) Muon energy spectrum.



(b) Zenith angle distribution of muons.



(c) Azimuth angle distributions of muons counted East to North.

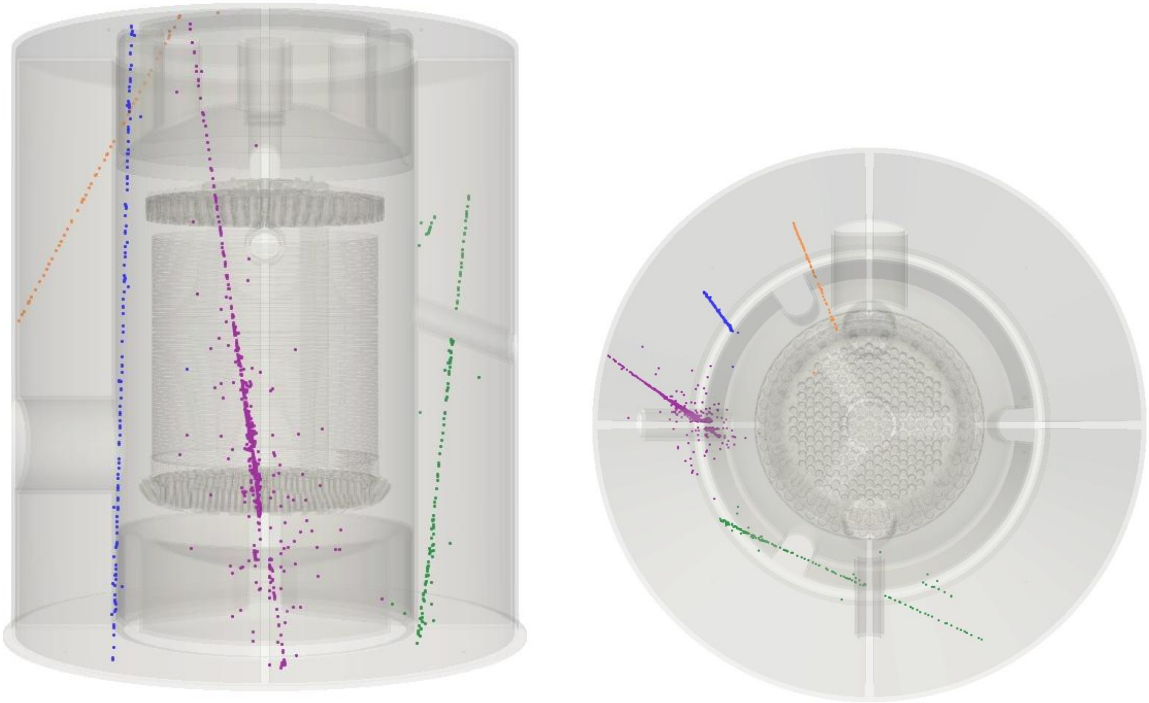


(d) 2D angular distribution of muons.

Figure 8.7: Angular distributions and the kinetic energy spectrum of muons at SURF's Davis Campus, as generated by the MUSUN model.

rock, cavern and detector geometry, energy depositions in all "sensitive volumes" are recorded. For this work, 4.82×10^7 muons have been propagated, corresponding to a live time of 9147 days and a rate of 0.0609874 muons per second. The simulation provides ~ 25 times higher statistics than for data collected during WS2022 and WS2024. Images of simulated muons passing through the LZ detector geometry and depositing energy in the sensitive volumes are displayed in Figure 8.8.

Previous measurements of muon fluxes at SURF, in the cavern where LZ is located, can be compared with muon fluxes calculated by a muon model, described in Ref. [86]. Vertical muon flux has been measured using the veto system of the Davis solar neutrino experiment as $(5.38 \pm 0.07) \times 10^{-9}$ cm^{-2} s^{-1} sr^{-1}, corrected for multiple muons [162], and



(a) (b)

Figure 8.8: Images made using Paraview software to plot positions of energy depositions from BACCARAT simulated muons and their secondaries as they travel through the LZ detector geometry.

the Majorana Demonstrator's veto system, located close to LZ a few tens of metres away, measured the total flux as $(5.31 \pm 0.17) \times 10^{-9}$ cm^{-2} s^{-1} [157]. The initial muon model estimates the vertical muon intensity as 5.18×10^{-9} cm^{-2} s^{-1} sr^{-1}, in good agreement with the Davis experiment measurement. The total muon flux through a spherical detector with unit cross-sectional area was calculated as 6.16×10^{-9} cm^{-2} s^{-1}, 16% higher than the Majorana measurement. Although the difference is relatively small, it highlighted the need for new LZ-based flux measurements to refine the muon model and inform other current and future experiments at SURF.

8.2.2 Data selection

Initially, LZLAMA was used to process BACCARAT files and generate observed quantities for direct comparison with those in the WIMP search data. However, it was ultimately decided to rely solely on BACCARAT simulations for two key reasons. Firstly, LZLAMA is not optimised for highly ionising tracks produced by muons passing through the TPC. Secondly, LZLAMA does not account for secondary particles such as pions and kaons, introducing a slight bias since these events would not be recorded, and such losses do not occur in real data. Overall, BACCARAT simulations were found to more closely resemble the data spectra and introduce fewer systematic uncertainties than LZLAMA when processing muons and their secondaries. Hence, only the BACCARAT output is compared to data.

8.2.2.1 Live time

WS2022 and WS2024 datasets are considered here, with operating conditions described in Refs. [79, 80]. There are different types of detector live time, summarised in Table 8.1 alongside the total run time. The datasets are divided into runs and the duration of those highlighted as "WIMP Search" comprises the total run time. The DAQ live time is

Table 8.1: Summary of relevant durations for the WIMP search runs WS2022 and WS2024. DAQ live time was used for this analysis.

Run	**Run time [days]**	**DAQ live time [days]**	**Physics live time [days]**
WS2022	99.5	98.8	96.4
WS2024	268.0	267.6	255.4
Total	367.5	366.4	351.8

defined as the total time during which DAQ waveforms could be recorded to disk, and the physics live time is defined as the total time during which a valid WIMP event could have been captured. For the rate calculation, DAQ live time (as opposed to the physics live time) was chosen as the appropriate live time, corresponding to 366.4 days. The physics live time applies more selections on data for active WIMP search that are unnecessary for this analysis. To skim the initial dataset, noise reduction cuts were made and the unique characteristic of a muon event producing a coincidental signal in each of the OD, Skin and TPC was employed.

8.2.2.2 Outer Detector and Skin selection

An OD energy threshold was implemented to reduce the probability of random coincidence between the OD, Skin and TPC detectors. The energy deposited in the OD by a muon is the largest, physical signal that will be observed in the OD. Other large physical signals anticipated are neutron captures, the most frequent of which are on gadolinium (see Section 8.1.3). Therefore, the OD threshold was set at the endpoint of the gadolinium neutron capture spectrum at ∼8 MeV, which corresponds to ∼2000 phd. This cut also rejects events induced by high-energy gamma-rays from radioactivity.

All that is required in the Skin detector is a pulse with an amplitude greater than 1 phd/ns to ensure a timing coincidence between volumes can be utilised and noise events are removed. Due to the highly non-uniform response of the Skin to an energy deposition, no energy threshold was applied as it would be difficult to make comparisons to the energy-only simulations produced using BACCARAT.

8.2.2.3 Inter-detector timing selection

Cosmic-ray muon events in the LZ experiment can be uniquely identified by their large energy deposits that occur nearly simultaneously across the three detector systems: OD, Skin and TPC. The time difference distributions between detector volumes allow for

distinguishing between muon interactions through all volumes and signals unrelated to muons. Events which exhibited coincidence were identified through the analysis of the inter-detector timing spectra, shown in Figure 8.9, and three different selection criteria were chosen as follows:

1. -200 ns $< \Delta t_{\text{OD - Skin}} < 200$ ns.
2. -1200 ns $< \Delta t_{\text{OD - TPC}} < 200$ ns.
3. -1200 ns $< \Delta t_{\text{Skin - TPC}} < 200$ ns.

Here, the pulse time, t, is described using two RQs: the start time of the pulse and the time at which the pulse has reached 5 % of its total pulse area. The differences between the distributions from WS2022 and WS2024, as seen in Figure 8.9 (particularly in Figure 8.9a), are due to changes made between the two runs; the extraction field was decreased, the cathode voltage was lowered, the trigger was optimised to increase the sensitivity to low-energy events of interest to WIMP analysis, and calibration parameters were retuned [80].

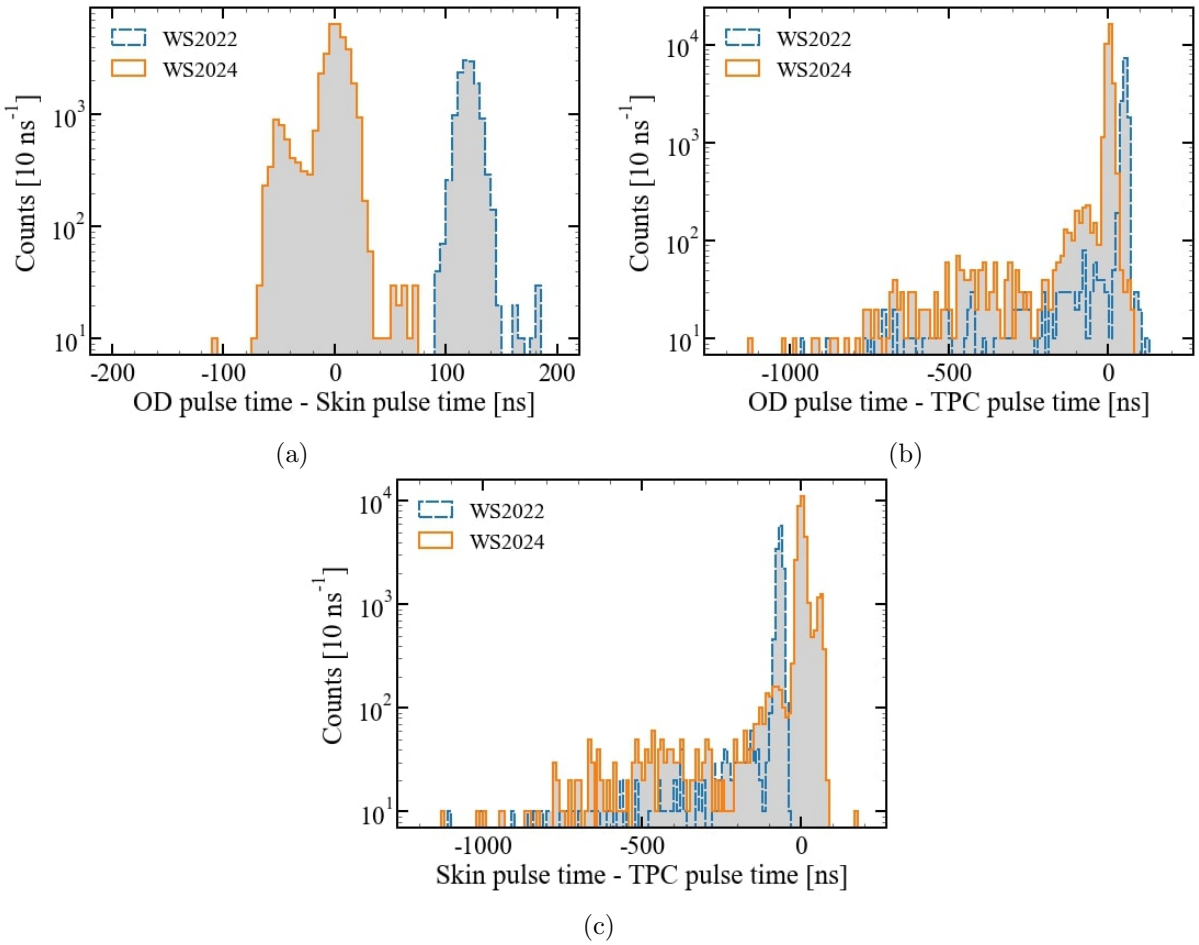


Figure 8.9: Distribution of events as a function of the time difference between signals in two detectors: (a) OD and Skin, (b) OD and TPC, (c) Skin and TPC. The events are from the WS2022 and WS2024 datasets with a pulse greater than 2000 phd in the OD.

Unlike in the OD and Skin, where a muon produces a singular pulse, the muon signal in the TPC consists of a single S1 pulse and a series of S2 pulses. The S2 pulses overlap because of the continuous muon ionisation track and, if the muon enters the TPC from

the top, there is no drift time and the S2 pulses begin immediately after the S1 pulse forming a long tail (as illustrated in Figure 8.10). When traversing the TPC, the first pulse in the tail is used in the inter-detector timing selection. Criterion 1 shows the time difference between the largest pulses in the OD and the Skin. Criterion 2 reflects the time difference between the largest pulse in the OD and the start of the muon tail in the TPC. Criterion 3 captures the time difference between the largest pulse in the Skin and the start of the muon tail in the TPC. Figure 8.11 highlights the effectiveness of the timing cut when used with the OD selection cuts, reducing the event rate per day from 119.4 to 13.3.

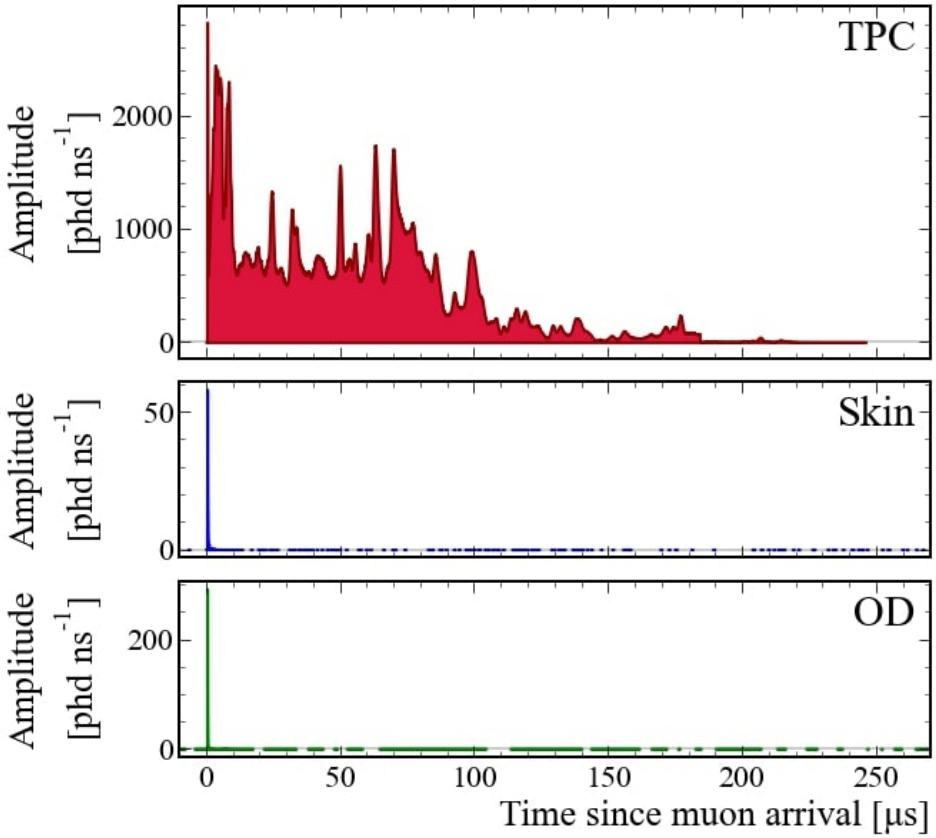
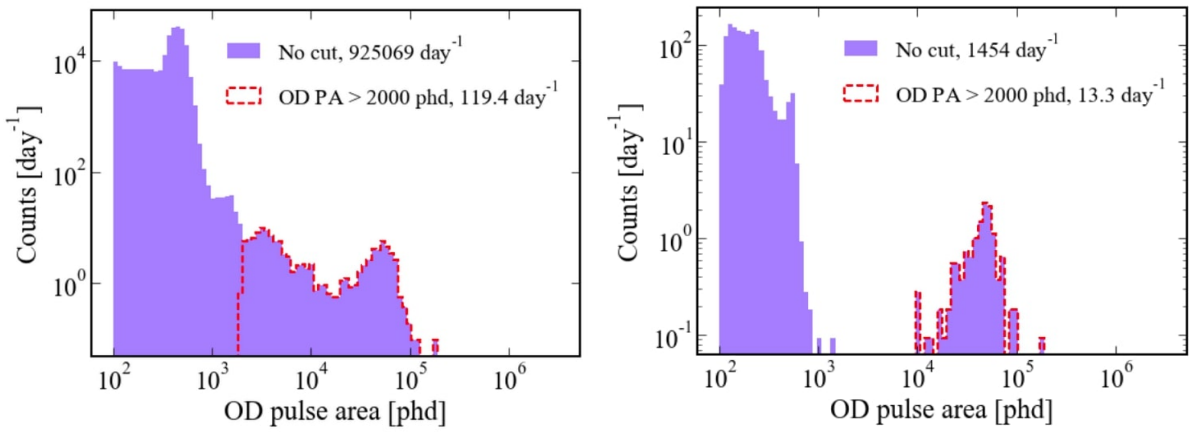


Figure 8.10: A typical muon event captured in a randomly triggered event.

8.2.2.4 TPC energy selection

Determining the energy threshold for the TPC is a critical part of obtaining an accurate muon rate. The effects of threshold cuts differ between simulations and data due to uncertainty associated with GEANT4 modelling of the muon shower, particularly with muon secondaries at lower energies (see Figure 8.12). Additionally, the TPC was calibrated at low energies (below a few MeV), but not at higher energies where the muon signal must lie (above a few tens of MeV), so accurate conversion from energy to phd was not possible. As the thresholds change, the rates change accordingly, but by possibly different factors for data and simulations. To optimise the energy threshold for the



(a) (b)

Figure 8.11: Histograms of the largest OD pulse areas in ∼12.5 million background events from WS2022 (a) before and (b) after applying inter-detector time coincidence cuts. The plots also show the impact of the 2000 phd cut. The peak at around 450 phd in (a) results from neutron captures on the nuclei of hydrogen atoms and the subsequent emission of a single 2.22 MeV gamma-ray.

TPC, the event rates in data and simulations needed to be compared, thus, an approximate conversion factor between light detected (phd) and the energy deposited in the TPC was determined. NEST [151] was used to convert the energy deposited by muons traversing the TPC into detected light. As the muons deposit energy in the LXe, a series of S1 and S2 pulses are produced which cannot be separated in data. NEST uses the mean $dE/dx = 2.1$ MeV cm^2 g^{-1} [163] for muons with the mean energy underground of 283 GeV, to generate light and charge along the muon path.

Sampling the start positions and direction vectors produced by the MUSUN simulations, all 48.2 million muons were projected down towards the LZ detector. 67909 muons from BACCARAT passed through the xenon volume. The positional information of where the muons entered and exited the TPC was used in the NEST simulations to obtain the number of photons detected in S1 and S2 pulses, allowing the linear relation between deposited energy and the collected photons. These simulations reconstructed the energy deposition through ionisation and the total S1 and S2 signals. The relation between the total number of photons in S1 and S2 pulses and the deposited energy from simulations was used to convert the number of detected photons in the data into the energy deposition. NEST was tailored for the WS2022 and WS2024 detector configurations to generate specific conversion factors for each dataset. The direct comparison of the spectra of detected photons and energy depositions in the TPC from data or simulations is not possible. This is due to the saturation of the PMTs that starts to be visible in the data spectrum at about 100 MeV of deposited energy, which can be seen in Figure 8.12.

Once the WS data could be compared with simulations by using the conversion factors, the difference between HG and LG channels was examined to see which gain would be best for normalising the muon model. HG and LG refer to parallel readout channels in the detector electronics, with HG optimised for high resolution of low-energy signals and LG designed to handle higher-energy signals without saturation. This comparison was accomplished by working backwards from the flux results described in Section 8.3. Comparing HG ratios of data rates to simulated rates with the corresponding LG ratios,

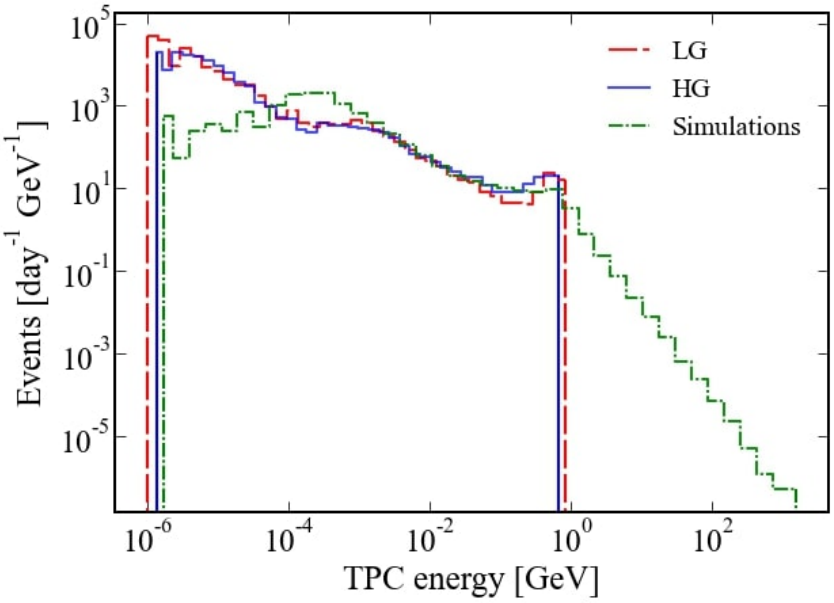


Figure 8.12: Spectra of deposited energy in the TPC from BACCARAT sumlations and data from WS2022 and WS2024 high gain (low gain) data periods (converted from TPC total pulse area).

as displayed in Figure 8.13, it is clear that the LG ratios remain steady within statistical uncertainties above 10 MeV. The uncertainties shown are purely statistical from data and simulated samples.

A low-energy threshold such as > 1 MeV, would not be useful because these events are not full muon events. They tend to be secondaries from a muon cascade in both data and simulations. Figure 8.14 demonstrates this by showing that most events with deposited energy > 10 MeV are muons, not muon secondaries, as it separates the events with a muon passing through the TPC from those that do not. A higher energy threshold such as > 50 MeV would also not be useful, as Figure 8.12 illustrates, the effect of PMT saturation can be seen above this energy in data. Therefore, the TPC energy threshold was chosen to be 10 MeV.

8.2.3 Energy deposition spectra in data and simulations

The cuts introduced in the simulations were designed to mimic those applied to data, namely a coincidence cut where a muon had to pass through each of the OD, skin and TPC within an event; and the 8 MeV energy threshold, previously explained in Section 8.2.2. Unlike in the TPC, PMTs in the OD do not suffer from saturation when a muon crosses the OD. Therefore, the spectra of energy depositions from muons in the data and simulation samples can be compared directly. The OD has been calibrated with numerous radioactive sources [164]. However, this calibration (conversion of phd into energy) works only at keV and MeV energies, thus, a one-to-one conversion of phd to energy at the muon energy scale in the OD based on a low-energy calibration is unfeasible.

To compare the shapes of the data and simulated spectra, we have superimposed the data spectrum (in phd) on top of the simulated spectrum (in energy units) to match the spectral features. The two spectra are shown in Figure 8.15 as a function of the energy

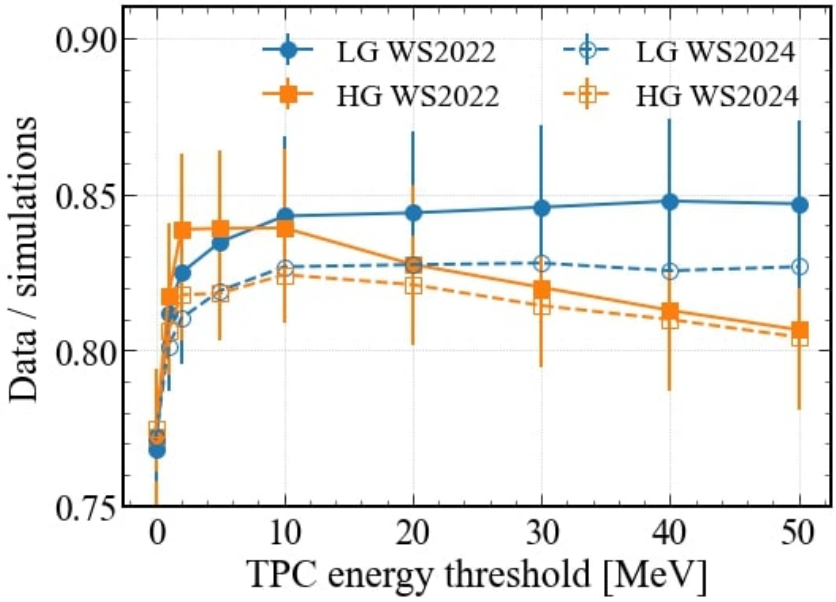


Figure 8.13: The ratios of HG (LG) WS2022 and WS2024 data to BACCARAT simulations as a function of the energy threshold in the TPC.

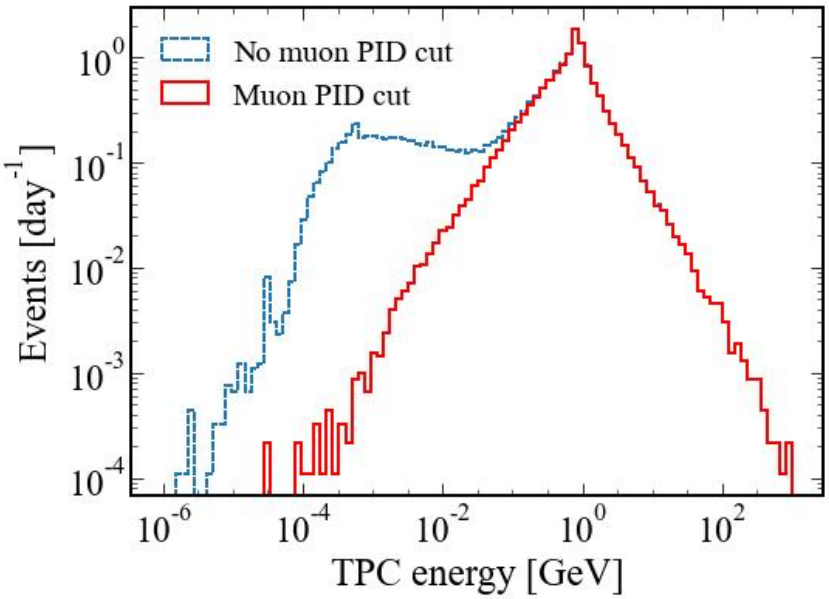


Figure 8.14: Energy deposition spectra of muon events from BACCARAT simulations with and without a muon particle ID (PID) cut. The cut selects events that had a muon depositing energy in the TPC directly.

deposition in the OD. Light emission, transport and detection in the OD have not been simulated due to the high number of emitted scintillation photons, so a perfect match of the two spectra is not expected. However, the shapes of the two spectra are consistent, with a lower rate of measured events than simulated ones. The conversion of phd to energy for both WS2022 and WS2024 is 6.5×10^{-6} GeV/phd.

After converting total pulse area in the OD and TPC from phd to energy, we were able to directly compare their combined energy maps to the simulated results. The plots displaying the full energy distributions (after coincidence and OD energy cuts in data and

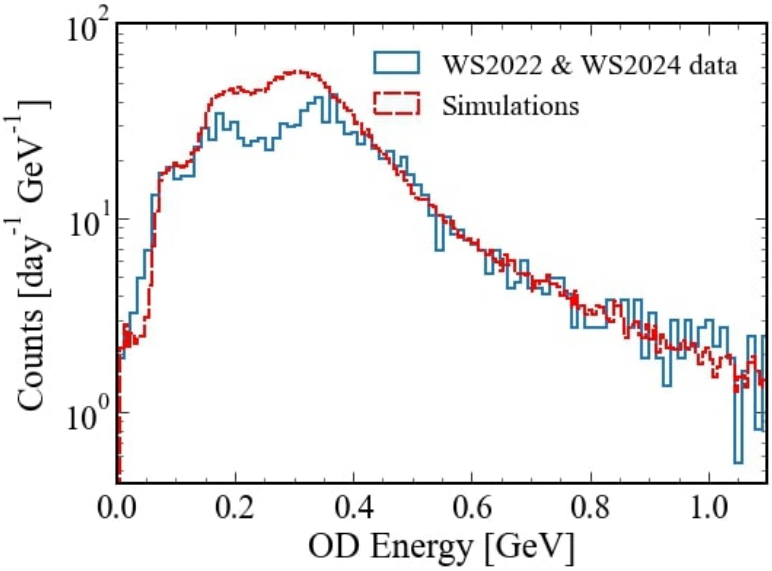


Figure 8.15: Energy deposited by BACCARAT simulated muons in the OD and the energy of events in data converted from the total pulse area in the OD.

simulations) and similar distributions after the TPC 10 MeV threshold is imposed are in Figure 8.16. Since we cannot distinguish with absolute certainty between secondaries of muons and actual muons in data, we need the cuts to ensure that this uncertainty, which is higher at lower energies, is reduced. The energy distributions show that the 10 MeV cut removes events with a small amount of energy deposited in the TPC and a large amount of energy deposited in the OD. This is characteristic of muon secondaries or muons that may have skimmed the edge of the TPC.

8.3 Evaluation of the muon flux

8.3.1 Muon rate measurements

Daily rates of muon events in data (HG and LG) and simulations are displayed in Figures 8.17a and 8.17b. These rates and their ratio (data/simulations) are presented in Tables 8.2a and 8.2b with increasing TPC energy thresholds. By varying the TPC energy threshold, the change in the ratio of the simulated muon rate to the muon rate from data can be tracked. Columns 4 and 6 in each table show these ratios for LG and HG data respectively, and they are also plotted in Figure 8.13. The final column in each table lists the differences between these HG and LG ratios for every threshold. Since the measured event rate and the ratio of data-to-simulations for the two sets of data remain the same within statistical uncertainties, in further analysis, the two data sets were combined into a single one. This data is presented in Table 8.3, with the daily rates plotted in Figure 8.18.

As described in Section 8.2.2, the steadiness of the LG ratio compared to the HG ratio above 10 MeV was a major factor in our decision to implement a 10 MeV threshold and use LG data for reconstructing the muon flux (see Section 8.3.2). As seen from Table 8.3 and Figure 8.18 the muon data rate is lower than that from simulations by

Table 8.2: Muon rates from simulations and (a) WS2022 data and (b) WS2024 data. The data and simulations include the 8 MeV OD energy cut and the cut on time coincidences between the three detectors: TPC, Skin and OD. The TPC energy thresholds correspond to the total energy deposited by a muon event in the TPC.

(a) **WS2022**

Energy threshold	**Simulation rate [day^{-1}]**	**Data LG rate [day^{-1}]**	**Data/sims LG ratio**	**Data HG rate [day^{-1}]**	**Data/sims HG ratio**	**LG ratio - HG ratio**
TPC > 1.44 keV	16.550 ± 0.043	12.709 ± 0.359	0.768 ± 0.022	12.780 ± 0.360	0.772 ± 0.022	-0.004 ± 0.031
TPC > 1 MeV	15.055 ± 0.041	12.224 ± 0.352	0.812 ± 0.023	12.305 ± 0.353	0.817 ± 0.024	-0.005 ± 0.033
TPC > 2 MeV	14.477 ± 0.040	11.940 ± 0.348	0.825 ± 0.024	12.143 ± 0.351	0.839 ± 0.024	-0.014 ± 0.034
TPC > 5 MeV	13.760 ± 0.039	11.485 ± 0.341	0.835 ± 0.025	11.546 ± 0.342	0.839 ± 0.025	-0.004 ± 0.035
TPC > 10 MeV	13.275 ± 0.038	11.191 ± 0.337	0.843 ± 0.025	11.141 ± 0.336	0.839 ± 0.025	0.004 ± 0.036
TPC > 20 MeV	12.840 ± 0.037	10.837 ± 0.331	0.844 ± 0.026	10.625 ± 0.328	0.827 ± 0.026	0.017 ± 0.036
TPC > 30 MeV	12.597 ± 0.037	10.655 ± 0.328	0.846 ± 0.026	10.331 ± 0.323	0.820 ± 0.026	0.026 ± 0.037
TPC > 40 MeV	12.413 ± 0.037	10.524 ± 0.326	0.848 ± 0.026	10.088 ± 0.320	0.813 ± 0.026	0.035 ± 0.037
TPC > 50 MeV	12.258 ± 0.037	10.382 ± 0.324	0.847 ± 0.027	9.886 ± 0.316	0.807 ± 0.026	0.040 ± 0.037

(b) **WS2024**

Energy threshold	**Simulation rate [day^{-1}]**	**Data LG rate [day^{-1}]**	**Data/sims LG ratio**	**Data HG rate [day^{-1}]**	**Data/sims HG ratio**	**LG ratio - HG ratio**
TPC > 1.44 keV	16.550 ± 0.043	12.769 ± 0.218	0.772 ± 0.013	12.821 ± 0.219	0.775 ± 0.013	-0.003 ± 0.019
TPC > 1 MeV	15.055 ± 0.041	12.063 ± 0.212	0.801 ± 0.014	12.137 ± 0.213	0.806 ± 0.014	-0.005 ± 0.020
TPC > 2 MeV	14.477 ± 0.040	11.730 ± 0.209	0.810 ± 0.015	11.838 ± 0.210	0.818 ± 0.015	-0.007 ± 0.021
TPC > 5 MeV	13.760 ± 0.039	11.270 ± 0.205	0.819 ± 0.015	11.259 ± 0.205	0.818 ± 0.015	0.001 ± 0.021
TPC > 10 MeV	13.275 ± 0.038	10.975 ± 0.203	0.827 ± 0.015	10.941 ± 0.202	0.824 ± 0.015	0.003 ± 0.022
TPC > 20 MeV	12.840 ± 0.037	10.624 ± 0.199	0.827 ± 0.016	10.542 ± 0.198	0.821 ± 0.016	0.006 ± 0.022
TPC > 30 MeV	12.597 ± 0.037	10.430 ± 0.197	0.828 ± 0.016	10.258 ± 0.196	0.814 ± 0.016	0.014 ± 0.022
TPC > 40 MeV	12.413 ± 0.037	10.246 ± 0.196	0.825 ± 0.016	10.052 ± 0.194	0.810 ± 0.016	0.016 ± 0.022
TPC > 50 MeV	12.258 ± 0.037	10.134 ± 0.195	0.827 ± 0.016	9.858 ± 0.192	0.804 ± 0.016	0.023 ± 0.023

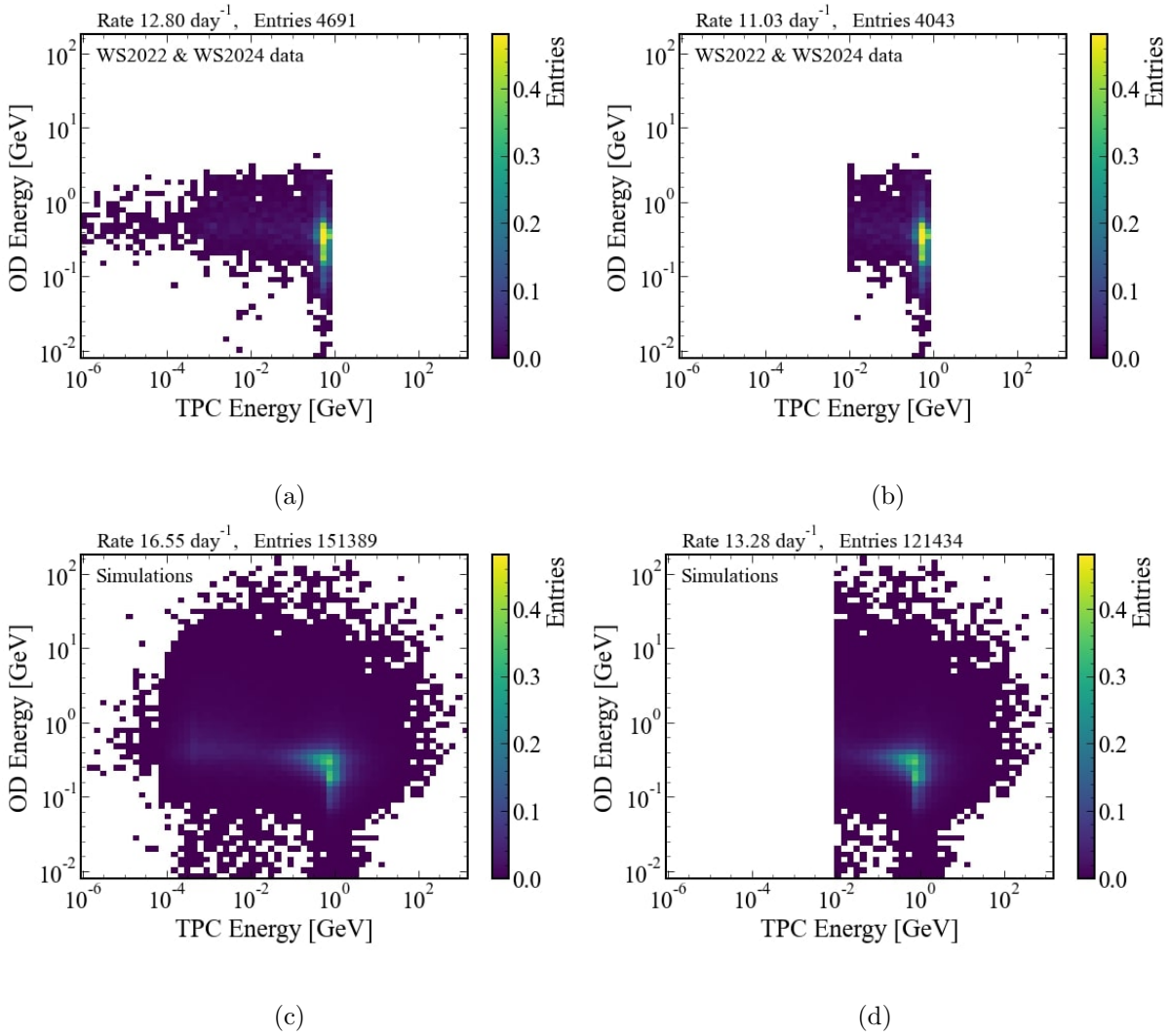
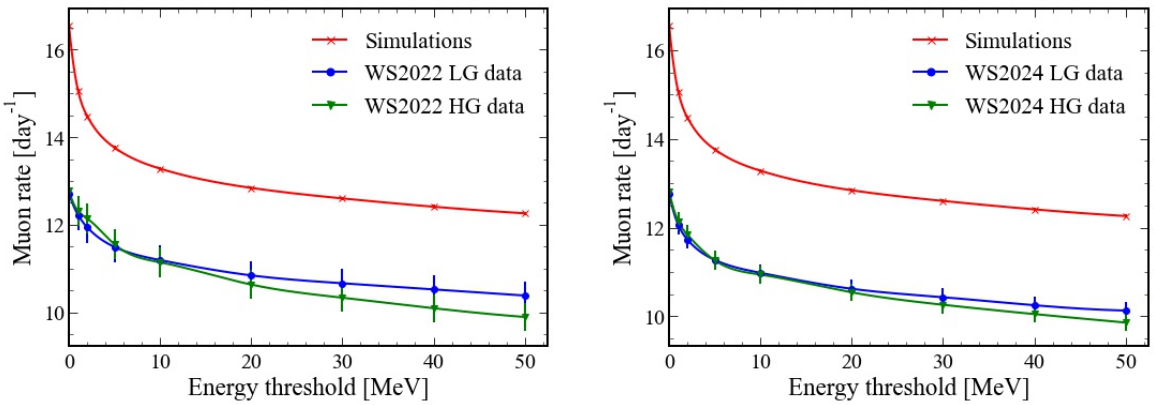


Figure 8.16: Energy depositions from events in the OD and TPC are shown. The total pulse area from WS2022 and WS2024 data have been converted to energy. (a) Only OD and inter-detector timing cuts are applied, (b) the 10 MeV cut is also included. The cut in measured TPC energy near 1 GeV is caused by PMT saturation. Similarly, BACCARAT simulations are plotted with the 8 MeV OD energy threshold and volume coincidence cut in (c), and with the additional 10 MeV TPC cut included in (d).

about 15 - 20 %. It is expected that the rate of muon events in data and simulations will decrease with the increase of the energy threshold in the TPC. However, due to possible uncertainties in modelling events where a muon did not pass through the TPC and its signal was caused by electrons or photons from muon interactions, the ratio of data-to-simulated muon events may change with the threshold. This is seen in Table 8.3 up to 5 - 10 MeV. At higher energy thresholds, the ratio stays constant. As simulations show (see Figure 8.14), practically all muon events above 10 MeV are caused by muons leaving at least a short track in the TPC. The muon daily rate above this threshold is 11.03 $\pm$ 0.17 (stat.) in data and the ratio is 0.831 ± 0.013. The variation of this ratio above 5 MeV has been used to evaluate the systematic uncertainty for the measured muon rate, which is about 1 %.



(a) (b)

Figure 8.17: The changes in daily muon rates as the energy threshold increases. Analysis cuts have been applied to both simulations and (a) LZ WS2022 and (b) WS2024 data. See the caption of Table 8.2 for descriptions of these thresholds and analysis cuts.

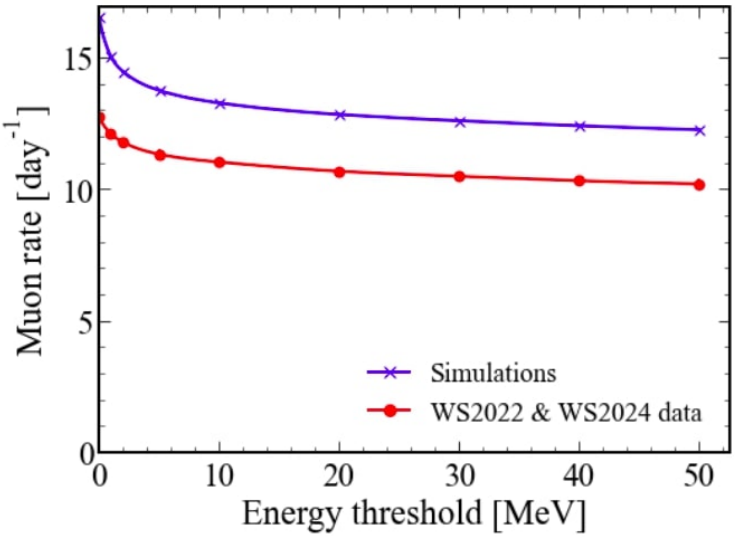


Figure 8.18: The changes in muon rates as the energy threshold increases, after analysis cuts have been applied to both simulations and LZ WS2022 and WS2024 data. See the caption of Table 8.2 for descriptions of these thresholds and analysis cuts.

8.3.2 Reconstruction of the muon flux

Reconstruction of the muon flux from the measured muon rate has been done by scaling the simulated muon flux by the same ratio as that for the measured-to-simulated rate:

$$F_m = F_s \times \frac{R_m}{R_s}, \tag{8.7}$$

where F_m and F_s are the measured (reconstructed from the measured rate) and simulated muon fluxes through a surface of a sphere (unit detection efficiency at all angles), respectively, and R_m and R_s are the measured and simulated muon rates through the detector.

Table 8.3: Muon rates from simulations and the combined WS2022 and WS2024 datasets, LG only. See the Table 8.2 caption for descriptions of the applied cuts and energy thresholds.

Energy threshold	**Simulation rate [day^{-1}]**	**Data LG rate [day^{-1}]**	**Data/sims LG ratio**
TPC > 1.44 keV	16.55 ± 0.04	12.75 ± 0.19	0.770 ± 0.012
TPC > 1 MeV	15.06 ± 0.04	12.11 ± 0.18	0.804 ± 0.012
TPC > 2 MeV	14.48 ± 0.04	11.79 ± 0.18	0.814 ± 0.013
TPC > 5 MeV	13.76 ± 0.04	11.33 ± 0.18	0.823 ± 0.013
TPC > 10 MeV	13.28 ± 0.04	11.03 ± 0.17	0.831 ± 0.013
TPC > 20 MeV	12.84 ± 0.04	10.68 ± 0.17	0.832 ± 0.013
TPC > 30 MeV	12.60 ± 0.04	10.49 ± 0.17	0.833 ± 0.014
TPC > 40 MeV	12.41 ± 0.04	10.32 ± 0.17	0.832 ± 0.014
TPC > 50 MeV	12.26 ± 0.04	10.20 ± 0.17	0.832 ± 0.014

This scaling is based on the common inputs to the muon model, specifically the muon energy spectra and angular distributions at SURF. It also relies on the assumption that muon transport through the detector and detector response are correctly simulated in BACCARAT. However, simulating muon-induced cascades and their development both inside and outside the detector introduces uncertainties that are difficult to quantify. By requiring the energy deposition in the TPC to be greater than 10 MeV, we effectively select events when a muon traverses the TPC and remove a relatively small fraction of events in which only low-energy secondary particles enter the TPC without an accompanying muon. No additional energy cuts are applied, ensuring that all events containing a muon in the TPC (both in data and simulations) are included in the analysis. The simulation of the muon track passing through the detector and muon energy loss from ionisation along the track is reliably handled by GEANT4. Furthermore, the assumption about an accurate simulation of detector response becomes non-critical, as the event rate is independent of specific energy deposition details beyond the applied threshold.

The ratio of measured-to-simulated muon rates in Table 8.3 remains constant within statistical uncertainty for TPC energy thresholds of 5 - 50 MeV. For the TPC threshold of 10 MeV, this ratio is 0.831 ± 0.013 (stat.) ± 0.008 (syst.), where systematic uncertainty is estimated from the change in the ratio when changing the threshold above 5 MeV. Note that reducing the threshold will increase the fraction of events when a muon does not enter the detector, consequently increasing the dependence on simulation details. Using Equation (8.7), the data-to-simulations rate ratio of 0.831 ± 0.013 (stat.) ± 0.008 (syst.) and the simulated muon flux of 6.16×10^{-9} cm^{-2} s^{-1}, we derive the value for the muon flux from the rate measurements as $(5.12 \pm 0.08$ (stat.) ± 0.05 (syst.)$) \times 10^{-9}$ cm^{-2} s^{-1}. This flux agrees well with the measurement in the nearby cavern reported in Ref. [157] ($(5.31 \pm 0.17) \times 10^{-9}$ cm^{-2} s^{-1}).

8.3.3 Evaluation of average rock density

The difference in the reconstructed and simulated muon fluxes is primarily due to a lower density of rock used in the muon model. We assume that the surface profile and laboratory position are known with sufficient accuracy. There is a small dependence of the flux on the position within the laboratory, but it is below the statistical uncertainty. The impact of the rock composition on the flux is a second-order effect. By attributing the lower muon flux from the measurements to the higher average rock density, we can estimate the realistic average rock density above and around the LZ location.

The muon flux at SURF has been calculated with different densities of rock above the laboratory to match the reconstructed measurement and are plotted in Figure 8.19. A simple 'flat' surface profile was assumed, which accounted for Earth's curvature, but not for any features in the surface profile. The simulated flux matched the measured one with an average rock density of (2.78 ± 0.01) g cm^{-3}, which is 3.0 % higher than the initial muon model assumption, but lower than that reported in Ref. [157] ((2.89 ± 0.06) g cm^{-3}).

The muon flux has been reconstructed for the surface of the box where muons were originally sampled in the simulations, namely 7 m into rock above the cavern. Since muons are mostly near vertical, we can neglect muons passing through vertical surfaces of the box around the cavern. The flux depends on the position in and around the cavern. The muon flux at the top surface of the cavern is about 3% lower and is equal to $(4.97 \pm 0.08\ (\text{stat.}) \pm 0.05\ (\text{syst.})) \times 10^{-9}$ cm^{-2} s^{-1}.

The precise rock composition around and above the laboratory is not known and the rock is not uniform. Hence, choosing a different rock composition, for instance for the rock Yates amphibolite [165] present around the laboratory (with $< Z > = 12.6$ and $< A > = 25.3$) results in a slightly different evaluated density from our muon rate measurements, namely: (2.76 ± 0.01) g cm^{-3}. The average of the two values can be taken as an estimate of the average rock density and the difference between the two values for the density and their average can be taken as an additional systematic uncertainty, resulting in a density of $(2.77 \pm 0.01\ (\text{stat.}) \pm 0.01\ (\text{syst.}))$ g cm^{-3}.

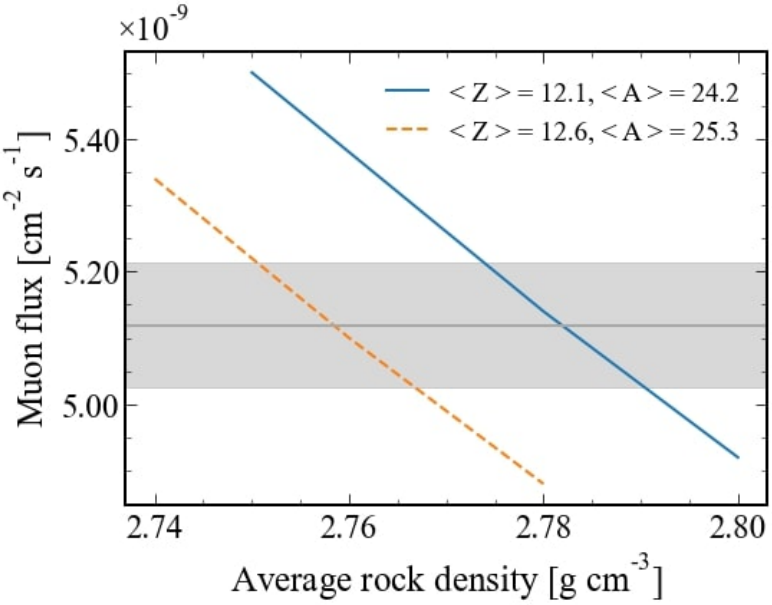


Figure 8.19: The muon flux dependence on average rock density within the muon model. The horizontal line and shaded section mark, respectively, the measured flux value and the combined statistical and systematic uncertainties, $(5.12 \pm 0.09) \times 10^{-9}$ cm^{-2} s^{-1}. The diagonal lines represent flux-density relationships for muon flux simulations using different rock parameters: the solid line reflects parameters from rock samples around SURF, while the dashed line corresponds to Yates Amphibolite, a prevalent rock type near the laboratory.

8.3.4 Conclusions

The LZ experiment has measured the rate of muons passing through the three detectors: TPC, Skin, and OD, as 11.03 ± 0.17 (stat.) day^{-1}. This rate is lower than calculated from the original muon model by a factor of 0.831 ± 0.013 (stat.) $\pm$ 0.008 (syst.). By scaling the simulated muon flux by the ratio of data-to-simulated rates and extrapolating the flux to the top of the cavern we derived the muon flux from the measurements as $(4.97 \pm 0.08$ (stat.) ± 0.05 (syst.)$) \times 10^{-9}$ cm^{-2} s^{-1}. Assuming that the difference between the measured and calculated muon rates is due primarily to an unduly low rock density used in the muon model and that the density is uniform above and around the detector, the corrected rock density has been found as $(2.77 \pm 0.01$ (stat.) ± 0.01 (syst.)) g cm^{-3}, 3.0 % higher than in the original model.

Chapter 9

Conclusions

This thesis has assessed key background sources relevant to rare-event searches and evaluated the suitability of the Boulby Underground Laboratory for hosting a next-generation dual-phase xenon detector that will search for WIMP dark matter and $0\nu\beta\beta$ decay. A full GEANT4 Monte Carlo simulation was employed to assess shielding requirements for suppressing gamma-ray backgrounds from rock. The studies demonstrated that 4 m of water and GdLS shielding on the top and sides, and 2 m on the bottom with a 30 cm thick steel plate base, are sufficient to limit background contributions from typical rock radioactivity (1 Bq/kg of ^{40}K, ^{232}Th, and ^{238}U) to < 1 event per year in the WIMP ROI and < 1 event per 10 years in the $0\nu\beta\beta$ decay ROI. It has been estimated that reducing the water shielding by 1 m on all sides of the detector increases TPC event rates in the WIMP ROI from $\left(1.5^{+1.1}_{-0.6}\right) \times 10^{-3}$ to $0.12^{+0.09}_{-0.05}$ year^{-1} (Bq/kg)$^{-1}$ and from $\left(2.2^{+2.5}_{-1.4}\right) \times 10^{-4}$ to $\left(2.5^{+2.8}_{-1.6}\right) \times 10^{-2}$ year^{-1} (Bq/kg)$^{-1}$ for ^{232}Th and ^{238}U, respectively. This necessitates stricter fiducial cuts to keep the $0\nu\beta\beta$ decay ROI below 1 event per 10 years, reducing fiducial xenon mass from 39.3 to 19.1 tonnes for ^{232}Th and from 59.6 to 30.9 tonnes for ^{238}U. Additional backgrounds from detector materials would further limit this fiducial mass.

Polyhalite rock samples from Boulby Mine, which were measured with HPGe detectors, revealed low levels of ^{232}Th and ^{238}U, with specific activities of, respectively, $(1.14 \pm 0.37\,(\text{stat.}) \pm 0.10\,(\text{syst.})) \times 10^{-2}$ Bq/kg and $0.354 \pm 0.008\,(\text{stat.}) \pm 0.054\,(\text{syst.})$ Bq/kg. Normalising the simulation results to these measurements gives rates of ^{232}Th and ^{238}U in the WIMP ROI as $\left(1.7^{+1.3}_{-0.6}\right) \times 10^{-5}$ year^{-1} (Bq/kg)$^{-1}$ and $\left(2.2^{+2.5}_{-1.4}\right) \times 10^{-4}$ year^{-1} (Bq/kg)$^{-1}$. If the water shielding thickness were to be reduced by 1 m on all sides of the detector, leaving 2.5 m of water on the top and sides and 1.5 m on the bottom, these rates can be reduced to $(1.4^{+1.0}_{-0.6}) \times 10^{-3}$ year^{-1} (Bq/kg)$^{-1}$ and $(8.9^{+9.9}_{-5.7}) \times 10^{-3}$ year^{-1} (Bq/kg)$^{-1}$, respectively. Similarly to the simulation results, this shielding reduction would lead to a

reduced FV in the $0\nu\beta\beta$ decay ROI, but only for ^{238}U background, as the ^{232}Th background rate is still less than 1 event in 10 years at $(8.96 \pm 5.64) \times 10^{-2}$ year^{-1} (Bq/kg)$^{-1}$. These results demonstrate that Boulby offers an exceptionally low-background environment, making Boulby Mine a suitable location for hosting future high-sensitivity detectors.

Complementing this, the Boulby radon emanation facility demonstrated a minimum detectable activity of 42.0 µBq at 95 % CL after 7.4 days, underscoring its capability for precision screening. The surface emanation and specific activity from Boulby polyhalite were measured as 3.92 ± 0.37 µBq cm^{-2} and 1.221 ± 0.094 µBq kg^{-1}, respectively. To fully commission the radon system, several upgrades are proposed, including calibration of a second detector, optimisation of the CAEN digitiser, and completion of the concentration line radon trap.

Muon flux measurements were performed with the LZ experiment. Using data from 366 live days of the experiment taking data, the underground muon flux was found to be 20 % lower than predicted by the original muon model. This discrepancy was attributed to an underestimated average rock density, which was subsequently revised with a 3.0 % increase to 2.77 ± 0.01 (stat.) $\pm$ 0.01 (syst.) g cm^{-3}. Scaling the simulation to measured rates yielded a corrected muon flux of $(4.97 \pm 0.08\,(\text{stat.}) \pm 0.05\,(\text{syst.})) \times 10^{-9}$ cm^{-2} s^{-1} at the top of the cavern.

Glossary of Terms

(α, n) reaction
: A process where an alpha is captured by a nucleus and if the resulting compound nucleus has sufficient energy, a neutron is emitted.

activated charcoal
: A highly porous material made from carbon-rich substances that have been heated to a high temperature, then physically or chemically activated. Activation creates a vast network of pores inside the carbon, resulting in a very large surface area that can attract and hold organic (and some inorganic) chemicals.

bolometer
: A thermal detector that measures the power of incident electromagnetic radiation by recording the small temperature rise it produces in an absorbing element.

Czochralski method
: A technique used to grow bulk semiconductor crystals. A solid crystal seed is placed in contact with the raw crystal material in liquid form (the melt) in a crucible. The seed is slowly rotated in the top, cooler region of the melt, pulling in material that gradually solidifies.

fiducial volume (FV)
: A region within a detector defined by analysis cuts rather than physical boundaries, typically chosen to reduce surface-related backgrounds.

GEANT4 physics list
: A pre-defined class that specifies the particles and their corresponding physics processes for a simulation.

inductively coupled plasma mass spectrometry (ICP-MS)
: An elemental analysis technique in which a sample is ionised by an argon plasma, and the resulting ions are then measured by a mass spectrometer.

mass flow controller (MFC)
: A device that measures and controls the flow of liquids and gases.

multipole
: In the context of the CMB, a multipole (ℓ) is an integer representing a specific angular scale on the sky.

naturally occurring radioactive materials (NORM)
: Materials (minerals and ores) found in the environment that contain radioactive elements of natural origin.

neutron activation analysis (NAA)
: An analysis technique in which a sample is irradiated with neutrons. As the radioactive isotopes decay, the resultant gamma spectra is measured.

neutron-transmutation-doped (NTD)
: A method of introducing dopants into semiconductors (eg. germanium) through neutron irradiation.

Q-value
: In nuclear physics, the Q-value is the energy released in a nuclear disintegration eg. in neutrinoless double beta decay.

reduced quantity (RQ)
: Processed data that has been derived from raw waveforms (processed by LZAp) and is ready to use for analysis. Includes pulse-level and event-level information.

reverse field region (RFR)
: In dual-phase xenon dark matter detectors, the RFR is a region near the bottom of the TPC, below the cathode, where the electric field direction is opposite to that of the main drift field.

shotcrete
: Concrete that is pneumatically projected through a hose at high velocity onto a surface, forming layers of hardened concrete.

transition edge sensor (TES)
: A temperature sensor made from a superconducting film operated near its critical temperature. During the transition from superconductor to normal metal, a small change in temperature causes a large change in resistance.

trigger
: In LZ, the trigger is the DAQ that decides whether detector signals should be recorded, distinguishing candidate events from noise.

vacuum ultraviolet (VUV) photons
: Photons with a wavelength range of 10 - 200 nm.

Bibliography

[1] N. Aghanim et al. (Planck Collaboration), Planck 2018 results: VI. Cosmological parameters, Astron. Astrophys. 641, A6 (2020). doi:10.1051/0004-6361/201833910.

[2] F. Zwicky, Die Rotverschiebung von extragalaktischen Nebeln, Helv. Phys. Acta 6 (1933) 110–127. doi:10.1007/s10714-008-0707-4.

[3] G. Bertone and D. Hooper, History of dark matter, Rev. Mod. Phys. 90 (2018) 045002. doi:10.1103/RevModPhys.90.045002.

[4] V. Rubin and W. K. Ford Jr., Rotation of the Andromeda Nebula from a spectroscopic survey of emission regions, Astrophys. J. 159 (1970) 379. doi:10.1086/150317.

[5] Y. Sofue and V. Rubin, Rotation curves of spiral galaxies, Annu. Rev. Astron. Astrophys. 39 (2001) 137–174. doi:10.1146/annurev.astro.39.1.137.

[6] K. G. Begeman, A. H. Broeils and R. H. Sanders, Extended rotation curves of spiral galaxies: dark haloes and modified dynamics, Mon. Not. R. Astron. Soc. 249 (1991) 523–537. doi:10.1093/mnras/249.3.523.

[7] A. Einstein, Lens-like action of a star by the deviation of light in the gravitational field, Sci. 84 (1936) 506–507. doi:10.1126/science.84.2188.506.

[8] R. Nemiroff and J. Bonnell, A horseshoe Einstein ring from Hubble, Astronomy picture of the day: 21st Dec. 2011. Accessed online 11th Apr. 2025.

[9] D. Clowe et al., A direct empirical proof of the existence of dark matter, Astrophys. J. 648 (2006) L109–L113. doi:10.1086/508162.

[10] A. A. Penzias and R. W. Wilson, A measurement of excess antenna temperature at 4080 Mc/s., Astrophys. J. 142 (1965) 419–421. doi:10.1086/148307.

[11] G. Hinshaw et al., Three-year Wilkinson Microwave Anisotropy Probe (WMAP) observations: Temperature analysis, Astrophys. J. (2006) 288–334doi:10.1086/513698.

[12] N. Aghanim et al. (Planck Collaboration), Planck 2018 results: I. Overview and the cosmological legacy of Planck, Astron. Astrophys. 641, A1 (2020). doi:10.1051/0004-6361/201833910.

[13] P. Ade et al. (Planck Collaboration), Planck 2013 results I. Overview of products and scientific results, Astron. Astrophys. 571, A1 (2014). doi:10.1051/0004-6361/201321529.

[14] R. H. Cyburt, B. D. Fields and K. A. Olive, Primordial nucleosynthesis in light of WMAP, Phys. Lett. B 567 (2003) 227–234. doi:10.1016/j.physletb.2003.06.026.

[15] R. J. Cooke, M. Pettini, K. N. Nollett and R. Jorgenson, The primordial deuterium abundance of the most metal-poor damped Lyα System, Astrophys. J. 830 (2016) 142. doi:10.3847/0004-637X/830/2/148.

[16] S. Navas et al. (Particle Data Group Collaboration), Review of particle physics, Phys. Rev. D 110 (2024) 030001. doi:10.1103/PhysRevD.110.030001.

[17] L. Roszkowski, E. Sessolo and S. Trojanowski, WIMP dark matter candidates and searches—current status and future prospects, Rep. Prog. Phys. 81 (2018) 066201. doi:10.1088/1361-6633/aab913.

[18] S. P. Martin, A supersymmetry primer, World Scientific, 1998, Ch. 1, pp. 1–98. doi:10.1142/9789812839657_0001.

[19] H. Abdallah et al. (H.E.S.S. Collaboration), Searches for dark matter annihilation signatures in H.E.S.S. observations of the Galactic Centre region, Phys. Rev. Lett. 117 (2016) 111301. doi:10.1103/PhysRevLett.117.111301.

[20] M. Ackermann et al. (Fermi-LAT Collaboration), Searching for dark matter annihilation from Milky Way dwarf spheroidal galaxies with six years of Fermi Large Area Telescope data, Phys. Rev. Lett. 115 (2015) 231301. doi:10.1103/PhysRevLett.115.231301.

[21] M. G. Aartsen et al. (IceCube Collaboration), Search for dark matter annihilation in the Sun with 79-string IceCube, Phys. Rev. Lett. 110 (2013) 131302. doi:10.1103/PhysRevLett.110.131302.

[22] M. Aguilar et al. (AMS-02 Collaboration), Antiproton flux, antiproton-to-proton flux ratio, and properties of elementary particle fluxes in primary cosmic rays measured with the Alpha Magnetic Spectrometer on the International Space Station, Phys. Rev. Lett. 117 (2016) 091103. doi:10.1103/PhysRevLett.117.091103.

[23] N. Trevisani, Collider Searches for Dark Matter (ATLAS + CMS), in: Selected Papers from the 7th International Conference on New Frontiers in Physics), Vol. 4, Universe, 2018. doi:10.3390/universe4110131.

[24] K. Griest and M. Kamionkowski, Unitarity limits on the mass and radius of dark matter particles, Phys. Rev. Lett. 64 (1990) 615. doi:10.1103/PhysRevLett.64.615.

[25] G. Arcadi et al., The waning of the WIMP? A review of models, searches, and constraints, Eur. Phys. J. C 78 (2018) 203. doi:10.1140/epjc/s10052-018-5662-y.

[26] M. Schumann, Direct detection of WIMP dark matter: concepts and status, J. Phys. G Nucl. Part. Phys. 46 (2019) 103003. doi:10.1088/1361-6471/ab2ea5.

[27] J. Lavalle and S. Magni, Making sense of the local galactic escape speed estimates in direct dark matter searches, Phys. Rev. D 91 (2015) 023510. doi:10.1103/PhysRevD.91.023510.

[28] A. H. Abdelhameed et al. (CRESST Collaboration), First results from the CRESST-III low-mass dark matter program, Phys. Rev. D 100 (2019) 102002. doi:10.1103/PhysRevD.100.102002.

[29] L. Voltano, The Gran Sasso Laboratory, Eur. Phys. J. Plus 127 (2012) 109. doi:10.1140/epjp/i2012-12109-8.

[30] L. Pattavina, Light dark matter investigation with CRESST, in: Proceedings of Science (Neutrino Oscillation Workshop 2018), Sissa Medialab, 2019, p. 096. doi:10.22323/1.337.0096.

[31] E. Armengaud et al. (EDELWEISS Collaboration), Searching for low-mass dark matter particles with a massive Ge bolometer operated above ground, Phys. Rev. D 99 (2019) 082003. doi:10.1103/PhysRevD.99.082003.

[32] R. W. Schnee et al., The SuperCDMS Experiment, in: Dark Matter in Astro- and Particle Physics, Springer Berlin Heidelberg, Berlin, Heidelberg, 2006, pp. 259–268. doi:10.1007/3-540-26373-X_20.

[33] F. Piquemal, Modane underground laboratory: Status and project, Eur. Phys. J. Plus 127 (2012) 110. doi:10.1140/epjp/i2012-12110-3.

[34] J. Hall, The SNOLAB underground laboratory, J. Phys.: Conf. Ser. 1468 (2020) 0122252. doi:10.1088/1742-6596/1468/1/012252.

[35] M. F. Albakry et al. (SuperCDMS Collaboration), A strategy for low-mass dark matter searches with cryogenic detectors in the SuperCDMS SNOLAB Facility (2023). arXiv:2203.08463.

[36] G. Angloher et al., EURECA conceptual design report, Phys. Dark Univer. 3 (2014) 41–74. doi:10.1016/j.dark.2014.03.004.

[37] Y. Meng et al. (PandaX-4T Collaboration), Dark matter search results from the PandaX-4T commissioning run, Phys. Rev. Lett. 127 (2021) 261802. doi:10.1103/physrevlett.127.261802.

[38] A. Abdukerim et al., PandaX-xT—A deep underground multi-ten-tonne liquid xenon observatory, Sci. China Phys. Mech. Astron. 68 (2025) 221011. doi:10.1007/s11433-024-2539-y.

[39] J. Cheng et al., The China Jinping Underground Laboratory and its early science, Annu. Rev. Nucl. Part. Sci. 67 (2017) 231–251. doi:10.1146/annurev-nucl-102115-044842.

[40] I. Manthos, DarkSide-20k: Next generation direct dark matter searches with liquid argon, Proc. Sci. EPS-HEP2023 (2024) 113. doi:10.22323/1.449.0113.

[41] E. Aprile et al. (XENONnT Collaboration), First dark matter search with nuclear recoils from the XENONnT experiment, Phys. Rev. Lett. 131 (2023) 041003. doi:10.1103/physrevlett.131.041003.

[42] D. S. Akerib et al. (LZ Collaboration), The LUX-ZEPLIN (LZ) experiment, Nucl. Instrum. Meth. A 953 (2020) 163047. doi:10.1016/j.nima.2019.163047.

[43] J. Heise, The Sanford Underground Research Facility at Homestake, J. Phys.: Conf. Ser. 606 (2015) 012015. doi:10.1088/1742-6596/606/1/012015.

[44] J. Aalbers et al. (XLZD Collaboration), A next-generation liquid xenon observatory for dark matter and neutrino physics, J. Phys. G Nucl. Part. Phys. 50 (2022) 013001. doi:10.1088/1361-6471/ac841a.

[45] V. Chepel and H. Araújo, Liquid noble gas detectors for low energy particle physics, JINST 8 (2013) R04001. doi:10.1088/1748-0221/8/04/r04001.

[46] J. Chen, Nuclear data sheets for A = 39, Nucl. Data Sheets 149 (2018) 1–251. doi:10.1016/j.nds.2018.03.001.

[47] A. S. Barabash, Average and recommended half-life values for two-neutrino double beta decay, Nucl. Phys. A 935 (2015) 52–64. doi:10.1016/j.nuclphysa.2015.01.001.

[48] M. J. Dolinski, A. W. P. Poon and W. Rodejohann, Neutrinoless double-beta decay: Status and prospects, Annu. Rev. Nucl. Part. Sci. 69 (2019) 219–251. doi:10.1146/annurev-nucl-101918-023407.

[49] S. Davidson, E. Nardi and Y. Nir, Leptogenesis, Phys. Rep. 466 (2008) 105–177. doi:10.1016/j.physrep.2008.06.002.

[50] A. Campani, V. Dompè and G. Fantini, Status and perspectives on rare decay searches in tellurium isotopes, Univer. 7 (2021) 212. doi:10.3390/universe7070212.

[51] A. Alessandrello et al., Measurements on radioactivity of ancient roman lead to be used as shield in searches for rare events, Nucl. Instrum. Meth. B 61 (1991) 106–117. doi:10.1016/0168-583X(91)95569-Y.

[52] P. Gorla et al. (CUORE Collaboration), The CUORE experiment: status and prospects, J. Phys.: Conf. Ser. 375 (2012) 042013. doi:10.1088/1742-6596/375/1/042013.

[53] M. J. Martin, Nuclear data sheets for A = 208, Nucl. Data Sheets 108 (2007) 1583–1806. doi:10.1016/j.nds.2007.07.001.

[54] S. Zhu and E. A. McCutchan, Nuclear data sheets for A = 214, Nucl. Data Sheets 175 (2021) 1–149. doi:10.1016/j.nds.2021.06.001.

[55] J. Chen, Nuclear data sheets for A = 40, Nucl. Data Sheets 140 (2017) 1–376. doi:10.1016/j.nds.2017.02.001.

[56] C. R. Cothern and J. E. Smith (Editors), Environmental Radon, Springer New York, 1987. doi:10.1007/978-1-4899-0473-7.

[57] B. Singh et al., Nuclear data sheets for A = 218, Nucl. Data Sheets 160 (2019) 405–471. doi:10.1016/j.nds.2019.100524.

[58] B. Singh et al., Nuclear data sheets for A = 215, Nucl. Data Sheets 114 (2013) 2023–2078. doi:10.1016/j.nds.2013.11.003.

[59] J. Aalbers et al. (LZ Collaboration), Background determination for the LUX-ZEPLIN dark matter experiment, Phys. Rev. D 108 (2023) 012010. doi:10.1103/physrevd.108.012010.

[60] T. Gaisser, Cosmic rays and particle physics, Cambridge University Press, 1990.

[61] J. A. Simpson and M. Garcia-Munoz, Cosmic-ray lifetime in the Galaxy - experimental results and models, Space Sci. Rev. 46 (1988) 205–224. doi:10.1007/BF00212240.

[62] F. Aharonian et al., High-energy particle acceleration in the shell of a supernova remnant, Nat. 432 (2004) 75–77. doi:10.1038/nature02960.

[63] P. L. Biermann, AGN and galactic sites of cosmic ray origin, World Scientific, 1994, pp. 217–286. doi:10.1142/9789814354158_0007.

[64] K. Nakamura et al. (Particle Data Group Collaboration), Review of particle physics - cosmic rays, J. Phys. G: Nucl. Part. Phys. 37 (2010) 075021. doi:10.1088/0954-3899/37/7A/075021.

[65] D. Atri and A. L. Melott, Modeling high-energy cosmic ray induced terrestrial muon flux: A lookup table, Rad. Phys. and Chem. 80 (2011) 701–703. doi:10.1016/j.radphyschem.2011.02.020.

[66] C. Waltham, Through-going muons in the Sudbury Neutrino Observatory, in: 27th International Cosmic Ray Conference, Vol. 3, Copernicus Gesellschaft, 2001, p. 991, ADS bibcode: 2001ICRC....3..991W.

[67] M. Aglietta et al. (LVD Collaboration), Neutrino-induced and atmospheric single-muon fluxes measured over five decades of intensity by LVD at Gran Sasso Laboratory, Astropart. Phys. 3 (1995) 311–320. doi:10.1016/0927-6505(95)00012-6.

[68] M. Ambrosio et al. (MACRO Collaboration), Vertical muon intensity measured with MACRO at the Gran Sasso Laboratory, Phys. Rev. D 52 (1995) 3793–3802. doi:10.1103/PhysRevD.52.3793.

[69] Ch. Berger et al. (Fréjus Collaboration), Experimental study of muon bundles observed in the Fréjus detector, Phys. Rev. D 40 (1989) 2163–2171. doi:10.1103/PhysRevD.40.2163.

[70] M. Crouch, An improved world survey expression for cosmic ray vertical intensity vs. depth in standard rock, in: 20th International Cosmic Ray Conference, Vol. 6, Nauka, 1987, p. 165, ADS bibcode: 1987ICRC....6..165C.

[71] Y. M. Andreyev, V. I. Gurentsov and I. M. Kogai, Muon intensity from the Baksan Underground Scintillation Telescope, in: 20th International Cosmic Ray Conference, Vol. 6, Nauka, 1987, p. 165, ADS bibcode: 1987ICRC....6..200C.

[72] I. A. Belolaptikov et al., The Baikal underwater neutrino telescope: Design, performance, and first results, Astropart. Phys. 7 (1997) 263–282. doi:10.1016/S0927-6505(97)00022-4.

[73] J. Babson et al. (DUMAND Collaboration), Cosmic-ray muons in the deep ocean, Phys. Rev. D 42 (1990) 3613–3620. doi:10.1103/PhysRevD.42.3613.

[74] C. Waltham, Response of AMANDA-II to cosmic ray muons, in: 28th International Cosmic Ray Conference (ICRC), Vol. 3, University Academy Press, 2003, p. 1373, ADS bibcode: 2003ICRC....3.1373W.

[75] G. F. Knoll, Radiation detection and measurement, 3rd Edition, John Wiley & Sons, Ltd., 1999.

[76] G. R. Gilmore, Practical gamma-ray spectrometry, 2nd Edition, John Wiley & Sons, Ltd., 2008.

[77] P. Y. Yu and M. Cardona, Fundamentals of Semiconductors: Physics and Materials Properties, Springer Berlin Heidelberg, 2010. doi:10.1007/978-3-642-00710-1_8.

[78] I. Mirion Technologies, Ultra low-background detector systems, application note (1995).

[79] J. Aalbers et al. (LZ Collaboration), First dark matter search results from the LUX-ZEPLIN (LZ) experiment, Phys. Rev. Lett. 131 (2023) 041002. doi:10.1103/physrevlett.131.041002.

[80] J. Aalbers et al. (LZ Collaboration), Dark matter search results from 4.2 tonne-years of exposure of the LUX-ZEPLIN (LZ) experiment, arXiv (2024). doi:10.48550/arXiv.2410.17036.

[81] G. Adhikari et al., nEXO: neutrinoless double beta decay search beyond 10^{28} year half-life sensitivity, J. Phys. G Nucl. Part. Phys. 49 (2021) 015104. doi:10.1088/1361-6471/ac3631.

[82] S. Abe et al., Search for the Majorana nature of neutrinos in the inverted mass ordering region with KamLAND-Zen, Phys. Rev. Lett. 130 (2023). doi:10.1103/physrevlett.130.051801.

[83] N. Abgrall et al. (LEGEND Collaboration), LEGEND-1000 preconceptual design report, arXiv (2021). doi:10.48550/arXiv.2107.11462.

[84] D. S. Akerib et al. (LUX Collaboration), The Large Underground Xenon (LUX) experiment, Nucl. Instrum. Meth. A 704 (2013) 111–126. doi:10.1016/j.nima.2012.11.135.

[85] S. Agostinelli et al., GEANT4 - a simulation toolkit, Nucl. Instrum. Meth. A 506 (2003) 250–303. doi:10.1016/S0168-9002(03)01368-8.

[86] D. S Akerib et al. (LZ Collaboration), Simulations of events for the LUX-ZEPLIN (LZ) dark matter experiment, Astropart. Phys. 125 (2021) 102480. doi:10.1016/j.astropartphys.2020.102480.

[87] J. Allison et al. (GEANT4 Collaboration), Recent developments in GEANT4, Nucl. Instrum. Meth. A 835 (2016) 186–225. doi:10.1016/j.nima.2016.06.125.

[88] V. V. Uzhinsky (GEANT4 Collaboration), The Fritiof (FTF) model in GEANT4, in: International Conference on Calorimetry for the High Energy Frontier, LLR, 2013, pp. 260–264.

[89] D. H. Wright and M. H. Kelsey, The GEANT4 Bertini cascade, Nucl. Instrum. Meth. A 804 (2015) 175–188. doi:10.1016/j.nima.2015.09.058.

[90] V. Pěč, V. A. Kudryavtsev, H. M. Araújo and T. J. Sumner, Muon-induced background in a next-generation dark matter experiment based on liquid xenon, Eur. Phys. J. C 125 (2024). doi:10.1140/epjc/s10052-024-12768-9.

[91] J. H. Hubbell and S. M. Seltzer, NIST, PML, X-ray mass attenuation coefficients, NIST Standard Reference Database 126 (2004). doi:10.18434/T4D01F.

[92] J. Aalbers et al. (LZ Collaboration), First constraints on WIMP-nucleon effective field theory couplings in an extended energy region from LUX-ZEPLIN, Phys. Rev. D 109 (2024) 092003. doi:10.1103/physrevd.109.092003.

[93] D. S. Akerib et al. (LZ Collaboration), Projected sensitivity of the LUX-ZEPLIN experiment to the $0\nu\beta\beta$ decay of ^{136}Xe, Phys. Rev. C 102 (2020) 014602. doi:10.1103/physrevc.102.014602.

[94] G. Pereira, C. Silva and V. N. Solovov, Energy resolution of the LZ detector for high-energy electronic recoils, JINST 18 (2023) C04007. doi:10.1088/1748-0221/18/04/C04007.

[95] D. S. Akerib et al. (LZ Collaboration), Projected WIMP sensitivity of the LUX-ZEPLIN dark matter experiment, Phys. Rev. D 101 (2020). doi:10.1103/physrevd.101.052002.

[96] B. J. Mount et al., LUX-ZEPLIN (LZ) technical design report (LZ Collaboration) (2017). arXiv:1703.09144.

[97] D. S. Akerib et al. (LUX Collaboration), Calibration, event reconstruction, data analysis, and limit calculation for the LUX dark matter experiment, Phys. Rev. D 97 (2018). doi:10.1103/physrevd.97.102008.

[98] G. J. Feldman and R. D. Cousins, Unified approach to the classical statistical analysis of small signals, Phys. Rev. D 57 (1998) 3873. doi:10.1103/PhysRevD.57.3873.

[99] A. Murphy and S. Paling, The Boulby Mine underground science facility: The search for dark matter, and beyond, Nucl. Phys. News 22 (2012) 19–24. doi:10.1080/10619127.2011.629920.

[100] P. R. Scovell et al., Low-background gamma spectroscopy at the Boulby Underground Laboratory, Astropart. Phys. 97 (2018) 160–173. doi:10.1016/j.astropartphys.2017.11.006.

[101] P. R. Scovell and S. M. Paling, Private communication, 2023.

[102] P. R. Scovell et al., Radioassay facilities at the STFC Boulby underground laboratory, Front. Phys. 11 (2023). doi:10.3389/fphy.2023.1310146.

[103] B. Ahmed et al., The NAIAD experiment for WIMP searches at Boulby mine and recent results, Astropart. Phys. 19 (2003) 691–702. doi:10.1016/S0927-6505(03)00115-4.

[104] J. B. R. Battat et al. (DRIFT Collaboration), Low threshold results and limits from the DRIFT directional dark matter detector, Astropart. Phys. 91 (2017) 65–74. doi:10.1016/j.astropartphys.2017.03.007.

[105] I. Ivaniouchenkov et al., ZEPLIN-I: A single phase liquid Xe detector for dark matter search, in: The third international workshop on the identification of dark matter, World Scientific, 2001, pp. 433–437. doi:10.1142/4684.

[106] G. J. Alner et al., The ZEPLIN II dark matter detector: Data acquisition system and data reduction, Nucl. Instrum. Meth. A 587 (2008) 101. doi:10.1016/j.nima.2007.11.005.

[107] T. J. Sumner, ZEPLIN-III: A two-phase xenon dark matter detector, in: The third international workshop on the identification of dark matter, World Scientific, 2001, pp. 452–456. doi:10.1142/4684.

[108] D. Malczewski, J. Kisiel and J. Dorda, Gamma background measurements in the Boulby Underground Laboratory, J. Radioanal. Nucl. Chem. 298 (2013) 1483–1489. doi:10.1007/s10967-013-2540-9.

[109] P. R. Scovell et al., Ultra-low background germanium assay at the Boulby Underground Laboratory, JINST 19 (2024) P01017. doi:10.1088/1748-0221/19/01/P01017.

[110] D. S. Akerib et al. (LZ Collaboration), The LUX-ZEPLIN (LZ) radioactivity and cleanliness control programs, Eur. Phys. J. C 80 (2020) 1044. doi:10.1140/epjc/s10052-020-8420-x.

[111] K. Hosokawa et al., Development of ultra-pure gadolinium sulfate for the Super-Kamiokande gadolinium project, Prog. Theor. Exp. Phys. 2023 (2022) 013H01. doi:10.1093/ptep/ptac170.

[112] E. Fairstein and S. Wagner, IEEE standard test procedures for germanium gamma-ray detectors, IEEE Std 325-1996 (1997). doi:10.1109/IEEESTD.1997.82400.

[113] COWI, AIT Boulby Mine geological and ground investigation report, Tech. rep., ICL Boulby mine (2021).

[114] C. J. Talbot, C. P. Tully and P. J. E. Woods, The structural geology of Boulby (potash) mine, Cleveland, United Kingdom, Tectonophys. 85 (1982) 167–204. doi:10.1016/0040-1951(82)90102-0.

[115] A. Barba-Lobo, V. M. Expósito-Suárez, J. A. Suárez-Navarro and J. P. Bolívar, Robustness of LabSOCS calculating Ge detector efficiency for the measurement of radionuclides, Rad. Phys. Chem. 205 (2023) 110734. doi:10.1016/j.radphyschem.2022.110734.

[116] A. Caño et al., Determination of a standard efficiency using the ISOCS uncertainty estimator for calculating the activity concentration of ^{226}Ra, ^{232}Th, and ^{40}K in concrete, Meas. 242 (2025) 115856. doi:10.1016/j.measurement.2024.115856.

[117] S574 LabSOCS calibration software, Tech. rep., Mirion Technologies, Inc. (2017).

[118] R. Britton and A. V. Davies, Characterisation of a SAGe well detector using GEANT4 and LabSOCS, Nucl. Instrum. Meth. A 786 (2015) 12–16. doi:10.1016/j.nima.2015.03.036.

[119] W. Johnson et al., Interspec v. 1.0.9, [Computer Software] (2021). doi:10.11578/dc.20221016.3.

[120] P. J. Karpius, Introduction to InterSpec for gamma-ray analysis [slides] (2020). doi:10.2172/1679988.

[121] M. McCartney, P. J. Kershaw, D. S. Woodhead and D. C. Denoon, Artificial radionuclides in the surface sediments of the Irish Sea, 1968–1988, Sci. Total Environ. 141 (1994) 103–138. doi:10.1016/0048-9697(94)90022-1.

[122] D. S. Akerib et al., Measurement of the gamma ray background in the Davis cavern at the Sanford Underground Research Facility, Astropart. Phys. 116 (2020) 102391. doi:10.1016/j.astropartphys.2019.102391.

[123] D. Malczewski, J. Kisiel and J. Dorda, Gamma background measurements in the Gran Sasso National Laboratory, J. Radioanal. Nucl. Chem. 295 (2013) 749–754. doi:10.1007/s10967-012-1990-9.

[124] K. Hosokawa et al., Development of a high-sensitivity 80 L radon detector for purified gases, Prog. Theor. Exp. Phys. 2015 (2015) 033H01. doi:10.1093/ptep/ptv018.

[125] Y. Takeuchi et al., Development of high sensitivity radon detectors, Nucl. Instrum. Meth. A 421 (1999) 334–341. doi:10.1016/S0168-9002(98)01204-2.

[126] Y. Fukuda et al. (Super-Kamiokande Collaboration), The Super-Kamiokande detector, Nucl. Instrum. Meth. A 501 (2003) 418–462. doi:10.1016/S0168-9002(03)00425-X.

[127] J. Mott, Search for double beta decay of ^{82}Se with the NEMO-3 detector and development of apparatus for low-level radon measurements for the SuperNEMO experiment, Ph.D. thesis, University College London (2013).

[128] X. R. Liu, Low background techniques for the SuperNEMO experiment, Ph.D. thesis, University College London (2017).

[129] U. Utku, Background and sensitivity studies for the LUX-ZEPLIN experiment, Ph.D. thesis, University College London (2020).

[130] E. Perry, Background mitigation in LZ and next generation rare event searches, Ph.D. thesis, University College London (2024).

[131] G. Pronost et al., Development of new radon monitoring systems in the Kamioka mine, Prog. Theor. Exp. Phys. 2018 (2018) 093H01. doi:10.1093/ptep/pty091.

[132] P. Pagelkopf and J. Porstendörfer, Neutralisation rate and the fraction of the positive ^{218}Po-clusters in air, Atmos. Environ. 37 (2003) 1057–1064. doi:10.1016/S1352-2310(02)00997-4.

[133] S. Shefsky, D. Rose and C. G. Parsons, A study of radon adsorption on activated carbon as a function of temperature, in: International Radon Conference, 1993, pp. V12–V18.

[134] R. Arnold et al. (SuperNEMO Collaboration), Probing new physics models of neutrinoless double beta decay with SuperNEMO, Eur. Phys. J. C 70 (2010) 927–943. doi:10.1140/epjc/s10052-010-1481-5.

[135] X. R. Liu, Radon mitigation strategy and results for the SuperNEMO experiment, J. Phys.: Conf. Ser. 888 (2017) 012085. doi:10.1088/1742-6596/888/1/012085.

[136] G. Alimonti et al. (Borexino Collaboration), The Borexino detector at the Laboratori Nazionali del Gran Sasso, Nucl. Instrum. Meth. A 600 (2009) 568–593. doi:10.1016/j.nima.2008.11.076.

[137] G. Heusser et al., ^{222}Rn detection at the μBq/m^3 range in nitrogen gas and a new Rn purification technique for liquid nitrogen, Appl. Radiat. and Isot. 52 (2000) 691–695. doi:10.1016/S0969-8043(99)00231-6.

[138] B. Singh et al., Nuclear structure and decay data for A = 222 isobars, Nucl. Data Sheets 192 (2023) 315–421. doi:10.1016/j.nds.2023.10.002.

[139] M. S. Basunia, Nuclear Data Sheets for A = 210, Nucl. Data Sheets 121 (2014) 561–694. doi:10.1016/j.nds.2014.09.004.

[140] H. Bateman, The solution of a system of differential equations occurring in the theory of radio-active transformations, Vol. v.15 (1908-1910), Cambridge Philosophical Society, 1910, pp. 423–427.

[141] B. Abi et al. (DUNE Collaboration), Deep Underground Neutrino Experiment (DUNE), Far detector technical design report, Volume II: DUNE Physics, arXiv (2020). arXiv:2002.03005.

[142] D. S. Akerib et al. (LZ Collaboration), Discrimination of electronic recoils from nuclear recoils in two-phase xenon time projection chambers, Phys. Rev. D 102 (2020) 112002. doi:10.1103/PhysRevD.102.112002.

[143] A. Manzur et al., Scintillation efficiency and ionization yield of liquid xenon for monoenergetic nuclear recoils down to 4 keV, Phys. Rev. C 81 (2010) 025808. doi:10.1103/PhysRevC.81.025808.

[144] J. Lindhard, M. Scharff, and H. Schiott, Range concepts and heavy ion ranges, Matt. Fys. Medd. Dan. Vid. Selsk 33, 14 (1963).

[145] P. Sorensen and C. E. Dahl, Nuclear recoil energy scale in liquid xenon with application to the direct detection of dark matter, Phys. Rev. D 83 (2011) 063501. doi:10.1103/PhysRevD.83.063501.

[146] D. S. Akerib (LUX Collaboration), Data acquisition and readout system for the LUX dark matter experiment, Nucl. Instrum. Meth. A 668 (2012) 1–8. doi:10.1016/j.nima.2011.11.063.

[147] S. Shaw and W. Turner, LZ data analysis: Software and frameworks [slides] (2021).

[148] G. Barrand et al., GAUDI - A software architecture and framework for building HEP data processing applications, Comput. Phys. Commun. 140 (2001) 45–55. doi:10.1016/S0010-4655(01)00254-5.

[149] A. Manalaysay et al., Spatially uniform calibration of a liquid xenon detector at low energies using ^{83m}Kr, Rev. Sci. Instrum. 81 (2010) 073303. doi:10.1063/1.3436636.

[150] D. S. Akerib et al. (LUX Collaboration), LUXSim: A component-centric approach to low-background simulations, Nucl. Instrum. Meth. A 675 (2012) 63–77. doi:10.1016/j.nima.2012.02.010.

[151] M. Szydagis et al., A review of basic energy reconstruction techniques in liquid xenon and argon detectors for dark matter and neutrino physics using NEST, Instrum. 5 (2021) 13. doi:10.3390/instruments5010013.

[152] P. Antonioli et al., A three-dimensional code for muon propagation through the rock: MUSIC, Astropart. Phys. 7 (1997) 357. doi:10.1016/s0927-6505(97)00035-2.

[153] V. A. Kudryavtsev, Muon simulation codes MUSIC and MUSUN for underground physics, Comput. Phys. Commun. 180 (2009) 339. doi:10.1016/j.cpc.2008.10.013.

[154] D. M. Mei et al., Early results on radioactive background characterization for Sanford laboratory and DUSEL experiments, Astropart. Phys. 34 (2010) 33. doi:10.1016/j.astropartphys.2010.04.003.

[155] C. Zhang, private communication (2014).

[156] J. Heise, The Sanford Underground Research Facility at Homestake, J. Phys.: Conf. Ser. 606 (2015) 012015. doi:10.1088/1742-6596/606/1/012015.

[157] N. Abgrall et al. (MAJORANA Collaboration), Muon flux measurements at the Davis campus of the Sanford Underground Research Facility with the MAJORANA DEMONSTRATOR veto system, Astropart. Phys. 93 (2017) 70–75. doi:10.1016/j.astropartphys.2017.01.013.

[158] V. A. Kudryavtsev, E. V. Korolkova and D. Woodward, Muon simulations for LZ using MUSIC and MUSUN, LZ note (2015).

[159] M. Richardson, Cosmic ray background estimations in large liquid argon detectors for proton decay via $p \to k + \nu$ and ν_e appearance from ν_μ beams, Ph.D. thesis, University of Sheffield (2015).

[160] M. Aglietta et al. (LVD Collaboration), Muon 'Depth intensity' relation measured by LVD underground experiment and cosmic ray muon spectrum at sea level, Phys. Rev. D 58 (1998) 092005. doi:10.1103/PhysRevD.58.092005.

[161] J. Ahrens, B. Geveci and C. Law, Paraview: An end-user tool for large data visualization, The Visualization Handbook (2005) 717–731.

[162] M. L. Cherry et al., Multiple muons in the Homestake underground detector, Phys. Rev. D 27 (1983) 1444–1447. doi:10.1103/PhysRevD.27.1444.

[163] D. E. Groom, N. V. Mokhov and S. I. Striganov, Muon stopping power and range tables 10 MeV-100 TeV, At. Data Nucl. Data Tables 78 (2001) 183–356. doi:10.1006/adnd.2001.0861.

[164] J. Aalbers et al. (LZ Collaboration), The design, implementation, and performance of the LZ calibration systems, JINST 19 (2024) P08027. doi:10.1088/1748-0221/19/08/p08027.

[165] S. W. Caddey et al., The Homestake gold mine, an early proterozoic iron-formation-hosted gold deposit, Lawrence County, South Dakota, US Geological Survey Bulletin 1857-J (1991) J1–J67. doi:10.3133/b1857J.

Appendices

A Principles of semiconductor detectors

When a gamma-induced electron interacts with a semiconductor, it imparts energy to the atomic structure. This energy causes an electron (negative charge carrier) in the valence band to be excited to the conduction band, leaving a hole (positive charge carrier). The valence band is populated with electrons bound to specific lattice sites, whereas in the conduction band electrons are free to move within the material and carry a current under an applied electric field. The minimum energy required to excite an electron to the conduction band from the top of the valence band furthest away from the atomic nuclei is called the band gap energy, E_g. In insulators, E_g is too high for the thermal excitation of electrons regardless of the applied temperature or the strength of the applied electric field. Conversely, in metals, the valence band is either only partially filled or overlaps with the conduction band, resulting in the absence of a distinct band gap. Consequently, neither of these types of materials is suitable for gamma spectroscopy as insulators cannot carry a current, while metals, due to the constant population of electrons in the conduction band, exhibit continuous current flow under an applied electric field; there would be negligible signal above the background from a gamma-ray interaction.

The background from charge carriers in semiconductors arises from thermal excitation of valence electrons due to lattice vibrations at any temperature above 0 K. Reducing the temperature, T, reduces this background (often referred to as "leakage current"), as the probability that an electron-hole pair will be produced is proportional to T. This relation is given by the following equation [76]:

$$P(T) \propto T^{\frac{3}{2}} e^{-\frac{E_g}{2kT}}, \tag{A1}$$

where k is the Boltzmann constant.

The gamma-ray energy absorbed, E_{abs}, will often be higher than E_g and the resultant excited electrons in the valence band will interact with other electrons, even those in lower energy bands, and multiple electron-hole pairs will be produced. Under an applied electric field, the electrons and holes will migrate in opposite directions causing a current to flow, which can be detected as a signal. The number of pairs, N, is related to E_{abs} by the following equation [76]:

$$N = \frac{E_{abs}}{\epsilon}, \tag{A2}$$

where ϵ is the average energy needed to create a pair of charge carriers in semiconductors, or one detectable quantum in scintillators. In semiconductors, ϵ is much smaller than in scintillators, as more photons/electrons are produced per interaction, leading to a better energy resolution and an improved signal-to-noise ratio.

There will be some impurities throughout a semiconductor such as a germanium crystal. However few, these impurities will disrupt the lattice structure and introduce either excess electrons, called negative donor impurities making an "n-type" semiconductor, or excess holes, called positive donor impurities making a "p-type" semiconductor. Natu-

rally, a germanium crystal will fall into either of these categories*, but to create specific p- or n-type crystals, certain impurities can be added purposefully; this action is called doping. Doping either increases the electron or hole population and as a result, decreases the band gap, increasing the conductivity of the crystal.

Semiconductor gamma-ray detectors operate based on electronic redistribution, which occurs when p-type and n-type semiconductors are in contact with each other. At the junction, charge carriers diffuse across and recombine, creating a region devoid of free charge carriers known as the depletion region. A diagram of this effect can be seen in Figure A1. The diffusion of carriers generates a natural potential voltage across the

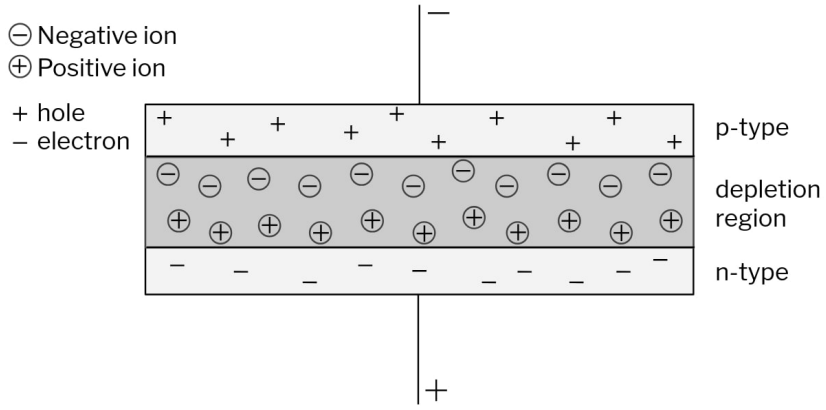


Figure A1: A diagram of the depletion region, created when contact is made between p-type and n-type semiconductors. The recombination of charge carriers occurs regardless of an applied voltage, but a reverse bias voltage widens this depletion region and is applied in this image.

junction, termed the contact or diffusion voltage, typically around 0.4 V for germanium. Applying an external voltage in reverse bias (positive to the n-side and negative to the p-side) widens the depletion region, reducing carrier recombination (a larger distance physically separates them) and improving charge collection. This process enhances the detector's signal and reduces noise. The depletion region is thicker on the side of the junction with the lowest dopant concentration. The depletion depth, d, can be estimated with the following equation [75]:

$$d \cong \left(\frac{2\kappa V_b}{eN}\right)^{\frac{1}{2}}, \tag{A3}$$

where κ is the dielectric constant of germanium, V_b is the applied reverse bias voltage, e is the charge on an electron and N is the concentration of dopant atoms on the side of the junction which has the lower concentration. In the depletion region, the majority carrier differs: holes dominate in p-type semiconductors, while electrons dominate in n-type. Even without a bias voltage, signals can be observed due to interactions within the depletion layer, but biasing significantly enhances performance, allowing precise gamma-ray detection.

*It is unlikely that the positive and negative impurities would cancel out, but if they did the semiconductor would be described as "compensated" [76].

B Muon traversing the LZ detector

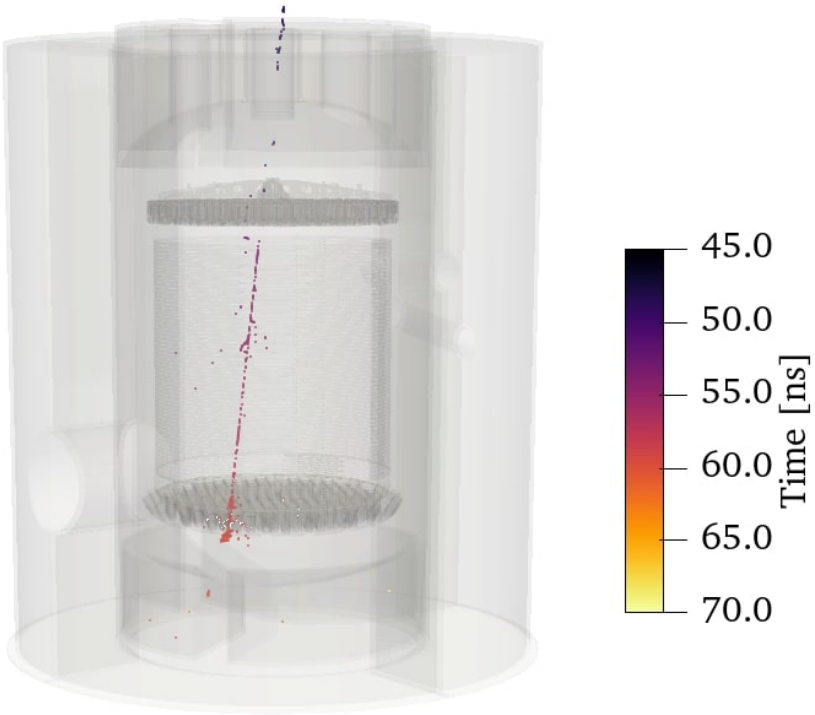


Figure B1: A reconstructed muon event from BACCARAT simulations. The (x, y, z) coordinates and time stamps of each energy deposition were plotted in Paraview to recreate the muon as it travelled through the OD, Skin and TPC of the LZ detector. BACCARAT geometries of these three detectors are shown is included in this image.

C Macro files for generating gamma lines from ^{232}Th and ^{238}U decay chains

```
# Macro file for simulating
the Th232 decay chain
/control/verbose 2
/control/saveHistory
/run/verbose 1
# Initialize kernel
/run/initialize
/gps/particle gamma
/gps/number 1 # per event
/gps/ene/type User
/gps/hist/type energy
# Th-232 decay chain gammas from
low to high energies
# b.r = branching ratio the values
are multiplied by
# Ac-228
/gps/hist/point 0.057766 0.0000
/gps/hist/point 0.057767 0.0047
/gps/hist/point 0.057768 0.0000
/gps/hist/point 0.099509 0.0000
/gps/hist/point 0.09951 0.0126
/gps/hist/point 0.099511 0.0000
# Pb-212
/gps/hist/point 0.115182 0.0000
/gps/hist/point 0.115183 0.00596
/gps/hist/point 0.115184 0.0000
# Ac-228
/gps/hist/point 0.129064 0.0000
/gps/hist/point 0.129065 0.0243
/gps/hist/point 0.129066 0.0000
/gps/hist/point 0.145848 0.0000
/gps/hist/point 0.145849 0.0016
/gps/hist/point 0.14585 0.0000
/gps/hist/point 0.153976 0.0000
/gps/hist/point 0.153977 0.0072
/gps/hist/point 0.153978 0.0000
/gps/hist/point 0.191352 0.0000
/gps/hist/point 0.191353 0.0012
/gps/hist/point 0.191354 0.0000
/gps/hist/point 0.199406 0.0000
/gps/hist/point 0.199407 0.0032
/gps/hist/point 0.199408 0.0000
.....
.....
.....
(many more gamma lines)
.....
.....
# Bi-212 (b.r = 0.6406)
/gps/hist/point 1.620499 0.0000
/gps/hist/point 1.6205 0.0094
/gps/hist/point 1.620501 0.0000
# Ac-228
/gps/hist/point 1.625059 0.0000
/gps/hist/point 1.62506 0.00255
/gps/hist/point 1.625061 0.0000
/gps/hist/point 1.630626 0.0000
/gps/hist/point 1.630627 0.0151
/gps/hist/point 1.630628 0.0000
/gps/hist/point 1.63828 0.0000
/gps/hist/point 1.638281 0.0047
/gps/hist/point 1.638282 0.0000
/gps/hist/point 1.666522 0.0000
/gps/hist/point 1.666523 0.00178
/gps/hist/point 1.666524 0.0000
# Tl-208 (b.r = 0.3594)
/gps/hist/point 2.61451 0.0000
/gps/hist/point 2.614511 0.3575
/gps/hist/point 2.614512 0.0000
/gps/pos/type Volume
/gps/pos/shape Cylinder
/gps/pos/centre 0.  0.  10.03 m
/gps/pos/radius 15.505 m
/gps/pos/halfz 15.505 m
# confine to physical volume
# "Rock_Daughter"
/gps/pos/confine Rock_Daughter
/gps/ang/type iso
/run/beamOn 1000000
```

```
# Macro file for simulating
the U238 decay chain
/control/verbose 2
/control/saveHistory
/run/verbose 1
# Initialize kernel
/run/initialize
/gps/particle gamma
/gps/number 1 # per event
/gps/ene/type User
/gps/hist/type energy
# Th-232 decay chain from low to
high energies
# b.r = branching ratio the values
are multiplied by
# Pb-210
/gps/hist/point 0.046538 0.0000
/gps/hist/point 0.046539 0.0425
/gps/hist/point 0.046540 0.0000
# Th-234
/gps/hist/point 0.063291 0.0000
/gps/hist/point 0.063292 0.0370
/gps/hist/point 0.063293 0.0000
/gps/hist/point 0.092380 0.0000
/gps/hist/point 0.092381 0.0213
/gps/hist/point 0.092382 0.0000
/gps/hist/point 0.092801 0.0000
/gps/hist/point 0.092802 0.0210
/gps/hist/point 0.092803 0.0000
/gps/hist/point 0.112849 0.0000
/gps/hist/point 0.112850 0.0021
/gps/hist/point 0.112851 0.0000
# Ra-226
/gps/hist/point 0.186210 0.0000
/gps/hist/point 0.186211 0.0364
/gps/hist/point 0.186212 0.0000
# Pb-214
/gps/hist/point 0.241994 0.0000
/gps/hist/point 0.241995 0.0726
/gps/hist/point 0.241996 0.0000
# Bi-214
/gps/hist/point 0.273799 0.0000
/gps/hist/point 0.273800 0.0013
/gps/hist/point 0.273801 0.0000
# Pb-214
/gps/hist/point 0.295223 0.0000
/gps/hist/point 0.295224 0.1847
/gps/hist/point 0.295225 0.0000
# Bi-214
/gps/hist/point 0.348919 0.0000
/gps/hist/point 0.348920 0.0011
/gps/hist/point 0.348921 0.0000
# Pb-214
/gps/hist/point 0.351931 0.0000
/gps/hist/point 0.351932 0.3572
/gps/hist/point 0.351933 0.0000
.....
.....
.....
(many more gamma lines)
.....
.....
.....
# Bi-214
/gps/hist/point 0.934060 0.0000
/gps/hist/point 0.934061 0.0309
/gps/hist/point 0.934062 0.0000
/gps/hist/point 0.964079 0.0000
/gps/hist/point 0.964080 0.0037
/gps/hist/point 0.964081 0.0000
# Pa-234m
/gps/hist/point 1.001309 0.0000
/gps/hist/point 1.001310 0.0102
/gps/hist/point 1.001311 0.0000
# Bi-214
/gps/hist/point 2.118549 0.0000
/gps/hist/point 2.118550 0.0116
/gps/hist/point 2.118551 0.0000
/gps/hist/point 2.204209 0.0000
/gps/hist/point 2.204210 0.0492
/gps/hist/point 2.204211 0.0000
/gps/hist/point 2.293399 0.0000
/gps/hist/point 2.293400 0.0031
/gps/hist/point 2.293401 0.0000
/gps/hist/point 2.447689 0.0000
/gps/hist/point 2.447690 0.0155
/gps/hist/point 2.447691 0.0000
/gps/pos/type Volume
/gps/pos/shape Cylinder
/gps/pos/centre 0.  0.  10.03 m
/gps/pos/radius 15.505 m
/gps/pos/halfz 15.505 m
# confine to physical volume
# "Rock_Daughter"
/gps/pos/confine Rock_Daughter
/gps/ang/type iso
/run/beamOn 1000000
```

D Systematic uncertainties of Boulby rock measurements

- Uncertainty on weight: ± 1 g.
- Uncertainty on branching ratio (b.r) is peak dependent and taken from Ref. [76].
- Uncertainty on efficiency, ϵ, with respect to a sample's density, length and diameter values entered into LabSOCS is peak dependent:
  - diameter ± 1 mm
  - length ± 5 mm
  - density ± 10%
- Uncertainty on LabSOCS software efficiency calculations at 1σ [117]:
  - Peak energies 0 - 50 keV: $< 20\%$
  - Peak energies 50 - 400 keV: 7 - 11%
  - Peak energies > 400 keV: 4 - 5%

To be conservative, the upper ends of the uncertainty ranges were used. Each peak in every sample has an efficiency calculated by LabSOCS. The uncertainty on this efficiency was calculated according to the peak's energy. Separate geometrical sources of systematic uncertainty were calculated as follows:

$$\sigma_{\epsilon\ geom} = \sqrt{\sigma^2_{diameter} + \sigma^2_{length} + \sigma^2_{density}}. \tag{D1}$$

The systematic uncertainty for each peak in each sample is found by summing all uncertainties in quadrature:

$$\sigma_{peak} = \sqrt{\left(\frac{\sigma_{\epsilon\ geom}}{\epsilon}\right)^2 + \left(\frac{\sigma_{\epsilon\ labsocs}}{\epsilon}\right)^2 + \left(\frac{\sigma_m}{m}\right)^2 + \left(\frac{\sigma_{b.r}}{b.r}\right)^2}. \tag{D2}$$

For each parent isotope, ^{40}K, ^{232}Th, ^{238}U and ^{235}U in a sample, the total systematic uncertainties of the weighted mean activities are:

$$\sigma_{systotal} = \frac{1}{\sqrt{\sum_{peak=1}^{n} \frac{1}{\sigma^2_{peak}}}}. \tag{D3}$$

This last step is repeated when the mean activity of a type of rock is calculated, for example, the mean ^{232}Th activity of all samples that were of the rock type anhydrite. Finally, to get the absolute error, σ_{total} is multiplied by the mean radioactivity for each of ^{40}K, ^{232}Th, ^{238}U and ^{235}U for each rock type.

E Gamma-rays from NORM isotopes identified in Boulby Mine rock samples

Table E1: Rock samples from Boulby Mine were screened by germanium detectors and their gamma spectra were analysed to find abundances of NORM isotopes. The most significant gamma-rays emitted by NORM isotopes were searched for (as listed in Ref. [76]) and of these, the following were detected across the samples. Some of these values differ slightly, but negligibly, from those published by NNDC as of 2024.

Series	Nuclide	Energy [keV]	Branching ratio
^{40}K	^{40}K	1460.82	0.1066
^{232}Th	^{212}Pb	238.63	0.436
	^{228}Ac	338.32	0.1127
	^{208}Tl	583.19	0.850
	^{208}Tl	860.56	0.125
	^{228}Ac	911.20	0.258
	^{228}Ac	968.97	0.158
	^{212}Bi	1620.74	0.0151
	^{208}Tl	2614.51	0.997
^{238}U	^{210}Pb	46.54	0.0425
	^{234}Th	63.28	0.048
	^{226}Ra	186.21	0.0356
	^{214}Pb	295.22	0.1841
	^{214}Pb	351.93	0.356
	^{214}Bi	609.31	0.4549
	^{214}Bi	1120.29	0.1491
	^{214}Bi	1764.49	0.1531
	^{214}Bi	2204.21	0.0491
^{235}U	^{235}U	143.76	0.1096
	^{235}U	163.33	0.0508
	^{235}U	185.72	0.572
	^{223}Ra	269.46	0.068
	^{219}Rn	271.23	0.108

F Calibrating a germanium detector

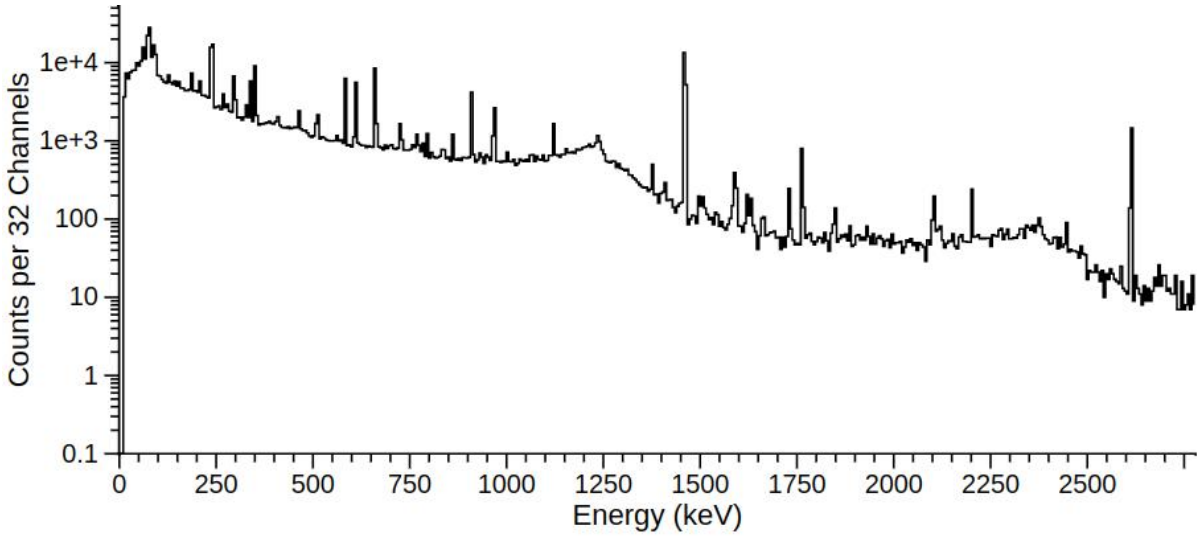


Figure F1: Energy spectra of a sample of Irish Sea sediment as measured by "Chaloner", a germanium detector. The many peaks from various radioisotopes enable Chaloner to be calibrated (a linear, channel-to-keV conversion).

G Detecting radon with the CAEN digitiser

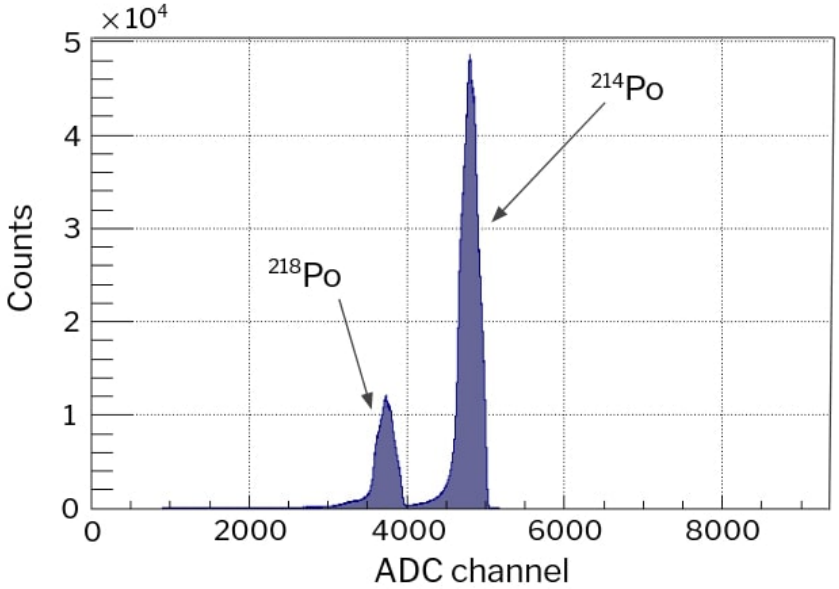


Figure G1: The counts collected over ∼11 days from an arbitrary amount of radon injected into a radon detector connected to the CAEN digitiser.

H Systematic uncertainties in radon detector calibration and radon emanation measurements

- Uncertainty of emanation time, t_{em}: 5 s
- Uncertainty of ^{222}Rn, ^{218}Po and ^{214}Po half-lives taken from Refs [138, 57, 54].
- Uncertainty of decay constants for ^{222}Rn, ^{218}Po and ^{214}Po is estimated by propagating the uncertainty of each corresponding half-life with the following equation:

$$\lambda = \frac{\ln(2)}{t_{\frac{1}{2}}}. \tag{H1}$$

- Uncertainty in ^{226}Ra activity, A_{-1}, from the Pylon source: ± 4 %
- Uncertainty in the number of radon atoms emanated from the Pylon source, N_0, during emanation time t_{em} is estimated by propagating the uncertainties of A_{-1}, λ_0 and t_{em} with Equation (7.16).
- Uncertainty in the detector efficiency, ϵ, is calculated by combining the statistical uncertainty in the activity from the Pylon source, σ_{A_0}, and the systematic uncertainty in the decay curve fitted to the data, σ_{A_i}, in quadrature:

$$\frac{\sigma_\epsilon}{\epsilon} = \sqrt{\left(\frac{\sigma_{A_0}^{\text{syst.}}}{A_0}\right)^2 + \left(\frac{\sigma_{A_i}^{\text{stat.}}}{A_i}\right)^2}, \tag{H2}$$

  where $i = 1$, 4 for ^{218}Po, ^{214}Po.
- Uncertainty in radon activity, A_0, is found by propagating the relative uncertainties of the decay curve fitted to the data and the efficiencies found above:

$$\frac{\sigma_{A_0}}{A_0} = \sqrt{\left(\frac{\sigma_{A_i}}{A_i}\right)^2 + \left(\frac{\sigma_\epsilon}{\epsilon}\right)^2}. \tag{H3}$$

I Minimum detectable signal derivation

Here, the Poisson distributions described by Equations (7.18) and (7.20) in Section 7.3.3 are approximated as Gaussian distributions to find the minimum detectable activity of a radon detector. To account for the continuous nature of the normal distribution, the continuity correction is applied: $N_C \to N_C - \frac{1}{2}$. Equation (7.18) can be rewritten as as follows:

$$P(N \geq N_C) \approx \frac{1}{2} - \int_0^{N_C - \frac{1}{2}} \frac{1}{\sqrt{2\pi B}} e^{-\frac{(N-B)^2}{2B}} dN. \tag{I1}$$

Let t $= \frac{N-B}{\sqrt{2B}}$,

$$P(N \geq N_C) \approx \frac{1}{2} - \int_0^{\frac{N_C - \frac{1}{2} - B}{\sqrt{2B}}} \frac{1}{\sqrt{\pi}} e^{-t^2} dt. \tag{I2}$$

Substituting in the error function, erf(x), gives

$$P(N \geq N_C) \approx \frac{1}{2}\left(1 - \text{erf}\left(\frac{N_C - \frac{1}{2} - B}{\sqrt{2B}}\right)\right) \leq 1 - \text{CL}, \tag{I3}$$

where by definition

$$\text{erf}(x) = \frac{2}{\sqrt{\pi}} \int_0^x e^{-t^2} dt. \tag{I4}$$

Similarly, Equation (7.20) can be expressed as:

$$P(N \geq N_C) \approx \frac{1}{2}\left(1 + \text{erf}\left(\frac{N_C - \frac{1}{2} - (S+B)}{\sqrt{2(S+B)}}\right)\right) \leq 1 - \text{CL}. \tag{I5}$$

By introducing the notation $E = \text{erf}^{-1}(2\,\text{CL} - 1)$, Equations (I3) and (I5) can be combined to find the inequality:

$$S - E\sqrt{2B} \geq E\sqrt{2(S+B)}, \tag{I6}$$

where the solutions to this are

$$S \begin{cases} \leq 0 \\ \geq 2E(E + \sqrt{2B})\,. \end{cases} \tag{I7}$$

Ignoring the unphysical solution of $S \leq 0$, the minimum detectable signal, N_D, is found when the above inequality is equal:

$$N_D = 2E(E + \sqrt{2B}). \tag{I8}$$